OCEAN BOTTOM FRICTION STUDY USING HYDRODYNAMIC MODELLING AND SEASAT-ALT DATA

by

R.C.W. Tang

A thesis
presented to The University of Manitoba
in partial fulfillment of the
requirements for the degree of
Master of Science
in
Geophysics

Winnipeg, Manitoba, 1984

OCEAN BOTTOM FRICTION STUDY USING HYDRODYNAMIC MODELLING AND SEASAT-ALT DATA

BY

ROGER C.W. TANG

A thesis submitted to the Faculty of Graduate Studies of
the University of Manitoba in partial fulfillment of the requirements
of the degree of

MASTER OF SCIENCE

TABLE OF CONTENTS

VI Ocean Bottom Friction Study

LIST OF FIGURES

LIST OF TABLES

ACKNOWLEDGEMENTS

I would like to thank my supervisor, Prof. W. Moon, for suggesting this topic and his help in every aspect of this thesis.

I am indebted to Mr. B. Atkinson of Atmospheric Environment Services (CANADA), who kindly made the weather charts available.

Special thank to Mr. A. Carswell for allowing use of his interactive digitization computer program to analyse the meteorological data.

I would like to thank Dr. B.H. Choi of Department of Civil Engineering, Sung Kyun Kwan University, for introducing me to the nonlinear hydrodynamic theory and its application, during his visit to the University of Manitoba. The discussions with Dr. Choi on ocean tide and storm surge modellings were invaluable.

The author was finanically supported by the Faculty of Graduate Studies Graduate Fellowship Committee and the Canadian Society of Exploration Geophysicists Scholarship Trust Fund (Gulf Canada Resources Ltd.) during this research.

ABSTRACT

Hydrodynamic models are used to analyse the sea surface elevations derived from the SEASAT altimetry over Hudson Bay (55°-62°N to 77°- 95°W) and. the East China Sea and Yellow Sea (25°- 38°N to 120°- 130° E). Periods of significant atmospheric disturbances during the SEASAT mission are selected for this study. These includes periods of Aug 4-6 and Aug 18-21 for Hudson Bay and July 28 - Aug 2 and Aug 18-21 for the East China Sea and Yellow Sea area. Meteorological forcing functions, which are needed by the sea model, are derived by a 2-dimensional grid that is governed by a set of theoretical and empirical meteorological relations over the study area. Over the East China Sea and Yellow Sea, in particular, tides are known to be important and introduce a large spatial and time variability in the sea surface elevation. They are thus also included in the sea model (M_2, S_2, K_1 and O_1 tidal constituents only). Through these models and some knowledge regarding other known sea surface phenomena (body tide, loading tide and steric variation of the ocean), a major part of the time-dependent sea surface variation can be predicted to compare statistically with the satellite altimetric measurements and can achieve the objectives of ocean bottom friction study. An optimization approach to estimate the ocean bottom frictional coefficient in the numerical sea models with respect to the altimeter data is described. To obtain a proper representation of the sea surface wind stress for this investigation, a number of recently published quadratic wind stress formulae have been tested prior to the modelling. Two of the most common frictional laws for the ocean bottom are dealt with as

described in this thesis. From a total of 15 satellite orbit tracks over the areas, the optimization results based on the linear and quadratic frictional laws indicate that the true ocean bottom friction coupling mechanism may be different from the conventionally adopted one. During calm to moderate wind speed (< 10 m/s) environment (Hudson Bay experiment), a range of linear friction coefficients between 0.239 cm/s and 0.712 cm/s was obtained while the quadratic friction coefficient was found ranging from 0.0019 to 0.00465. When the same experiment was performed during two tropical storm periods over the area of East China Sea and Yellow Sea, a consistent and smaller range of quadratic friction coefficient of 0.0023 to 0.0027 was obtained.

Part of this thesis is devoted to the study of the transient sea state in SEASAT altimetry. The SEASAT Geophysical Data Record (GDR) file contains a number of corrections for satellite instruments, atmospheric delay, oceanographic and geophysical effects. However, the transient sea surface variation due to ocean circulation and wind surge is not implemented. The magnitude of the variation demonstrates its significance in satellite (SEASAT) altimetry through the application of the Hudson Bay sea model on the selected time periods. The results also illustrate that the transient sea state modelling technique can easily be accommodated to other correction algorithms provided for the altimeter data.

Since the accuracy of the simulated sea surface elevation relies, in turn, on the accuracy of the input atmospheric forcing, comparisons between the geophysically derived wind fields and the

SEASAT-ALT retrieved wind fields are made and discussed. The geostrophic wind is extracted from the MSL pressure chart by a finite difference approximation of the atmospheric pressure gradient. From a large wind speed database of 780 data points, comparisons are made in the Hudson Bay experiment and values of 1.4 m/s for the mean difference and 1.8 m/s for the standard derivation are obtained over a wind speed ranging from 1 m/s to 10 m/s.

CHAPTER I

INTRODUCTION

For many years, efforts in geodynamics have been spent involving the development of the global ocean tide model (Schwiderski (1980) and Pekeris and Accad (1969)), the study of the lunar orbit, and the investigation of the variable rotation of the Earth (Munk and MacDonald (1960) and Lambeck (1975)). Most of these problems require some degree of knowledge about the ocean bottom friction and, even more importantly, the understanding of the coupling mechanism between the fluid ocean and the solid earth. In the development of the global ocean tide model, for example, one arrives at the bottom friction term through the integration of the Navier-Stokes equations with the Boussinesq replacement of the Reynolds stress tensor. A certain form of the ocean bottom friction term has to be assumed to complete the problem. Another well known example is the evaluation of tidal dissipation by finding the rate of work per unit surface done by the current at the sea floor (Jeffreys (1920,1921)). The success of this approach relies on the knowledge of the frictional coefficient (or constant) which links the frictional force at the ocean floor, either linearly or quadratically, with the current velocity. Not only is the frictional coefficient important in the context just described, a variety of storm surge and local ocean tide modelling problems require a similar dissipation mechanism to integrate the results more accurately (e.g. Heaps (1969), Tang and Moon (1984), Moon and Tang (1984), Stock (1976), and Grace (1930)).

The main objective of this thesis is to estimate the ocean bottom frictional coefficient. Two laws of friction are seperately considered: Frictional force proportional to (1) the depth-averaged current velocity and (2) the square of the depth-averaged current velocity. The methodology used to accomplish this objective requires the processed SEASAT altimetric-derived sea surface height data and the results of simulation from numerical models. The SEASAT altimeter data including some correction algorithms were obtained from the U.S. Department of Commerce, National Oceanic and Atmospheric Administration (NOAA). The time varying part of the sea surface elevation is extracted from the altimeter data by removing the time-independent geoid. This is done by employing the time varying sea surface equation derived in Chapter II (also discussed by Cartwright and Alcock (1981) and Le Provost (1983)). The periodical components of the time varying sea surface elevation can be analysed from various sources for their contribution to the net observation. Here, the global ocean tide tape prepared by Schwiderski (1978) is ultilized. As far as the non-periodical components, which are due to the meteorological driving forces, are concerned, a numerical sea model is used to reproduce their magnitudes. This 2-dimensional sea model explictly includes the ocean bottom term in the formulation, so that direct adjustment to the frictional coefficient can be performed to study the similarity between the model and the observations.

Two regions of coastal areas are selected in this study: (1) Hudson Bay area of Canada and (2) East China Sea and Yellow Sea area. As a first attempt, a 2-dimensional sea model based on the vertically integrated hydrodynamic differential equations is developed over Hudson Bay. This model is capable of reproducing the response of the sea caused by meteorological forcing, atmospheric pressure gradient and wind stress, imposed at the sea surface. As a consequence to the development, a 2-dimensional atmospheric model is also developed, using the finite difference form of the geostrophic wind-pressure gradient balance equation. This model operates at some height above the sea model and provides the necessary input forcings as a function of time and space to the sea model.

The finite difference sea model of the East China Sea and Yellow sea is a slightly different version, as it includes the modelling of advection phenomena and ocean tide beside the meteorological-induced motion (Choi (1980,1983)). Atmospheric model is also required to compute the forcings prior to the computation of the sea surface response. These models and the ones used in Hudson Bay form the fundamental algorithms for the objective of estimating the frictional coefficient from satellite altimeter data.

Since the model set up for a particular area is fully computerized, it provides an additional correction algorithm to the altimeter data collected by a satellite. Important physical parameters such as the ocean bottom topography and the shoreline geometry are built into the model with a selected resolution grid size. The correction algorithm which deals with the sea surface height variation caused by random meteorological forcings is not included in the SEASAT Geophysical Data Record (GDR) for the users. Although this correction procedure is only demonstrated for the selected time periods here, it can be used routinely once the correction scheme is set up for an area of interest. The results of this algorithm show that the sea surface elevation change along the satellite tracks can be sufficiently large to affect the accuracy for the SEASAT measurements needed for the geophysical and oceanographic applications.

This thesis also reports some results of wind speed comparison between the SEASAT-ALT inferred wind speed and the geostrophically derived sea surface wind speed. Beside the necessity of an independent set of data, the number of the comparisons also has to be sufficiently large so that any discrepancy observed during the correlation may be statistically evaluated. This type of comparison can be made possible in this study partly because of the size of the wind prediction model and partly because of the available frequency of the SEASAT passes during the selected time periods. Since the surface wind fields are derived from the Mean Sea Level (MSL) pressure charts, they are assumed to be good estimates of the ground truth. This assumption is also important in the comparison. The results of 780 wind speed comparisons, made during the periods of August 4 to 6 and August 18 to 21, during the Hudson Bay experiment are presented. To make an objective assessment of our comparison, recent results by various authors (Fedor and Brown (1982) and Wentz et al. (1982)) are also presented (Table 5.5).

CHAPTER II

ALTIMETER DATA AND THEIR USES FOR OCEAN BOTTOM STUDY

The general equation of time varying sea surface topography is discussed in this chapter. The analysis of such equation allows one to combine the corrected satellite observations with model results and to extract information regarding ocean bottom friction. Each component in the total time varying sea surface elevation equation is described.

First, two common problems in geophysics and oceanography that need the knowledge of ocean bottom friction coefficient are reviewed. These problems are not treated in this thesis, but they are outlined to signify the importance of ocean bottom friction. SEASAT objectives are then presented with an introduction to the algorithms which were used to process them into usable form. Some corrections due to the time varying meteorological forcings, but not implemented in the SEASAT GDR file, are then discussed and a modelling algorithm is proposed to solve these problems. Finally, based on the formulation of the time varying sea surface equation, an unique approach to study the ocean bottom friction is described.

1. Two Geodynamic Problems Involving Ocean Bottom Friction

(a) Tidal Dissipation

Although tidal dissipation has long been recognized as an important dynamic link to the behaviour of lunar orbit and the Earth's rotation, the actual mechanism of how the energy is lost is yet a fascinating problem that attracts researchers from various branches of physical science. As more and more evidence has pointed towards the ocean as a major energy sink (Lambeck (1975,1977, and 1980), Zahel (1978), and Pekeris and Accad (1969)), it has become critical to understand the role of the ocean in whole earth geodynamics and particularly the mechanism through which the tidal energy is dissipated.

To investigate the tidal energy dissipation in the world's ocean, one general approach is to use the energy integrals of Laplace's tidal equations. Substituting the momentum equations into the continuity equation (eq. Lambeck (1980) and Stock (1976)), gives:

$$\frac{d}{dt}\,(\mathrm{KE} + \mathrm{PE}) + \frac{d}{dt}\,\vec{\nabla}_s \cdot (\text{energy flux}) = \frac{dW}{dt} + \frac{dE}{dt} \qquad \ldots\ldots(2.1)$$

where the first and second terms on the left-hand side correspond to the rate of change of kinetic and potential energy per unit ocean surface. The last term on the left-hand side is the rate of divergence of the energy flux carried by the current. W is the work done on the unit ocean surface by the tidal potential and the movement of the sea floor due to solid tide and ocean tidal loading. The last term on the right-hand side is the rate of tidal energy dissipation. Equation (2.1) is the generally accepted formulation for tidal energy balance in ocean tidal problems. Despite different assumptions on the mechanism of dissipation, quite consistent results in the estimation of energy dissipation rate for M_2 tide were obtained by different authors. These are summarized by Lambeck

(1980). The mathematical form of the energy dissipation mechanism is usually expressed by ocean bottom friction but an other unspecified mechanism has also been used. Averaged over one tidal cycle P, equation (2.1) is simplified to:

$$0 = \left\langle \frac{dE}{dt} \right\rangle + \int_{OCEAN} \left\langle \frac{dW}{dt} \right\rangle \, ds \qquad \text{.....(2.2)}$$

with

$$\left\langle \frac{dW}{dt} \right\rangle = \frac{1}{P} \int_{T_o}^{T_o+P} \frac{dW}{dt} \, dt \qquad \text{.....(2.3)}$$

Since there is no transport of water across the ocean-continent boundaries, the energy flux term in equation (2.1) vanishes. Hence the rate at which the energy is dissipated throughout the ocean is proportional to the rate at which work is done on it by total tidal force.

To evaluate this dissipation term three approaches are possible (Munk and MacDonald (1960) and Lambeck (1975)):

(i) the rate of work per unit surface done by the current on the sea floor,

(ii) the rate of work per unit time and per unit area across the entrances to shallow sea, and/or

(iii) the mean rate of work per unit area done by the sun and moon on the ocean surfaces.

The first approach depends on the third power of the velocity and the rate of energy dissipation is expressed as:

$$\frac{dE}{dt} = \vec{U} \cdot \vec{F} \qquad \text{.....(2.4)}$$

where $\vec{F} = \rho\, C\, \vec{U}\, |\vec{U}|$ is the ocean bottom friction and C is the dimensionless coefficient of friction (quadratic friction coefficent). The exact value of C is unknown but experiences in tidal modelling indicate that the magnitude of C is approximately 0.003 (Schwiderski (1978)). An other form of ocean bottom friction can also be used to represent the dissipation mechanism (Jeffreys(1921) and Perkeris and Accad (1969)). For example, Perkeris and Accad (1969) introduce the friction force that is linearly proportional to the tidal velocity ($\vec{F} = \rho\, \eta\, \vec{U}$) rather than to the square of the velocity to model the M_2 tide in the world oceans. Unlike the dimensionless quadratic friction coefficient, the constant of proportionality in linear bottom friction law has dimension of velocity.

Lambeck (1977,1980) has presented an argument to show that most of the tidal energy is dissipated in shallow seas by comparing the rate of energy dissipation in open oceans to astronomical observed tidal accelerations. If the argument is indeed true, then energy dissipation can also be evaluated by calculating the rate of energy flux across the entrances to shallow sea through the divergence theorem plus the work done on the enclosed sea by the moon (Miller (1964,1966)). The last approach is the torque method. It is a direct calculation of the rate of at which work is done by the sun and moon on the ocean surface. This requires the ocean tide to be known everywhere and the inadequacy of present tidal models is often the weakness of this approach.

(b) Mechanism of Surge-Tide Interaction

An important physical oceanographic problem is the study of the interaction mechanism between wind surge and tide. In the last two decades, a surge forecasting program has actively been developed in the Great Britian for the North Sea area (Heaps (1965, 1969 and 1983), Davies (1976 and 1978) and Flather (1972, 1976 and 1979)). The major difficulty of operating such a program has been the influence of tide on the surge propagation. The ocean tide not only changes the surge amplitude but also the phase speed of the propagating surge.

It is only very recently that the interaction between these two phenomena has quantatively been studied (Prandle and Wolf (1978a and 1978b)). In their approach, the surge and tide interaction was examined by the cross-linkage terms representing the effect of surge on tide and that of the tide on surge. Their results show that the interaction mechanism between tide and surge is primarily associated with the bottom friction term.

2. An Oceanography Satellite: SEASAT

The SEASAT project was initiated in 1975 after completion of Phase A and B pre-project studies in 1973 and 1974. It was sponsored by the National Aeronautics and Space Adminstration (NASA) and the design of the spacecraft and the management of the project were the responsibility of various government agenies and scientific organisations; Goddard Space Flight Center (GSFC), Jet Propulsion

Laboratory (JPL), Lockheed Missiles and Space Company (LMSC), Wallops Flight Center (WFC), and Langley Research Center (LRC). The primary objective of the project was to demonstrate the feasibility of satellite remote sensing techniques for both oceanographic and geophysical applications.

The project featured a satellite that carried five mircowave sensors (see Figure 2.1) including a radar altimeter (ALT), a SEASAT-A satellite scatterometer (SASS), a synthetic aperture radar (SAR), a visible and infrared radiometer (VIRR), and a scanning mutichannel mircowave radiometer (SMMR). Its purpose was to give a continous global monitoring of oceanographic and surface meteorological features and phenomena. The data collected by SEASAT can be broadly classified into two types:

(1) Oceanographic data - wave heights, internal waves, sea ice, ocean topography, sea-surface temperature and winds, and the marine geoid.

(2) Meterorological data - clear air-sea temperature, cloud position, atmospheric water vapour concentration, and cloud-top brightness and temperature.

The SEASAT satellite, which was launched on June 28, 1978, carried the sensors onboard the 2290 kg platform in a nearly circular orbit with an inclination of 108 deg at an altitude of 800 km. It circled the earth 14 times per day (101 min orbit period), covering 95% of the global oceans every 36 hrs, and returned useful data until it experienced a massive short circuit in the power system. Shortly after the satellite's failure on day 105, NASA

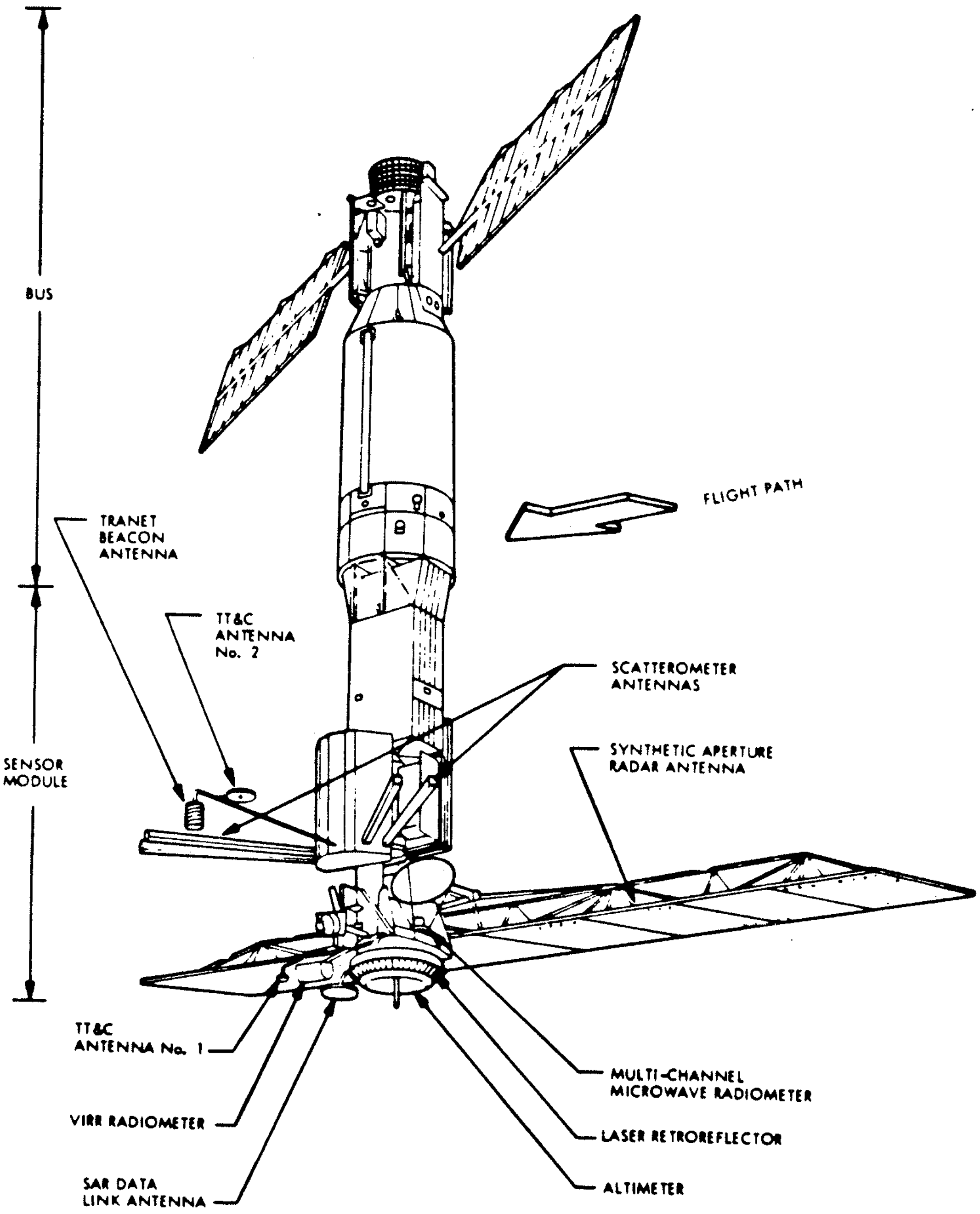

Figure 2.1: SEASAT Configuration.

reviewed the achievement of the SEASAT mission objectives and concluded that most of the original goals could be attained with the available data. To evaluate the SEASAT performance, the Seasat Data Ultilization Project was formed by NASA to determine the reliability of the data. The evaluation process is divided into 4 stages; engineering assessment, sensor evaluation, geophysical evaluation, and evaluation through applications.

The first and second stages are primarily concerned with the comparison of the in-flight data with prelaunch test data and the verification of the instrumental calibration and correction algorithms. While the first two stages have been completed for all sensors (Lame et al. (1980)), the third stage, which concentrates on the accuracy assessment of the geophysical parameters derived from the sensors, is only completed for the altimeter and scatterometer; the mircowave radiometer and synthetic aperture radar are currently under evaluation. Although the evaluation of the SEASAT data has not entirely been accomplished, the Seasat evaluation teams have demonstrated the feasibility of spaceborne microwave remote sensing techniques for measuring both oceanographic and atmospheric parameters to an useful accuracy. Some the evaluation results are presented in the Journal of Geophysical Research (AGU), Volume 87, Number C5, 1982 (SEASAT evaluation and accuracy assessment special issue). In this thesis an application of the SEASAT altimeter data is carried out to incorporate with final stage of the evaluation process, which is dealing with the usefulness of the altimeter data on different type of oceanographic and geophysical research tasks. In addition, comparisons between the wind speed retrieved from the altimeter data and that obtained from an independent source of data are made as part of the accuracy assessment on the oceanographic parameter derived from the altimeter.

Table 2.1 SEASAT Altimeter Data Gap Durations Greater Than Three Hours and Twenty Minutes in 1978

	Start Time		End Time		Duration	
Data Gap	Day*	Time,UT	Day	Time,UT	Days	Time,UT
1	178	1938:34	184	1917:04	5	2338:30
2	184	2142:15	185	0418:39		0636:24
3	185	0001:00	185	0418:39		0417:39
4	185	0426:17	187	0314:22	1	2248:05
5	187	0818:25	188	0421:44		2003:19
6	198	1918:15	205	1016:48	6	1458:33
7	206	0140:23	207	0258:41	1	0118:18
8	227	0112:30	227	1028:26		0915:56
9	230	0107:13	230	0937:26		0915:56
10	235	0916:19	235	1254:07		0337:48
11	238	0705:01	238	1117:14		0412:13
12	240	1340:33	244	1648:08	4	0306:35
13	244	1655:01	249	0144:20	4	0849:19
14	250	2223:56	253	0230:52	2	0347:56
15	253	0432:03	256	0243:38	2	2211:35
16	256	0407:01	256	1738:14		1331:13
17	256	1746:01	258	0006:24	1	0620:23

* Counting from the beginning of 1978.

Although the SEASAT mission was planned to have a continous sensor operation, there were a number of breaks in the data due to satellite maneuvers, engineering assessment activities, and hardware problems which gave rise to data anomalies. These anomalies include altimeter internal temperature changes above design limit, altimeter transmitter tripped off due to spacescraft bus voltage dropped below the design minimum, and the droping of the transmitter power. Table 2.1 lists the data gaps greater than more than 3 hours and 20 minutes. In addition, SEASAT data set also suffers from data anomalies due to geographic surface features. The most general types of these features, which result in an increase in automatic gain control (AGC) followed by an apparent increase in the Significant Wave Height (SWH), are islands, peninsulars, the edge of land boundaries, smooth open oceans, ocean ice, and raincells in open ocean. Fortunately, these types of anomalies occured infrequently and the processing algorithm would limit these effects to a constant values of 20 m in significant wave height (SWH) environment whenever they occured.

(a) SEASAT Altimetry

The SEASAT altimeter physically consists of two main components, (i) RF section with antenna attached and (ii) signal processor section. The first section is 1.048 m in diameter by 0.781 m high and the second component is 50.8 cm long by 34.2 cm wide by 25.3 cm high. The total weight of the altimeter is 93.8 kg which is approximately 1/25 of the weight of the satellite itself.

The altimeter coverage varies from 2.4 to 12 km depending on sensor pointing angle, field-of-view, and sea state. The main feature of the instrument, which is installed in the signal processor section, is the mircoprocessor implementation of the closed-loop range tracking, automatic gain control(AGU), and real-time estimation of SWH. In addition, a linear FM transmitter with 320 MHz bandwidth yields a 3.125 n-sec time delay resolution. Such a high resolution design of instrumentation is made in conjuction with the requirements of the experiment objectives.

Functionally, the altimeter measures the following quantities:

(1) the altitude between the spacecraft and the sea surface to 10 cm root-mean-square precision for 1 sec average.

(2) the significant wave height (SWH) from 1 to 20 m with an accuracy of 0.5 m or 10% , whichever is greater.

(3) the radar backscatter coefficients of the ocean surface beneath the satellite with an accuracy of at least 1 db.

All these accuracy specifications are based on the requirements of the geodetic and oceanographic communities. The requirement of 10 cm rms accuracy for height measurements enables the SEASAT altimeter to separate time varying features such as geostropic currents, tides, wind pile-up, and storm surge. A closely related function of the altimeter to the first requirement is the measurement of SWH. The necessity of SWH measurement is to remove the surface roughness bias in order to reach the 10 cm rms specification in altitude measurement. However, the SWH measurement also has its own purpose which is, when combined with surface temperature, wave spectra, and wind measurement, to forcast the world wide sea state. The last function of the altimeter is the measurement of the nadir wind magnitude at an elevation of 19.5 m. This requries the conversion of backscatter coefficients to wind speed by the Three Branch Algorithm which will be described in a later chapter.

(b) Observation on the Sea Surface Height and Wind Speed

The measurements of the distance between the satellite and the sea surface is based on the round-trip travel time , Δt, required for an electromagnetic pulse with a repetition rate of 1020 Hz, emitted from the altimeter antenna and then reflected back to the antenna by the sea surface. Since the pulse is transmitted from the altimeter electronics, the distance, h, between the altimeter antenna and the ocean surface measured by the altimeter has to be adjusted accordingly as follows:

$$h = \frac{\hat{c}}{2} (\Delta t + te) \qquad .....(2.5)$$

where $\hat{c}$ is the speed of light and te is the two-way travel time of the pulse from the antenna to eletronics. Each measurement given by the altimeter equipment is based on 10 pulses which occured during an interval of 0.1 s. The final height measurement provided in the altimeter GDR tape is the averaged value of 100 pulses in one second interval. This interval corresponds to a distance of 700 m between the centers of two circular satellite's eye views formed by the intersection of the sea surface and the wave front. In this manner, the altimeter gives a continuous observation as a function of latitude, longitude, and time.

Using an empirically determined ground processing algorithm, the information regarding the backscatter coefficient, σ_0 , of the ocean surface beneath the spacecraft can be obtained. The derivation of the backscatter coefficient is essentially based on the calibrated data from the AGC loop that is implemented in the Adaptive Tracker Unit(ATU) inside the signal processor section. The ATU is a microcomputer where height tracking, AGC, and the real time estimate of SWH are performed (Townsend (1980)). The algorithm, which is used to accomplish the estimation of σ_0 , was determined on the basis of prelaunch experimental data and is given by:

$$\sigma_0 = 39.93 - \mathrm{Cal}_i - \Delta \mathrm{AGC}_i + 30 \log \frac{h}{794.44} + L_{att} + L_{atm} + B \quad .....(2.6)$$

where

σ_0 - ocean backscatter coefficient in db.

Cali - measured value of the calibrate mode attenuator for step i.

ΔAGCi - AGCi-AGC; AGCi is the calibrated mode AGC for step i and AGC is the measured AGC of the ocean surface.

h - measured altitude

Latt - loss in antenna gain at the nadir due to off nadir pointing.

Latm - atmospheric loss.

B - bias determined from evaluating on orbit data.

The integer value i is chosen to minimize Δ AGCi in the process. The determinations of Latt and Latm require knowledge of the antenna pointing direction and local atmospheric condition. The value of B, which is roughly -1.5 db, has been determined tentatively during the Gulf of Alaska Experiment(GOASEX) with the available data from the GEOS and SEASAT orbit intersections. However, the source of error associated with this bias is not currently understood and this leads to an uncertainty to the wind speed inferred from the backscatter coefficient.

All the collected data were recorded by the NASA Satellite Tracking Data Network (STDN) where these data were then transmitted to the Goddard Space Flight Center (GSFC) for processing.

At GSFC the data are sorted, merged, and time tagged to produce a time ordered file called Project Master Data File (PMDF). There, the Attitude-Orbit (A-O) File was also created that contains both the Definitive Orbit File (DOF) and Definitive Attitude File (DAF). The DOF is a record of the SEASAT orbit defined by a set of earth centered coordinate system at 2 min intervals, whereas the DAF is a record of SEASAT attitude defined on a set of geocentric orbital reference axes as a function of time. All these files produced by GSFC were shipped to JPL for further processing.

The operations in the processing center at JPL were described by Tapley et al. (1982). These include data decommutation, units conversion, foot print calculation, instrument calibrations & corrections, blunder point editing, etc. The file produced after this step is called the Master Sensor Data Record (MSDR) which was then separated for individual sensor called the Sensor Data Record (SDR). The last step is the production of the Geophysical Data Record (GDR). This was formed by adding to each SDR the orbital information, coefficients and constants for data corrections due to oceanographic and atmospheric effects, and ancillary information such as marine geoid, ocean and solid earth tide models.

(c) Processing of Altimeter Data

In order to achieve the precision of 10 cm rms over 1 s interval specification, a number of corrections have to be applied to the raw measurements. The satellite height above the ocean surface, h, measured by the altimeter can be expressed as (Tapley et al. (1982)):

$$h = h^{*} - (h_{sg} \pm h_{in} + h_{atm} + h_{sr} \pm h_{g} \pm h_{t} \pm h_{o} + \epsilon) \qquad .....(2.7)$$

where

h^{*} - the distance from satellite center of mass to reference ellipsoid at the altimeter sub - satellite point as determined from SEASAT orbit computation.

h_{sg} - the effect of the spacecraft geometry including the distance from altimeter feed to satellite center of mass and the effect of spacecraft pointing in a nonvertical direction.

h_{in} - the sum of total instrumental delays including constant residual bias after all instrument corrections are made.

h_{atm} - sum of the atmospheric path length corrections due to the dry troposphere, wet troposphere, and ionosphere.

h_{sr} - the correction due to the sea surface and radar pulse interaction including the electromagnetic focusing and skewness of the surface waveheight distribution.

h_{g} - the geoid height.

h_{t} - the correction of the soild earth and ocean tides.

h_{o} - time varying ocean surface topography due to ocean circulation phenomena, inverse barometric response, wind setup, etc.

ϵ - random measurement noise.

These elements which contribute to the altimeter height measurement can be grouped into 3 components on the basis of their physical characteristics; (1) fundamental effects - orbital error, atmospheric effects, timing error from instruments, and orientation of the spacecraft, (2) ancillary effects - geoid model, solid earth and marine tides, time varying ocean surface features, and lastly (3) random error including unknown height contribution error. Except for the influence of the time varing ocean surface phenomena, the analysis and accuracy assessment of the rest of the effects have been conducted by variour authors and the results are summarized by Marsh (1982) and Tapley et al. (1982). Table 2-2 gives the source, type, and magnitude of errors for each of the above corrections.

As shown, the dominant source of error in the measurement is due to the inaccuracy of satellite orbit computation which in turn depends on the precision of the earth's gravity model, lunar and solar gravitational effects, solar radiation pressure, atmospheric drag, and tracking stations coordinates. The SEASAT orbit on GDR tape was determined to have approximately 1.5 m rms accuracy and it is long wavelength in nature of roughly once per revolution (Marsh and Williamson (1980)). Thus, studies of time dependent ocean surface features shorter than a few thousand kilometers should not be greaty affected by this. This inaccuracy in orbital determination, however, may result in a 'DC' shifting of the altimeter height measurements in regional or small scale study.

Table 2.2 SEASAT Altimeter Data Error Budget*.

Types of Error	Source of Error	Amplitude of Error (cm)	Residual Error After Modelling (cm)
Altimeter	Noise		5.0
Altimeter	Bias	10.0	2.0
Sea State Bias	Waveheight & tracker	7 2% of H	2% of H
Troposphere	Air Mass	240.0	0.7
Troposphere	Water Vapour	10.0-40.0	3.0
Ionosphere	Free eletrons	2.0-20.0	3.0
Liquid Water	Cloud Rain	10.0-100.0	
Orbital Error	Gravity	10.0 km	140.0
Orbital Error	Drag	300.0	30.0
Orbital Error	Solar Radiation	300.0	30.0
Orbital Error	Station Location	100.0	10.0
Timing	Data time tag		5.0
Depression of Sea level	Atmospheric Pressure	50.0	3.0
Geoid	Mass Distribution	100.0 m	2.0 m
Body Tide	Lunar and Solar Gravity	20.0	2.0
Ocean Tides	Lunar and Solar Gravity	100.0	10.0

* Tapley et al. (1982)

In the altimeter GDR tape, both the raw measurements and the sea surface height above the reference ellipsoid are included. The measurements of the sea surface height above the standard ellipsoid, defined by a semimajor axis of 6378.137 km and a flattening of 1/298.257, have been corrected for the instrumental effects from the sensor record and atmospheric effects using orbit information suppiled by GSFC. Also, values of geoid height, solid earth and ocean tides, and barometric pressure are also given in the GDR tape for the users. Although the 1.5 m rms orbital accuracy is observed, the experience from the investigation indicates that a value of 10 cm radial orbital accuracy can be achieved for future satellite if there is any improvement in both the geopotential field model and spacecraft design so that the effects of atmospheric drag and other forces exerted on the satellite are minimized. Two additional constant biases of height and time tag are also adopted for the GDR production. The value of the timing bias ,-79.4 ms, was confirmed by Tapley et al. (1979) and Schultz et al. (1982) from analysing global set of altimeter cross over measurements. The height bias was obtained by comparing the altimeter measurements with laser measurements over Bermuda (Kolenkiewicz and Martin, 1982). A value of 7 cm is reported. The analysis of the above corrections are very well documented and for more detailed discussion on their assessments, the reader is refered to the references given by Tapley et al. (1982).

3. Sea Truth Equation

For the global study, the corrections described by equation (2.7) are considered to be sufficient for the minimum requirements. However, if a detailed study for a certain area of interest is to be carried out, it is necessary to investigate and implement the time dependent sea surface variations due to the prevailing wind conditions, the shoreline geometry, and ocean bottom topography. Not only are they important in regional study, the ability of modelling both the vertical and horizontal motions of the sea are also useful for the correlation of sediment transport and the prediction of local water level.

When an oceanographic study which involves knowledge of the sea surface elevation change is desired in a small area that is comparable to the size of Hudson Bay or the East China Sea and Yellow Sea, the time varying ocean surface features have to be taken into account precisely. One can classify this time varying phenomena broadly into two types based on their periodicity of occurrences. The periodical components include the solid earth and ocean tides whereas the transient components are the ones due to the varying sea surface wind and pressure gradient fields. The sea surface height $h'(\phi,\lambda,t)$ above the standard ellipsoid is basically of type

$$h'(\phi,\lambda,t) = h_{or}(\phi,\lambda,t) - h_{a}(\phi,\lambda,t) - h_{re}$$

where (ϕ,λ,t) are the spatial and time coordinates, $h_{or}(\phi,\lambda,t)$ is the estimated orbital radius of satellite by ground tracking system, $h_{a}(\phi,\lambda,t)$ is the altimeter height after removing instrumental error and atmospheric delay, and h_{re} is the adpoted reference (or standard) ellipsoid. This equation is closely approximated by the geoid plus other known time varying sea surface phenomena (Le Provost (1983) and Cartwright and Alcock (1981)):

$$G(\phi,\lambda,t) + h_{b} + h_{ot} + h_{l} + h_{s} + h_{w} + h_{pg} + \epsilon_{0} = h'(\phi,\lambda,t) \qquad .....(2.8)$$

where

$G(\phi,\chi,t)$ - geoid above the standard ellipsoid
h_b - body tide of the solid earth
h_{ot} - ocean tide
h_{ℓ} - ocean induced loading tide of the earth crust
h_s - long wavelength (low frequency) steric variations of the ocean
h_w - sea surface fluctuation caused by wind
h_{pg} - sea surface fluctuation caused by pressure gradient
ϵ_o - contains unmodelled error of both satellite measurements and the time invariant part of the steric ocean surface set up by quasi-steady currents.

The time varying part of the sea surface $T(t)$ can then be expressed by:

$$T(t) = h_b + h_{ot} + h_{\ell} + h_s + h_w + h_{pg} \qquad \text{.....(2.9)}$$

Most of the items in the above equation are given in the SEASAT-ALT GDR except for the effects due to the meteorological forcings which require accurate information of local weather conditions. However, these effects can be attacked by solving the hydrodynamic differential equations in a given area. As will be shown later, this meteorologically induced sea surface height can be computed by the storm surge type of modelling approach (Tang and Moon (1984)). In continental shelf areas or coastal sea basins, some of these given items are considered to be insufficiently precise for specific application. For example the two global ocean tide models in the GDR by Schwiderski (1978) and Parke and Hendershott (1980) are primarily for deeper parts of the ocean, and their values in shelf areas may need to be recomputed. To study the ocean bottom friction from the SEASAT-ALT data, equation (2.8) is slightly rearranged as follow:

$$H'(\phi,\chi,t) - G(\phi,\chi,t) + \epsilon = T(t) + \epsilon_c \qquad .....(2.10)$$

where ϵ_c is introduced to represent error in the computation. Therefore, the left side of this equation corresponds to the altimetric-derived sea surface height with respect to a mean equilibrium signiture, normally the geoid, plus errors in altimeter data processing algorithms, while the other side is the computed total time varying sea surface height with respect to an initial state of rest, with some computational uncertainties.

The variable $G(\phi,\chi,t)$ can be substituted by any existing geoid model, although a local geoid will be the best to use. In SEASAT-ALT GDR, a fairly accurate geoid surface proposed by the Goddard Space Flight Center is included. The GEM 10B gravimetric geoid was constructed using global set of GEOS 3 altimeter data with GEM 9 data plus a global set of $1^\circ \times 1^\circ$ surface gravity data. Although this model was completed to degree and order of 36, it was found to have up to a few meters of error in some areas (Marsh and Martin (1982)). These uncertainties are significant since they may be included in the measurements if they were true anomalies. Thus an altimeteric-derived reference surface, SS3 surface, is chosen as the equilibrium sea surface in equations (2.8) and (2.10). This mean ocean surface is given above the standard ellipsoid and was constructed by Marsh and Martin (1982) using the the SEASAT ephemeris calculated by the Preliminary Gravity Solution - SEASAT 3 (PGS-S3) and SEASAT altimeter data from the period 28 July to 14 August. PGS-S3 contains data from GEM 9, SEASAT laser, S band, global gravimetry and GEOS 3 (GEM 10B (Lerch et al. (1981))) altimetry. In their analysis, both data sets are combined by accurate gridding techniques to yield global contour maps of the mean sea surface topography (SS3). The data of SS3 surface north of 60 degree and south of 63 degree are set to zero due to the possibility of ice bergs. This SS3 surface is believed to give a more accurate representation of the equilibrium sea surface than those computed previously (Marsh and Martin (1982) and Fu (1983)). Hence, the SEASAT altimeter GDR tape also accompanies the SS3 data set as an alternative reference geoid to the Goddard Earth Model 10B (GEM10B) earth gravity model which was adopted for the GDR production.

Figure 2.2 is a schematic diagram showing the SEASAT data collecting geometry. Equations (2.8) and (2.10) are inevitably contaminated by a number of errors which include (1) the SEASAT ephemeris error which was up to 1.5 m rms, (2) the numerical errors of gridding and interpolation for the production of the SS3 surface, and (3) some unknown systematic errors which can not be minimized by the gridding procedure.

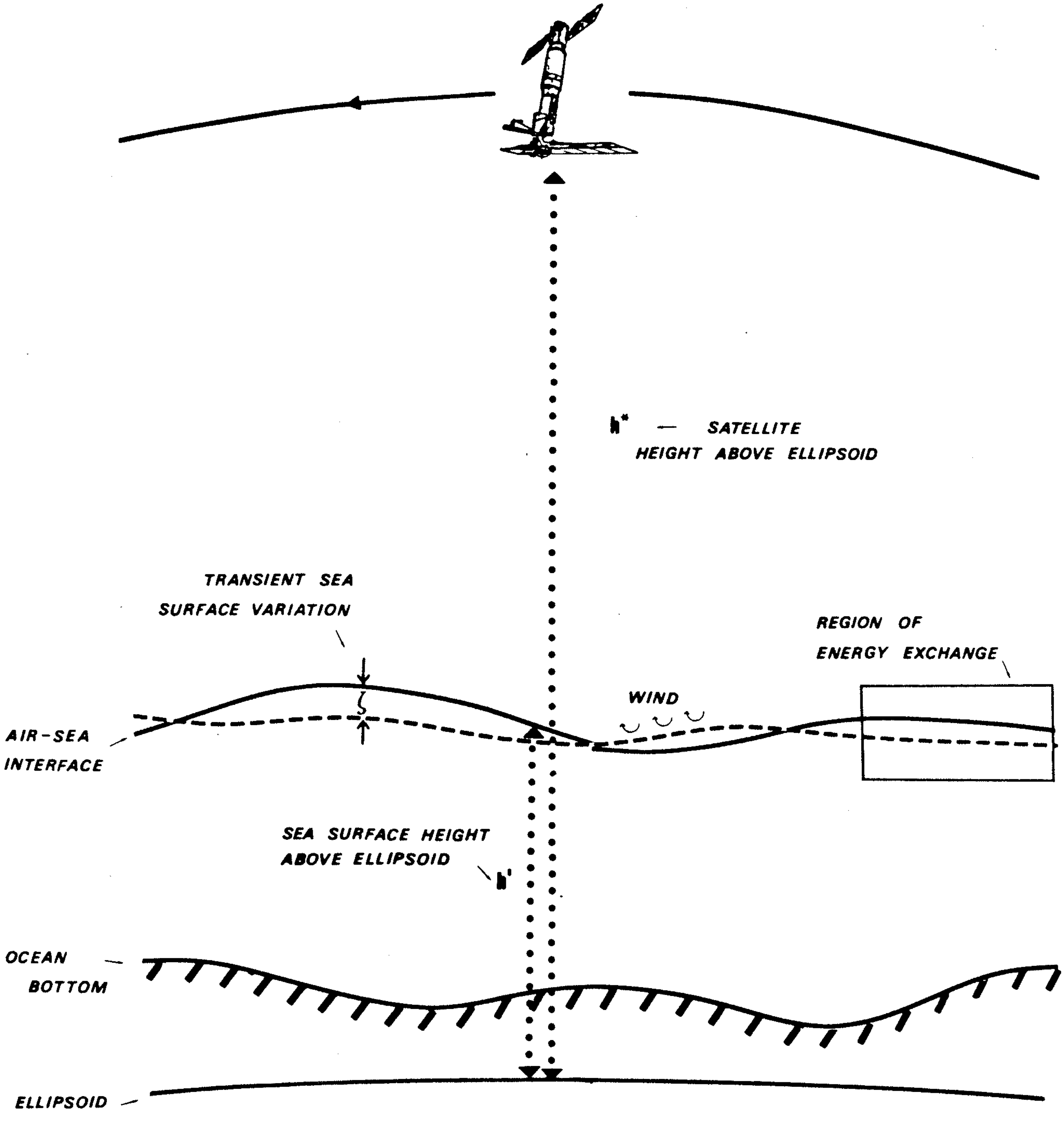

Figure 2.2 Schematic of SEASAT Data Collection. The Total Transient Sea Surface Variation Includes the Effect of Wind and Pressure Gradient.

(a) Equations of Time Varying Sea Surface Elevation for Study Areas

Equations (2.8) to (2.10) represent all time-dependent sea surface phenomena, as far as they are known, but obviously, the importance of each individual component varies significantly on locality. In the study of sea surface elevations and slopes of the northeast Atlantic Ocean (Cartwright and Alcock (1981)), for example, loading tide was completely ignored over the North Sea region, but its effect on open ocean was taken as a constant fraction of the ocean tide. Also, the meteorologically induced sea surface variation was calculated differently for shelf area and open ocean. In North Sea and adjacent shelf areas, it was computed by a surge-forecasting model while the same component was estimated by simple hydrostatic law in open sea. Similar simplifications were introduced by Le Provost (1983) in the English Channel where the body tide, loading tide, and steric variations of the ocean were ignored simply because of their small magnitudes compare to other oceanic events. The following gives a consideration to the relative magnitude of each component in the time varying sea surface equation for the study areas. Note that the wavelength of the periodical components is also considered.

Hudson Bay

The magnitude of the body tide in Hudson Bay was investigated by a computer program supplied by the U.S. Naval Surface Weapons Center (Schwiderski (1978)). This program allows the computation in form of a uniform grid, with grid spacing and tide constituents specified by the users. As a result, a $2^{\circ} \times 2^{\circ}$ grid over this area was constructed to analyze the distribution and magnitude of the body tide. It is unfortunate that the program is not capable to generate values for ocean loading in this area. The results of computation using M_2, S_2, K_1 and O_1 tidal constituents during selected time periods indicate an averaged value of body tide of less than 2.5 cm. Thus this effect was ignored in the time varying sea surface equation. Also the loading tide and the low frequency steric variations of the ocean were ignored due to their low frequency of occurence and probably small magnitude in this area. Hence the final time varying sea surface equation is given by:

$$h'(\phi,\chi,t) - G\ (\phi,\chi,t) = h_{ot} + h_{\omega} + h_{pg} + \epsilon_c \qquad \ldots\ldots(2.11)$$

where G (ϕ,χ,t) is the SS3 mean sea surface. Although the equation includes the ocean tide, its magnitude and wavelength are not well known in this area. Some justifications of it for Hudson Bay are discussed in the last chapter with results from numerical computations.

East China Sea and Yellow Sea.

Employing the same gridding program by Schwiderski (1978), the loading tide and body tide were calculated during the two selected mission times. As a first attmept, a 0.5° x 0.5° grid was used with all available tidal constituents (11 of them). This grid required excess computational time, thus it was cut down to two 1° x 1° grids for East China Sea and Yellow Sea, separately, with the first 4 major constituents as for the analysis in Hudson Bay. The loading tide in this part of the continental shelf was found to be less than 4.5 cm, a value which is negligible compare to the ocean tide itself. Ocean tide is a well known ocean phenomenon in that area and it dominates all other components in the time varying sea surface equation. The body tide values along the satellite tracks will be presented later, but their effects in the modelling of the ocean bottom friction coefficient are also negligible due to their extreme low frequency characteristic along each orbit tracks. Their largest and smallest magnitude are about -12 cm and 3 cm according to the computations. Consequently the time varying sea surface equation is also the same one used in the Hudson Bay study.

By tuning the ocean bottom friction coefficient in the equation of motion, adjustments of the computed sea surface elevation with respect to the altimeter observations can be made. This procedure is performed through the use of the sea truth equation (2.11). Results of these adjustments allow a set of frictional coefficients to be obtained for these areas. These set of values are then subjected to a mean square error type analysis to find the most optimum value of ocean bottom coefficient which gives the best agreement between modelled and observed sea surface elevation profiles.

CHAPTER III

THEORY OF HYDRODYNAMIC MODELLING

1. Hydrodynamic Theory

There are fundamentally two different approaches to storm surge forecast. The empirical method relates the storm surge to meteorological data from a regressive analysis. The theoretical method determines the storm surge from numerical integration of the equations of motion and continuity, with appropriate initial and boundary conditions.

The problems of reproducing the sea surface elevation by means of hydrodynamic theory have been the nonlinearity of the basic equations and the complexity of the natural sea basin topography. However, it is often assumed that the amplitude of the surge is small compared to the depth and that the horizontal scale is large compared to the depth. By these assumptions, the nonlinear terms in the dynamical equations are therefore negligible, resulting in an acceptable linear numerical sea model (or linear shelf model) (Heaps (1969,1983) and Tang and Moon (1984)). For the latter problem, one can either extensively simplify the geometry of the basin to obtain an analytical solution, or use numerical approximation to obtain a solution that is capable of matching the observation. With the advance of computer technology, the latter approach is more feasible in that only the stability and convergency of the solutions have to be considered.

When modelling is desired for both tide and surge, the nonlinear interaction between them may become important. As a consequence, a much improved nonlinear version was developed based on the linear shelf model. This nonlinear model is sometimes termed continental shelf model.

(a) Basic Equations of Linear Model

The hydrodynamical equations which constitute the motion of the sea due to barometric pressure and wind set up at the air-sea interface are well documented (e.g. Proudman (1954), Heaps (1969) and Zahel (1978)). Consider a water covered area, large enough so that the curvature of the earth and the latitudinally varying Coriolis acceleration have to be taken into account, then the linearized depth-integrated continuity equation and equations of motion are given by:

$$\frac{1}{R\cos\phi}\left\{\frac{\partial}{\partial\phi}(U\cos\phi)+\frac{\partial V}{\partial\chi}\right\}+\frac{\partial\zeta}{\partial t}=0 \qquad \ldots\ldots(3.1)$$

$$\frac{\partial U}{\partial t}+2\omega V\sin\phi=\frac{-gH}{R}\frac{\partial\zeta}{\partial\phi}-\frac{H}{\rho R}\frac{\partial P_a}{\partial\phi}+\frac{1}{\rho}(F_s-F_B) \qquad \ldots\ldots(3.2)$$

$$\frac{\partial V}{\partial t}-2\omega U\sin\phi=\frac{-gH}{R\cos\phi}\frac{\partial\zeta}{\partial\chi}-\frac{H}{\rho R\cos\phi}\frac{\partial P_a}{\partial\chi}+\frac{1}{\rho}(G_s-G_B) \qquad \ldots\ldots(3.3)$$

where

ϕ, ψ - latitude and east longitude

t - the time

ζ - the elevation of the sea surface

p_a - atmospheric pressure

U, V - the components of the depth-averaged current

F_s, G_s - the components of the friction of the wind on sea surface

F_B, G_B - the components of the friction on the ocean bottom

Equations (3.1) to (3.3) are written in spherical coordinates to allow more accurate application to global oceanographic problems. The components of the total stream U and V, are found by integrating the components of the horizontal current at depth Z below the undisturbed sea surface. The directions of the components are those of increasing ϕ, ψ (i.e. to the east and to the north respectively). The last two terms on the right-hand sides of the equations of motion ((3.2) and (3.3)) are the forcing terms of the hydrodynamic system. The input forces are those due to the atmospheric pressure gradient and wind stress whereas the dissipative force is that of the bottom friction. The basic assumption on the validity of the above equations is that the depth of the water is comparably larger than the amplitude of the transient surge. The time varying sea surface elevation ζ is then solved interactively with the atmospheric driving forces, which are derived from the atmospheric pressure gradient and sea surface wind, initialized to the equations at regular intervals. In addition, ancillary information is needed to complete the entire modelling procedure. This includes the radius of the earth R, the water depth field H, the density of the sea water ρ , the gravitational acceleration g, and the Earth's rotation ω .

Due to the integration with respect to depth, the solution derived contains no information regarding the vertical structure of the current within the body of water, which also implies that the sea water is well mixed and the buoyancy force is ignored. This assumption is quite general since the interfaces between layers within the water are not fixed and how they vary with time is often poorly known and thus they are very difficult to take into account. However, this vertically integrated sea model is adequate in most storm surge studies where one is mainly interested in the sea surface topography (Heaps (1969)).

This linear shelf model is applied to the Hudson Bay area (HB Sea Model) to demonstrate meteorologically induced surge phenomena that could have contributed to the SEASAT altimeter data. An application and results of this model with the satellite observations are presented and discussed in a later chapter.

(b) Basic Equations of Nonlinear Model

In the past decade, considerable progress has been made on the linear shelf model (Heaps (1969)). The result is a much improved non-linear version capable of simulating the main tides, surge, and tidal interaction. The major difference between the vertically integrated model and the non-linear version is the inclusion of the shallow water advection process (Heaps (1983), Flather (1976,1979), Davies and Flather (1978)). This feature has been shown to be important in coastal areas (Charnock and Crease (1957)). Including both the atmospheric driving force terms and the non-linear advective terms in the equations of motion, the non-linear version of the hydrodynamical equation is given by (Davies and Flather (1978) and Choi (1980)):

$$\frac{1}{R \cos\phi} \left\{ \frac{\partial}{\partial \phi} (U \cos\ ) + \frac{\partial U}{\partial \chi} \right\} + \frac{\partial \zeta}{\partial t} = 0 \qquad \ldots\ldots(3.4)$$

$$\frac{\partial U}{\partial t} + 2\,\omega\, V \sin\phi + \frac{V}{RH \cos\phi} \frac{\partial U}{\partial \chi} + \frac{U}{RH} \frac{\partial U}{\partial \phi} + \frac{V^2}{RH} \tan\phi$$

$$= \frac{-gH}{R} \frac{\partial \zeta}{\partial \phi} - \frac{H}{\rho R} \frac{\partial P_a}{\partial \phi} + \frac{1}{\rho} (F_s - F_B) \qquad \ldots\ldots(3.5)$$

$$\frac{\partial V}{\partial t} - 2\,\omega\, U \sin\phi + \frac{V}{RH \cos\phi} \frac{\partial V}{\partial \chi} + \frac{U}{RH} \frac{\partial V}{\partial \phi} - \frac{UV}{RH} \tan\phi$$

$$= \frac{-gH}{R \cos\phi} \frac{\partial \zeta}{\partial \chi} - \frac{H}{\rho R \cos\phi} \frac{\partial P_a}{\partial \chi} + \frac{1}{\rho} (G_s - G_B) \qquad \ldots\ldots(3.6)$$

The last three terms on the left-hand sides of equations (3.5) and (3.6) are the non-linear advective terms in spherical coordinate system, introduced to take proper account of the shallow water effects. Also different tidal constituents with surge can be computed together to include their interaction.

Similar to the linear shelf model, equations (3.4) through (3.6) are solved iteratively through time for ζ , U and V starting at an initial state of rest. Because of the capability of handling shallow water effects and modelling of different types of motion, this model has been used for sometime in the East China Sea and Yellow Sea (ECSYS) continental shelf to study the nature of tides without meteorological input forcings, i.e. pressure gradient and wind stress at the sea surface (Choi (1980)). Some agreeable comparisons between the model results with a number of measurements conducted across the continental shelf during the joint USA-China Marine Sedimentation Dynamics Study have been reported by Larson and Cannon (1983) and Choi (1983). In this thesis, this model is modified to include the meteorological forcing in addition to the original tidal forcing. The tidal constituents considered are of four kinds; two semi-diurnal tides (M_2 and S_2) and two diurnal tides (K_1 and O_1). The model results will be utilised to compare with the corrected SEASAT observations to study the ocean bottom friction coefficient in that area.

(c) Surface and Bottom Stress Terms

During the transient surge simulation, windfields over the sea surface has to be prescribed as a function of time and spatial coordinates. One method of doing this is to divide the study area into subareas where the neccessary atmospheric driving forces are extracted from weather charts by hand. This approach has been used by Heaps (1969) for the Irish Sea numerical modelling experiment in which the ground observations were included. Undoubtedly, this is a very tedious approach and not suitable for very lengthy computation.

A fast and efficient operation to replace this manual approach is devised in this study.

The wind stress is usually taken as a quadratic function of wind velocity, although linear stress law can also be considered at the air-sea interface. However, accumulated knowledge on the air-sea interaction shows that the wind has more tendency to satisfy the quadratic relation and furthermore, the quadratic coefficient that links the stress and velocity together has shown to be a linear function of wind speed. In this thesis, the quadratic wind stress law is adopted along with the quadratic stress coefficient proposed by Wu(1980,1982). Further discussion on the sea surface stress law in transient surge modelling is given in chapter 4.

In contrast, the mechanism of bottom stress that takes place at the sea floor is not well understood and two alternative representations are acceptable in numerical moelling. If the linear stress law is assumed to be the bottom frictional dissipation mechanism for the transient surge, the bottom stress terms are given by:

$$F_B = \frac{\eta \rho}{H} U \quad , \quad G_B = \frac{\eta \rho}{H} V \qquad .....(3.7)$$

where η is the linear stress coefficient having a typical value of 0.24 cm/s (Weenink (1958)). For both surge and tide modelling, the linear law has been demonstrated to be a reasonable approximation (e.g. Grace (1931) and Heaps (1969)).

The second, more commonly used, alternative of frictional dissipation is to express the bottom stress in terms of square of the velocity. This is expressed as:

$$F_B = \frac{C\rho}{H^2}\,\vec{U}\cdot\vec{U} \quad , \quad G_B = \frac{C\rho}{H^2}\,\vec{V}\cdot\vec{V} \qquad .....(3.8)$$

where C is the quadratic stress coefficient which traditionally takes values close to 0.003. Although these values have been used in a variety of hydrodynamic modelling with sucess (Flather and Heaps (1975), Flather and Davies (1978) and Choi (1980)), whether the particular numerical value used is applicable to global ocean or different continental shelf remains unknown. The investigation of both linear and quadratic bottom coefficients constitute the major objective in this thesis. Using equation (3.7) as frictional dissipation, linear shelf equations can be written, without loss of generality, as (Heaps (1969)):

$$\frac{\partial \zeta}{\partial t} = -\frac{\alpha}{\cos\phi}\left(\frac{\partial}{\partial \phi}\left(U \cos\phi\right) + \frac{\partial V}{\partial \chi}\right) \qquad .....(3.9)$$

$$\frac{\partial U}{\partial t} = -\lambda U - 2\omega \sin\phi\, V - \beta H \frac{\partial \zeta}{\partial \phi} + \gamma P \qquad .....(3.10)$$

$$\frac{\partial V}{\partial t} = -\lambda V - 2\omega \sin\phi\, U - \frac{\beta H}{\cos\phi} \frac{\partial \zeta}{\partial \chi} + \gamma Q \qquad .....(3.11)$$

where

$$P = F_s - \delta H \frac{\partial P_a}{\partial \phi} \qquad \text{.....(3.12)}$$

$$Q = G_s - \frac{\delta H}{\cos\phi} \frac{\partial P_a}{\partial \chi} \qquad \text{....(3.13)}$$

and $\alpha = 0.5922$, $\beta = 0.31780$, $\gamma = 0.63008$, and $\delta = 0.01645$.

The constants 0.5922, 0.31780, 0.63008, and 0.01645 are introduced for unit conversions. In the present analysis, $R = 6371$ km, $g = 9.80$ m/s^2, and the density of water is taken to be 1025 km/m^3. The first terms on the right-hand side of equations (3.10) and (3.11) can be identified as the result after rearranging the linear frictional dissipation of equation (3.7) (Lui (1982)).

(d) Initial and Boundary Conditions

The supply of atmospheric energy and the dissipation of frictional energy in the sea model occur continuously during the computation of the sea elevation, and after a period of time the influence of the initial conditions becomes negligible. To solve both types of basis equations (equations (3.1) through (3.3) and (3.4) through (3.6)), the following initial conditions are used:

$$\zeta(\phi,\chi,t) = U(\phi,\chi,t) = V(\phi,\chi,t) = 0 \quad \text{at } t=0 \qquad \text{.....(3.14)}$$

These conditions imply that the sea surface elevation change is generated from an initial state of rest and the sea surface at this state is called the initial state of equilibrium.

There are basically two types of boundary conditions:

(i) Condition of vanishing flow across the coastal boundaries at any time, i.e.,

$$U \cos \psi + V \sin \psi = 0 \qquad \ldots\ldots (3.15)$$

where ψ denotes the inclination of the normal to the northernly direction.

(ii) Condition at the open boundaries:

There are several alternative expressions for open boundaries depending on the type of modelling and the structure of the numerical scheme. For tide and surge simulation, Davies and Flather (1978) used the following open boundary condition for sea surface elevation in their North Sea model which was previously developed by Davies (1976):

$$\zeta(\phi, \chi, t) = \zeta_m(\phi, \chi, t) + \zeta_T(\phi, \chi, t) \qquad \ldots\ldots (3.16)$$

where $\zeta_m(\phi, \chi, t)$ is the surge elevation due to the meteorological influence either observed or computed by simple hydrostatics law at the open boundaries and $\zeta_T(\phi, \chi, t)$ is the part due to tidal motion given by:

$$\zeta_T(\phi,\chi,t) = \zeta_0(\phi,\chi) + \sum_i f_i \hat{H}_i(\phi,\chi) \operatorname{Cos}(\hat{V}_i + \hat{\alpha}_i t + \hat{U}_i - \hat{g}_i(\phi,\chi)) \quad ..(3.17)$$

where

$\zeta_0(\phi,\chi)$ - mean sea level is taken to be zero

f_i , $\hat{U}_i$ - nodal factors

$\hat{H}_i(\phi,\chi)$ - the amplitude of constituent i

$\hat{\alpha}_i$ - the speed of the constituent

$\hat{V}_i$ - the phase corresponding equilibrium constituent at time = 0 at Greenwich

$\hat{g}_i(\phi,\chi)$ - the phase lag of the tidal constituent behind the equilibrium constituent

The above two open boundary conditions are used in the ECSYS sea model. Alternatively, the tidal current and surge current can be specified at the open boundaries through the radiation condition used by Flather (1976):

$$q = q_m + q_T + \sqrt{\frac{g}{H}}\,(\zeta - \zeta_m - \zeta'_T) \quad .....(3.18)$$

where

q_T - ith consitutent tidal current at the open boundary

ζ'_T - ith consitutent tidal amplitude at the open boundary

q_m - surge current at the open boundary

ζ'_m - surge amplitude at the open boundary

The tidal part of the normal current q_T is determined from the following:

$$q_T = \sum_i f_i \hat{Q}_i \cos(\hat{\sigma}_i t + \hat{V}_i + \hat{U}_i - \hat{\gamma}_i)) \qquad \ldots\ldots(3.19)$$

where

$\hat{Q}_i$ - amplitude of the normal component of the depth-averaged current of constituent i

$\hat{\gamma}_i$ - phase of the current of tidal constituent i

Slightly different expressions can be derived from the above conditions in different type of simulation. For example, Flather (1979) used equations (3.18) and (3.19) with only M_2 and S_2 tidal constituents in storm surge modelling whereas Heaps and Jones (1979) and Davies (1976) used exactly the same consitutents but employed equation (3.16) instead.

Perhaps the simplest open boundary condition in surge modelling is

$$\zeta(\phi, \chi, t) = 0 \qquad \ldots\ldots(3.20)$$

(Heaps (1969)).

Although this condition does not take proper account of the damping due to loss of energy from a model to the neighbouring ocean, it is found to be a good first approximation if the sea basin is relatively shallow compared to the nearby ocean (Heaps (1969) and Groen and Groves (1962)). In Heaps'(1969) experiment, the surge along the continental shelf edge, marked roughly by a 200 m depth contour was assumed to be permanently zero. The simulated results were satisfactory in comparison to observations. It appears that a proper representation of the open boundary condition is still an unresolved problem. In the present numerical HB sea model, the condition of equation (3.20) is used.

2. Numerical Implementation

The hydrodynamic equations ((3.1) through (3.6)) are now represented by an explicit finite difference method. A finite difference method is said to be explicit if the solutions of the difference equations at a certain point are calculated from the known/previous calculated values. On the other hand, the method is said to be implicit if some new unknown values are coupled by a set of equations which must be solved simultaneously. The numerical structure used in the HB sea model is an explicit one and is characterized by Heaps (1969):

(1) Time derivatives in the dynamical equations are replaced by the combination of forward and backward time difference.

(2) Space derivatives , on the other hand, are replaced by the averaged central space difference.

The finite difference technique to approximate the nonlinear dynamical equations is the angled derivative method by Roberts and Weiss (1976). This is an explicit method that relies on the sequential updating of the current values over the grid to evaluate derivatives in the advective terms at middle time step. The method employed for implementing this experiment is described by Flather and Heaps (1975), Flather and Davies (1978), and Choi (1980).

(a) The Grid and Depth Field

Hudson Bay Sea Model

The type of finite difference grid used in the solution of the basic differential equations is a staggered grid (Figure 3.1). The grid lines consist of parallels of latitude spaced at interval $\Delta \chi$ and lines of longitude spaced at interval $\Delta \phi$ degree. There are two types of points defined by the grid: elevation points (circles) where ζ is evaluated and stream points (crosses) where U and V are evaluated. The natural sea basin is modelled by this grid so that the coastal boundaries are formed by line segments connecting stream points with the open sea boundaries connected by elevation points (Ramming and Kowalik (1980)). These are in conjuction with the boundary conditions (equations (3.15) and (3.20)). Figure 3.2 illustrates this method of boundary reconstruction for Hudson Bay, with the grids for elevation and stream points which are superimposed in ϕ and χ plane.

Since the grid is set up in this fashion, one can classify many types of elevation and stream points based on their locations within the grid. For example, an elevation or stream point may be located in the grid as follows:

Elevation points - outside the model sea, or on one of its open boundaries, or within the sea.

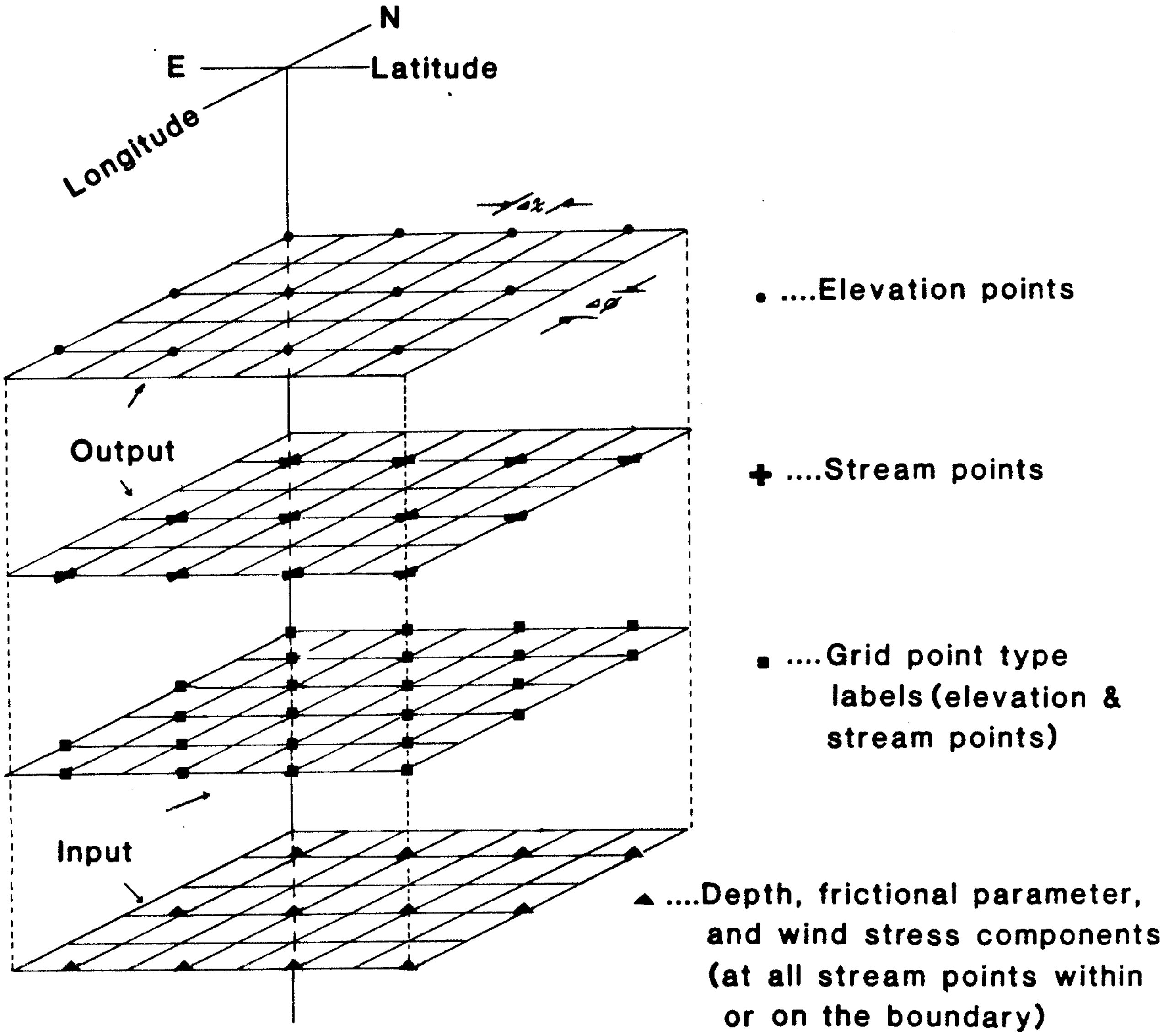

Figure 3.1: Finite Differnece Grid Construction: Schematic Staggered Finite Difference Grid Showing the Arrangement of the Input and Output Points. The Input Points Consist of Water Depth, Sea Surface Stress Components, and Frictional Coefficient (assumed uniform everywhere) Whereas the Output Points Contain the Time Varying Sea Surface Elevation and Depth-integrated Current Components.

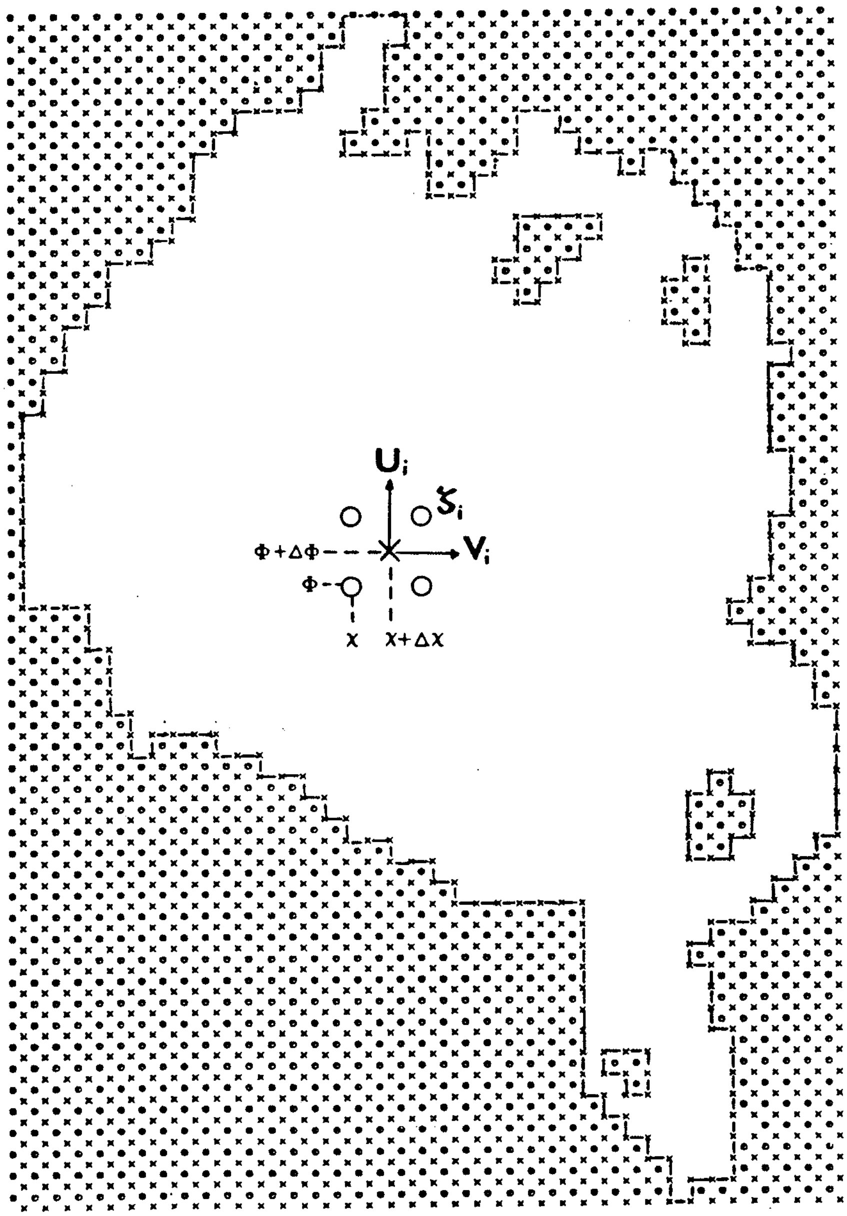

Figure 3.2: Hudson Bay Numerical Grid. Diagram Showing the Finite Difference Grid Representation of Hudson Bay, Canada. Symbols are; o Elevation Points, x Stream Points, o--o--o Open Boundary, and x-x-x Coastal Boundary.

Stream points - outside the model sea, or on one of its coastal boundaries, or within the sea.

Thus, there are 22 different types of grid point location which can readily be identified, 3 for elevation points and 19 for stream points. Table 3.1 summarizes the grid point types which are denoted by integers 1 to 22. Figure 3.3 shows some of their geometry and orientation for the stream point locations in the model sea and Figure 3.4 indicates the corresponding labels at every stream point in Hudson Bay (Heaps (1969) and Lui (1982)).

The water depth field of Hudson Bay is obtained from the bathymetric chart published by the Canadian Hydrographic Service, Department of Fisheries and the Environment in 1977 (Figure 3.5). The bottom topography of Hudson Bay is characterized by a central depression having a typically value of 200 m. This area occupies roughly 10% of the total model area. About 60% of Hudson Bay has water depth between 100 m to 150 m. The coast line is relatively smooth except at the south end of the model, James Bay. This makes the set up of the grid relatively easy. The digitized depth Hi, wind stress components Pi and Qi, and bottom friction components Fb and Gb are defined at every stream point of the model (Figure 3.1).

Label 5 (Stream point at a 90 deg corner of the coastal boundary)

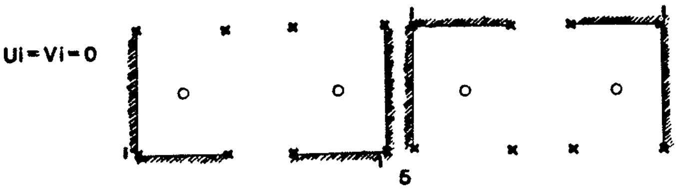

Label 6 to11 (Stream point on a longitudinal section of the coastal boundary)

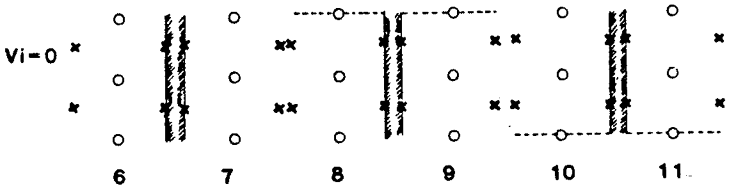

Label 12 to 17 (Stream point on a latitudinal section of the coastal boundary)

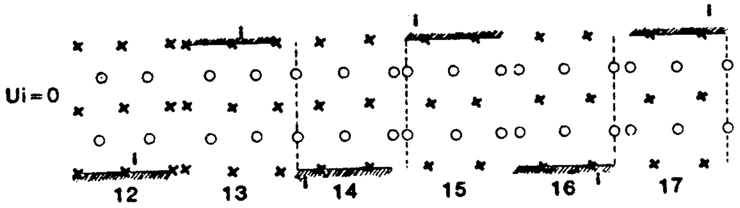

Label 18 to 21 (Stream point at a 270 deg corner of the coastal boundary)

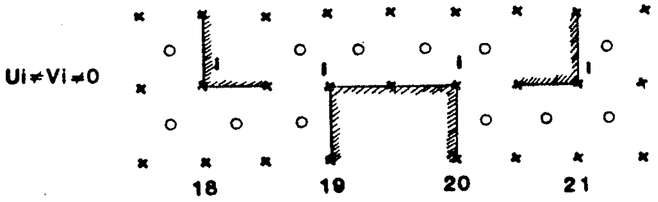

Figure 3.3: Elemental Grid Point Arrays for Model Boundary. Elements of the Sea Model Illustrating Different Types of Stream Points i With Respect to the Boundary Locations.

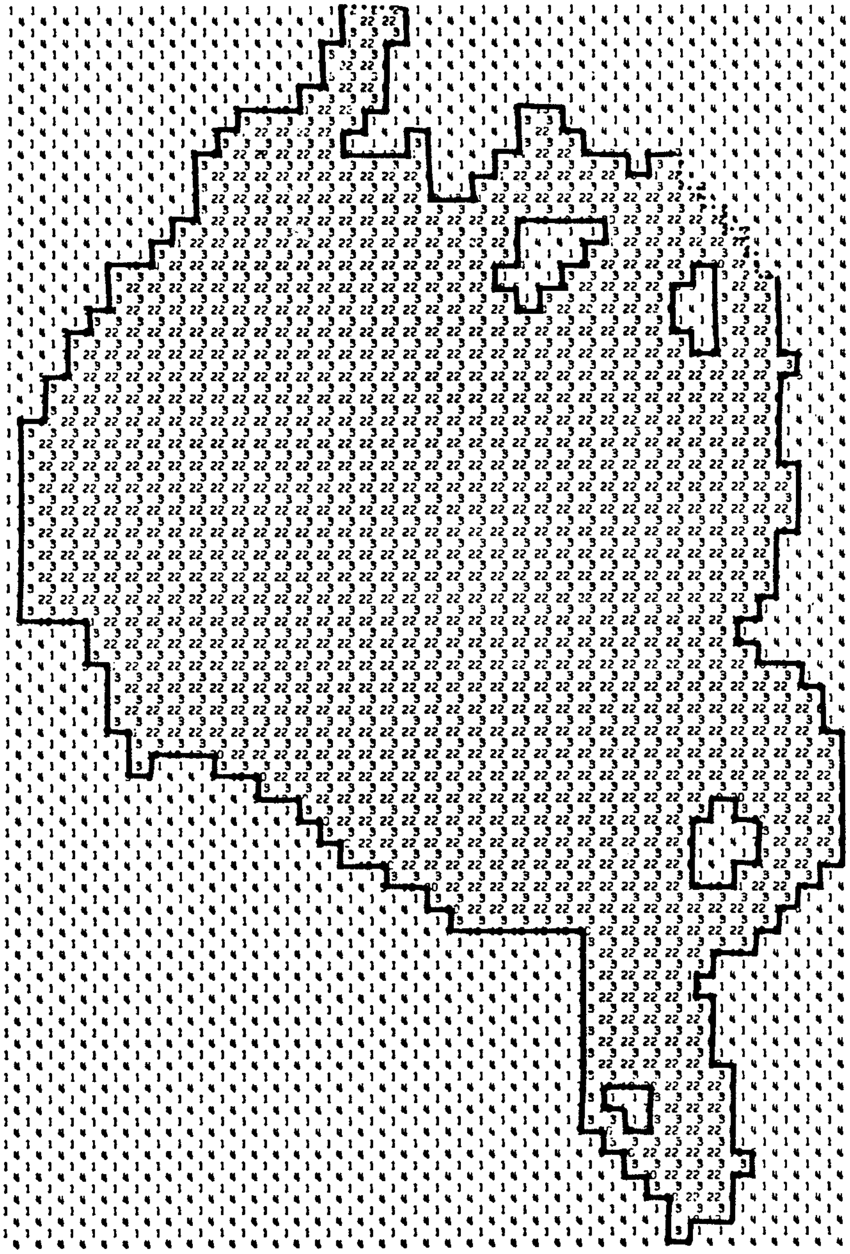

Figure 3.4: Numbering System for the Grid Point Locations. The Labels Defining the Relative Boundary Positions in Hudson Bay Model. See Table 3.1 for Label Meaning.

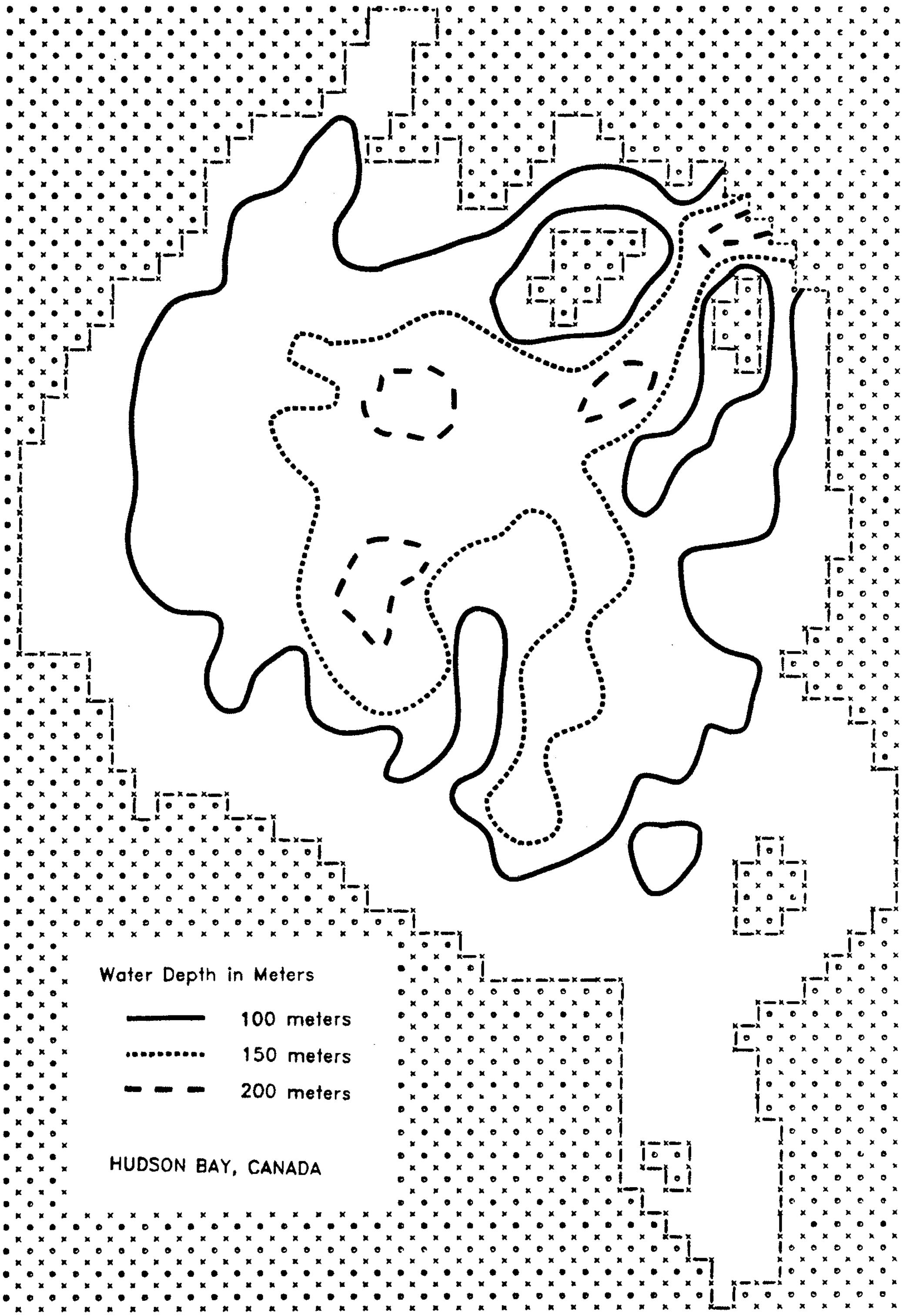

Figure 3.5: Bathymetric Chart of Hudson Bay

Table 3.1 Labels for Different Types of Grid Point Location in Hudson Bay Model.

Elevation point	Label
- outside the model boundary	1
- on the open boundary	2
- within the boundary	3
Stream point	
- outside the model boundary	4
- at a 90 degree corner of the boundary	5
- on a longitudinal section of the boundary	6 to 11
- on a latitudinal section of the boundary	12 to 17
- at a 270 degree corner of the boundary	18 to 21
- within the boundary	22

East China Sea and Yellow Sea Model

The equations of motion and continuity (equations (3.4) to (3.6)) are represented in time and space using a staggered spatial grid in which ζ, U, and V are computed at different grid points (Hansen type). This is a slightly different approach (Roberts and Weiss (1976)) from the one discussed in the previous section in which it centers the advective terms in space and time. Figure 3.6 shows the finite difference scheme used to develop ECSYS sea model (Choi (1980)). This consists of a rectangular array of 1 row and n columns with a grid space of $\Delta\phi$ in north-south direction and $\Delta\chi$ in the east-west direction. Unlike the finite difference set up of the HB sea model, both land and open sea boundaries are modelled by separated U and V grid points, which allows the coastal boundary condition of equation (3.15) and the radiation conditions of equations (3.16)-(3.19) to be applied. Figure 3.7a depicts the ECSYS finite difference grid. This model extends to the south as far as northern Taiwan and seaward as far as the edge of the continental shelf.

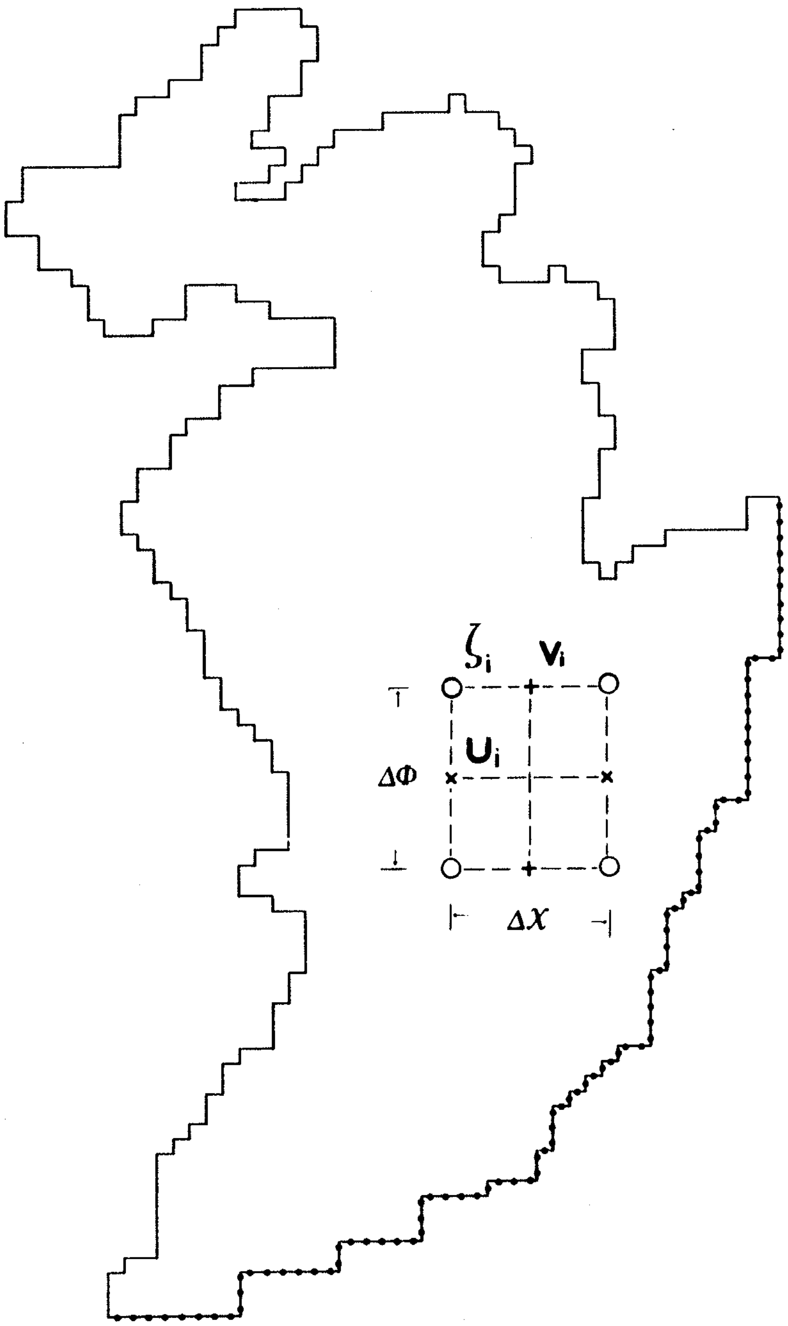

Figure 3.6: Numerical Scheme for East China Sea and Yellow Sea (Hansen Type of Finite Difference Grid).

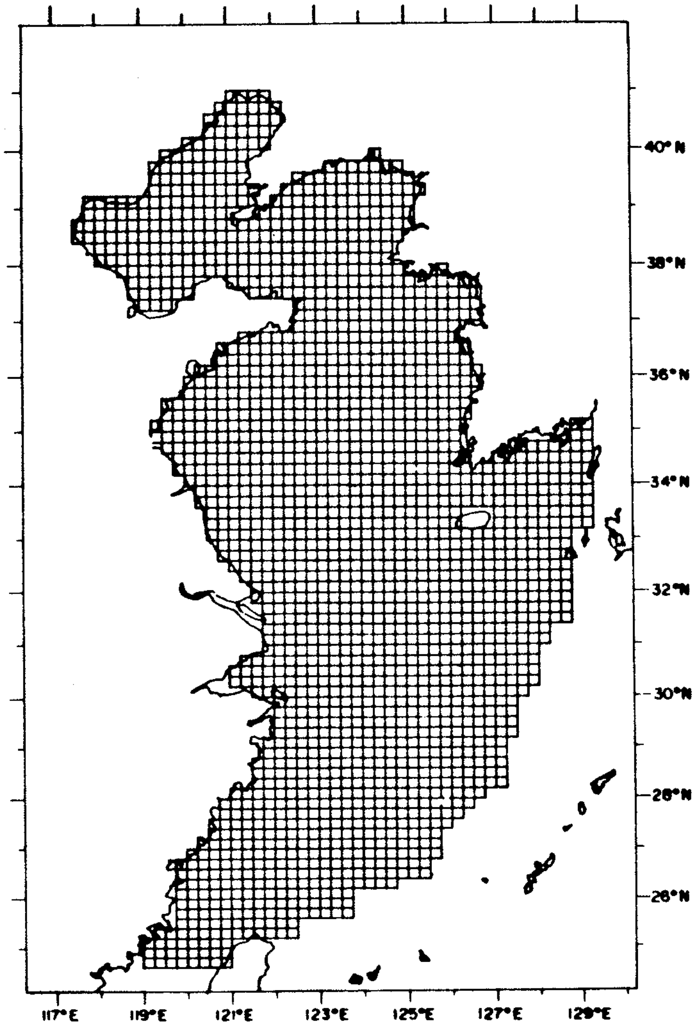

Figure 3.7a: Finite Difference Grid of East China Sea and Yellow Sea.

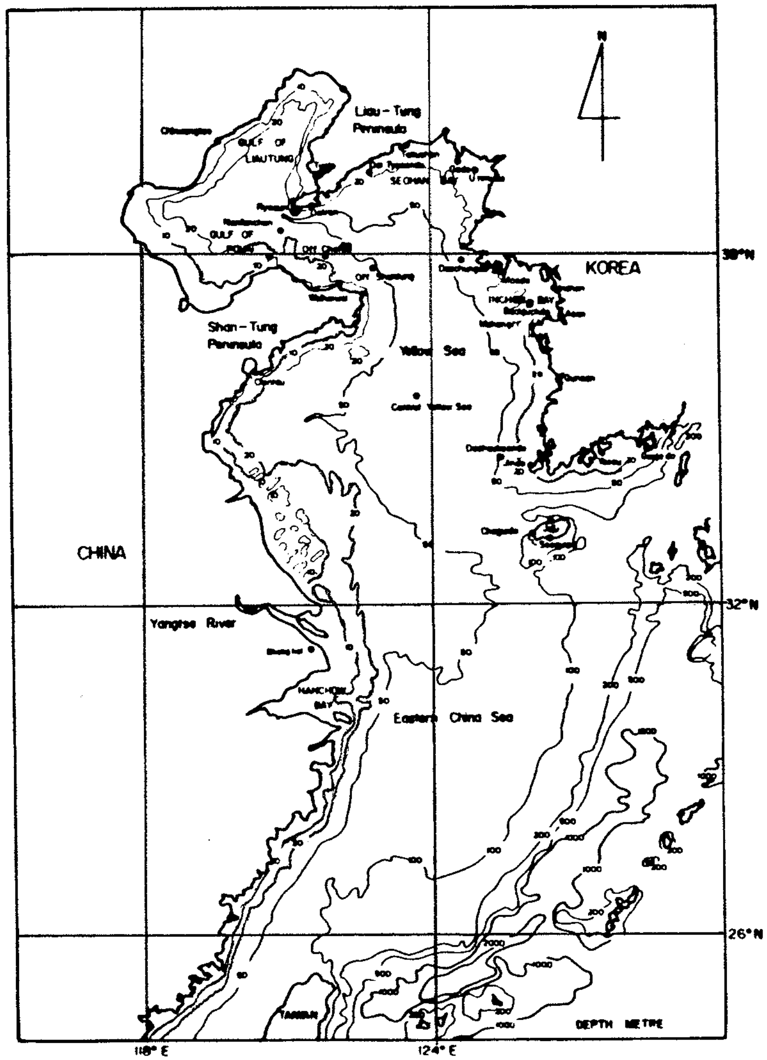

Figure 3.7b: East China Sea and Yellow Sea Bathymetric Chart (Choi (1980)).

There are basically eight types of open boundary conditions; northern, southern, eastern, western, north-western convex corner, north-eastern convex corner, south-western convex corner, and south-eastern convex corner. The finite difference representation of various types of open boundary can be obtained by rearranging the equation of continuity with the elevation prescribed adjacent to the model boundary. Description of each finite difference representation of boundary equations is given by Choi (1980) and Flather and Heaps (1975).

Figure 3.7b shows the bottom topography of the model. The discrete water depth values were obtained from various sources; Korean Admiralty charts #1262 and #2347 and Japanese hydrographic charts #182a, #182b, #187, #210, and #302. The open sea boundary of the model is chosen to be bound by a 200 m water depth contour and the entire continental shelf has a typical water depth value of about 80 m. Unlike the small open sea boundary of the HB sea model, approximately 33% of the ECSYS model is enclosed by open sea boundary.

(b) Finite Difference Representation

Hudson Bay Sea Model

From Table 3.1, one can observe that the elevation points outside the model boundary (label 1) have no physical meaning. Hence, they are not included in the numerical scheme. Similar situation is also noticed for label number 4. The numerical implementation of the elevation points on the open boundary (label 2) are completely dependent on the nature of the sea model and they are prescribed by the open boundary condition of equation (3.20) (Heaps (1969) and Lui (1982)).

The most common type of elevation and stream points found in the grid are those locate within the boundary (label 3 and 22). Replacing the time and space derivatives in equations (3.9) to (3.13) by the finite difference formula, we have the followings fundamental equations for labels 3 and 22

$$\zeta(t+\Delta t) = \zeta_i(t) - \frac{\alpha \Delta t}{\cos\phi_{2k-1}} \left\{ \frac{B_i(t+\Delta t)}{2\Delta\phi} + \frac{C_i(t+\Delta t)}{2\Delta\chi} \right\} \qquad \ldots\ldots(3.21a)$$

$$V_i(t+\Delta t) = (1-\Delta t\lambda_i)V_i(t) + 2\Delta t\,\omega \mathrm{Sin}\phi_{2K} U_i(t) - \frac{\Delta t\,\beta\,H_i\,E_i}{2\cos\phi_{2K}\,\Delta\chi} + \Delta t\,\gamma Q_i(t) \qquad \ldots\ldots(3.21b)$$

$$U_i(t+\ t) = (1-\Delta t\lambda_i)U_i(t) - 2\Delta t\,\omega \mathrm{Sin}\phi_{2K} V_i(t) - \frac{\Delta t\,\beta\,H_i\,D_i}{2\Delta\phi} + \Delta t\,\gamma P_i(t) \qquad \ldots\ldots(3.21c)$$

where

Δt - elementary time step in the calculation

i - location of the grid point solutions are to be evaluated

K - 1 + int ((i - 1)/n)

$$B_i = \frac{1}{2}\left(U_{i-n} \operatorname{Cos} \phi_{2k-2} - U_i \operatorname{Cos} \phi_{2k} + U_{i-n-1} \operatorname{Cos} \phi_{2k-2} - U_{i-1} \operatorname{Cos} \phi_{2k}\right) \quad .....(3.22a)$$

$$C_i = \frac{1}{2}\left(V_i - V_{i-1} + V_{i-n} - V_{i-n-1}\right) \quad .....(3.22b)$$

$$D_i = \frac{1}{2}\left(\zeta_i - \zeta_{i+n} + \zeta_{i+1} - \zeta_{i+n+1}\right) \quad .....(3.23a)$$

$$E_i = \frac{1}{2}\left(\zeta_{i+1} - \zeta_i + \zeta_{i+n+1} - \zeta_{i+n}\right) \quad .....(3.23b)$$

Equation (3.21a), (3.21b), and (3.23) describe the stream components while equations (3.21c) and (3.22) represent the time varying sea surface elevation. The remaining finite difference equations for labels 5 to 21 can be derived by applying the coastal boundary condition and three point lagrange interpolation formula (Heaps (1969)) to equation (3.21a), (3.21b), and (3.23). For example, stream points at the apex of 90 degree sector of the model boundary result in vanishing U and V components and thus equations (3.23a) and (3.23b) respectively become;

$$U_i = V_i = 0 \quad .....(3.24a)$$

$$D_i = \frac{\gamma P_i}{\beta H_i / 2\Delta\chi}\ , \quad E = \frac{\gamma Q_i}{\beta H_i / 2 \operatorname{Cos} \phi_{2k} \Delta\chi} \quad .....(3.24b)$$

Heaps (1969) summarizes the detailed formulation for all labels which form the basis of the iterative procedure for the development of the numerical solutions to the linearized dynamical equations.

East China Sea and Yellow Sea Model

Employing the angled-derivative scheme for the advective terms in the equations of motion, the U and V equations are centered in both space and time in terms of two sweeps (Flather and Heaps (1975), Davies and Flather (1978) and Choi (1980)); in the upsweep scan, U component is calculated first then V :

U - equation during upsweep

$$\frac{U_i(t+\Delta t) - U_i(t)}{\Delta t} = 2\omega \mathrm{Sin}\,\phi_m \hat{\hat{v}}_i(t) - \frac{\bar{U}_i(t)}{2\Delta x\, R\, \mathrm{Cos}\,\phi_m}$$

$$(u_{i+1}(t) + u_i(t+\Delta t) - u_i(t) - u_{i-1}(t+\Delta t)) + \frac{U_i(t)\,\hat{\hat{V}}_i(t)}{R}\,\mathrm{Tan}\,\phi_m -$$

$$\frac{1}{2R}\left(\frac{1}{2}[v_{i-n}(t) + v_{i-n+1}(t)]\,\frac{U_{i-n}(t+\Delta t) - U_i(t+\Delta t)}{\Delta\phi} +\right.$$

$$\left.\frac{1}{2}[v_i(t) + v_{i+1}(t)]\,\frac{U_i(t) - U_{i+n}(t)}{\Delta\phi}\right) - \frac{C\,U_i(t+\Delta t)}{d_i(t)}$$

$$(u_i^2(t) + \hat{\hat{v}}_i^2(t))^{\frac{1}{2}} - \frac{g}{R\,\mathrm{Cos}\,\phi_m}\,\frac{\zeta_{i+1}(t+\Delta t) - \zeta_i(t+\Delta t)}{\Delta x} + \frac{1}{\rho}$$

$$(-P_i(t) + \frac{F_i(t)}{d_i(t)}) \qquad \ldots\ldots(3.25a)$$

V - equation during upsweep

$$\frac{V_i(t+\Delta t) - V_i(t)}{\Delta t} = -2\omega \mathrm{Sin}\,\phi_{m+1} \hat{\hat{u}}_i(t+\Delta t) - \frac{\bar{V}_i(t)}{2\Delta\phi\, R}$$

$$(v_i\ (t) + v_{i-n}\ (t+\Delta t) - v_i\ (t+\Delta t)\ -\ v_{i+n}\ (t))\ -\ \frac{\hat{\hat{U}}_i^2(t)}{R}\ \mathrm{Tan}\ \phi_{m+1}\ -$$

$$\frac{1}{2R\,\mathrm{Cos}\,\phi_{m+1}}\ (\frac{1}{2}\ [u_{i-1}\ (t) + u_{i+n-1}(t)]\ \frac{V_i(t+\Delta t) - V_{i-1}(t+\Delta t)}{\Delta X}\ +$$

$$\frac{1}{2}\ [u_i\ (t) + u_{i+n}\ (t)]\ \frac{V_{i+n}(t)\ -\ V_i(t)}{\Delta X}\ )\ -\ \frac{C\ V_i(t+\Delta t)}{e_i(t)}$$

$$(\hat{\hat{u}}_i^2\ (t)\ +\ v_i^2\ (t)\ )^{\frac{1}{2}} - \frac{g}{R}\ \frac{\zeta_i(t+\Delta t) - \zeta_{i+n}(t+\Delta t)}{\Delta\phi}\ +\ \frac{1}{\rho}$$

$$(-Q_i(t)\ +\ \frac{G_i(t)}{e_i(t)}) \qquad \ldots\ldots(3.25b)$$

in downsweep scan, V component is calculated first then U :

V - equation during downsweep

$$\frac{V_i(t+\Delta t)\ -\ V_i(t)}{\Delta t} = -\ 2\omega \mathrm{Sin}\ \phi_{m+1}\ \hat{\hat{u}}_i(t)\ -\ \frac{\bar{V}_i(t)}{2\ \Delta\phi\ R}$$

$$(v_i\ (t+\ t) + v_{i-n}\ (t) - v_i\ (t)\ -\ v_{i+n}\ (t+\Delta t))\ -\ \frac{\hat{\hat{U}}_i^2(t)}{R}\ \mathrm{Tan}\ \phi_{m+1}\ -$$

$$\frac{1}{2R\,\mathrm{Cos}\,\phi_{m+1}}\ (\frac{1}{2}\ [u_{i-1}\ (t) + u_{i+n-1}\ (t)]\ \frac{V_i(t)\ -\ V_{i-1}(t)}{\Delta X}\ +$$

$$\frac{1}{2}\ [u_i\ (t) + u_{i+n}\ (t)]\ \frac{V_{i+1}(t+\Delta t)\ - V_i(t+\Delta t)}{\Delta X}\ )\ -\ \frac{C\ V_i(t+\Delta t)}{e_i(t)}$$

$$(\hat{\hat{u}}_i^2\ (t)\ +\ v_i^2\ (t)\ )^{\frac{1}{2}} - \frac{g}{R}\ \frac{\zeta_i(t+\Delta t)\ -\ \zeta_{i+n}(t+\Delta t)}{\Delta\phi}\ +\ \frac{1}{\rho}$$

$$(-Q_i(t)\ +\ \frac{G_i(t)}{e_i(t)}) \qquad \ldots\ldots(3.26a)$$

U - equation during downsweep

$$\frac{U_i(t+\Delta t)\ -\ U_i(t)}{\Delta t} = 2\ \omega \mathrm{Sin}\phi_m \hat{\hat{v}}_i\ (t+\Delta t)\ -\ \frac{\bar{U}_i(t)}{2\,\Delta X\ R\ \mathrm{Cos}\ \phi_m}$$

$$(u_{i+1}\ (t+\Delta t) + u_i\ (t) - u_i\ (t+\Delta t)\ -\ u_{i-1}\ (t))\ +\ \frac{U_i(t)\ \hat{\hat{V}}_i(t)}{R}\ \mathrm{Tan}\ \phi_m -$$

$$\frac{1}{2R}\left(\frac{1}{2}\left[v_{i-n}(t)+v_{i-n+1}(t)\right]\frac{U_{i-n}(t)-U_i(t)}{\Delta\phi}+\right.$$

$$\left.\frac{1}{2}\left[v_i(t)+v_{i+1}(t)\right]\frac{U_i(t+\Delta t)-U_{i+n}(t+\Delta t)}{\Delta\phi}\right)-\frac{C\,U_i(t+\Delta t)}{d_i(t)}$$

$$\left(u_i^2(t)+\hat{v}_i^2(t)\right)^{\frac{1}{2}}-\frac{g}{R\cos\phi_m}\,\frac{\zeta_{i+1}(t+\Delta t)-\zeta_i(t+\Delta t)}{\Delta\chi}+\frac{1}{\rho}$$

$$\left(-P_i(t)+\frac{F_i(t)}{d_i(t)}\right) \qquad \ldots\ldots(3.26b)$$

The finite difference form of continuity equation is :

$$\frac{\zeta_i(t+\Delta t)-\zeta_i(t)}{\Delta t}+\frac{1}{R\cos\phi_m}\left(\frac{d_i(t)\,U_i(t)-d_{i-1}(t)\,U_{i-1}(t)}{\Delta\chi}\right.$$

$$\left.+\frac{e_{i-n}(t)\cos\phi_{m-1}V_{i-n}(t)-e_i(t)\cos\phi_{m+1}V_i(t)}{\Delta\phi}\right)=0 \qquad \ldots\ldots(3.27)$$

where

$d_i = 0.5\ (h_i+\zeta_i+h_{i+1}+\zeta_{i+1})$

$e_i = 0.5\ (h_i+\zeta_i+h_{i+n}+\zeta_{i+n})$

$\hat{U}_i = 0.25\ (u_i+u_{i-1}+u_{i+n-1}+u_{i+n})$

$\hat{V}_i = 0.25\ (v_i+v_{i-n+1}+v_{i+1}+v_{i-n})$

$\bar{U}_i = 0.25\ (u_{i+1}+2\,u_i+u_{i-1})$

$\bar{V}_i = 0.25\ (v_{i-n}+2\,v_i+v_{i+n})$

$P_i = 1/R\cos\phi\ (\partial P_a/\partial\chi)$ at u-point i

$Q_i = 1/R\ (\partial P_a/\partial\phi)$ at v-point i

$F_i = F_s$ at u-point i

$G_i = G_s$ at v-point i

By altering the order in which the U and V equations are evaluated with each sweep direction, the Coriolis term can also be centered in time which enhances the stability of the numerical scheme.

(c) Stability Criteria

Hudson Bay Sea Model

The coordinate increments and chosen are 0.12 and 0.24 degrees, respectively, and the time increment t, is chosen to satisfy the stability criterion (Courant-Fredrich-Lewy or CFL criterion):

$$\Delta t < L \left\{ \frac{2}{\sqrt{gH}} \min \left(R \,\Delta\phi \,,\; R \cos\phi \,\Delta\chi \right) \right\} \qquad \ldots\ldots(3.28)$$

where

L - lower bound.

min - minimum of the quantity.

After several stability tests in time step, a value of 0.1 hour was used for the iteration interval. The above inequality was given by Heaps (1969) from analyzing the cartesian dynamical equation with vanishing external forcing function. The derived stability criteria in this coordinate is then transformed to the difference scheme in spherical Earth. In the present investigation, it was found that the iteration procedure has been very stable and the simplified stability criteria given above provides only a precautionary guide.

East China Sea and Yellow Sea Model

The grid resolution of the ECSYS sea model are 0.2 degree in latitude and 0.25 degree in longitude. According to Flather (1972) and Choi (1983), the stability criterion of a lineraized version of the scheme in retangular coordinates is closely approximated by the CFL criterion as follows;

$$\Delta t < \sqrt{\frac{2}{gH}} \left(\frac{\Delta S}{2} \right) \qquad \text{.....(3.29)}$$

where

ΔS - grid spacing in cartesian coordinates

The above condition gives a minimun time step of 3.75 min. Since it is also obtained from a simplified assumption and thus may be treated as a guide for numerical computation.

CHAPTER IV

TWO-DIMENSIONAL ATMOSPHERIC MODEL

1. Meteorological Approximation

At higher levels of the atmosphere (above the frictional boundary at about 500 to 1000 m), there are two main forces acting upon the air mass. The pressure gradient force causes the air from areas of high pressure to move into regions of low pressure. However, as soon as the air begins to move, an earth's rotational deflective (Coriolis) force exists and changes the direction of motion parallel to the isobars (Figure 4.1a). The Coriolis acceleration is always perpendicular to the velocity and hence the associated force changes the direction of motion but keeps the speed invariant. As a result the wind blows essentially parallel to the isobars with, for the northern hemisphere, the high pressure core on the right and the low pressure core on the left when viewed downwind. Applied to pressure with curved isobars, this means that the air moves clockwise about the center of high pressure, and counterclockwise about the center of a low pressure.

When the wind blows along a curved isobar, a third effect due to centrifugal force influences the motion. Since its effects are restricted to minor variations in wind speed and direction as compared to other forces, this centrifugal force is usually ignored in weather prediction and related study.

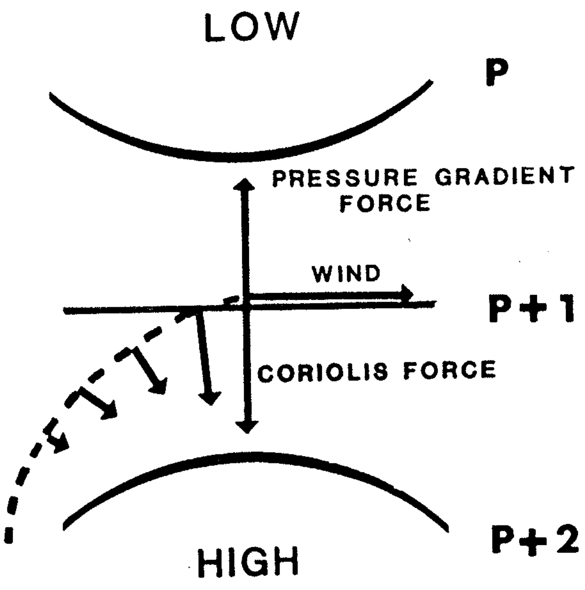

Figure 4.1a: Geostrophic Wind (High Level Wind).

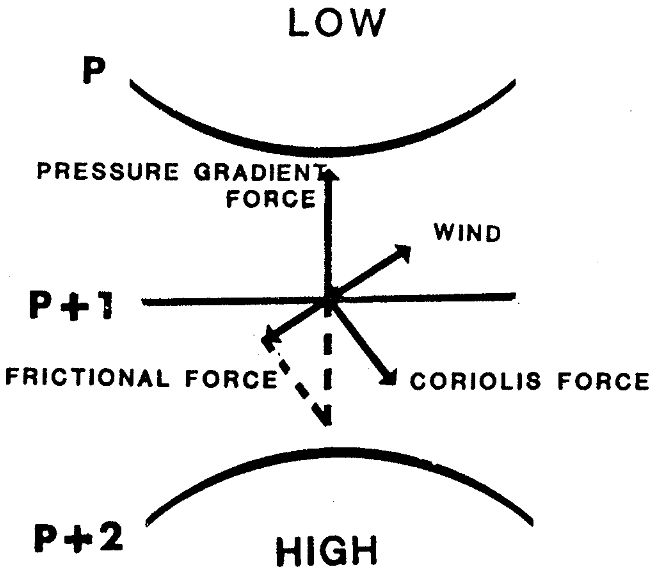

Figure 4.1b: Sea Surface Wind.

Another effect that is commonly found at lower altitude and has a great influence on wind speed and direction, is the force of friction (Figure 4.1b), or the retarding effect of the earth's surface topography. The result is that the wind speed is less than the speed indicated by the pressure gradient in the weather map, and the direction is changed so that the wind blows across the isobars at a slight angle into a center of low pressure and out a center of high pressure. The change of direction of motion due to interaction between wind and earth's surface is known as the angle of backing and its value seldomly exceeds 40 deg over land mass (Hess (1959)).

This chapter describes a method of extracting a two dimensional windfield from a weather chart. The main purpose of the development is to facilitate a simple input structure of windfield for the sea model. Examples of applying this method to real situation are given in the next chapter.

(a) Equations of Geostrophic Flow

For equilibrium horizontal motion as shown in Figure 4.1a, the components of the wind vector are given by (Hess, 1959)

$$Ug = \frac{1}{f\rho_a}\frac{\partial P_a}{\partial Y} = \frac{1}{2\omega \sin\phi\, \rho_a}\frac{\partial P_a}{\partial Y} \qquad \ldots\ldots(4.1)$$

$$Vg = \frac{-1}{f\rho_a}\frac{\partial P_a}{\partial X} = \frac{-1}{2\omega \sin\phi\, \rho_a}\frac{\partial P_a}{\partial X} \qquad \ldots\ldots(4.2)$$

where

U_g , V_g - geostrophic wind components in rectangular coordinate.

ρ_a - density of the atmosphere, assumed uniform.

P_a - pressure from weather map.

ω - Earth's rotational speed.

f - Coriolis parameter.

The major practical usefulness of these expressions lies in the fact that they enable one to delineate the horizontal wind field by analyzing the pressure field instead. In general, near the surface of the earth, variations in atmospheric density are minor compared to other variables in the equations. If a mean value is taken, the equations state that at any location there is a unique velocity that gives a balance between any pressure gradient force and the resulting Coriolis force.

Except for disturbance such as hurricanes, the geostrophic wind approximation provides good approximation of the true wind speed as well as the wind direction. One also notices that if the isobars are purely in the y direction, Ug reduces to zero in equation 4.1 since the pressure gradient term is zero. The facts that the surface of the earth is not uniform and the temperature varies from place to place are usually superimposed resulting in wavy patterns in the pressure contours. Thus one can combine equations 4.1 and 4.2 to obtain the total geostrophic wind magnitude:

$$W_g = (U_g^2 + V_g^2)^{\frac{1}{2}} \qquad \ldots\ldots(4.3)$$

where the direction is defined by its components.

(b) Surface Wind Vector

When one considers the wind within the first few kilometers of the earth's surface, friction plays a very important role in determining wind speed and direction. If the frictional force is small, the air flow differs very little from the geostrophic value. However, the wind vector will change in direction and decrease in speed when it encounters earth's rough surface topography. The angle between the geostrophic wind and surface wind is called the back angle. To estimate the surface wind from geostrophic wind, empirical laws similar to the following can be used (Hasse and Wagner, 1971)

$$
\begin{aligned}
&\text{(Unstable)} \quad && Ws = 0.56\ Wg + 3.0 \ \text{m/s} \\
&\text{(Neutral)} \quad && Ws = 0.56\ Wg + 2.4 \ \text{m/s} \qquad \ldots\ldots(4.4) \\
&\text{(Stable)} \quad && Ws = 0.56\ Wg + 1.5 \ \text{m/s}
\end{aligned}
$$

where

Ws - total surface wind magnitude.

Wg - total geostrophic wind magnitude.

The above equations were obtained from surface measurements taken in the German Bight. The recorded pressure data and air-sea temperature differences were used as experimental parameters to determine the stability of the sea state and the relationship between the geostrophic wind and surface wind. The corresponding differences (air temperature minus sea temperature) are -2.7° C (unstable), -0.2° C (neutral), and 1.7° C (stable) respectively.

The direction of the surface wind estimated from the geostrophic wind depend upon the roughness of the earth surface. Over the relatively smooth ocean surface, where friction is low, the surface air moves at a back angle, θ_b , of 10 to 20 degree and at speed roughly 2/3 that of geostrophic wind. If the angle of the geostrophic wind vector is measured clockwise from the south, the direction of the surface wind is then given by

$$\theta_s = \theta_g - \theta_b \qquad \ldots\ldots(4.5)$$

where

θ_s - surface wind angle measured from the south.

θ_g - geostrophic wind angle measured from the south.

2. Modelling and Practical Consideration

(a) Weather Information - Hudson Bay Area

The meteorological data input to the respective sea model consists of surface wind vectors and pressure gradients specified as a function of time and spatial coordinate. They are derived from the mean sea level pressure maps supplied by the Atmospheric Environment

Services, Environment Canada. The weather charts used in this study are produced from the information based on the observations from ground stations and weather satellites.

To calculate the input parameters, an uniformly spaced grid is defined on a sterographic projection on which the isobars had been drawn. The dashed lines in Figure 4.2 correspond to the atmospheric model whereas the solid line outlines the boundary of the sea model. The relationship between the rectangular atmospheric model and the latitude and longitude of the sea model is given by

$$X = \frac{2R\,(\cos\phi_0 \sin\phi - \sin\phi_0 \cos\phi \cos\delta\chi)}{1 + \sin\phi_0 \sin\phi + \cos\phi_0 \cos\phi \cos\delta\chi} \qquad .....(4.6)$$

$$Y = \frac{2R \cos\phi \sin\delta\chi}{1 + \sin\phi_0 \sin\phi + \cos\phi_0 \cos\phi \cos\delta\chi} \qquad .....(4.7)$$

where

ϕ, χ - latitude and longitude of sea model.

X,Y - north and east coordinate of atmospheric model.

R - radius of earth.

ϕ_0 - true of the map projection.

$\delta\chi$ - χ_0 minus χ .

This relationship is needed during the interpolation of the results obtained in the atmospheric model onto the sea model. In the numerical modelling procedure, the atmospheric pressure data are first weighted from the weather charts onto the atmospheric grid where the north and east components of the pressure gradient are

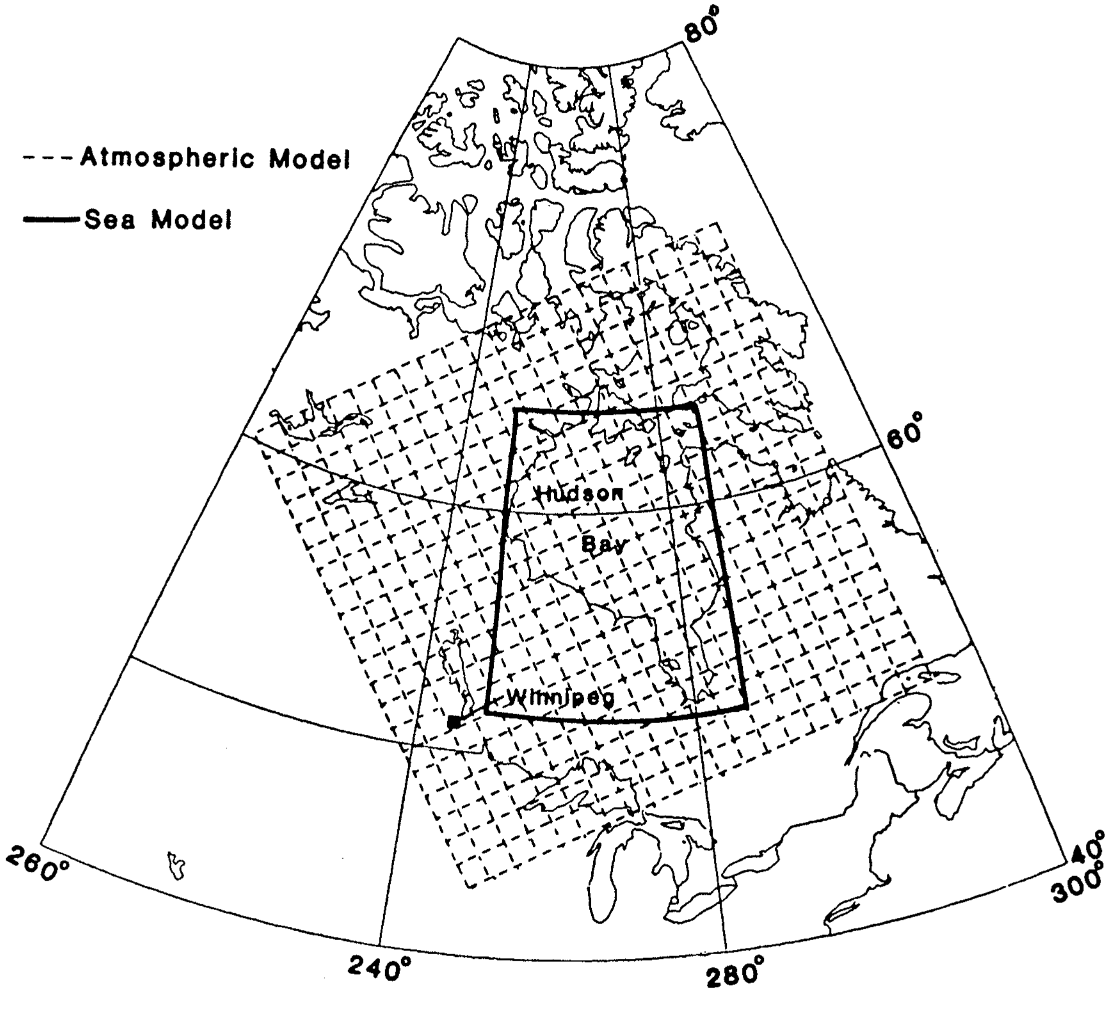

Figure 4.2: Hudson Bay 2-Dimensional Atmospheric Model. The Atmospheric Pressure Gradient is Calculated at Each Grid Points (line intersections) in the Model. The Size of the Atmospheric Model is Made Considerably Larger Than the Sea Model (solid line) to Avoid Edge Effects in Numerical Approximation.

calculated by the central difference approximation. The weighting scheme used is a three points distance averaged function commonly used by meteorologists.

(b) Finite Difference Approach

The north and east pressure gradient fields in finite difference representation are

$$\frac{\partial P_a}{\partial X}_{h=\Delta x}(i,j) = \frac{P_a(i,j+1) - P_a(i,j-1)}{2\Delta x} + 0(h^2) \qquad \ldots\ldots(4.8)$$

$$\frac{\partial P_a}{\partial Y}_{h=\Delta Y}(i,j) = \frac{P_a(i+1,j) - P_a(i-1,j)}{2\Delta \phi} + 0(h^2) \qquad \ldots\ldots(4.9)$$

where

$P_a(i,j)$ - weighted pressure values at each rectangular grid

h - north and east grid increments ($h = \Delta x = \Delta y$)

$0(h^2)$ - error associated with the approximation

Experiments showed that the error associated in this calculation can be large depending on the increment size of the grid. In order to reduce the error, first order successive extrapolation technique (Gerald, 1980) is used and the total error is reduced to $0(h^4)$. Equations 4.8 and 4.9 can be written as follows in terms of extrapolation

$$\frac{\partial P_a}{\partial X}_{h=\Delta x}(i,j) = \frac{\partial P_a}{\partial X}_{h=\Delta x} + \frac{1}{3}\left\{ \frac{\partial P_a}{\partial X}_{h=\Delta x} - \frac{\partial P_a}{\partial X}_{h=2\Delta x} \right\} \qquad \ldots\ldots(4.10)$$

$$\frac{\partial P_a}{\partial Y}_{h=\Delta Y}(i,j) = \frac{\partial P_a}{\partial Y}_{h=\Delta Y} + \frac{1}{3}\left\{ \frac{\partial P_a}{\partial Y}_{h=\Delta Y} - \frac{\partial P_a}{\partial Y}_{h=2\Delta Y} \right\} \quad .....(4.11)$$

Using equations (4.8) to (4.11), the geostrophic wind components can be deduced with reasonably good numerical accuracy. The final atmospheric model is characterized by a 20x20 line grid with increment length of approximately 120 km. The adopted atmospheric grid covers almost the entire area of eastern Canada area to eliminate the boundary effects on the sea model. The calculation of the surface wind from geostrophic wind requires the use of an empirical law similar to those expressed in equations (4.4) and (4.5). However, although the optimum formulation of this law has been the objective of many different investigators for many years, not a single generally accepted formula has evolved yet. For modelling purpose in this research, the neutrally stability law of Hasse and Wagner (1971) is adopted . This equation assumes not only the relationship between the surface and geostrophic wind is linear but also the fact that the surface wind speed may exceed the geostrophic wind speed for small geostrophic wind magnitude. This was also discussed in Hasse and Wagner (1971) and they explained that the effect predicted by this equation is realistic and is due to the different in nature of the variables Ws and Wg . A constant angle of backing , θ_b = 20 deg, between the geostrophic wind and surface wind is also assumed in the calculation to approximate the frictional drag.

(c) Interpolation of Atmospheric Data

The pressure gradients and the surface wind field are interpolated onto the stream points of the sea model by a cubic Lagrangian polynomial, using the nearest 16 points in the atmospheric model. Let F(I,J) be any grid point of the sea model with rectangular atmospheric model coordinates (X,Y) and sea model coordinates (ϕ,χ) which are related by equations (4.6) and (4.7). F(I,J) can be found by (see Figure 4.3):

$$
\begin{aligned}
F(i',J) = {} & \frac{(J-j_{+1})(J-j_{+2})(J-j_{+3})}{(j-j_{+1})(j-j_{+2})(j-j_{+3})} F(i,j) + \frac{(J-j)(J-j_{+2})}{(j_{+1}-j)(j_{+1}-j_{+2})} \\
& \frac{(J-j_{+3})}{(j_{+1}-j_{+3})} F(i,j+1) + \frac{(J-j)(J-j_{+1})(J-j_{+3})}{(j_{+2}-j)(j_{+2}-j_{+1})(j_{+2}-j_{+3})} F(i,j+2) \\
& + \frac{(J-j)(J-j_{+1})(J-j_{+2})}{(j_{+3}-j)(j_{+3}-j_{+1})(j_{+3}-j_{+2})} F(i,j+3) \qquad \ldots\ldots (4.12)
\end{aligned}
$$

for $i' = i$, $i+1$, $i+2$, and $i+3$.

The variables i and j represent various locations of grid points in the atmospheric model. Now the intepolation is repeated vertically to calculate F(I,J) with four values of F(i',J). The variable F(i,j) can be pressure field, pressure gradients, or surface wind field.

Although the computational procedure employed here is rather lengthy, it is still worthwhile to perform since the results of the surge prediction are closely related to the accuracy of the meteorological input data. The modelling area discussed here can be

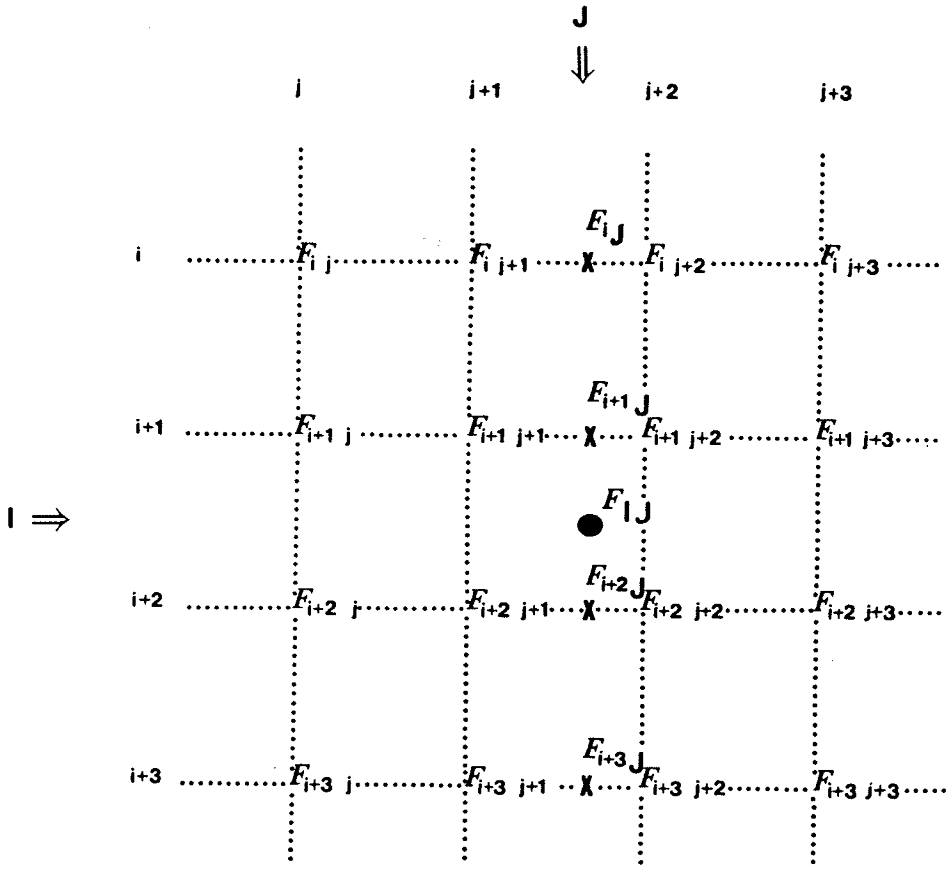

Figure 4.3: Lagrangian Interpolation Grid for Meteorological Data. Scheme for the Interpolation of Atmospheric Data to the Stream Points of the Sea Model (I,J).

extended flexibly to cover the whole earth's surface to estimate the global wind pattern. Particularly with the aid of the electronic digitizer the entire processing procedure becomes more efficient. This method is much more accurate in predicting wind in a large area than the one used by Heaps (1969) and Heaps and Jones (1979) in which only pressure gradients and wind speed are evaluated and assumed to be constant in each subarea of the sea model. Figure 4.4 summarizes the procedure of preparing the input meteorological data for this study. Every step except for the conversion of the sea surface wind to wind stress is performed in the atmospheric model (East China Sea and Yellow Sea atmospheric model includes this stage).

Due to the three-point smoothing and Lagrangian interpolation of pressure data, rapidly changing atmospheric features may not be adequately resolved. This could have a serious effect on the resulting wind estimates, particularly in the neighourhood of frontal regions. Improvement of the wind speed computation in this respect can be made by combining the model with observations from ground stations using least square type of gridding technique. Unfortunately, the number of ground stations in Hudson Bay area are rather limited and the solution to this problem can only be pursued with limited verification.

(d) Modelling of Typhoon Windfield - ECSYS

The major difficulty of predicting the surface wind speed of a typhoon using the above approach has been the lacking of a proper equation of converting geostrophic to surface wind speed. From the

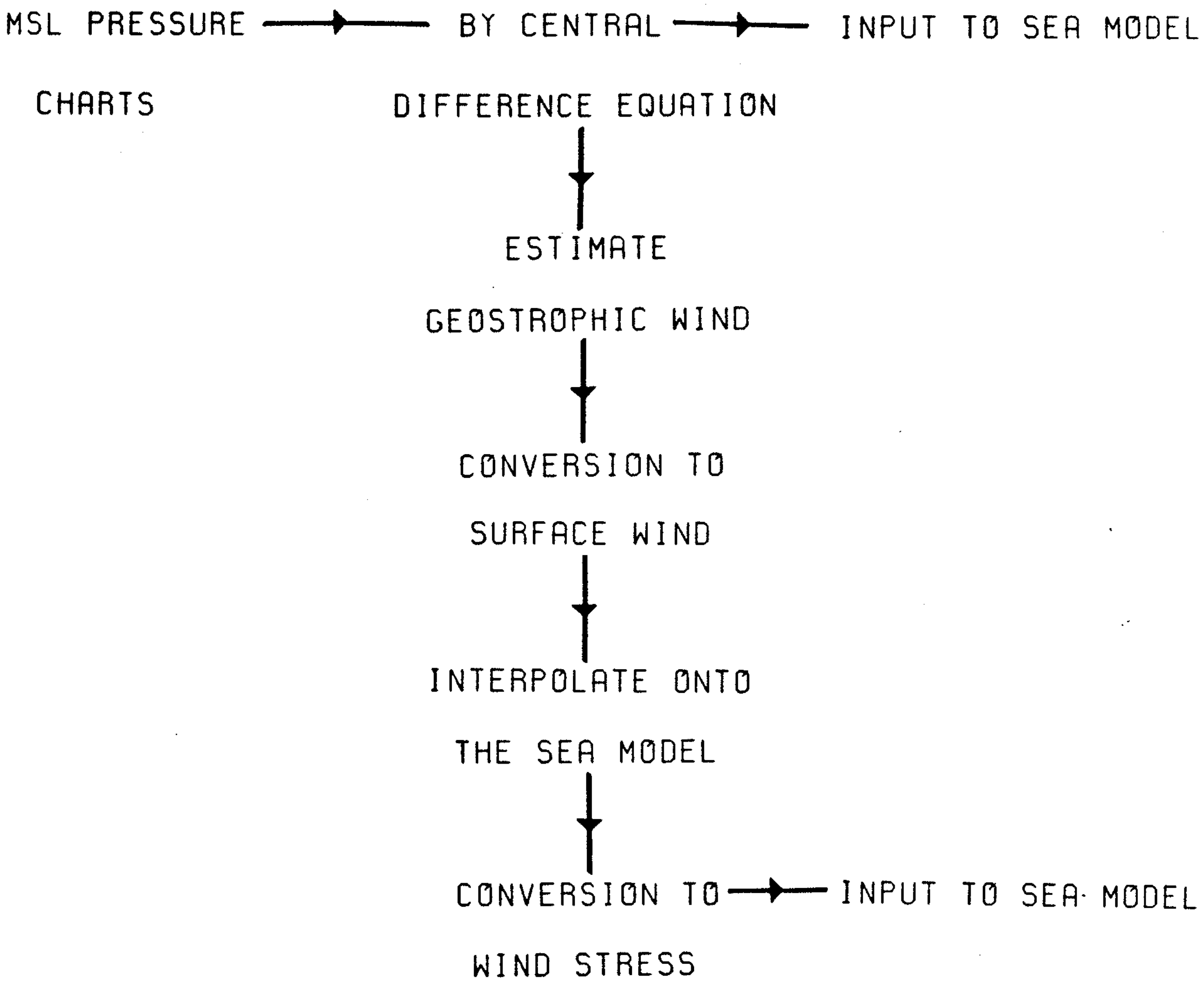

Figure 4.4: Computation Procedure for the Derivation of Atmospheric Driving Forces.

examinations of weather charts obtained from the Korean and Japanese meteorological offices, it is found that not only the weather systems move with an unpredictable speed and direction, the pressure gradient near the center of the typhoon may also give unrealistically high geostrophic wind speed. To correct the predicted wind speed to typical values of a typhoon, a number of numerical experiments were carried out for the East China Sea and Yellow Sea area.

Several formulae for converting geostrophic approximation to surface wind are reviewed and plotted in Figure 4.5. With those proposed by Hasse and Wagner (1971), four more geostrophic to surface wind relations were tested; the first two of these were modified from Hasse and Wagner (1971), while the last two were derived by Hsueh and Romea (1983) during the wintertime experiment (December 1, 1980 through March 31, 1981) over the East China Sea. The proposals by Hsueh and Romea (1983) were obtained by comparing the geostrophically approximated wind speed from weather charts (supplied by the Japanese Meteorological Agency) with the observations made around the Korean and Japanese coastal stations. Based on a practical stand point and the evaluations of testing results, the geostrophic to surface wind speed conversion equation is given by :

$$W_s = 0.443\ W_g + 2.92\ \text{m/s} \qquad \text{.....(4.13)}$$

for the East China Sea and Yellow Sea area. The back angle is assumed to be 20 degrees. The adoption of equation (4.13) is aimed

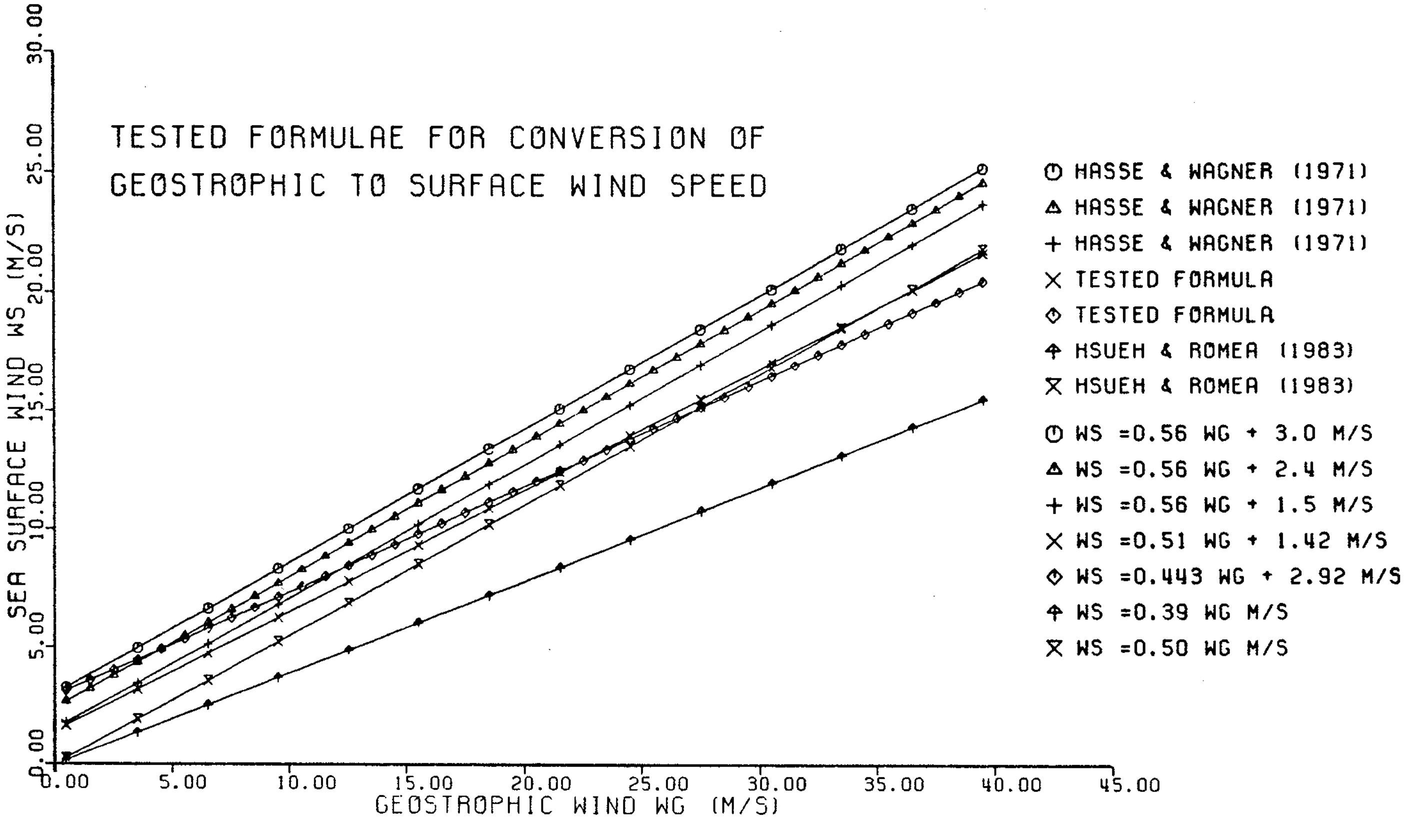

Figure 4.5: Geostrophic Wind to Surface Wind Relations.

to reduce the magnitude of surface wind and, in addition, the inequality below is added to ensure a realistic range of deduced typhoon wind speed:

$$Ws > 28 \text{ m/s} \quad , \quad Ws = 0.1657 \; (Ws \; \pm 20 \text{ m/s}) + 20 \text{ m/s}$$

where

Ws - components of sea surface windfield vector derived by model

The inequality gives a reasonably acceptable pattern of the two dimensional windfield since it suppresses unrealistic high wind near the typhoon center while it retains near normal wind speed away from it.

To apply the method of extracting wind speed for the East China Sea and Yellow Sea sea model, a 18x23 atmospheric model grid is set up over the region with resolution of 1 degree by 1 degree. Figure 4.6 shows some the grid points in and near the study area. A smaller resolution of 0.5 degree (longitude) by 0.4 degree (latitude) was also examined, however the computation time increases significantly with only a slight improvement to the results. The entire procedure of extracting wind speed follow the block diagram as shown in Figure 4.4.

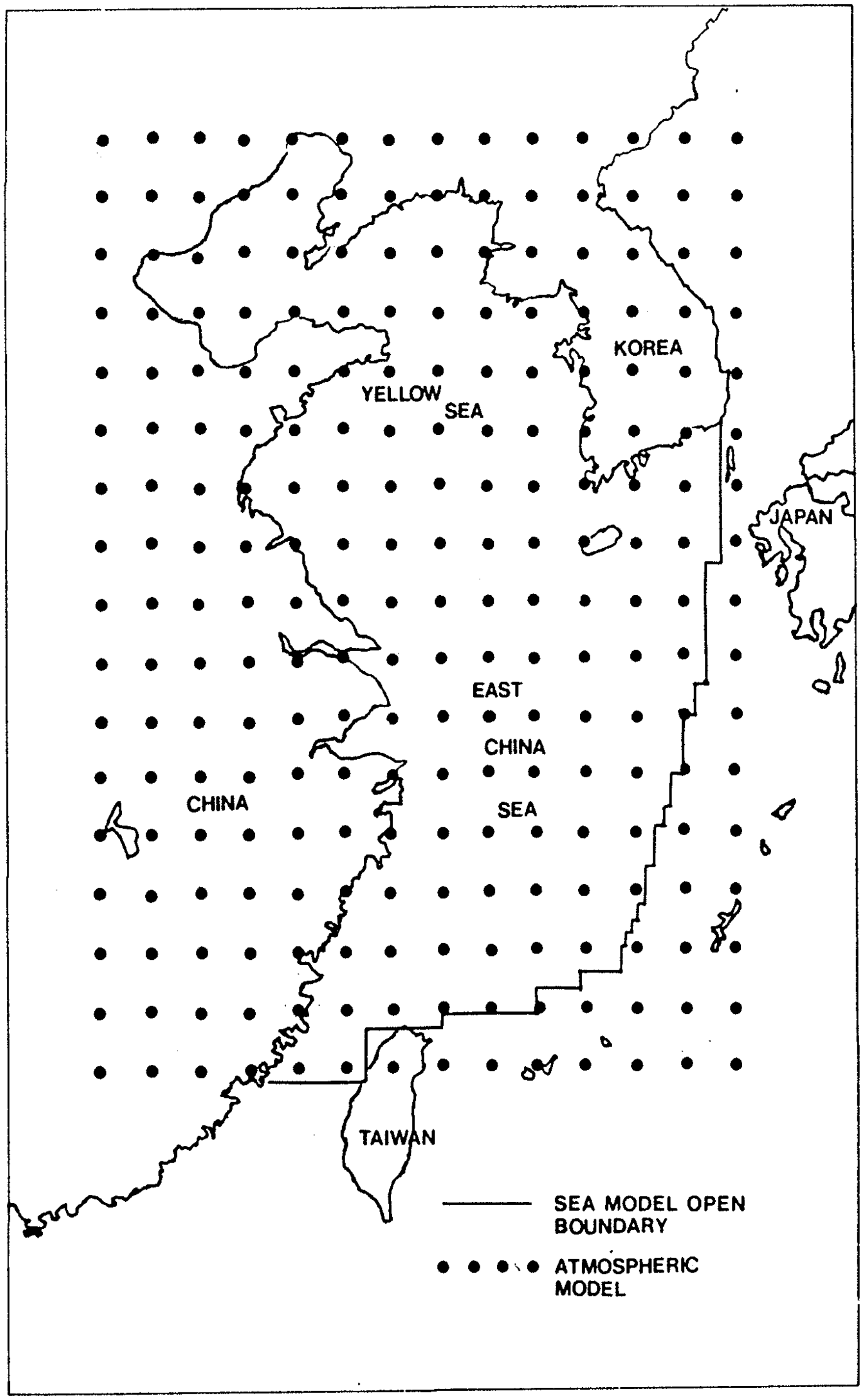

Figure 4.6: East China Sea and Yellow Sea 2-dimensional Atmospheric Model.

3. Wind Stress at the Air-Sea Interface

(a) Atmospheric Boundary Layer

Because of the frictional coupling at the air-sea interface, variation in sea surface elevation and the wind induced current are directly related. A significant proportion of downward momentum, as a result of wind stress, is transfered across the air-sea interface, while the rest is either reflected back to the atmosphere or converted to an other forms of energy before transfered into the sea. The coupling mechanism at the air-sea interface is not yet fully understood, although the magnitude of the coupling seems intuitively to rely on the magnitude of the wind speed and the nature of surface boundary layer. Part of the problem in understanding the coupling effect lies on the reliability and accuracy of the methods used to estimate wind stress as a function of wind speed. For this reason, the use of the correct surface wind stress remains a crucial and uncertain parameter in the transient surge modeling, as well as, in the study of the global scale oceanographic problem.

Recently, considerable amount of wind speed data have been accumulated which has allowed the proposal of empirical laws in terms of sea surface parameters (Brocks and Krugermeyer (1972) and Wu (1982)). The sources of surface parameter data are primarily from shipboard observations which can be regarded as a reasonable representation of true surface wind motion. Under the assumption of thermally neutral stability the surface wind velocity distribution above the sea surface is observed to behave logarithmically with height. In terms of friction velocity W_* , the surface wind speed is given by (Brocks and Krugermeyer (1972) and Hasse and Wagner (1971)):

$$W(z) = \frac{W^*}{K} \ln \left(\frac{Z}{Z_o}\right) \quad , \quad W_*^2 = \frac{\tau_s}{\rho_a} \qquad \text{.....(4.14)}$$

where

$W(z)$ - mean wind velocity measured at elevation Z above sea surface.

k - Von Karman constant (taken as 0.4).

z_o - vertical intercept of a semilogarithmic plot of z vs. W(z).

τ_s - surface wind stress.

ρ_a - atmospheric density.

The stress τ_s, can be determined from the slope of a straight line in the semilogarithmic plot of z vs. W(z) and an averaged value of atmospheric density. Another commonly used approach to determine the stress is known as the Reynold stress or Eddy Correlation technique. In this method the components of the flow in the direction of the main flow and the vertically upward are measured. The stress is then estimated by the mean value of their product with a value of the mean air density. The major difficulty associated with this approach is its sensitivity towards errors in measurements. Digital processing techniques such as sampling and filtering are often used to remove linear trend and random noise in data. These components in the measurements are very important especially in the case of thrust anemometer since a small amount of drift in the vertical sensor may cause large deviation in the computed wind stress.

(b) Quadratic Wind Stress

Because of the difficulties involved in measuring the wind velocity at different heights, it has become common to use the quadratic stress law which combines the wind speed directly with wind stress at a reference height z' ,given by

$$\tau_s = C' \rho_a W^2(z') \qquad \text{.....(4.15)}$$

where C' denotes a constant of proportionality which is known as the quadratic friction coefficient. The reference height is usually taken to be 10 m above sea level. Equation (4.15) is inherently a simple and yet an important relation between wind field and its stress exerted at the sea surface. Not only does this coefficient appear to depend on the distance above the sea surface, it has also been shown to be dependent on wind speed and in less extent related to the roughness of the sea surface. A large number of in-situ as well as laboratory measurements have been made in an attempt to accurately estimate the wind stress coefficient (e.g. Garratt (1977), Smith (1980), and Wu (1969,1980, and 1982)). The results demonstrate the dependency of wind stress coefficient on wind speed in various but consistent way. Figure 4.7 graphically depicts several relations published recently. One of the more comprehensive investigation was carried out by Wu (1969) using some thirty independent oceanic observations. In a recent review of older data,

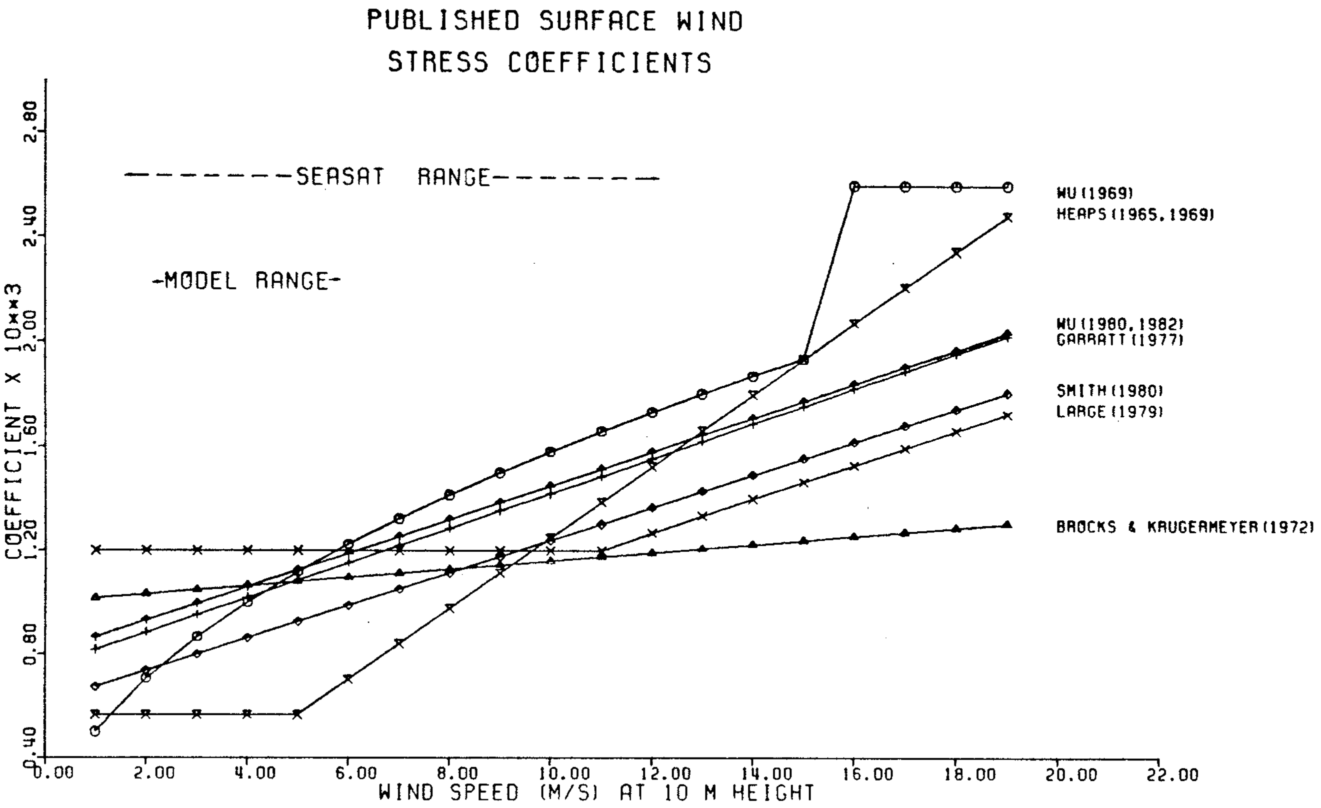

Figure 4.7: Quadratic Wind Stress Coefficient As a Function of Wind Speed.

Wu(1980, 1982) proposed a new wind stress coefficient formula and showed that the formula was applicable to both strong wind (>15 m/s) and light wind (< 15 m/s). The formula is very similar to that obtained by Garratt (1977) of which the data were largely based on the Reynold stress and wind profile measurements. Table 4.1 gives the quadratic wind stress coefficients formulated by different authors. Also listed with the formulae are the wind speed ranges from which the formulae were developed. Typically, wind magnitude below 15 m/s are termed 'light wind' and it is for these values that the response of the typical transient sea surface variation takes place. On the other hand, the wind speed greater than this range is usually associated with a storm and the sea surface elevation change computation for these values is called storm surge modelling (e.g. Heaps (1969)). Indicated in Figure 4.7 are the wind speed ranges during the Hudson Bay experiment as derived from the SEASAT altimeter and atmospheric model. As shown in this figure, the wind speed ranges from both sources in the Hudson Bay experiment are below the values categorized by storm surge, while typhoon wind speed (East China Sea and Yellow Sea experiment) generally covers the entire range. Therefore it is important to select the correct wind speed to wind stress formula that can be used to represent such a range of wind speed.

Although most of the formulae depicted in Figure 4.7 suggests that the wind stress coefficient is related to wind speed linearly (e.g. Smith (1980), Wu (1980,1982), and Garratt (1977)), whether similar numerical values in hydrodynamic modelling are reproducible remains unknown. In addition, a suitable formulation of wind stress at the sea surface is of particular importance because the amount of energy dissipated at the sea floor depends, to great extent, on the momentum transferred by sea surface stress. Thus, the formulae summarized in Table 4.1 and Figure 4.7 will be numerically tested to investigate their influences on the results of simulation of sea surface variation.

Table 4.1 Wind Stress Coefficient Formulae

Author	Proposed Form $C \times 10^3$	Magnitude Range (m/s)
Heaps (1965)	0.565	$Ws < 5$
	$-0.12 + 0.137\ Ws$	$5 < Ws < 19.22$
	2.513	$Ws > 19.22$
Wu (1969)	$0.5 \times Ws$	$1 < Ws < 15$
	2.6	$Ws > 15$
Brocks and Krugermuer (1972)	$1.18 + 0.18 + 0.016\ Ws$	$3 < Ws < 13$
Garratt (1977)	$0.75 + 0.067\ Ws$	$4 < Ws < 21$
Large (1979)	1.2	$5 < Ws < 11$
	$0.49 + 0.065\ Ws$	$11 < Ws < 26$
Smith (1980)	$0.61 + 0.063\ Ws$	$6 < Ws < 22$
Wu (1980, 1982)	$0.80 + 0.065\ Ws$	$0 < Ws < 50$

CHAPTER V

NUMERICAL MODELLING AND SEASAT ALTIMETER DATA

1. Hydrodynamic Modelling as an Altimeter Data Correction Algorithm

Based on the accuracy requirement of the geodetic and oceanographic communities, the SEASAT altimeter measurements have to satisfy the 10 cm rms precision over 1 sec averaged data. In chapter II the processing algorithms used to correct the raw data for this specification are described, with particular attention drawn to an nonimplemented correction to transient sea state due to meteorological forcing. Combining the sea model and the atmospheric model formulated in chapter III and IV, the transient sea surface variations in the SEASAT altimetry are modelled. Correction profiles of sea surface variation caused by meteorological effects are presented for Hudson Bay for two selected time periods.

To investigate the general effects of wind stress on transient sea surface elevation change, each wind stress coefficient formula shown in Figure 4.7 will be used to convert the derived sea surface wind to wind stress. The test runs are conducted for the Hudson Bay area since the atmospheric disturbances associated with the selected weather are more typical during the SEASAT mission period. Based on the reproduced sea surface elevation, a proper choice of the wind stress coefficient formula can also be made as will be discussed later. Beside the momentum transfer that takes places at the air-sea interface, an appropriate expression for the energy dissipation at the sea floor is also required to complete the problem formulation. To illustrate the modelling algorithm, the linear bottom stress law will be used, at this stage, with a value for the linear stress coefficient of 0.24 cm/s.

On examination of the quality of the weather charts and coverage of the satellite orbit tracks over Hudson Bay during the SEASAT mission time, two periods are selected to illustrate the transient sea surface elevation change. Figure 5.1 shows the satellite paths for August 4-6 (solid lines) and August 18-21 (dashed lines). Some of these paths are deleted due to their extreme short coverages through the model area. Also most of these paths are very close to the coastal area where the grid spacing of the numerical sea model may not be small enough to allow accurate interpolation along the satellite tracks. Table 5.1 gives the deleted satellite orbit tracks and the averaged sea water depth of the satellite coverage.

Table 5.1 Deleted SEASAT Orbit Tracks Over Hudson Bay

Time Period	Revolution Num.	Averaged Depth (m)
August 4-6	573 (Path 8)	20.0
August 18-21	774 (Path 11)	30.0
	775 (Path 12)	8.0
	796 (Path 24)	28.0

Although the correction profiles are presented for the Hudson Bay experiment, the same approach can be applied for any sea basin around the globe. Some examples of correction profiles for the meteorologically induced surge elevation and tides of M_2, S_2, K_1 and

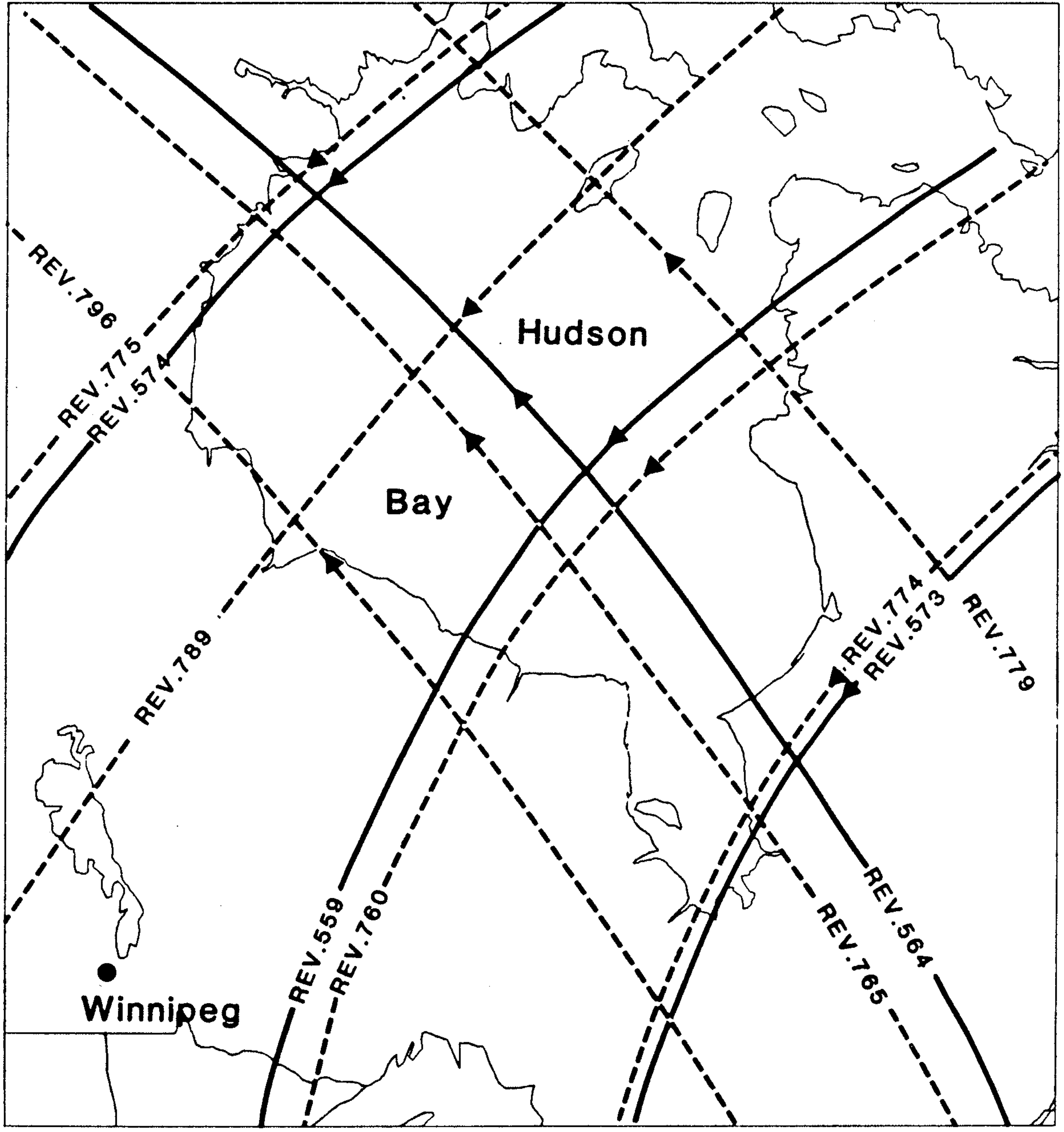

Figure 5.1: SEASAT Orbit Tracks Over Hudson Bay During August 4-6 (solid lines) and August 18-21 (dashed lines).

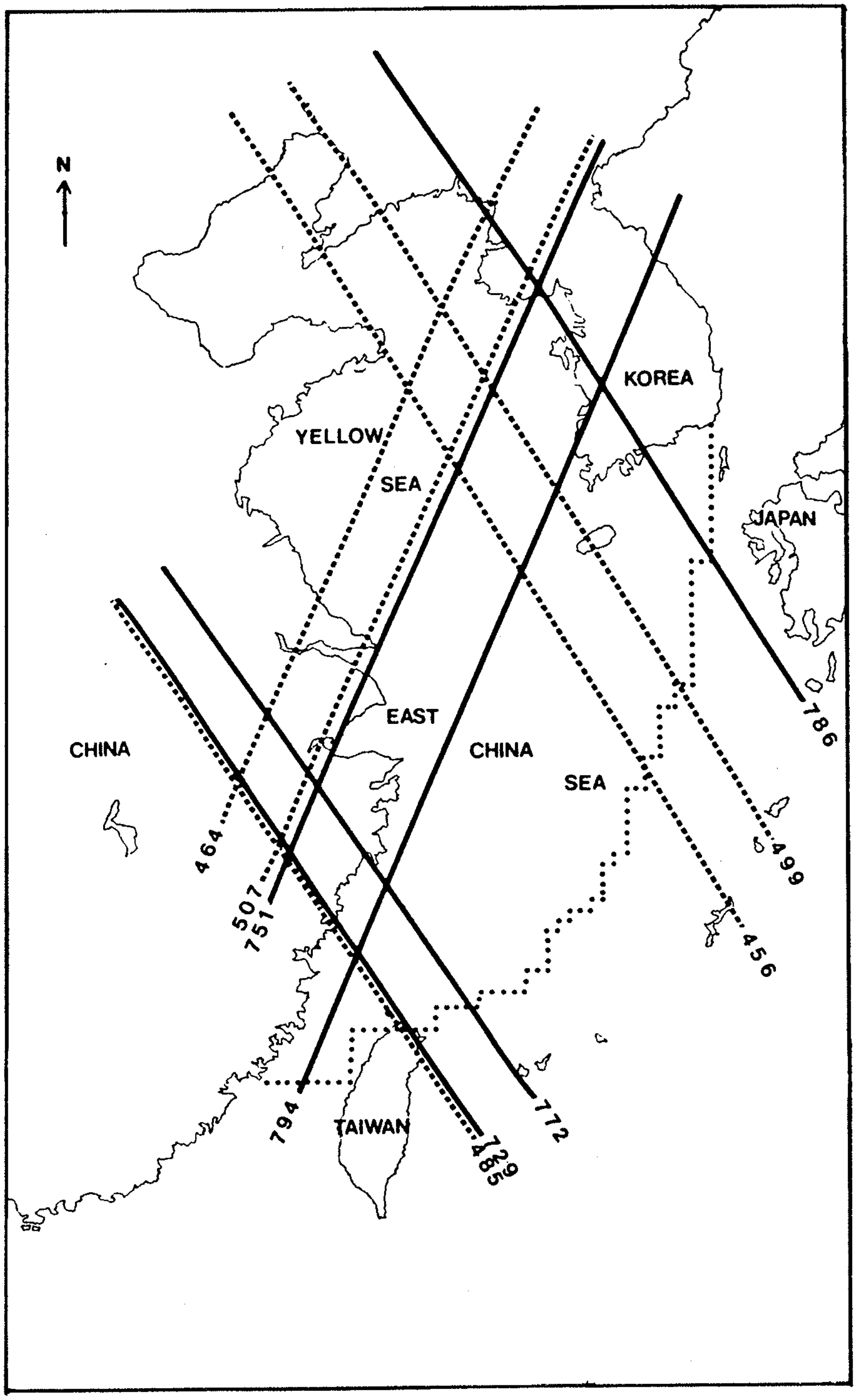

Figure 5.2: SEASAT Orbit Tracks East China Sea and Yellow Sea During 28 July to 2 Aug (dashed lines) and 15 Aug to 21 Aug (solid lines).

O_1 constituents will be illustrated for East China Sea and Yellow Sea area. Figure 5.2 shows the SEASAT paths over ECSYS area during two typhoon periods; Typhoon Wendy from 28 of July to 2 of August (dashed line) and Typhoon Carmen from 15 to 21 of August (solid line).

(a) Meterological Conditions and Derived Windfields

Hudson Bay Experiment

Figure 5.3 shows the tracks of the atmospheric disturbances which gave rise to the Hudson Bay transient surges. The solid line corresponds to a depression track of August 4-6. This low pressure disturbance moved approximately eastward with an averaged central pressure value of about 990 mb and became stationary at the north-eastern part of Hudson Bay during August 4 to August 5. As illustrated by the rate of the movement, one would expected that considerable wind induced sea surface elevation could be piled up at the south-east coast of Hudson Bay near the end of August 5 and the beginning of August 6.

A simliar but more stormy and rapid moving depression system is also recorded during August 18-21. The dashed line in Figure 5.3 shows the motion of this disturbance. Although it is less stationary than the depression system observed in August 4-6, it is believed to be adequate to give rise to transient sea surface variation. The weather charts in Figure 5.4 and 5.5 illustrate the developing depression systems associated with the SEASAT tracks shown in Figure

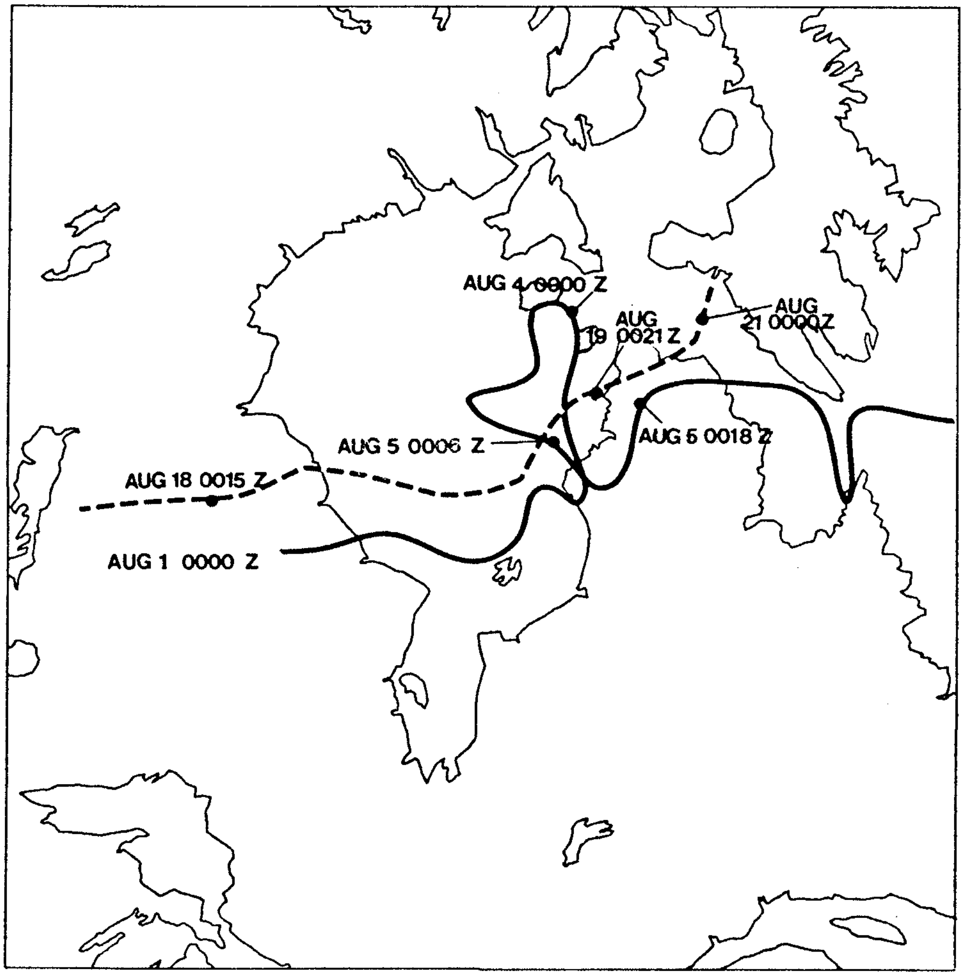

Figure 5.3: Depression Tracks for the Transient Surge During August 4-6 (solid line) and August 18-21 (dashed line).

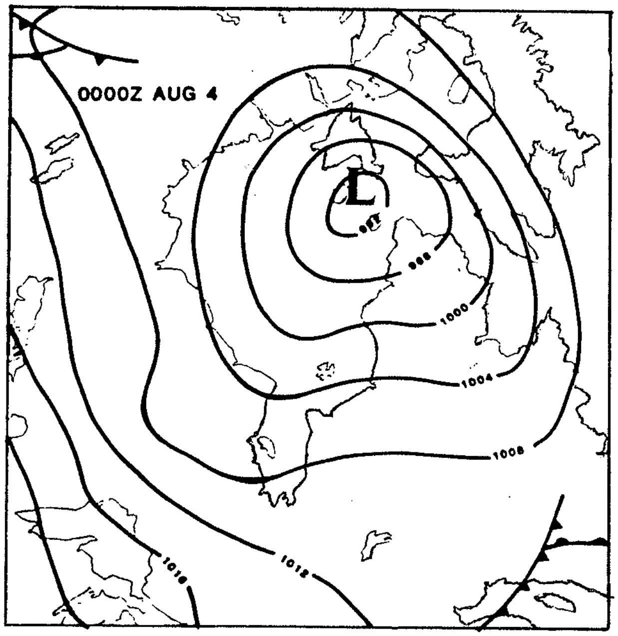

Figure 5.4a: Weather Chart for August 4, 0000Z.

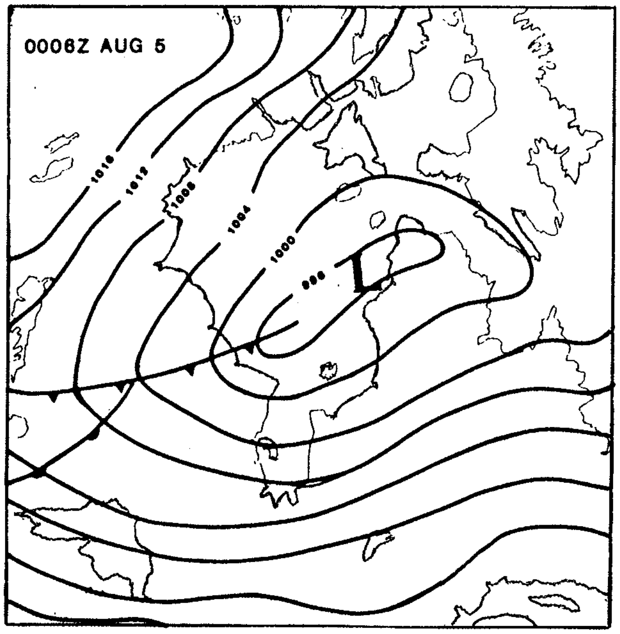

Figure 5.4b: Weather Chart for August 5, 0006Z.

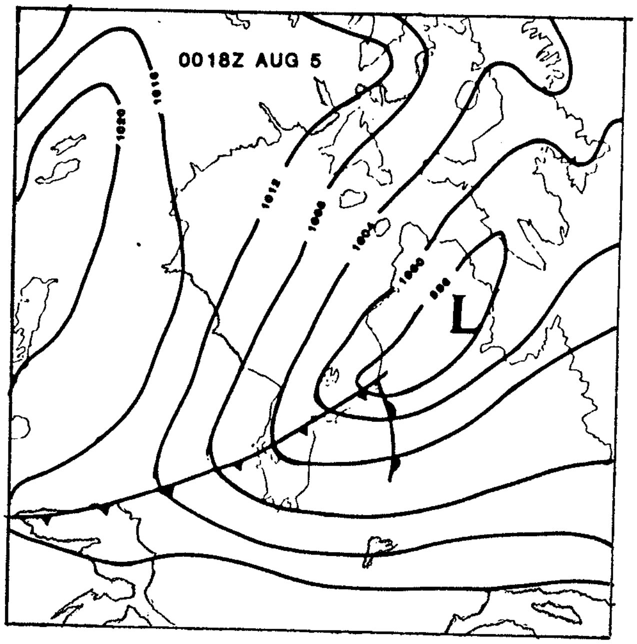

Figure 5.4c: Weather Chart for August 5, 0018Z.

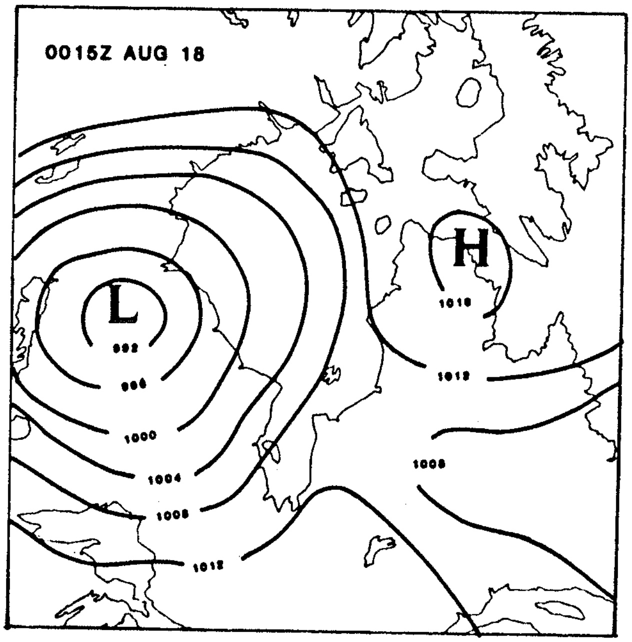

Figure 5.5a: Weather Chart for August 18, 0015Z.

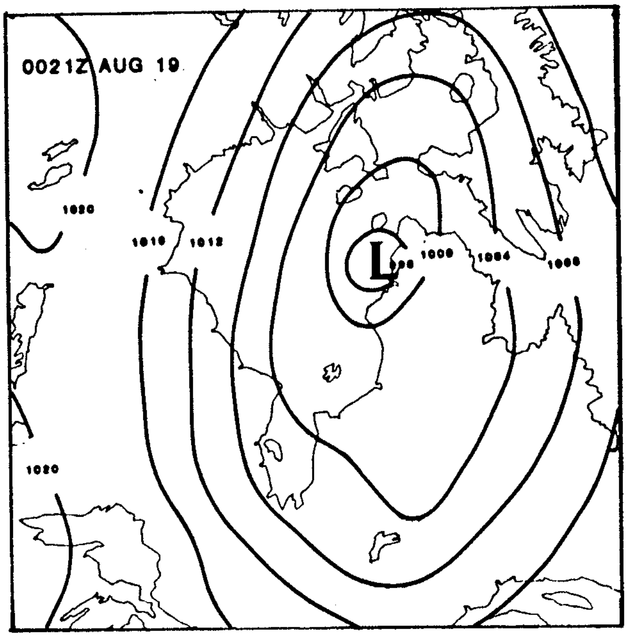

Figure 5.5b: Weather Chart for August 19, 0021Z.

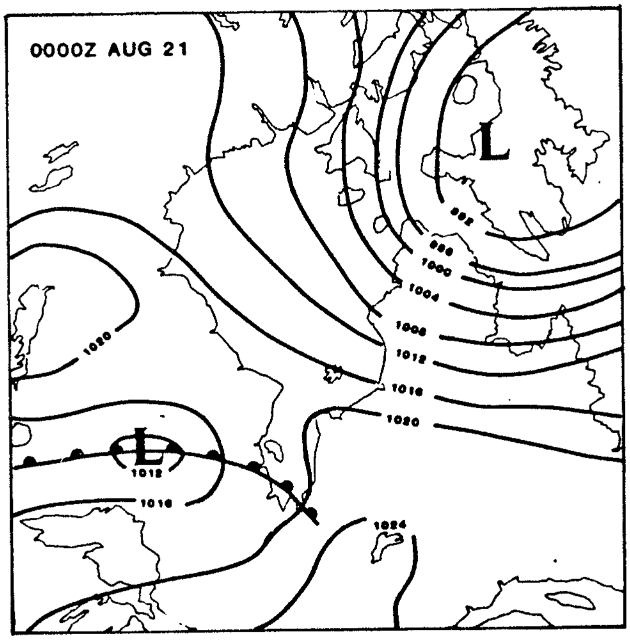

Figure 5.5c: Weather Chart for August 21, 0000Z.

5.3. These charts are produced every three hours from the Environment Services' pressure charts (Environment Canada) and the associated atmospheric disturbance is represented by the contour of isobars with an interval of 4 mb. Thus they can readily be used for the atmospheric model developed in the previous chapter.

The geostrophically derived sea surface windfields from the weather charts in Figure 5.4 are given in Figure 5.6. Superimposed on these diagrams are the isobars from the weather charts illustrating the direction of flow. The counterclockwise pattern of the windfields confirms the consequence of the flow direction caused by a depression in northern hemisphere. The maximum length of the wind vectors correspond to a wind speed of 4.01 m/s while the minimum wind magnitude is roughly 1.0 m/s (dots). The wind vectors are plotted in every second position of the stream points in the sea model grid for illustration purpose.

More complicated windfields patterns are depicted in Figure 5.7. They are derived from the weather charts shown in Figure 5.5. The wind speed associated with these plots ranges from 1m/s (dots) to 8 m/s. Figure 5.5a and 5.7a show a combination of high and low pressure systems over Hudson Bay at 0015Z in August 18. They evolved to a single major low pressure system with an additional depression of smaller magnitude moving toward Hudson Bay in the beginning of August 21. Figure 5.7c depicts the resulting windfield at this particular time period. The model predicts a very small wind speed at the south-western coast of Hudson Bay. This is an indication of vanishing atmospheric pressure gradient at the Col, a neutral area

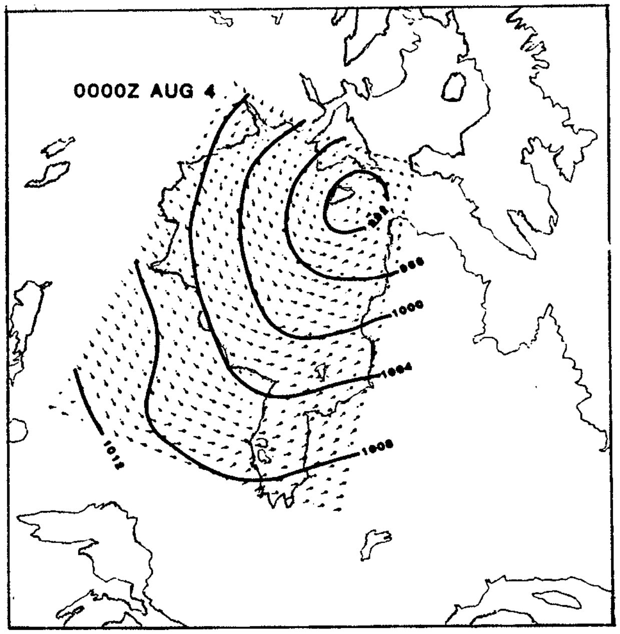

Figure 5.6a: Geostrophically Derived Sea Surface Windfield for August 4, 0000Z.

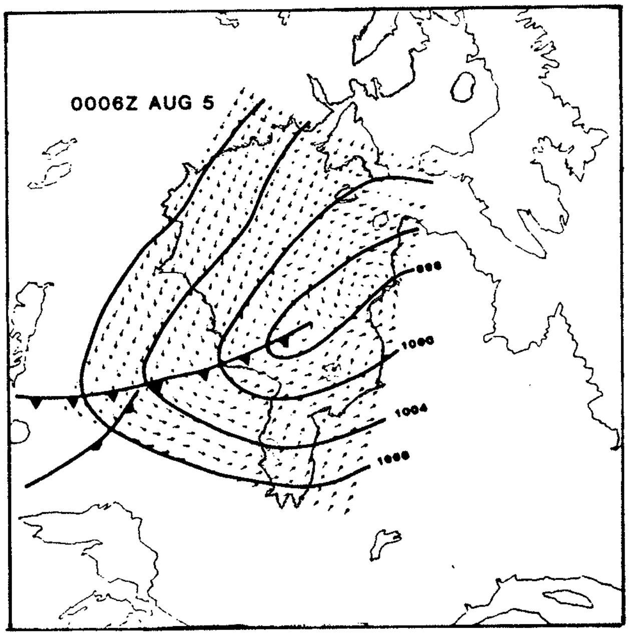

Figure 5.6b: Geostrophically Derived Sea Surface Windfield for August 5, 0006Z.

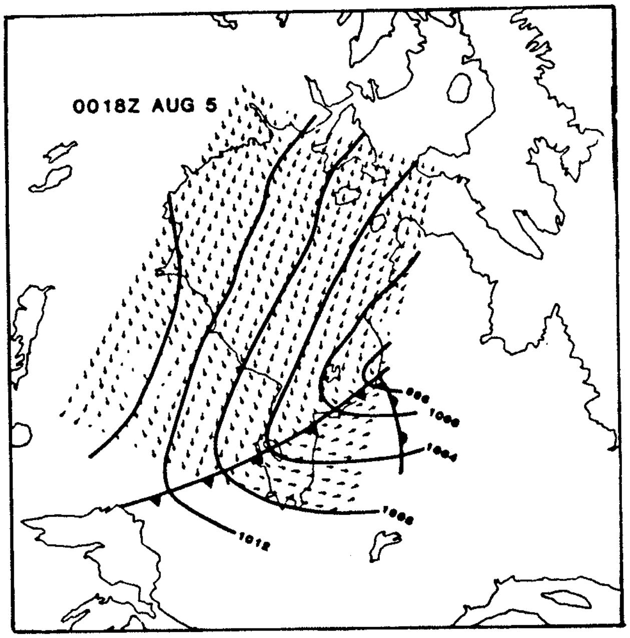

Figure 5.6c: Geostrophically Derived Sea Surface Windfield for August 5, 0018Z.

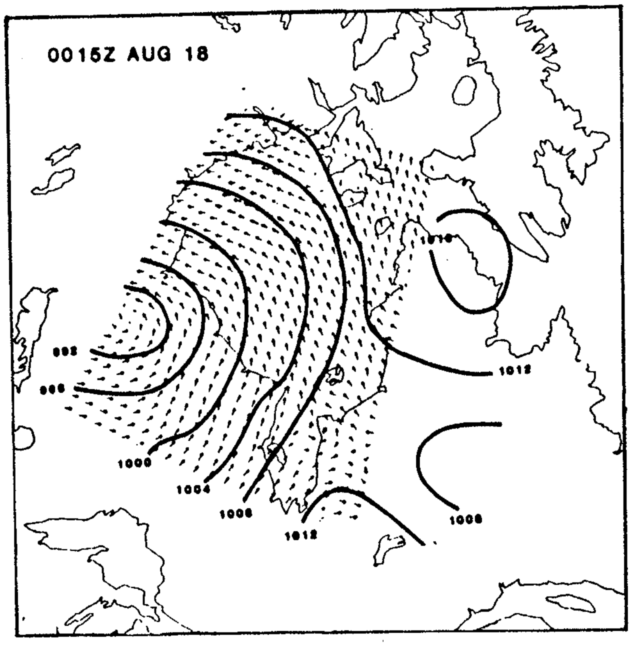

Figure 5.7a: Geostrophically Derived Sea Surface Windfield for August 18, 0015Z.

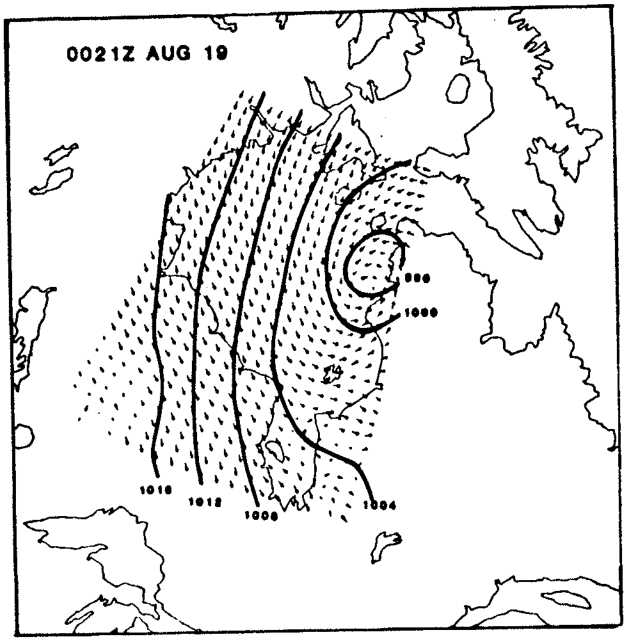

Figure 5.7b: Geostrophically Derived Sea Surface Windfield for August 19, 0021Z.

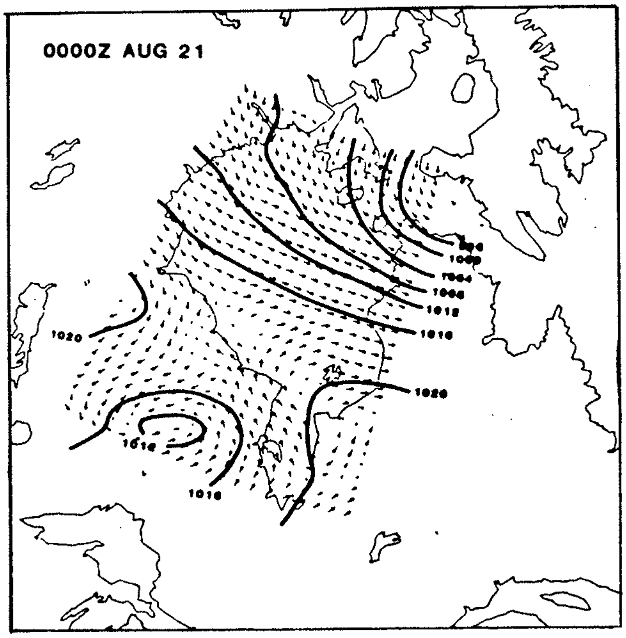

Figure 5.7c: Geostrophically Derived Sea Surface Windfield for August 21, 0000Z.

between two highs and two lows. Although some of the weather charts show a very complicated pressure distribution, the approximation of geostrophic to surface wind conversion method demonstrates its feasibility in practical application.

East China Sea and Yellow Sea Experiment

A total of 13 days (2 periods) of weather are considered over the East China Sea and Yellow Sea area during the SEASAT mission. Each period is characterized by a strong tropical weather disturbance (typhoon) with a duration of almost 6 days. Figure 5.8 depicts the tracks of the typhoons; Wendy as dashed line and Carmen as solid line. They enter the sea model at the south-east corner and become stationary over East China Sea region for about 4 days before they move away through the north-east corner of the model (Korea). Since the weather information is collected in every 6 hours, it is not continuous enough to describe the changing weather pattern as in Hudson Bay case. This may seriously affect the surge elevation computation by the sea model. Experiences from storm surge modelling in the North Sea and Irish Sea areas (from the research at the Institute of Oceanographic Sciences (IOS) at Bidston, UK) show that at least 3 hour intervals of weather are necessary to produce realistic surge phenomena (Choi (1984)). Thus interpolations of weather charts in time and space are performed for both periods along the disturbance tracks. This procedure assumes that the typhoon move linearly between two points at which the weather information was made available. Windfield is then recreated evenly along the line defined by these positions at hourly intervals.

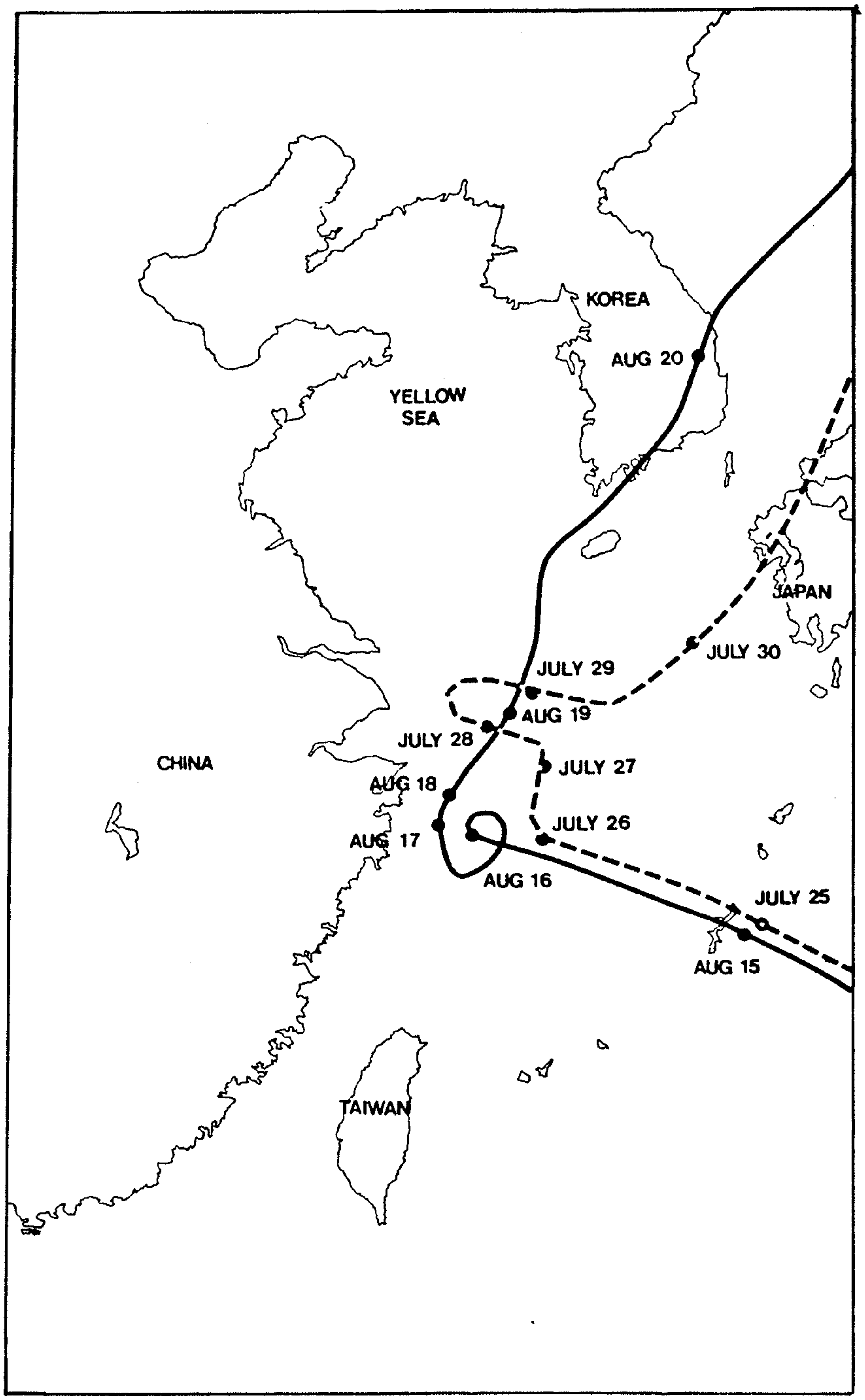

Figure 5.8: Disturbance Tracks for the Storm Surges During Wendy and Carmen Typhoons over East China Sea and Yellow Sea.

Figures 5.9 and 5.10 show some sample wind stress patterns calculated from the atmospheric model. Isobars are overlain in each diagram to show the direction of movement. The magnitude of the wind stress is related to surface wind speed through the stress law by Wu (1980,1982) as explained in previous sections.

(b) Computational Procedure and Transient Sea Surface Profiles

The flow diagram of Figure 5.11 illustrates the computational method used to reproduce the meteorologically induced surge. The depth field, initial and boundary conditions and the model grid are the fundamental parameters in the procedure. The next phase is to gather the necessary atmospheric information to simulate the actual weather conditions for surge generation. The transient sea surface height is computed iteratively at each elevation grid points for successive time step. The instantaneous sea surface topography is built up from an initial state of rest, satisfying the prescribed boundary conditions. In the present computation, wind stress and atmospheric pressure gradient are input to the stream points of the entire sea model in regular intervals. For numerical accuracy, the weather informations are input to the algorithm at least 24 hours prior to the first expected output. This allows sufficient time for the meteorological forces and friction to remove the influence of the inital conditions in the solution. Then the transient sea surface elevation change can iteratively be computed at any desired time period.

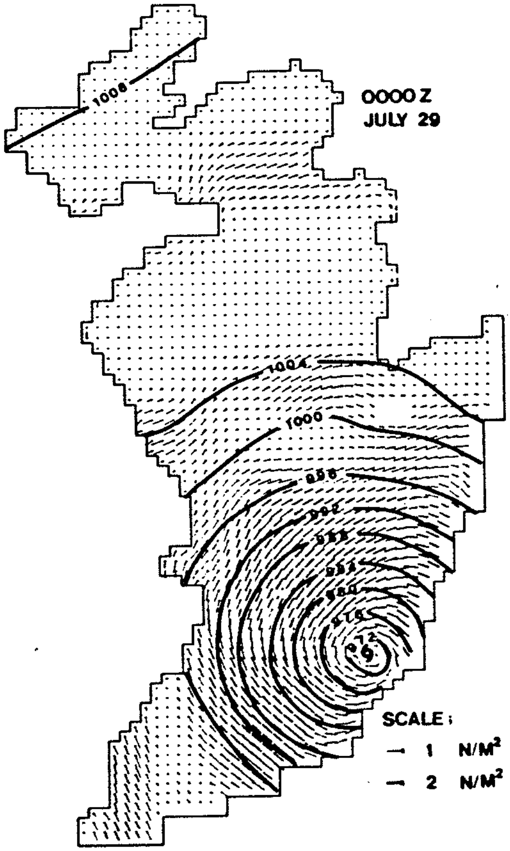

Figure 5.9a: Wind Stress Vector Field of July 29, 0000Z.

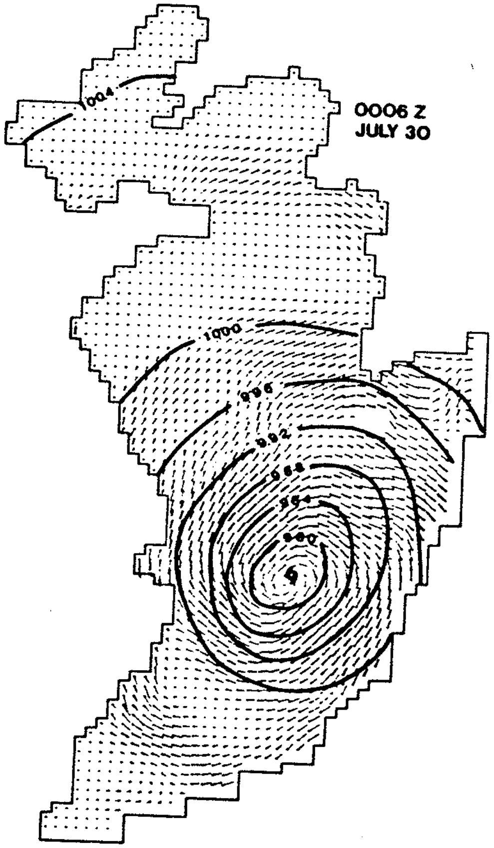

Figure 5.9b: Wind Stress Vector Field of July 30, 0006Z.

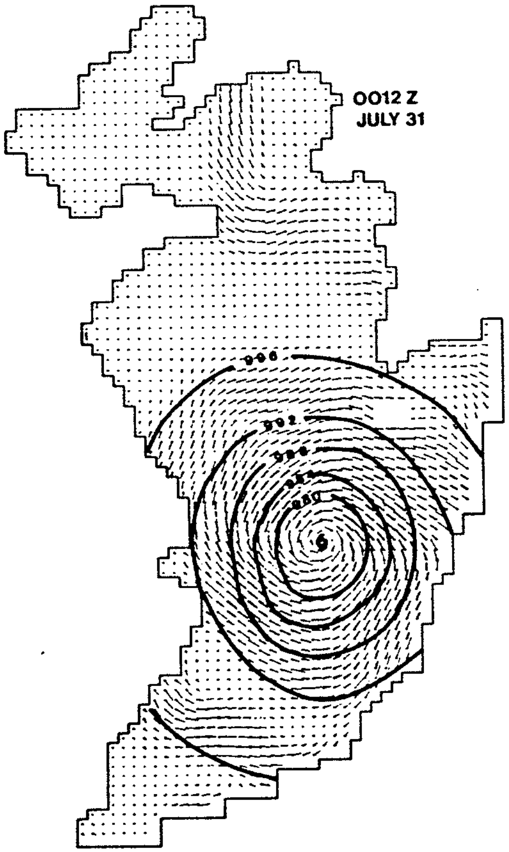

Figure 5.9c: Wind Stress Vector Field of July 31, 0012Z.

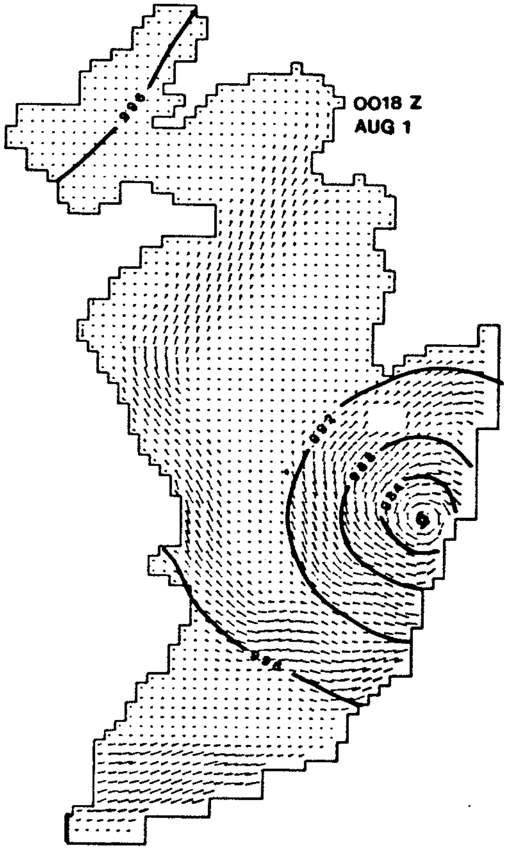

Figure 5.9d: Wind Stress Vector Field of Aug 1, 0018Z.

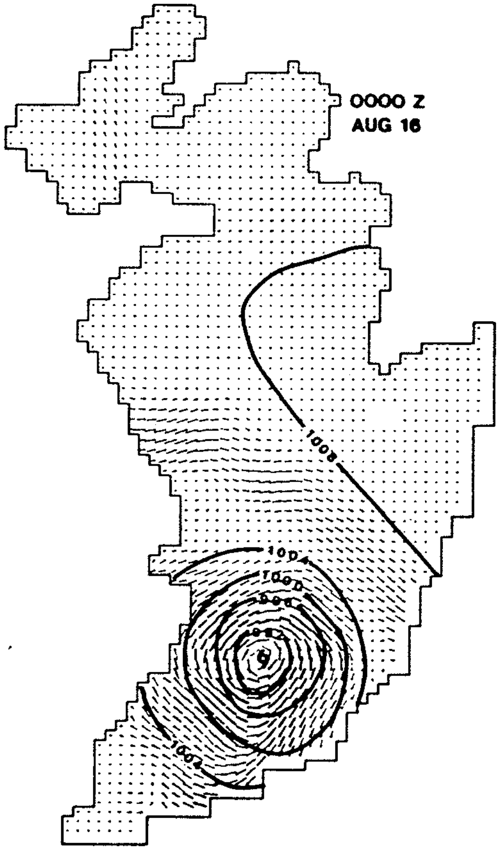

Figure 5.10a: Wind Stress Vector Field of Aug 16, 0000Z.

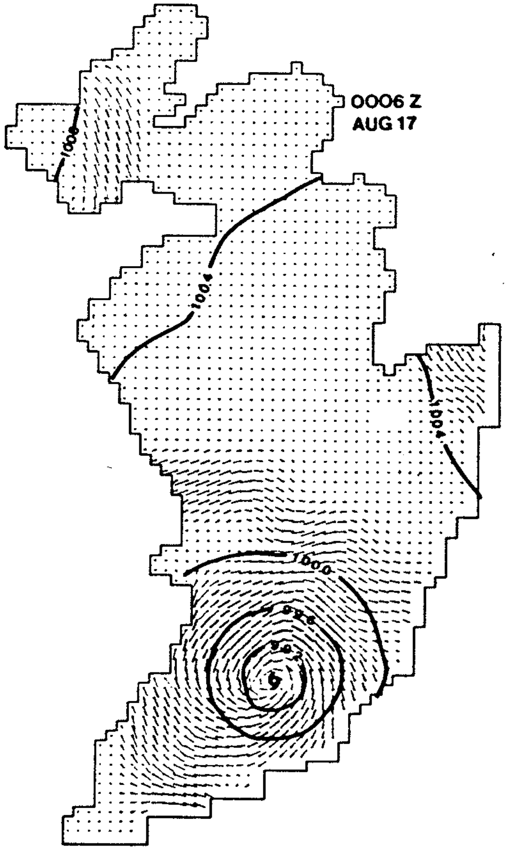

Figure 5.10b: Wind Stress Vector Field of Aug 17, 0006Z.

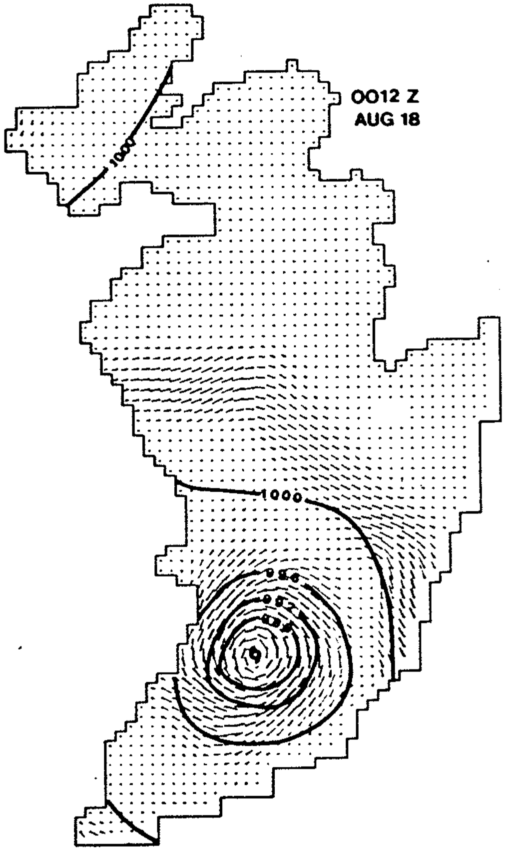

Figure 5.10d: Wind Stress Vector Field of Aug 18, 0012Z.

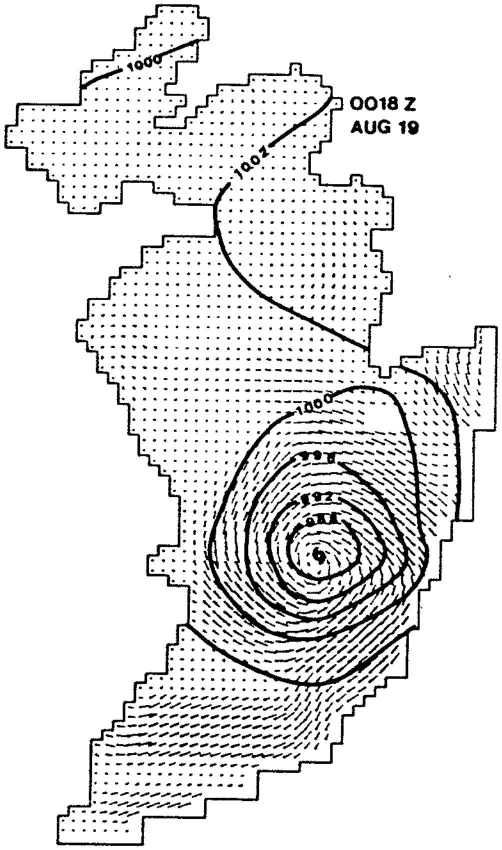

Figure 5.10c: Wind Stress Vector Field of Aug 19, 0018Z.

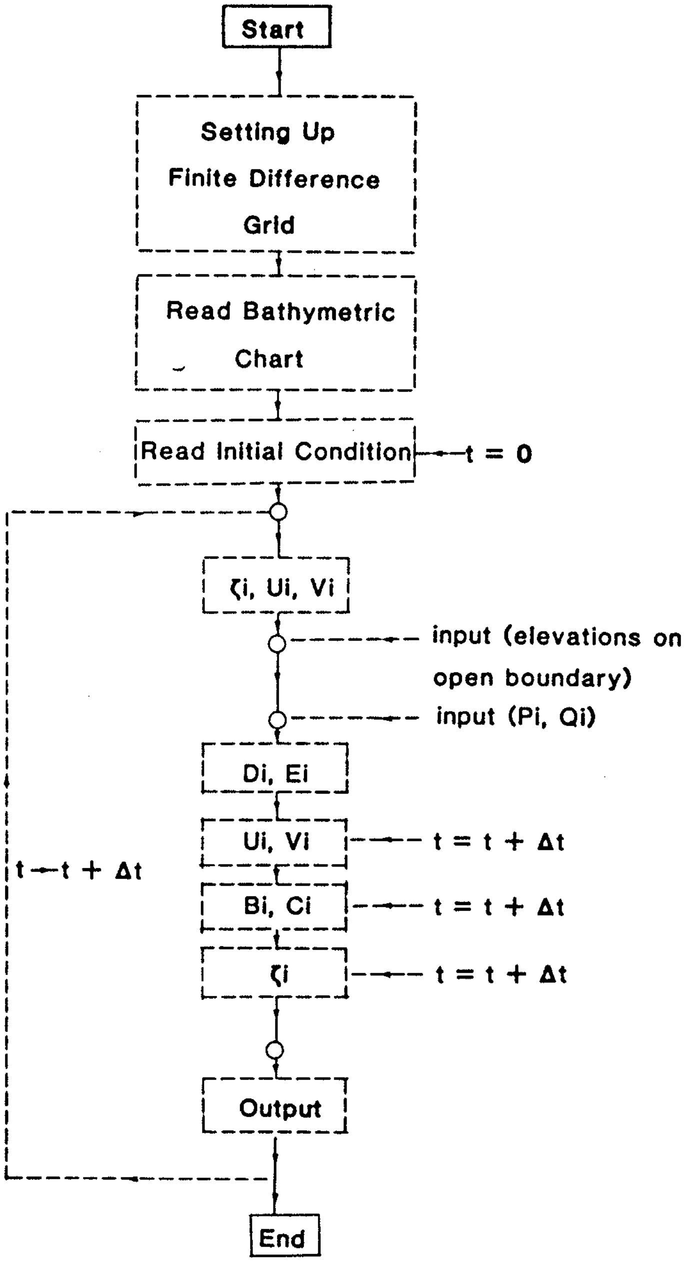

Figure 5.11: Summary of the Transient Sea Surface Computation Procedure.

During each time step of the iterative procedure, the wind speed is quadratically converted to wind stress as an external forcing function. A number of wind stress coefficient formulae have been tested in the simulations (described in previous chapter) before the final adoption of Wu's formula (Wu (1980,1982)). Both linear and quadratic bottom friction laws are used during the test runs to investigate the stability of the algorithm for the reproduction of transient sea surface variation. Although the stress estimated by using Brocks and Krugermeyer (1972) relation is about 2.5 times larger than that calculated by Heaps (1965,1969) at 3 m/s wind speed, a typical wind speed value for the period of August 4-6, an averaged change in sea surface height of less than 1.5 cm is observed in simulations. Similar results are obtained from higher wind speed environments (August 18-21) in which the wind stress computed using Wu's formula (Wu (1980,1982)) is about 2 times larger than the one predicted by Heaps(1965, 1969) at wind speed of 6 m/s. These results imply that the choice of the wind friction coefficient does not make too much difference for the wind speed range typical for this research.

Using the wind stress coefficient proposed by Wu (1980,1982), the transient sea surfaces along the satellite orbit tracks are computed using both quadratic and linear bottom stress laws. The values of 0.24 cm/s and 0.0025 are used for the constant coefficients of linear and quadratic bottom friction. Two features are observed in this comparison; (1) the peak to trough amplitudes of the sea surface oscillation associated with the quadratic bottom friction are considerably larger than those generated by linear bottom stress. The magnitude of oscillation increases with decrease of water depth but the wavelenght remains approximately the same in both cases, and (2) the absolute difference between the sea surface height resulted (from both laws) also varies with depth; the shallower the water, the larger the difference in computed sea surface elevations. In spite of these small differences in numerical values, the general magnitudes and dynamic shape of the transient sea surface profiles and the spatial distribution patterns remain much the same.

For orbit by orbit altimeter correction, a two dimensional interpolation scheme is used. Figures 5.12 and 5.13 are the simulated transient sea surface profiles along the selected satellite orbit tracks. In Figures 5.12 and 5.13, the horizontal (time) axis are assigned, for convenience, with respect to the computer searching time for the satellite orbit tracks over Hudson Bay. The actual mission time is given in the figure caption. The simulation results of August 4-6 (Figure 5.12) indicate that the difference in sea surface elevation along the satellite orbit tracks due to meteorological forces can be as large as 8 cm. More significant differences are observed in Figure 5.13 which show the simulated transient sea surface profiles during August 18-21. Path number 5 (revolution # 760) indicates a difference in sea elevation of up to 14 cm whereas path number 20 (revolution # 779) shows only 5 cm variation. Column 3 of Table 5.2 summarizes the magnitudes of the transient sea surface variation along the selected satellite orbit tracks. Also shown in this table are the wind speed ranges interpolated along the tracks that produce these variations.

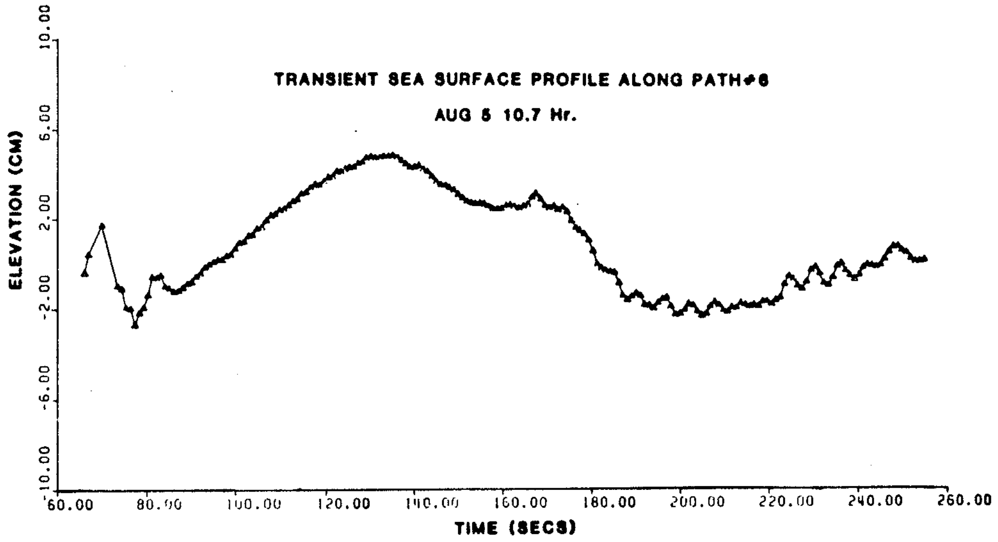

Figure 5.12a: Transient Sea Surface Profile of Hudson Bay Model for Revolution Number 559 (18671843 s to 18671944 s).

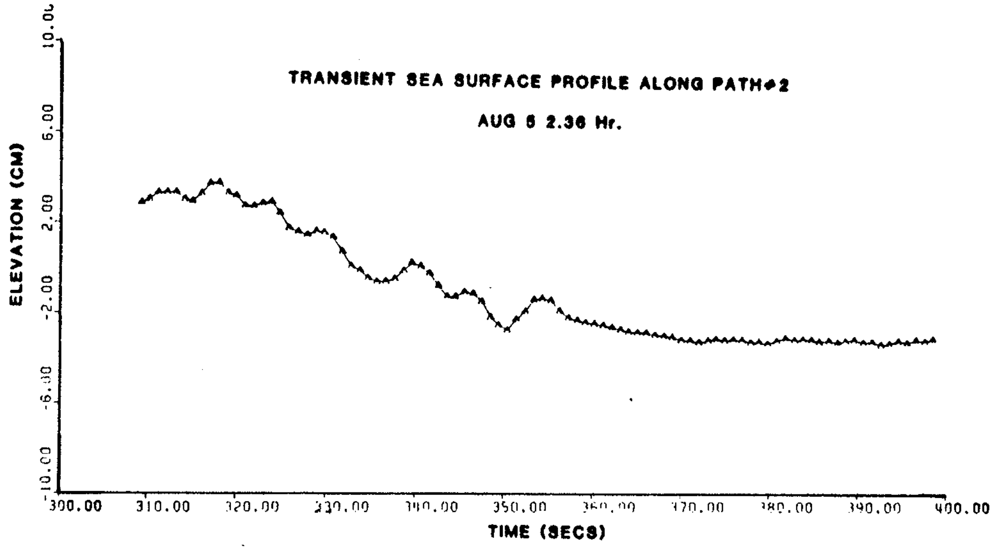

Figure 5.12b: Transient Sea Surface Profile of Hudson Bay Model for Revolution Number 564 (18701080 s to 18701246 s).

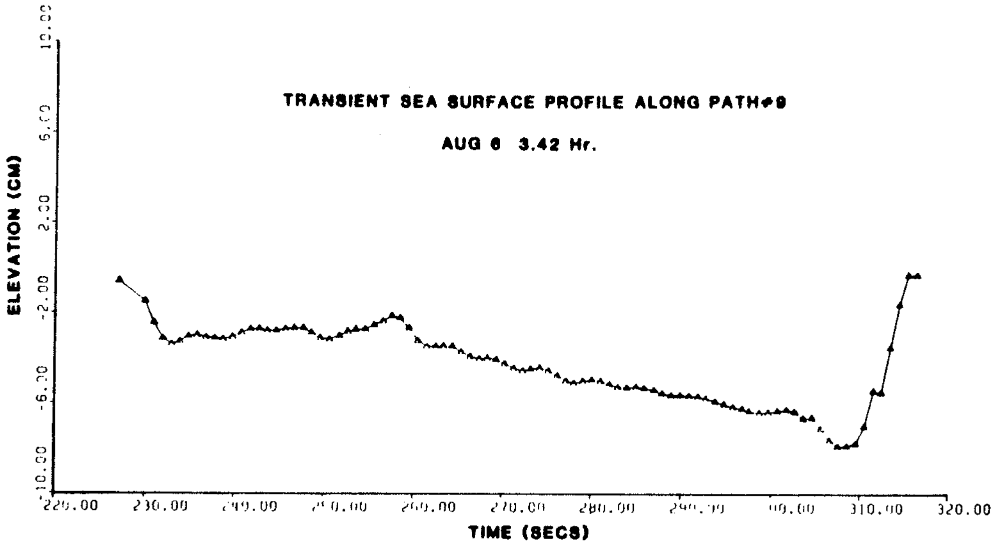

Figure 5.12c: Transient Sea Surface Profile of Hudson Bay Model for Revolution Number 574 (18762333 s to 18762405 s).

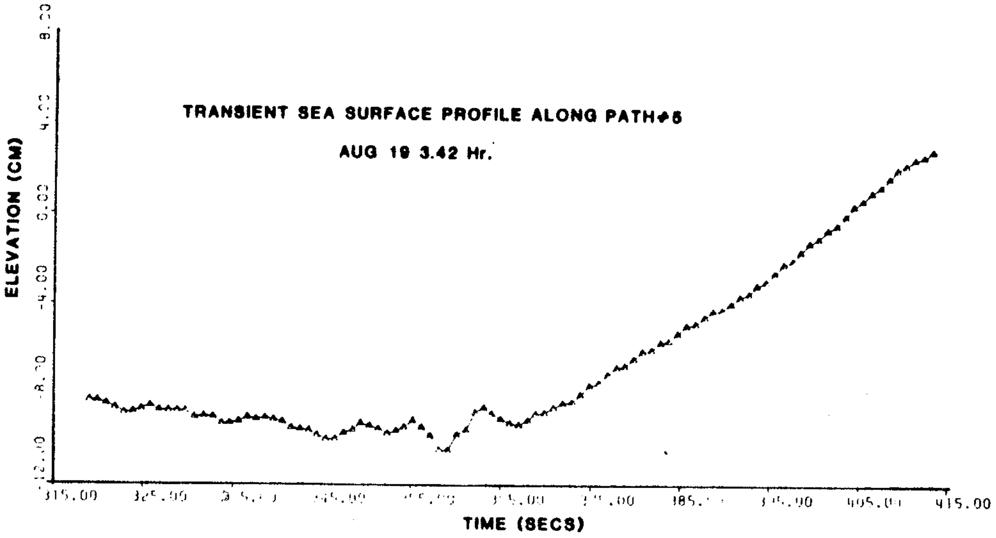

Figure 5.13a: Transient Sea Surface Profile of Hudson Bay Model for Revolution Number 760 (19885307 s to 19885408 s).

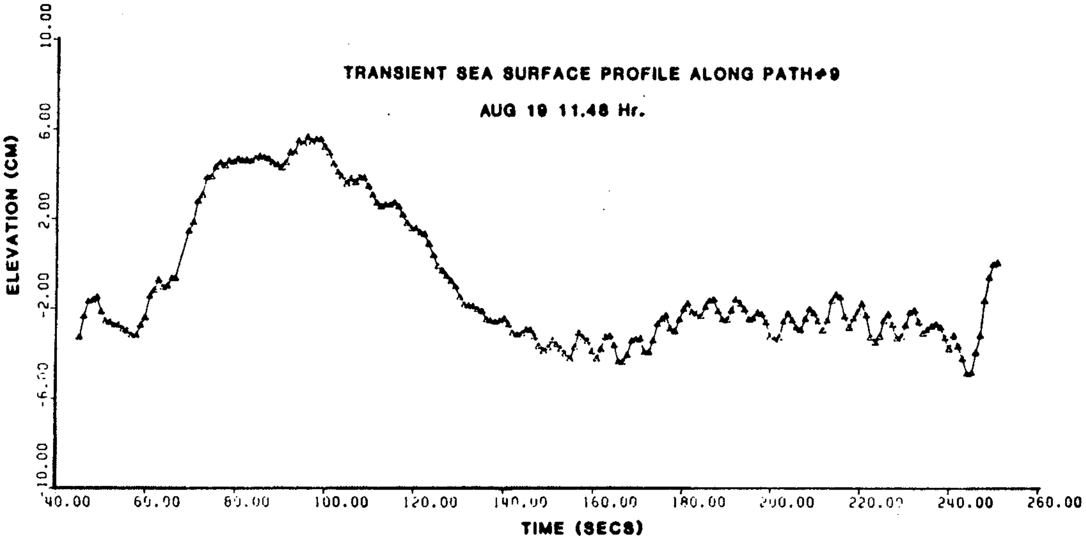

Figure 5.13b: Transient Sea Surface Profile of Hudson Bay Model for Revolution Number 765 (19914459 s to 19914829 s).

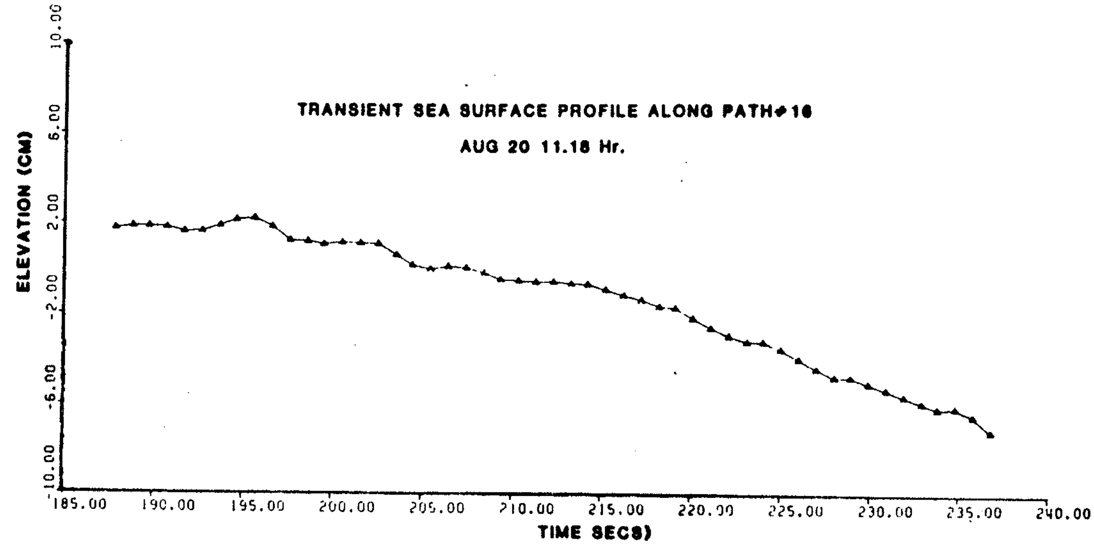

Figure 5.13c: Transient Sea Surface Profile of Hudson Bay Model for Revolution Number 779 (19999127 s to 19999126 s).

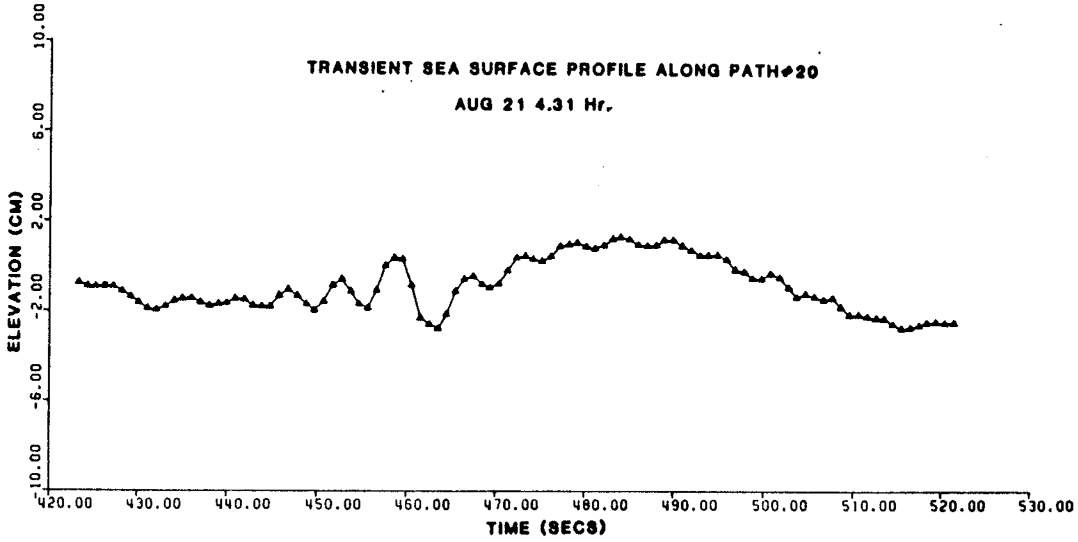

Figure 5.13d: Transient Sea Surface Profile of Hudson Bay Model for Revolution Number 789 (20060095 s to 20060536 s).

Table 5.2 Summary of Transient Sea Surface Variations and the Related Wind Speed Ranges.

Revolution Num.	Wind Speed Range (m/s)	Profile Variation (cm)	Model Variation (cm)
559 (path 2)	2.0 - 4.5	-3.0 - 4.0	-15.5 - 6.0
564 (path 6)	4.0 - 5.0	-3.0 - 5.0	-16.0 - 11.0
574 (path 9)	1.0 - 4.0	-8.0 - 0.0	-8.5 - 21.0
760 (path 5)	4.0 - 5.0	-10.0 - 4.0	-16.0 - 17.0
765 (path 9)	3.0 - 8.0	-4.5 - 6.0	-10.0 - 6.5
779 (path 16)	2.5 - 4.0	-7.0 - 2.0	-17.0 - 11.0
789 (path 20)	2.0 - 6.0	-3.0 - 2.0	-6.0 - 5.5

Figures 5.14 and 5.15 show the spatial distribution of the transient sea surface elevation while the satellite was in the middle of its tracks over Hudson Bay. The dotted lines are the footprints of the SEASAT tracks. The distribution of the transient sea surface elevation for August 6 at 3.42 hr (Figure 5.14c) is in very good agreement with the wind pattern resulting from the stationary depression system at the north-eastern part of Hudson Bay. An attempt was made to follow the development of the spatial distributions due to the disturbance during August 18-21, however, an examination of successive surface features did not reveal any clear trend in the changing distributions. It is concluded that the surface topography does not develop in a slow and gradual fashion as those observed for August 4-6. This is perhaps attributed to the fast moving character of the system, so that the trend of distributions does not have sufficient time to establish. From these diagrams it is clear that the magnitude of the transient sea surface variations of the entire model is larger than those reported

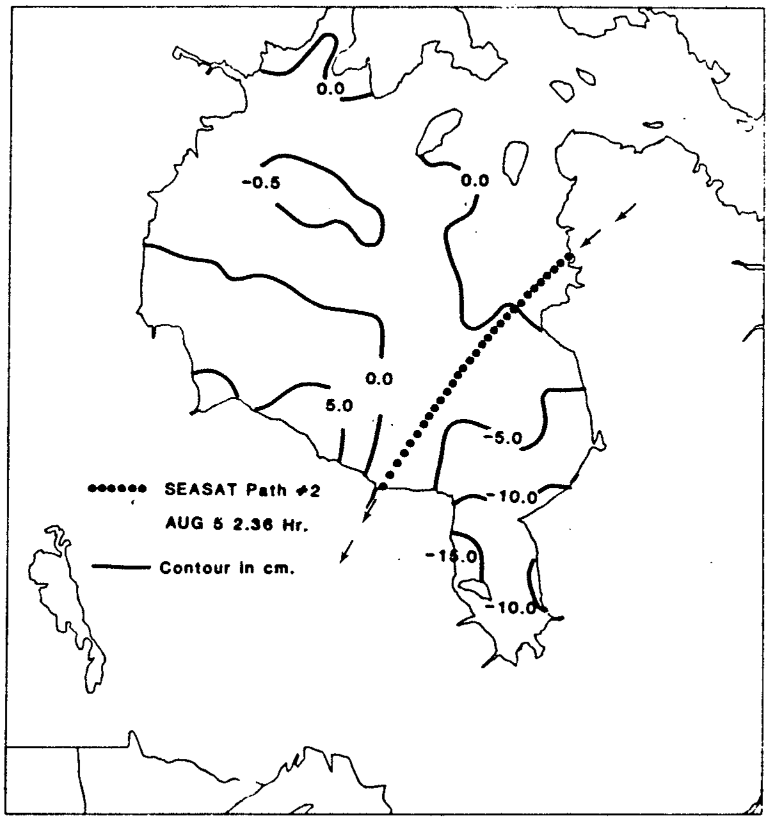

Figure 5.14a: Spatial Distribution of Sea Surface Elevation Corresponding to Figure 5.12a.

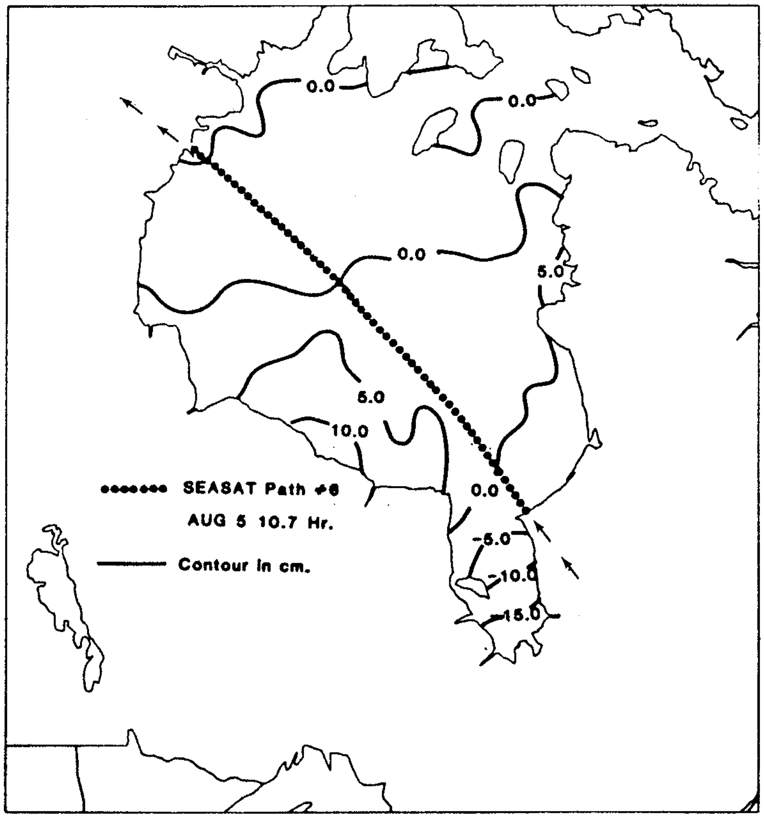

Figure 5.14b: Spatial Distribution of Sea Surface Elevation Corresponding to Figure 5.12b.

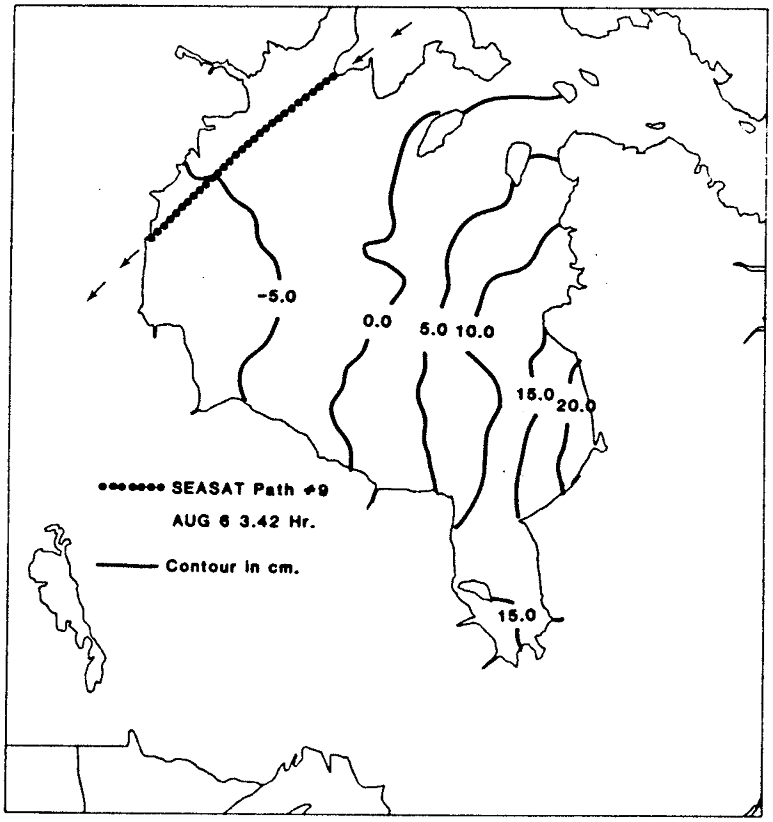

Figure 5.14c: Spatial Distribution of Sea Surface Elevation Corresponding to Figure 5.12c.

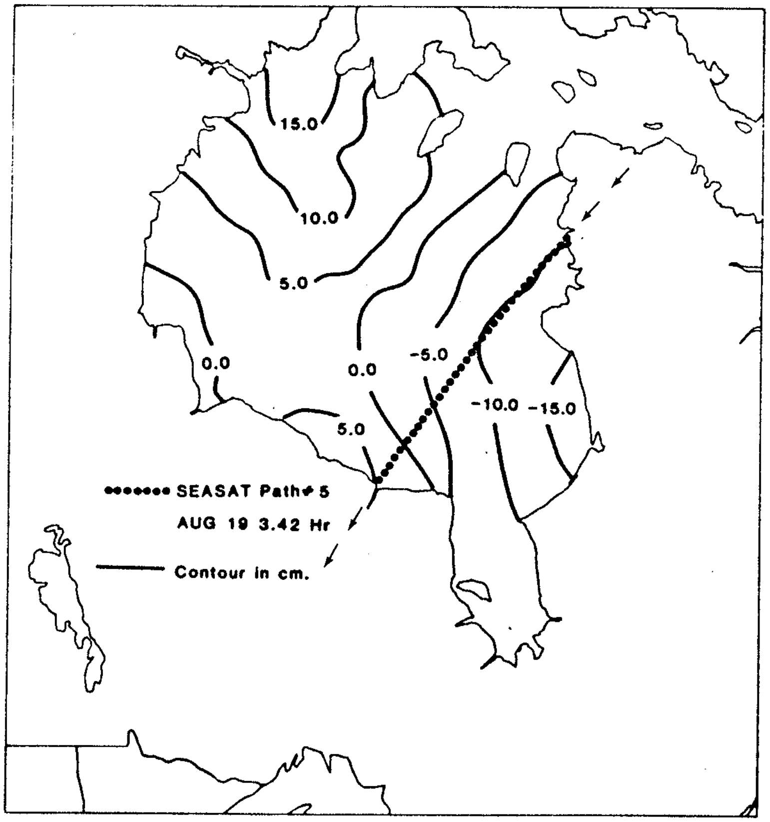

Figure 5.15a: Spatial Distribution of Sea Surface Elevation Corresponding to Figure 5.13a.

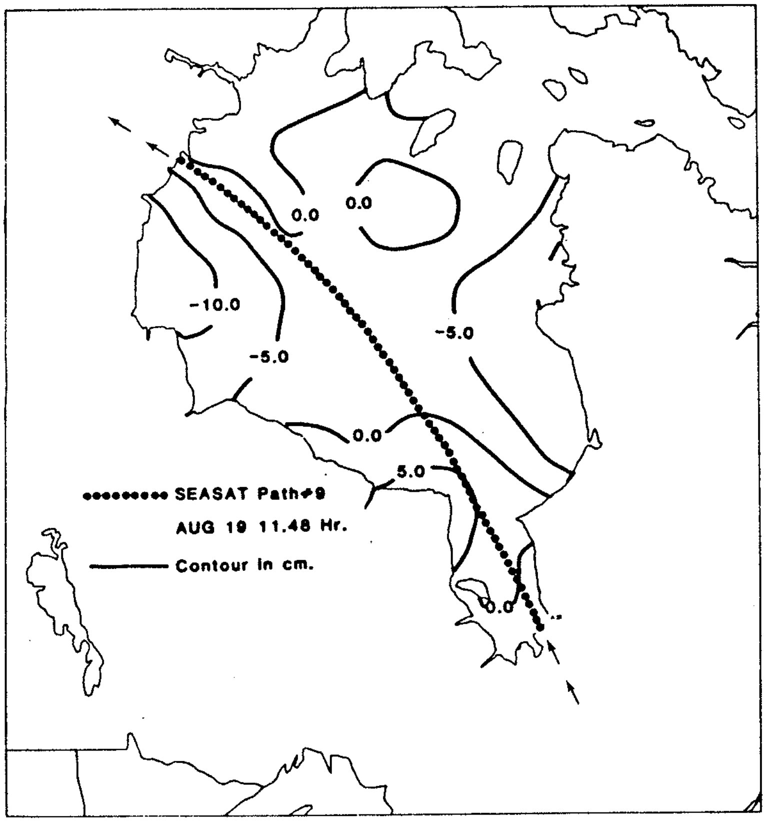

Figure 5.15b: Spatial Distribution of Sea Surface Elevation Corresponding to Figure 5.13b.

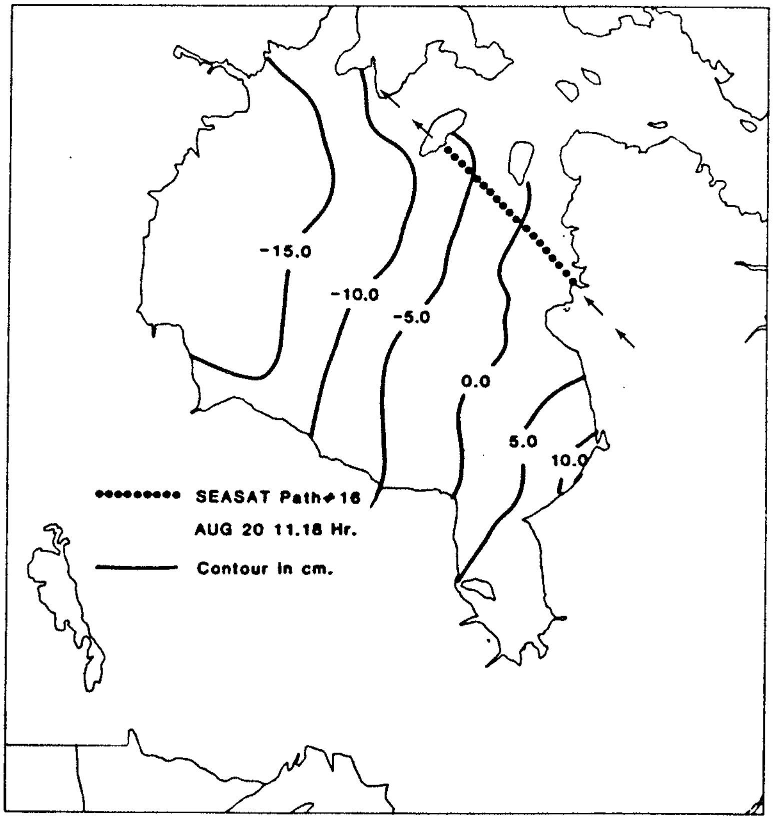

Figure 5.15c: Spatial Distribution of Sea Surface Elevation Corresponding to Figure 5.13c.

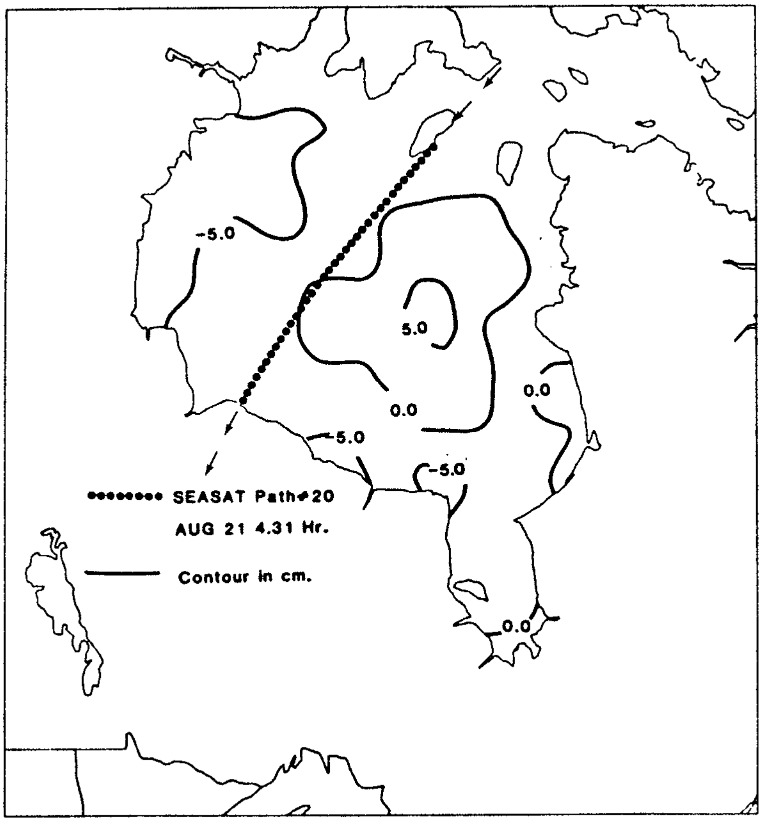

Figure 5.15d: Spatial Distribution of Sea Surface Elevation Corresponding to Figure 5.13d.

in column 3 of Table 5.2. The magnitude of the spatial distribution is also summarized in Table 5.2 as references to the variations along the orbit tracks.

The results presented in the Table 5.2 also imply that the wind speed is not the major constituent to the production of the transient sea surface elevation change. For example, the sea surface profiles of revolution # 564 shows an elevation change of 8 cm in wind speed range of 4.0 m/s to 5.0 m/s. However, the same wind speed range produces almost twice in the magnitude of the sea surface variation for revolution # 760. This difference is accounted for by the atmospheric pressure gradient and wind induced sea surface elevation piled up during, and more importantly, before the observation. The results of this study signify the importance of transient sea state in the precision requirement for the SEASAT geophysical data since the wind speed considered so far has a very low magnitude. However, through this research, an additional unimplemented correction is tested and provided for the SEASAT altimeter measurement and correction algorithm.

(c) Results from East China Sea and Yellow Sea

In the preceding section, a particular correction algorithm to sea surface height measurements has been discussed and suggested in addition to those given in the SEASAT-ALT GDR tape. Strictly speaking, if one recalls the total time varying sea surface T(t) in chapter II, there are other phenomena needed to be included. In most cases, however, the corrections due to body tide, loading tide, and marine tide are available. For example, the Global Ocean Tides model by Schwiderski (1978) contains all these corrections up to eleven tidal constituents. While this type of global model gives reasonable results in open sea, poor unacceptable values are given near coastal areas.

Since the nonlinear version of the modelling scheme is capable of reproducing surge and tide, some examples of transient surge modelling with tides are given here to illustrate that both of these phenomena can be simultaneously taken into account in one model. One important aspect of this is that the marine tide can be calculated for a few days yet the computation time is many times faster than the Global Ocean Tides tape prepared by Schwiderski (1978). Of course the marine tide will be the best computed by an array of response functions over the area, based on a dense network of observations in practice (Cartwight and Alcock (1981)).

Four examples of surge and tide computations from each period are shown in Figures 5.16 to 5.19. Dashed lines are the observed sea surface elevation profiles from the SEASAT after removing the SS3 profiles from them. The DC adjustments to the residual profiles have been performed in order to bring the observations to the datum of the model. Strategy of determining the amount of DC shifting is described in chapter 6. Diagrams (b) and (c) in the figures are respectively surge alone and tide alone computations, while the (a) diagrams are the computations of surge together with tides of M_2 , S_2 , K_1 and O_1 . Thus by removing the computed value of either tide alone or surge alone from all (a) diagrams, one can also study the

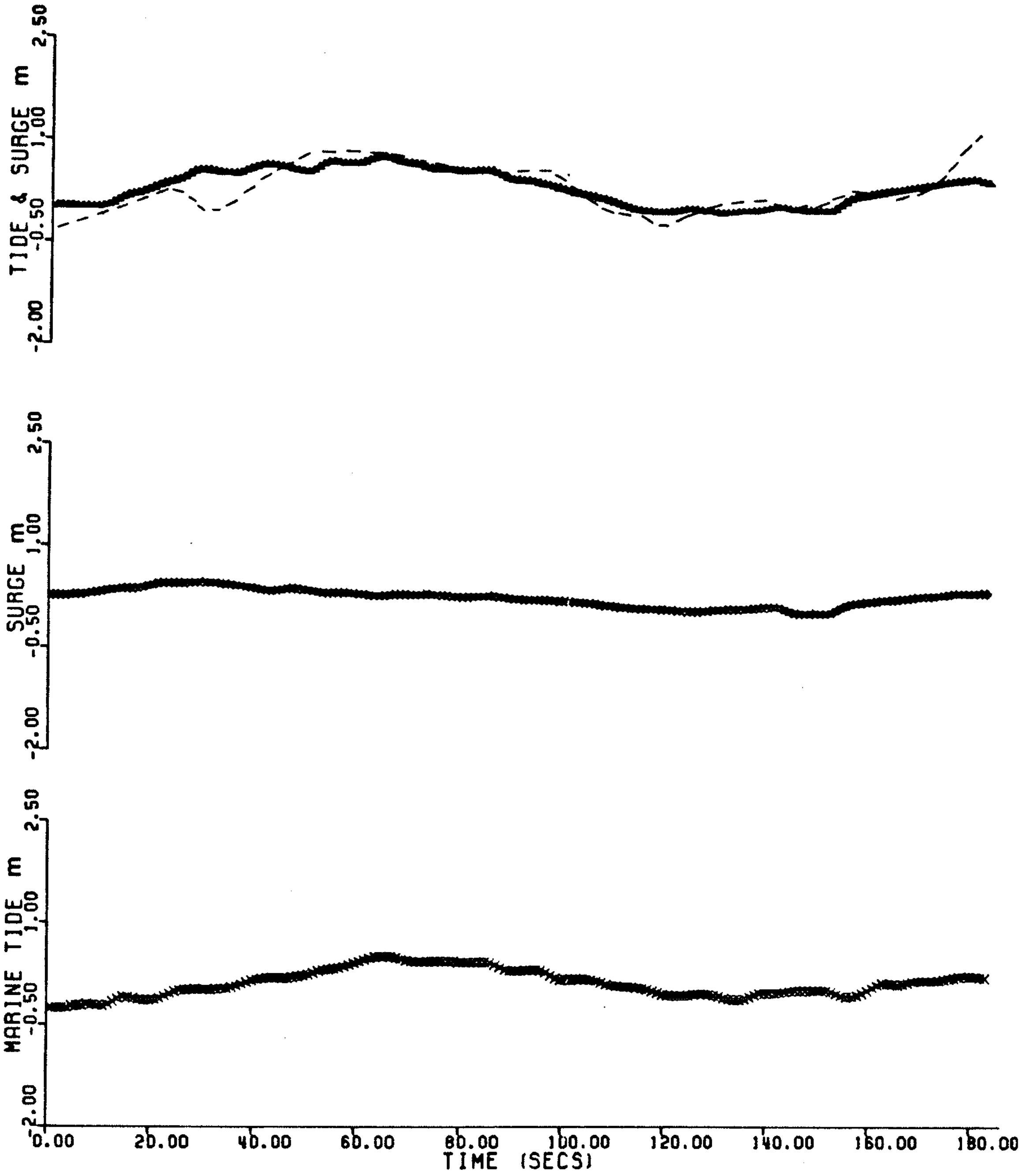

Figure 5.16: Tide and Surge, Surge Only and Tide Only Simulation for Revolution 456.

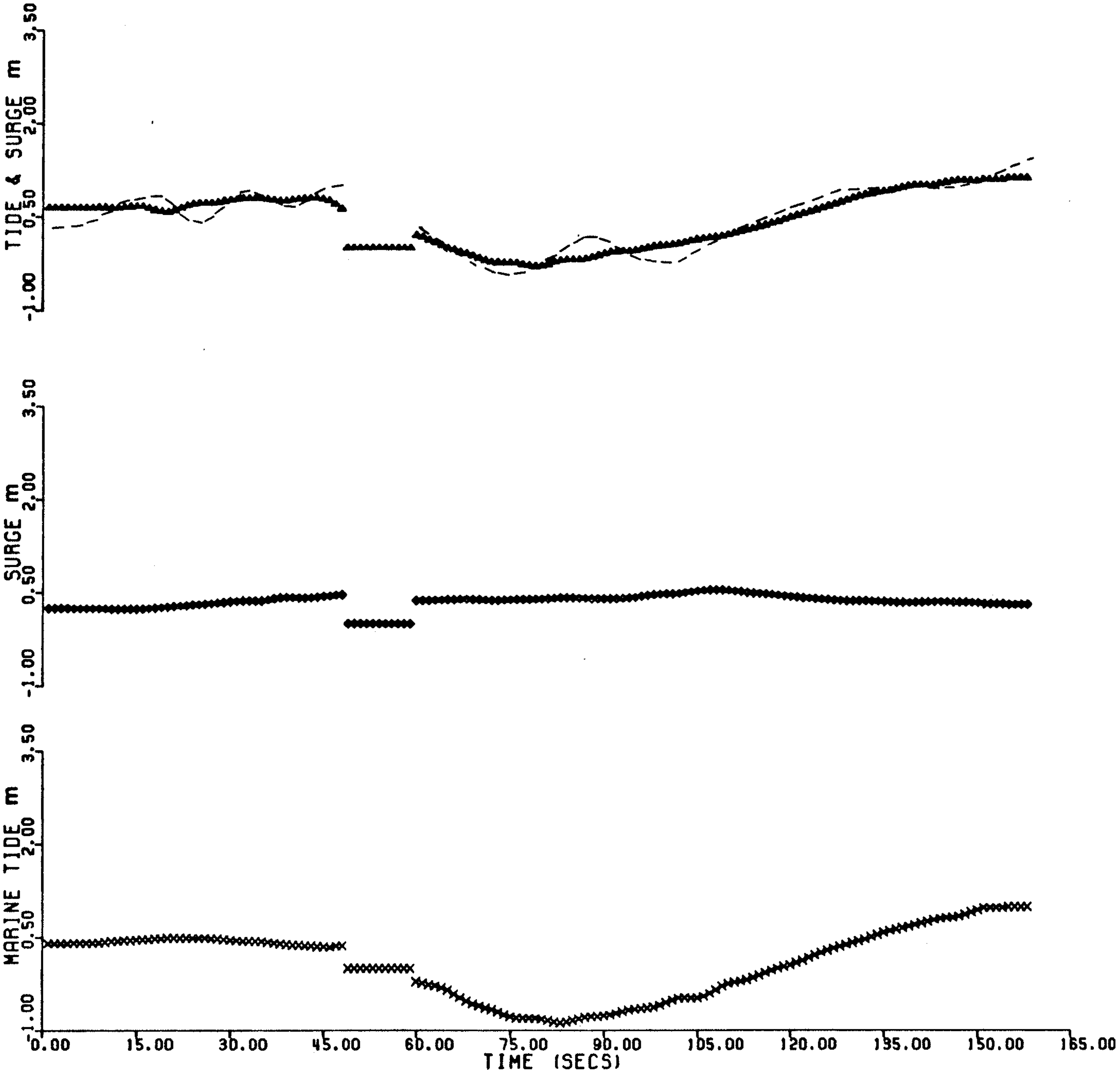

Figure 5.17: Tide and Surge, Surge Only and Tide Only Simulation for Revolution 499.

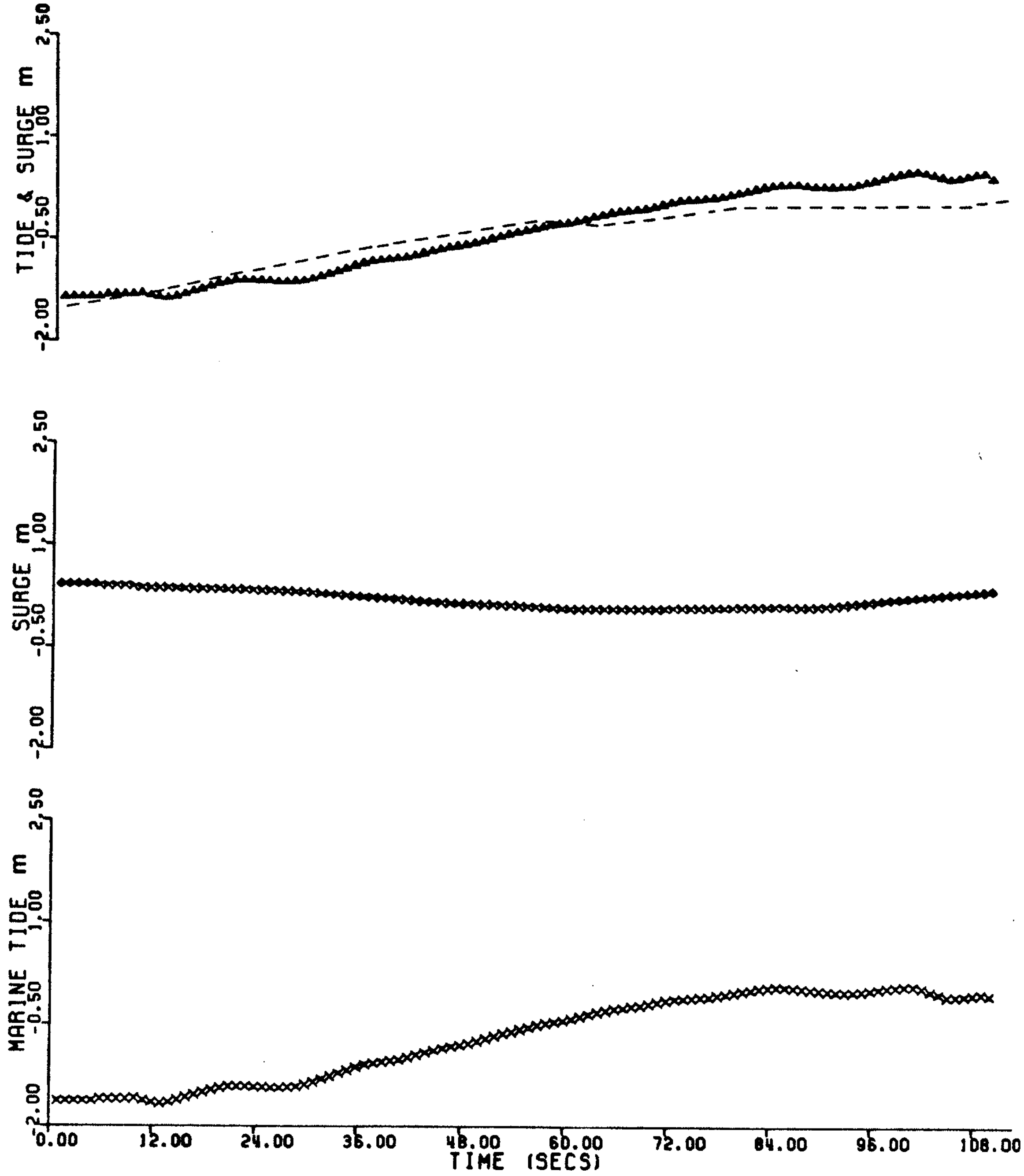

Figure 5.18: Tide and Surge, Surge Only and Tide Only Simulation for Revolution 751.

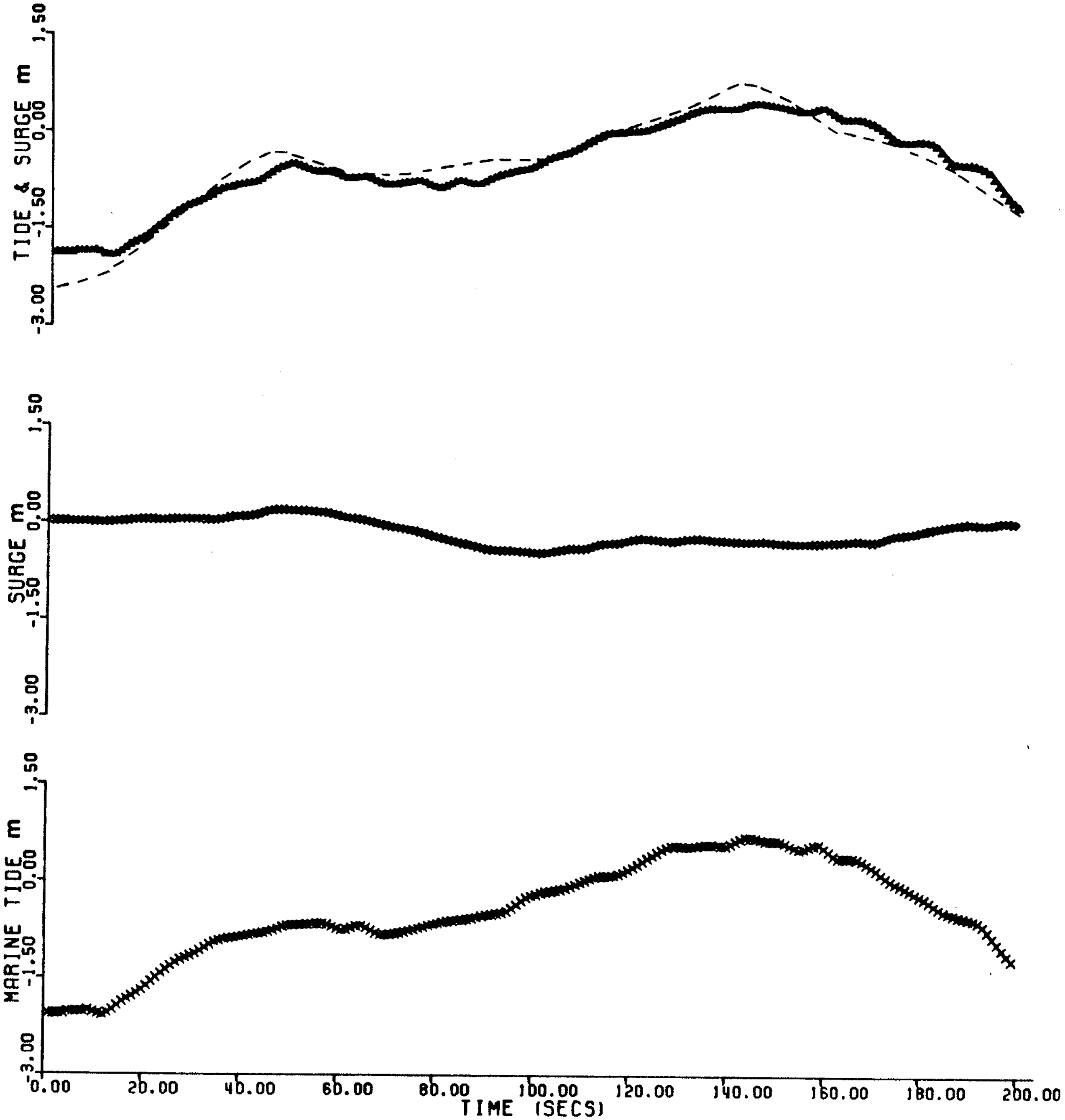

Figure 5.19: Tide and Surge, Surge Only and Tide Only Simulation for Revolution 794.

magnitude of interaction between surge and tide(Davies and Flather (1978)). From the figures and the rest of the computations, the typhoon induced surge elevation is found to be as large as 80 cm while tide alone is almost 2 to 4 times larger in magnitude. These indicate that the sea surface elevation change in the East China Sea and Yellow Sea is predominantly tides, phenomena which was also observed and numerical simulated in that area by Choi (1980,1983)).

2. On Wind Speeds from SEASAT Altimeter and MSL Pressure Charts

Beside the measurements of global sea surface topography, the SEASAT altimeter geophysical data set also contains valuable information on nadir wind speed. The microwave altimeter measures the radar echo power backscattered from the sea surface at vertical incidence, unlike the scatterometer which does its recording at a variety of incidence angles. The retrieval of nadir wind speed from the altimeter is possible because the strength of the backscatter is responding primarily to the sea surface roughness which is influenced by the surface winds. After an extensive study by Brown et al. (1981), a relationship between the vertical backscatter coefficient and wind speed at 10 m height above the sea surface is formulated. Accuracy assessments on the wind speed inferred from this relation have been carried out by Ferdor and Brown (1982) and Wentz et al. (1982). Their analysis was based on the comparison of altimeter inferred wind speed data to buoy measurements or those obtained from other two SEASAT microwave sensors; the SEASAT Microwave Scatterometer (SASS) and the Scanning Multichannel Microwave Radiometer (SMMR). The results obtained by Fedor and Brown (1982) show that Brown's algorithm yields unbiased wind speed estimate. While the main objective of SASS is to provide accurate wind vector measurements, the model function, which is used to convert the scatterometers' measurements to neutral stability wind vectors, requires further study as concluded by Jones at al. (1982).

On the other hand, the method used to derive the sea surface wind field from the MSL pressure charts is based on the assumption of geostrophic flow and an empirical relation obtained by Hasse and Wagner (1971), which convert the geostrophic wind to surface wind. The method also takes the Coriolis force and sea surface friction into account and is considered to give a good estimate to the surface truth. The following discussion presents the comparison between the geostrophically derived sea surface wind and satellite altimeter inferred wind during the Hudson Bay experiment.

(a) SEASAT Altimeter Wind Speed Algorithm

In microwave frequencies, the vertical backscatter coefficient is sensitive to the mean square slope of the low pass filtered replica of the true ocean surface. According to the spectral model by Phillips (1977), the mean square slope of the filter surface should vary logrithmically with the wind speed. Therefore, a correlation between the backscatter coefficient and wind speed can be established from observations. Using ship reports, aircraft measurements, buoy measurements, and data base from both the GEOS-3 and Skylab satellites, an empirical relationship is developed by Brown at al. (1981). The procedure of finding the empirical model function is accomplished by a least square algorithm which estimates the enviromental parameter vector $\vec{P}$ which minimizes the following sum of squares (SOS):

$$SOS = (\vec{M} - F(\vec{P},\vec{0}))^2 / Var^2 \qquad .....(5.1)$$

where

$\vec{0}$ - observation vector for the measurement
$\vec{M}$ - measurement vector
F - model function
Var - expected variance between measurement and model function

In SEASAT altimetry, the model function $F(\vec{P},\vec{0})$ relates the observed wind speed to the backscatter coefficient measured as vector $\vec{M}$. On careful analyses of many data sets by Brown et al.(1981), a three-branch logarithmic relationship between the backscatter coefficient and wind speed is proposed. This algorithm estimates the magnitude of the wind speed at 10 m height which is essentially a two-step numerical process. First, a three-branch relation converts the vertical backscatter coefficient (in dB) for WG (m/s), then the wind speed at 10 m is calculated as a function of WG. The first step is as follows:

$$WG = \exp\left(\frac{S - B}{A} \right) \qquad .....(5.2)$$

where

$$S = 10^{-(\sigma_o + 2.1)/10} \quad .$$

The constants A and B are function of backscatter coefficient and are given in Table 5.3. WG is then refined by a polynomial to yield W_{10} as:

$$W_{10} = WG \qquad \text{for } WG > 16 \text{ m/s}$$

and

$$W_{10} = \sum_{i=1}^{5} Ci\ WG^{i} \quad \text{for } WG < 16 \text{ m/s} \qquad .....(5.3)$$

where $C1 = 2.087799$, $C2 = -0.3649928$, $C3 = 0.04062421$, $C4 = -0.00190495$, and $C5 = 0.00003288189$.

Furthermore the conversion of wind speed at 10 m to SASS's wind

Table 5.3 Coefficients A and B for the Three-branch Wind Speed Algorithm Proposed by Brown et al.(1981).

Wind Speed Range (m/s)	Backscatter Coefficient Range (dB)	A	B
$WG \leqslant 7.81$	$\sigma_o \geqslant 10.9$	0.015950	0.017215
$7.81 < WG \leqslant 10.03$	$10.9 > \sigma_o \geqslant 10.12$	0.039893	-0.031996
$10.03 \leqslant WG$	$\sigma_o < 10.12$	0.080074	-0.124651

speed height (19.5 m) can be accomplished by multiplying the W_{10} by a constant which equals to 1.06 (Lorell et al. (1980)).

The algorithm described above is derived mainly from the GEOS-3 measurements and since the GEOS-3 radar had undergone extensive preflight backscatter coefficient testing, thus a comparison between the measurements of backscatter coefficient by SEASAT and GEOS-3, respectively, would give an assessment on SEASAT measurements (Fedor and Brown (1982)). Both data were searched to find the cross-over points within a maximum time difference of 1 hour. The results of comparison show an average difference between the two data sets of 1.6 dB. The source of this discrepancy is still unknown at present and for the purpose of wind speed study all measurements for SEASAT have been reduced by 1.6 dB. This correction is also included in the geophysical data available from NOAA Environmental Data and Information Service (EDIS).

(b) Comparison Statistics

The nadir wind speed at 10 m reference height along the selected paths of August 4-6 and August 18-21 are depicted in Figures 5.20 and 5.21 respectively. Also illustrated are the wind speeds derived from the MSL pressure charts. Table 5.4 gives the comparison statistics, i.e., the ranges of wind speed, the number of samples, the mean difference and the standard deviation. The correlation of the two wind profiles are reasonably good for revolution numbers 574, 765, and 789. To establish a statistical relation between the two data bases, a residual frequency plot of the difference of the two data sets for wind speed below 10 m/s is showed in Figure 5.22.

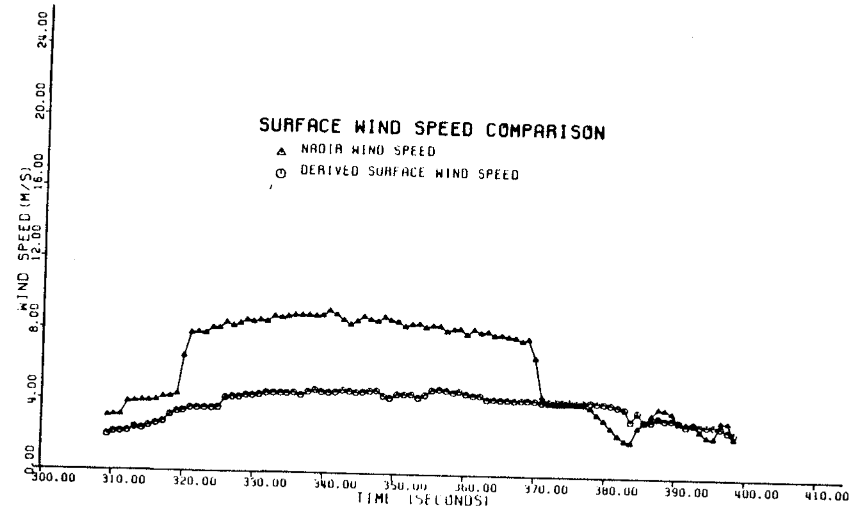

Figure 5.20a: Wind Speed Profiles Along Satellite Orbit Track of Revolution Number 559.

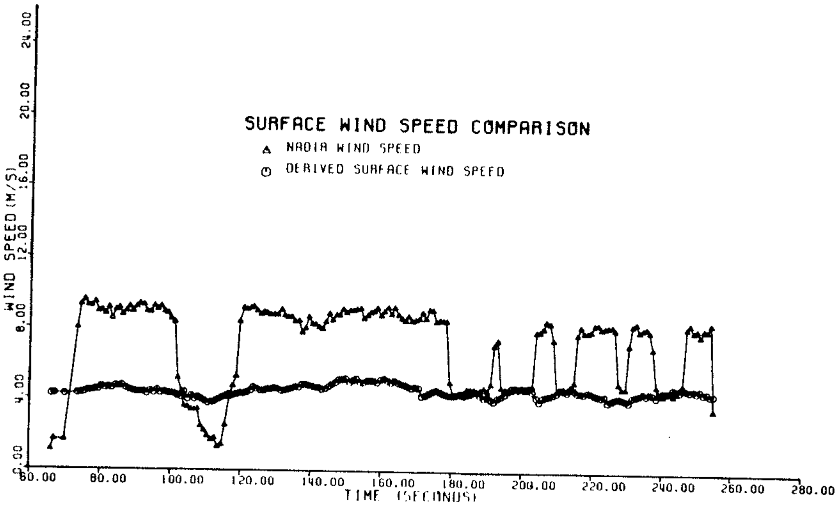

Figure 5.20b: Wind Speed Profiles Along Satellite Orbit Track of Revolution Number 564.

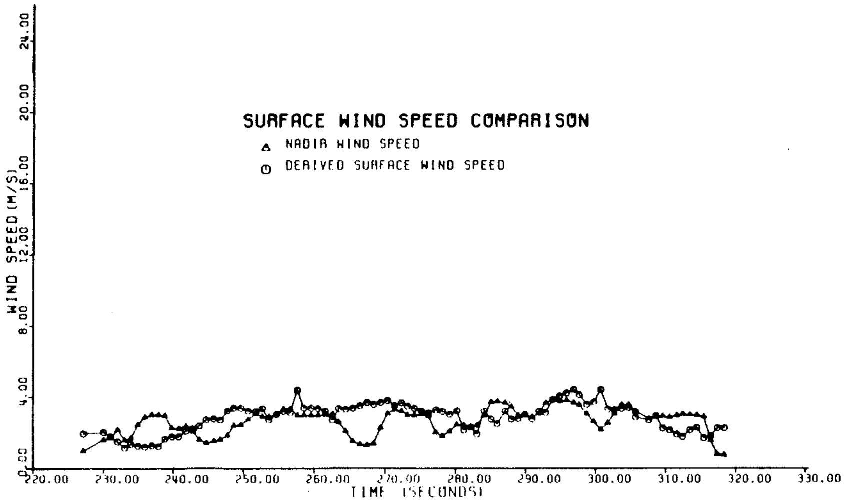

Figure 5.20c: Wind Speed Profiles Along Satellite Orbit Track of Revolution Number 574.

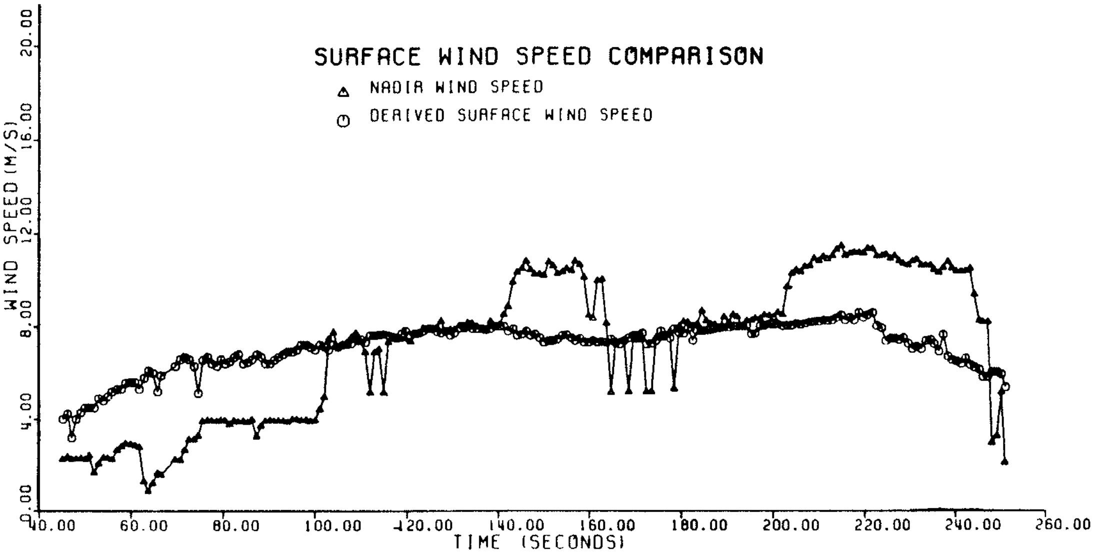

Figure 5.21a: Wind Speed Profiles Along Satellite Orbit Track of Revolution Number 760.

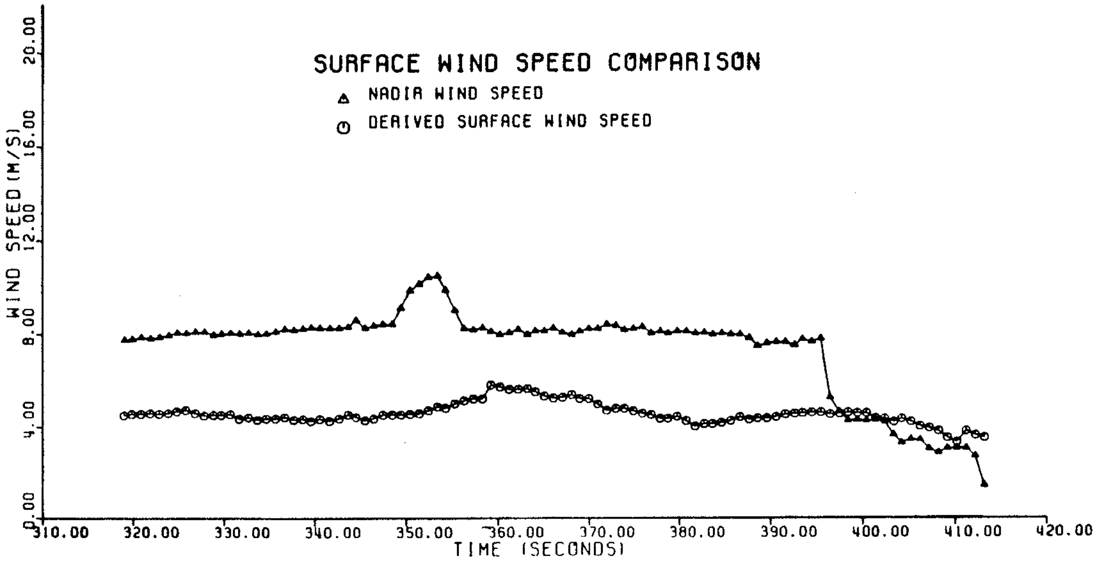

Figure 5.21b: Wind speed Profiles Along Satellite Orbit Track of Revolution Number 765.

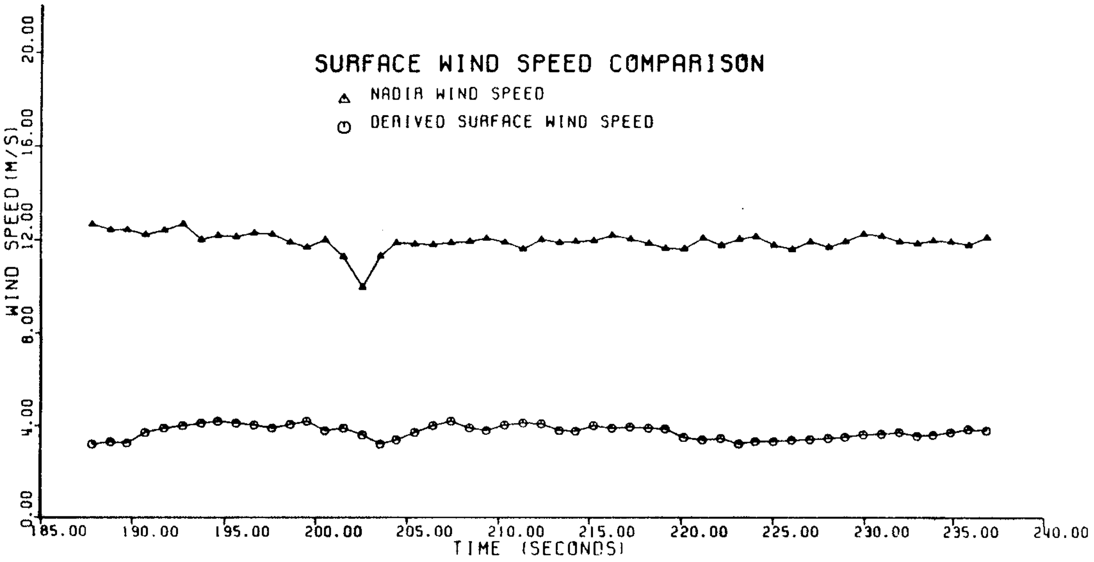

Figure 5.21c: Wind Speed Profiles Along Satellite Orbit Track of Revolution Number 779.

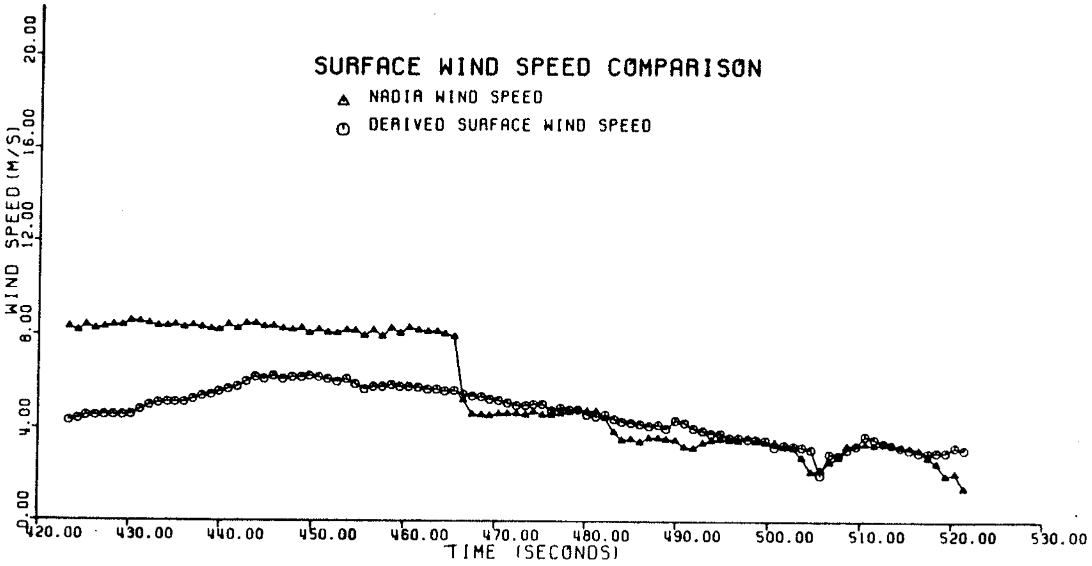

Figure 5.21d: Wind Speed Profiles Along Satellite Orbit Track of Revolution Number 789.

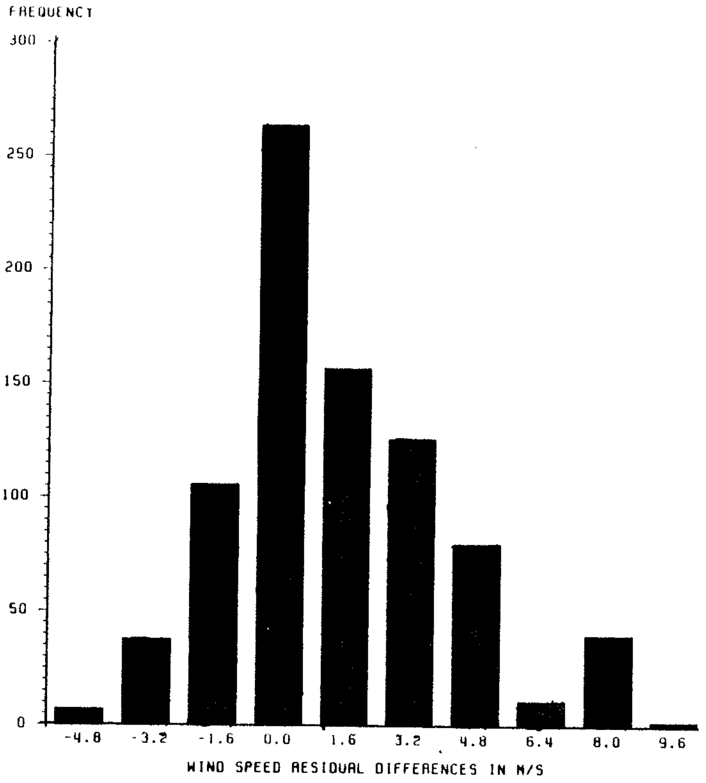

Figure 5.22: Wind Speed Comparison Statistics. Histogram of Residual Values of the SEASAT-ALT Wind Speed and the Geostrophically Derived Sea Surface Wind Speed. The Wind Speed Included is Ranging from 1 m/s to 10 m/s.

The general shape of the histogram follows a normal distribution with maximum located at zero residual. The overall mean difference for both periods is 1.41 m/s with a standard deviation of 1.80 m/s. These numbers are very similar to those obtained by Wentz et al. (1982) for altimeter inferred wind speed against insitu anemometer measurements. They reported a mean difference of -1.6 m/s and a standard deviation of 1.6 m/s for 6 comparisons over the range of 1 m/s to 5 m/s.

Table 5.4 Statistics of Wind Speed Comparisons

Revolution Number	Model Range (m/s)	SEASAT Range (m/s)	Number of Comparisons	Mean Difference (m/s)	Standard Deviation (m/s)
559	2.0-4.5	2.0-9.0	92	2.27	2.00
564	4.0-5.0	1.0-9.5	189	2.55	2.15
574	1.0-4.0	1.0-3.5	92	-0.20	0.90
760	4.0-5.0	3.0-9.0	97	2.79	1.73
765	3.0-8.0	1.0-10.0	209	0.09	2.38
779	2.5-4.0	10.0-13.0	51	8.18	0.48
789	2.0-6.0	2.0-8.0	101	1.00	1.63

One way to minimize the hidden discrepancy is to increase the size of the data set. Because of the nature of the wind speed prediction model, it has been possible in this research to compare considerably more data points along the satellite orbit tracks for a period of several days. Table 5.5 summarizes the overall statistics for all the revolutions along with the results obtained by other authors as comparisons.

The results (last row) are obtained from the revolutions listed in Table 5.4 (except for revolution number 779) with wind speeds ranging from 1 m/s to 10 m/s. The first three rows are obtained by Wentz et al. (1982) on wind speed retrived from the SEASAT scatterometer (SASS), altimeter (ALT), and radiometer (SMMR). Although they concluded that the SASS, ALT, and SMMR winds agree with the insitu anemometer measurements, the size of the data sets are very limited and this undoubtedly introduces some statistics uncertainties to the results. For the 87 comparisons made between the buoy measurements and satellite altimeter inferred wind speeds, Fedor and Brown (1982) give a mean difference of -0.25 m/s and a standard deviation of 1.6 m/s over the range of 1 m/s to 10 m/s.

Table 5.5 Summary of Different Type of Altimeter Inferred Wind Speed Comparisons

Comparison Type	Number of Comparisons	Mean Difference (m/s)	Standard Deviation (m/s)	Authors
ALT-Anemometer	6	-1.64	1.62	Wentz et al. (1982)
ALT-SMMR	6	3.08	1.67	Wentz et al. (1982)
ALT-SASS	5	-3.33	2.31	Wentz et al. (1982)
ALT-Buoy	87	-0.25	1.60	Fedor and Brown (1982)
ALT-MSL	689	1.41	1.80	in this thesis

Further statistics for the altimeter retrieved and the geostrophically derived sea surface wind speeds along the SEASAT orbit tracks are tabulated in Table 5.6. The percentage of reduction for the mean altimeter inferred wind magnitude $|\vec{Vs}|$ to the magnitude of the MSL derived wind $|\vec{Vd}|$ is given by:

$$\Delta_m = \frac{|\vec{V}_s| - |\vec{V}_d|}{|\vec{V}_s|} \qquad \ldots\ldots(5.4)$$

where Δ_m is the precentage of reduction. In almost all cases , $|\vec{V}d|$ is less than $|\vec{V}s|$ as shown in Table 5.6. The averaged reduction for all the selected SEASAT orbit tracks is approximately 28%.

Table 5.6 Precent Reduction Δ_m Required to Reduce the Mean Altimeter Inferred Wind to Model Derived Wind

Revolution Number	$\lvert\vec{V}s\rvert$ (m/s)	$\lvert\vec{V}d\rvert$ (m/s)	Percent of Reduction	Period Reduction	Total Reduction
559	6.19	3.91	36.8%		
564	7.10	4.53	36.1%	22.2%	
574	2.73	2.91	-6.50%		
					27.5%
760	7.36	4.45	37.9%		
765	7.25	7.15	1.40%	31.53%	
779	12.05	3.89	67.9%		
789	5.75	4.65	18.9%		

The finite jump discontinuities observed in the nardir wind speed profiles (Figures 20 through 21) indicate some deficiency of wind speed estimates from the altimeter. These discontinuities are likely caused by the empirical relation (equation (2.6)) which indirectly determines the backscatter coefficient from the AGU algorithm. Although the wind speeds profiles depicted in Figures 5.20 and 5.21 are functions of time alone, they are in fact functions of three independent variables; latitude, longitude, and time. For a meaningful comparison, it is necessary to have the measurements made as close to each other as possible in both space and time. As far as spatial interpolation of SEASAT tracks is concerned, it can be accurately done by fitting any 2-dimensional basis function to the derived windfield. Questionable results may, however, result in the time domain interpolation since wind field is highly variable in nature and also the MSL pressure charts used to extract them are only available every 3 hours. This is one of the main reasons why the comparison of wind speed is not performed for the weather charts obtained for East China Sea and Yellow Sea area. The derived wind speed profiles depicted in Figures 5.20 and 5.21 are interpolated linearly from two weather charts which are nearest to the average of the SEASAT orbit times over the Hudson Bay. Hence uncertainties in wind speed are undoubtedly inherent. If wind speed comparison is to be made for sufficiently long data set(a few revolution of data), then a more sophisticated interpolation technique will be necessary to retrieve wind speed informations from several weather maps.

CHAPTER VI

OCEAN BOTTOM FRICTION STUDY

1. Background Ocean Bottom Friction Study

In previous computations, the ocean bottom friction terms in the equations of motion have been parametrized in terms of (1) the depth-averaged current and (2) the square of the depth-averaged current. For deep water, these representations of the ocean bottom friction are sufficient. However, in extremely shallow water areas with water depth, less than 1 or 2 m, there may be some difficulties with numerical stability of the solution since both frictional laws are expressed in terms of inverse water depth. Therefore, other representations of ocean bottom stress may be desirable in hydrodynamic modelling, especially when the water depth is shallow. The allowable expression for the bottom friction law must, in general, satisfy the following criteria:

(1) It should give a reasonable magnitude of bottom stress in shallow water (less than 1 m), since both the linear and quadratic laws approach to infinity nearly exponentially as the depth approaches to zero.

(2) It must be computationally simple to use. A complex expression may be physically unrealistic in practice. Furthermore, the 'new' representation should somehow vary with

water depth, an important control parameter.

(3) It should be compatible with the conventional bottom friction laws, i.e., the linear or quadratic friction laws, as the water depth increases.

Given these conditions, the following generalization for the ocean bottom friction term can be used (Ramming (1978)):

$$\tau_b = a_o \frac{e^{-NH}}{H^M} \rho\, U^M \qquad \text{.....(6.1)}$$

where M = 1 or 2 and N = 0, 1, 2, ... The parameter M denotes the selection of frictional law with U corresponds to the magnitude of depth-averaged current. The parameter N denotes the selection of damping effect at shallow water and a_o ,is a constant with or without dimension, depends upon the selections. For N = 0, the generalized bottom friction law of equation (6.1) reduces to the familiar linear and quadratic friction laws for M = 1 and 2, respectively. In these cases, a_o becomes the linear stress coefficient and quadratic stress coefficient, accordingly. To see the behavior of the generalized law in shallow water, equation (6.1) is plotted for a few combinations of N and M against the water depth H, assuming both the current and the constant to be unity (Figure 6.1). From this diagram, it is evident that the functions 1/H (linear friction) and $1/H^2$ (quadratic friction) which are associated with depth-averaged current are not suitable for shallow water (e.g.

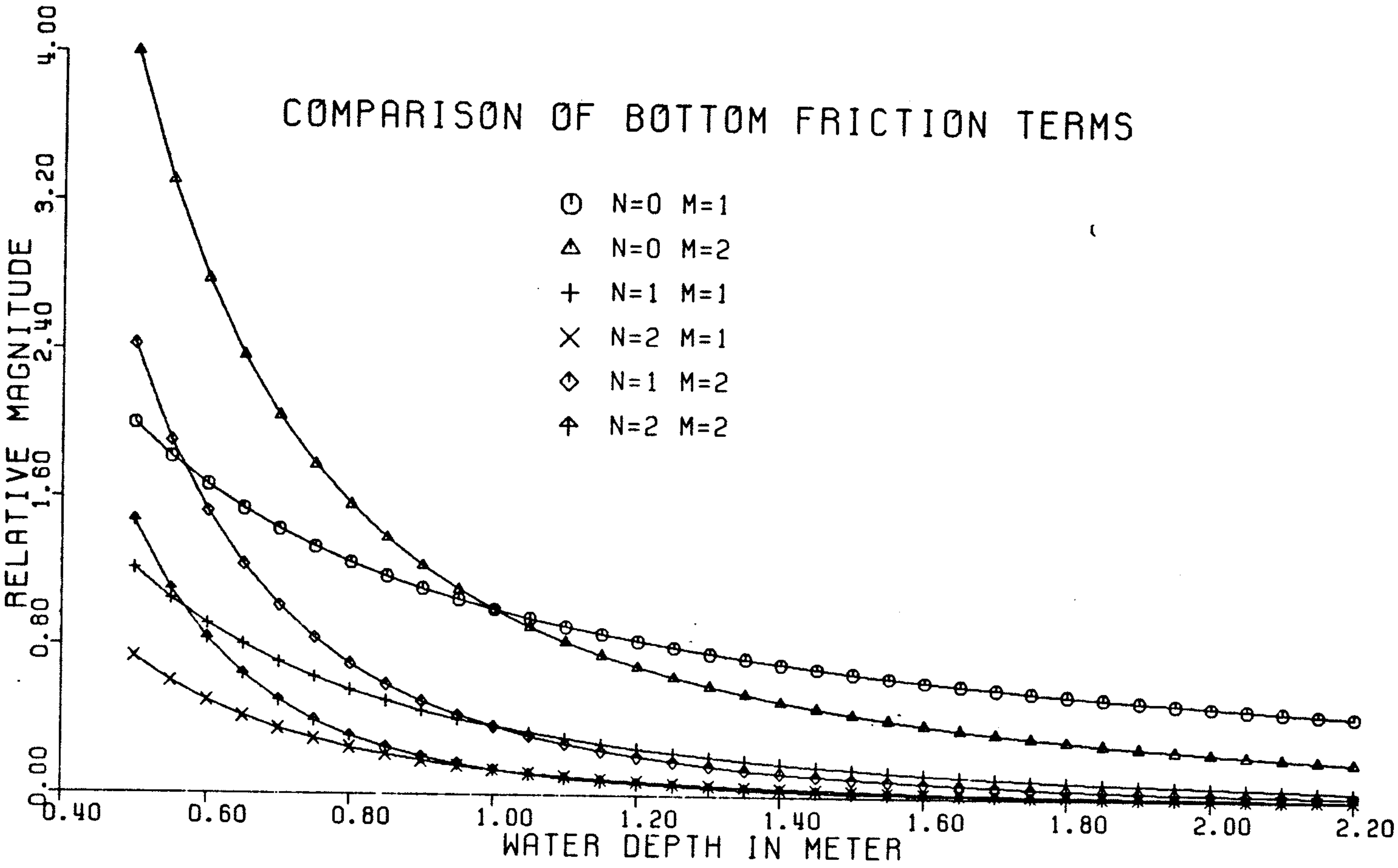

Figure 6.1: Graphical Representation of the Relative Magnitude of Equation (6.1) as a Function of Water Depth.

from 0.6 m to 1.2 m). In general, the addition of the inverse exponential function exp(-NH) in equation (6.1) reduces the magnitude of the bottom stress when the water depth is approaching zero. If the water depth field in the modelling area is restricted similar to the number given in the figure, equation (6.1) with N = 1 or 2 would be adequate to minimize the instability of the solution in shallow water. Further experiments have to be carried out to examine other treatments of the bottom friction defined by equation (6.1). This will require proper in situ measurements in coastal water areas. Further complications arise if the coefficient a_o in equation (6.1) is no longer simply a constant. From the experiences in sea surface wind stress coefficient, a_o may vary with current (for example, a linear proportionality of a_o to current speed). This is itself a very complicated matter to be studied with our present knowledge, although the possibility does exist for further experiment. Equation (6.1) however overcomes the problem of shallow water and converges to usual friction law when water depth increases.

2. Estimation of Ocean Bottom Stress and Friction Coefficient

There are several techniques which can be used to estimate boundary shear stress. Most of these techniques require in situ measurements, thus they were impractical until the last two decades. The most common ones are (1) Reynold Stress or Eddy Correlation, (2) Velocity Profile and (3) Quadratic Stress. They are briefly described as follows.

Reynold Stress Technique

In turbulent flow, the velocity in the vicinity of the ocean bottom can be considered to have two components: mean values over some interval of time and its instantaneous component u' and w' (Bowden (1978) and Bowden and Fairbairn (1956)). The total stress is given by:

$$\tau_b^R = \rho \mu \frac{\partial U}{\partial z} - \rho \overline{u'w'}$$

where the bar denotes the mean value of the product and μ is the kinematic coefficient of viscosity. The instantaneous current fluctuation in the main flow and its vertical component are respectively represented by u' and w'. The first term on the right-hand side is called the viscous stress while the last term is the Reynold stress. Since the viscous sublayer is about 1 cm in deep sea and 0.1 cm in continental shelf (Bowden (1978)), and since the viscous stress is small compared to the Reynold stress outside the viscous sublayer or in fully turbulent flow, the stress is usually expressed as:

$$\tau_b^R = - \rho \overline{u' \, w'} \quad . \qquad .....(6.2)$$

Equation (6.2) has been used by Bowden and Fairbairn (1956) and Heathershaw (1976) to estimate bottom stress and quadratic stress coefficient.

Velocity Profile Method

The logarithmic velocity profile was described in terms of the Karman - Prandtl equation as derived in Sverdrup et al. (1942). It is given by:

$$U(z) = \frac{U_*}{k_o} \ln \left(\frac{z + z_o}{z_o} \right)$$

where k_o is assumed to be 0.40. z_o is the length scale associated with bottom roughness and is small compare with z. U_* is the drag velocity or frictional velocity. The above equation is in exactly the same form as the one adpoted for the sea surface wind analysis (equation (4.14) in chapter 4). For z.<< z_o, it becomes:

$$U(z) = \sqrt{\frac{\tau_b^v}{\rho}} \frac{1}{5.75} \ln \frac{z}{z_o} \qquad .....(6.3)$$

where the boundary shear stress τ_b^v can be derived from the slope of the velocity profile.

Quadratic Stress Law

It has been experimentally shown that the shear stress at the boundary is proportional to the fluid density and square of the mean velocity:

$$\tau_b^Q = C \rho U_{z'}^2 \qquad .....(6.4)$$

where C is called the drag coefficient or quadratic bottom stress coefficient and z' is usually taken at a reference height above the sea bed. In oceanography, it is customary to take z' equal to 100 cm. Equations (6.4) and (3.8) are essentially the same only that the velocity term in equation (3.8) is a depth-averaged quantity.

In fact, all the above methods require highly sophisticated instruments and careful data processing and very often, they present considerable technical difficulties. For example, the Reynold stress method needs sensitive instrumentation to measure current fluctuation and time consuming time series analysis for data interpretation while the velocity profile technique demands measurements of current as a function of depth. Thus, the quadratic stress law has become a very popular alternative. Many experiments have been devoted to the estimation of the quadratic bottom stress coefficient C to better define the law. However, unlike the results obtained for the quadratic wind stress coefficient (chapter 4), the value of C is still uncertain and a wide range of value has been concluded.

In general, two approaches can be employed to determine the ocean bottom friction coefficient. The direct and usual approach is to measure the components of the current velocity, thereby extracting the stress on the bottom boundary using Reynold stress technique (e.q. Bowden and Fairbairn (1956)). However, if measurements of current can be made as a function of depth, stress can be deduced graphically. In either case, the computed stress may then be equated to either quadratic or linear stress law to estimate the constant of proportionality. The trouble with this approach is the assessibility to deep ocean environment where the installment and maintenance of equipments would be coastly and time consuming. On the other hand, the modelling approach uses theoretical calculations and makes possible comparisons with observations anywhere in the globe. For example, Grace (1930) provided a suitable value for the linear stress coefficient from observations made in ocean tidal modelling of the Gulf of Suez. This approach is further facilitated when a massive number of observations are available. The SEASAT-ALT data provide such an opportunity and are thus ultilized in this research. Tables 6.1 and 6.2 summarize some of the earlier as well as recent work done on the estimation of frictional coefficients.

Most of these values are derived from the tidally-induced current observations through a combination of the quadratic stress law with one of the above methods. These measurements are largely confined by the number of measurements, so that they can not be used as a reliable representation. From the Table (6.2) it is clear that the consistency of the quadratic friction coefficient is not satisfactory, although the values obtained from the Red Wharf Bay indicate a small deviation and fall in a range near the traditional value of 0.003.

Table 6.1 Values of Linear Friction Coefficients for Bottom Friction Process.

Author	Frictional Coefficient	Area
Weenink (1958)	0.17 - 0.31 cm/s	Southern North Sea
Stock (1976)	0.245 cm/s	Gulf of California

Table 6.2 Values of Quadratic Friction Coefficients for Bottom Friction Process.

Author	Frictional Coefficient	Area
Grace (1930)	0.003	Gulf of Suez
Bowden & Fairbairn (1952)	0.0036	Red Wharf Bay,Anglesey
Bowden & Fairbairn (1956)	0.0024	Red Wharf Bay,Anglesey
Bowden et al. (1959)	0.0035	Red Wharf Bay,Anglesey
Charnock (1959)	0.0034	Red Wharf Bay,Anglesey
Sternberg (1968)	0.0031	Puget Sound,Washington
Hearthershaw (1976)	0.0015-0.0019	Irish Sea
Stock (1976)	0.0015	Gulf of California
Wolf (1980)	0.0014-0.0271	Northern Irish Sea
Weatherly & Wimbus (1980)	0.0056	Blake-Bahama Outer Ridge
Chriss & Caldwell (1982)	0.0032-0.008	Oregon Shelf
Bowden & Fergurson (1980)	0.0040-0.0047	Eastern Irish Sea

3. Optimization Approach

The ocean bottom friction parameter, which relates the depth integrated current component to the bottom stress component, depends directly on a constant (linear stress coefficient) and inversely on the water depth. The linear bottom stress law is given earlier as:

$$F_B = \frac{\eta \rho}{H} U \quad , \quad G_B = \frac{\eta \rho}{H} V \qquad \ldots\ldots(6.5)$$

where is the linear stress coefficient having a typical value of 0.24 cm/s (Weenink (1958)). The only justification of the linear bottom friction law lies in its mathematical simplicity. For both storm surge and tide modelling, the linear law has been demonstrated to be a reasonable approximation (e.g. Grace (1930), Heaps (1969) and Pekeris and Accad (1969)). The wind stress coefficient formula of Wu (1980,1982) is used in the modelling of frictional coefficients at the air-sea interface and numerical tests have been carried out to study the transient sea surface height variation by varying the bottom stress coefficient. The results from the selected SEASAT mission periods show a general decrease of transient surge amplitude as the coefficient increases and also the smoothness of the sea surface topography seems directly proportional to the bottom stress coefficient. Not only is the determination of coefficient important in the transient sea surface elevation simulation, a proper value of it is also essential in ocean tidal modelling problem since the assumption of ocean bottom friction as dissipation mechanism has been preferred in some complex geophysical research (Grace (1930) and Pekeris and Accad (1969)).

The most commonly used alternative of frictional dissipation is to express the bottom stress in terms of the square of the mean current velocity, and is given by:

$$F_{\beta} = \frac{C\rho}{H^{2}} \vec{U}\cdot\vec{U} \quad , \quad G_{\beta} = \frac{C\rho}{H^{2}} \vec{V}\cdot\vec{V} \qquad \ldots\ldots(6.6)$$

where C is the dimensionless quadratic stress coefficient, which traditionally takes a value close to 0.0025. Equating the stress estimated from the linear law of equation (6.5) to the stress of quadratic friction law, the difference between the two coefficients is that the C contains a multiplicative term $(U^2+V^2)^{\frac{1}{2}}/H$. The handling of the quadratic frictional dissipation requires special attention on the water depth field. In extremely shallow water area, there may be some problems with the stability of the equations of motion and the resulting values of sea surface elevation and current could be unrealistically large. Also, the components U and V expressed by equation (6.6) are in the vicinity of the ocean bottom and they cannot arbitrarily be replaced by depth-averaged current values without any assumption. Kagan (1971) has summarized the published quadratic bottom stress coefficients since 1918 and his report contains coefficient values ranging from 6×10^{-3} to 2×10^{-3}, which probably imply that the coefficient may be dependent on different oceanic deposits and bed forms.

Recall the time varying sea surface equation of (2.11):

$$h'(\phi,\lambda,t) - G(\phi,\lambda,t) = T(t) \qquad .....(6.7)$$

If the SEASAT-ALT measurements can be assumed to be accurate as specified, the raw sea surface height data, after the application of necessary corrections (equation (2.7)), should provide desired information on the sea surface elevation due to the time-dependent effects. It should, however, be understood that the left hand side of equation (6.7) only represents an ideal situation for the time varying sea state. The long wavelength unmodelled error in the orbit computation due to insufficient accuracy in gravity model and the random noise are excluded. Since the unmodelled error is, in general, long wavelength of semi-cyclic per revolution (Marsh and Williamson, 1980), it would only have effect of local 'DC' shifting in the SEASAT-ALT data segments such as the ones used in this research. In fact, 'DC' shifting can also be true for other uncorrected long wavelength small amplitude anomalies of tidal loading of the solid earth, body tide and steric ocean variations.

The criterion used to determine a proper value for the linear bottom friction coefficient is based on the goodness of fit between the SEASAT-ALT measurement and the computed transient value. This is done by minimizing the difference between the computed and observed transient sea surface elevations for each incremental successive bottom friction coefficients. A similar approach of measurement, which is based on the numerical solution of the Laplace's Tidal Equations and in-situ observations, was used by Stock (1976) to model different tidal constituents in the Gulf of California. To accomplish the procedure systematically, a constant shifting of the SEASAT-ALT observations is required for all the linear trend errors. Since the time-dependent sea surface profiles can be computed at the instant when the satellite is directly over the sea model area, a constraint is provided to determine the amount of 'DC' shifting for the satellite observations. With the assumption that the interpolation between spatial coordinates are reasonably accurate, the goodness of fit between the model ζ_m and observation ζ_{OB} is defined by

$$V_K^i = \frac{1}{N} \sum_{j}^{N} |\zeta_m(k) - \zeta_{OB}^j(\hat{k})|^2 \qquad \ldots\ldots(6.8)$$

where

V_K^i - variance for path i

N - number of points in the satellite path i

k - experimental coefficient for the procedure

$\hat{k}$ - optimum value of k when V_k^i is minimized

The optimum frictional coefficient $\hat{k}$ in equation (6.8) is assumed to be the truth value that gives rise to the satellite recordings.

(a) Hudson Bay Results

Before one applies the optimization approach which combines the corrected SEASAT altimeter data with the model results, short wavelength geoid anomalies have to be investigated over the area. The sea surface height given in GDR is an averaged measurement of 1 sec interval. This is a sampling of surface distance of 7 km. Therefore, the smallest resolvable wavelength in the measurements along the tracks is approximately 14 km (a distance of 3 consecutive points), according to the Nyquist criteria. Small scale geoid anomalies of this order could be very important because they can contribute to observations which can not be accounted for in the sea model. Since the SS3 surface is used for the reduction of observations and since all the shallow water regions (less than 90 m) are discarded in the computations, only the geoidal signatures near the center of area which are below 60° N need to be considered. Figure 6.2 shows five geoid profiles, two tracks from Aug 4-6 and three tracks from Aug 18-21. Artificial constants were introduced to

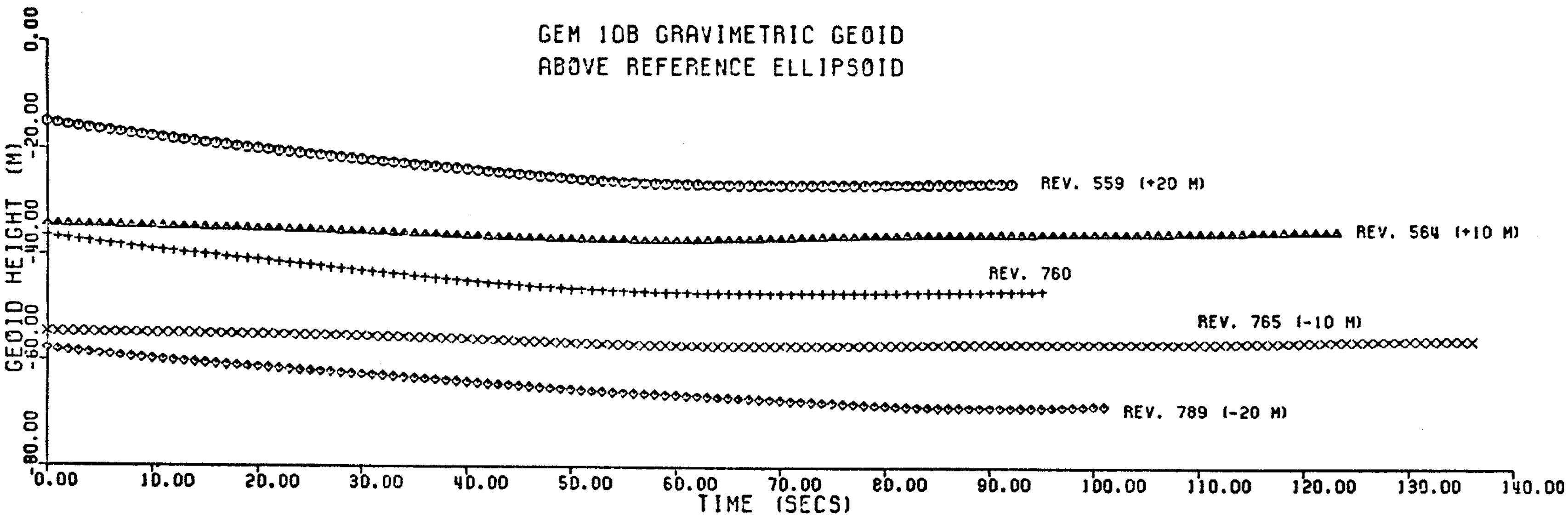

Figure 6.2: Geoid Profiles of the Satellite Orbit Tracks Used for the Modelling of Ocean Bottom Friction Coefficient in Hudson Bay Experiment.

each curve to separate them for illustration only. These profiles are derived from the gravimetric geoid (GEM 10B) which was included as one of the geophysical algorithm (G-7) in the SEASAT-ALT GDR Users Handbook (Lorell et al. (1980)). The profiles depicted in this figure clearly indicate the insigificance of short wavelength geoid anomalies, as the only known tectonic feature in this area is the glacial-isostatic uplifting of crust with scale comparable to the entire Hudson Bay and adjacent region.

Although the GEM 10B was only completed to harmonic degree and order of 36, it was one of the better geoid surfaces available for scentific use. For the reduction of the SEASAT-ALT data, however, an other reference surfaces which possibly include high frequency information should be used. Because of the use of laser, S band and altimeter data in constructing the altimetric-derived reference surface, it should contain far more high frequency information (or small wavelength time-invariant features) than any GEM models. Due to the gridding and contouring procedures in determining the SS3 surface, data within a 5 degree cap have been smoothed to some extent.

In addition to the geoid profiles displayed in Figure 6.2, small wavelength anomalies extracted by subtracting the GEM 10B from the SS3 altimetric-derived mean sea surface (or mean sea level) are depicted in Figure 6.3. Although these profiles are more undulating than the geoid profiles shown in Figure 6.2, they are primarily long wavelength in nature. They imply, again, the absence of small scale anomalies along the orbit tracks.

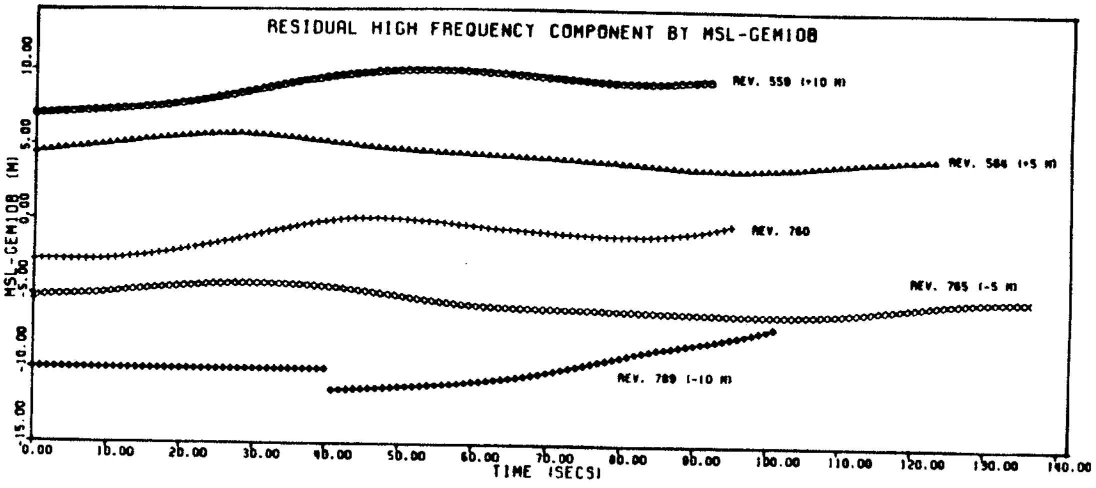

Figure 6.3: High Frequency Residual of the Altimetric Geoid (SS3) for the Tracks Shown in Figure 6.2.

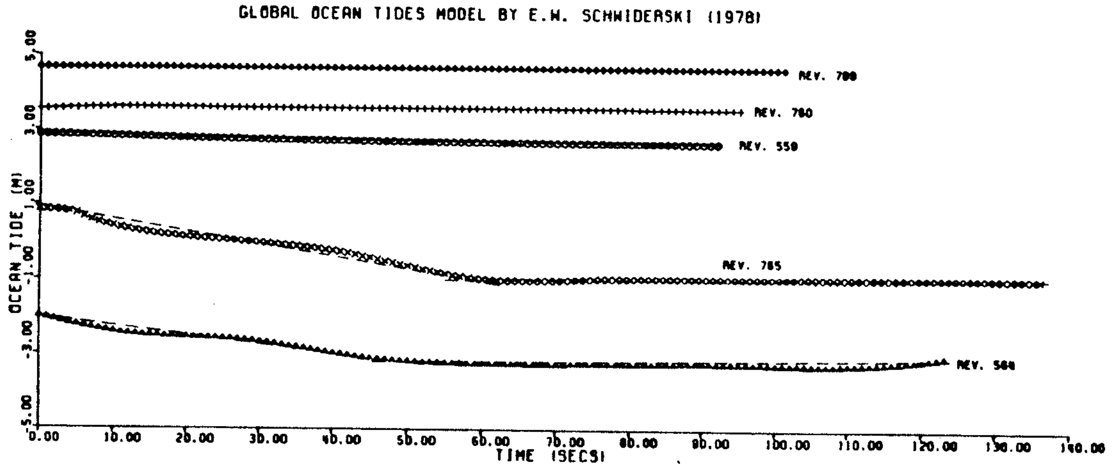

Figure 6.4: Low Frequency Ocean Tide Profiles from the Schwiderski Tide Model Along the Tracks Shown in Figure 6.2.

Since the largest signature in altimetry (the geoid) in the Hudson Bay area is quite smooth, ocean tide may become an important parameter in altimeter measurements beside the sea level fluctuations caused by the random meteorological forcings. The ocean tide values of the satellite tracks shown in Figure 6.2 are displayed in Figure 6.4. Although the values of the Schwiderski tide model (1978) is known to be erratic in this region, they are illustrated to show the characteristic of the ocean tidal signatures along the tracks. In terms of time series analysis, these signals (Figure 6.4) are of very low frequency, with dashed lines particularly on revolutions 765 and 564 indicating their linear trends and the most serious ocean tidal variations. If these characteristics reasonably reflect the truth, they will bring about a constant linear shifting to the altimeter measurements when applied as correction. In computing the error of higher frequency sea surface variations along the tracks for the determination of bottom friction, correction of ocean tide is not as important as some other areas.

Figures 6.5a through 6.5e display the variations in the variance $V_K^{'}$ as a function of linear bottom stress coefficient η for four SEASAT orbit tracks. The data used in the optimization procedure correspond to water depth greater than 90 m to avoid any possible shallow water nonlinear effects which can drastically affect the results. The optimum value for the coefficient obtained from these paths (except path 9 revolution #765) is 0.255 cm/s. The result from path 9 shows an extraordinary large value for the linear stress coefficient. This is mainly attributed to the absence of features in

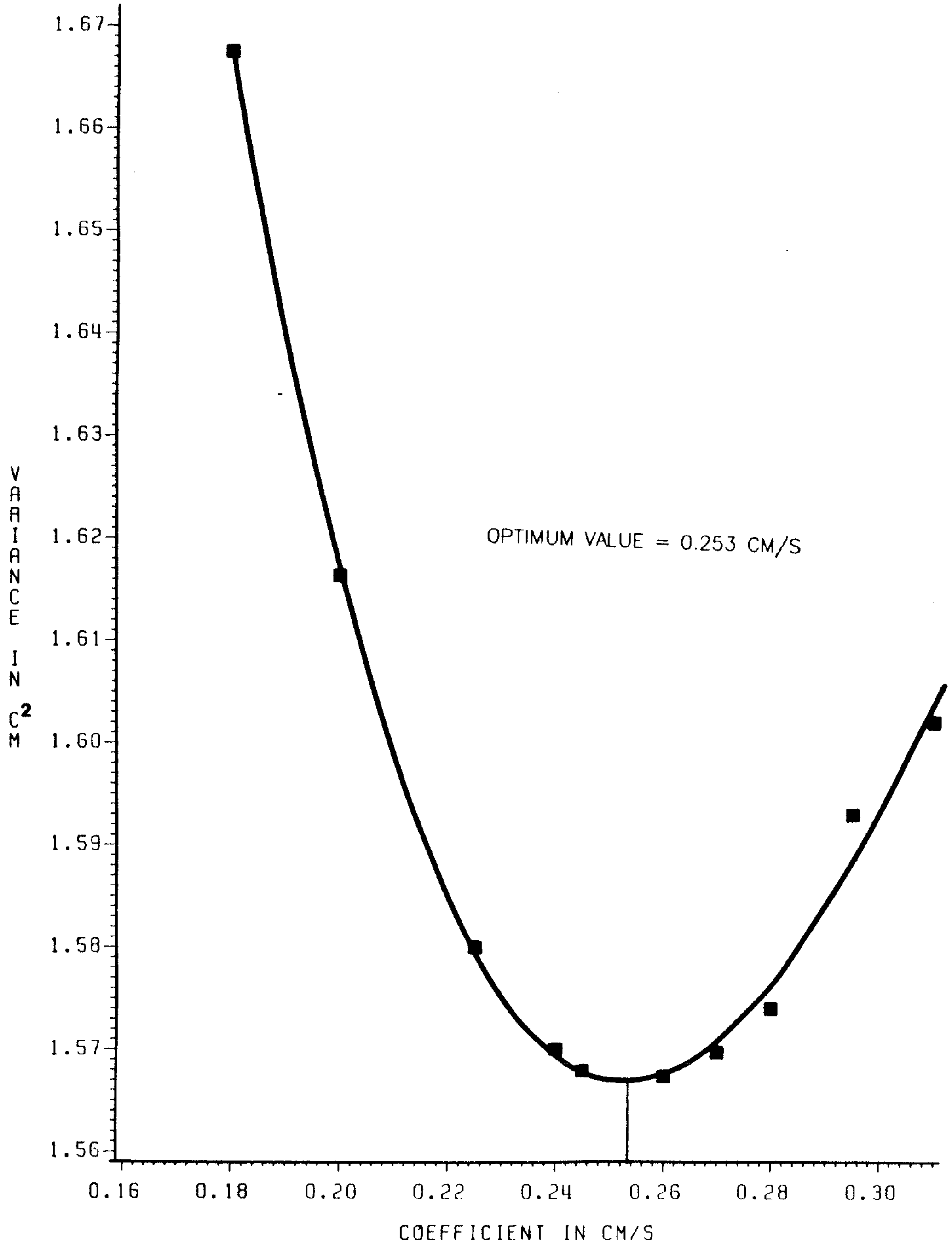

(a)

Figure 6.5: Hudson Bay Experiment Variance Curves Calculated from Observed and Simulated Sea Surface Profiles As a Function of Linear Frictional Coefficient: (a) Revolution 559, (b) Revolution 564, (c) Revolution 760, (d) Revolution 765 and (e) Revolution 789.

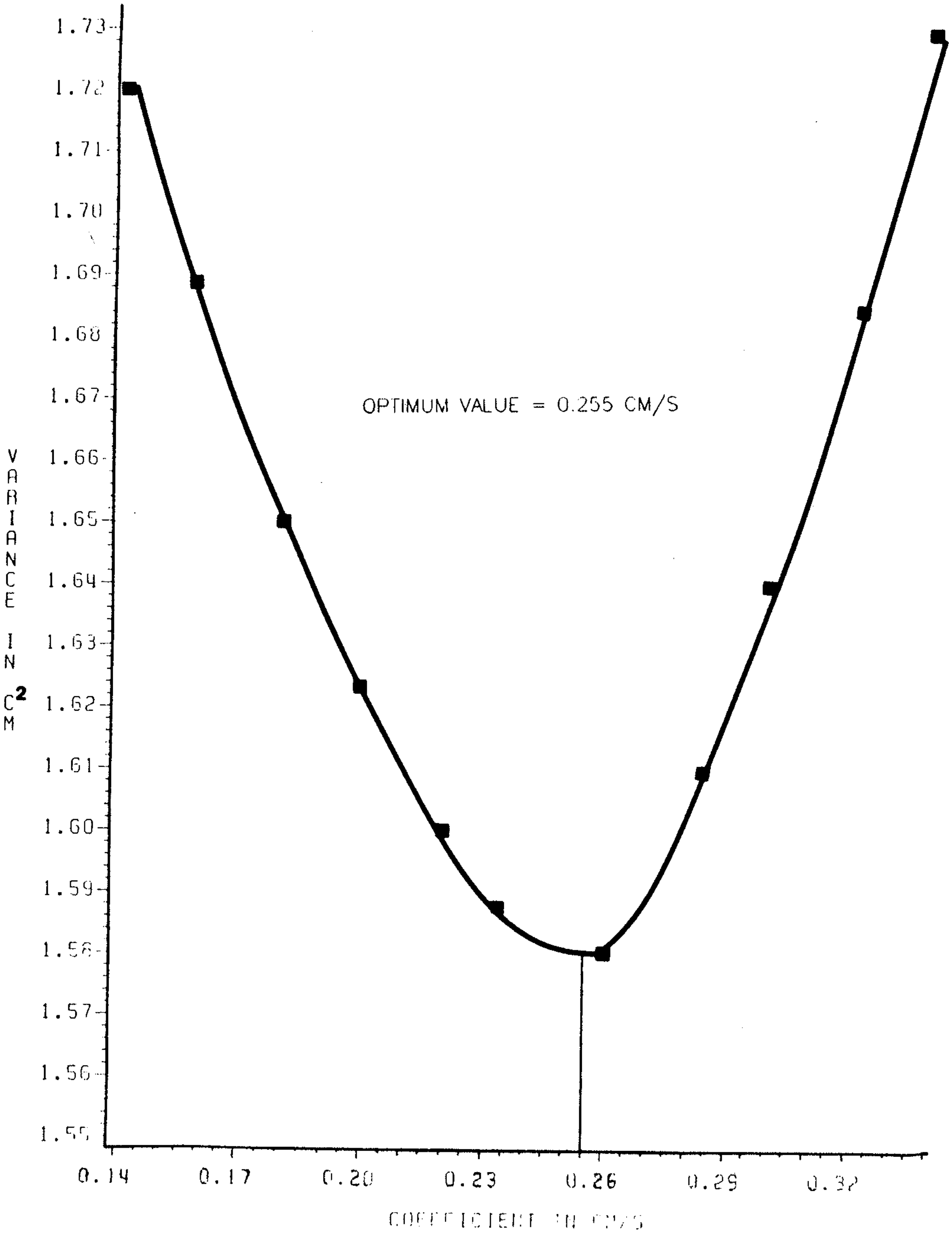

1.73
1.72
1.71
1.70
1.69
1.68
1.67
1.66
1.65
1.64
1.63
1.62
1.61
1.60
1.59
1.58
1.57
1.56
1.55
VARIANCE IN CM²
OPTIMUM VALUE = 0.255 CM/S
0.14
0.17
0.20
0.23
0.26
0.29
0.32
COEFFICIENT IN CM/S

(b)

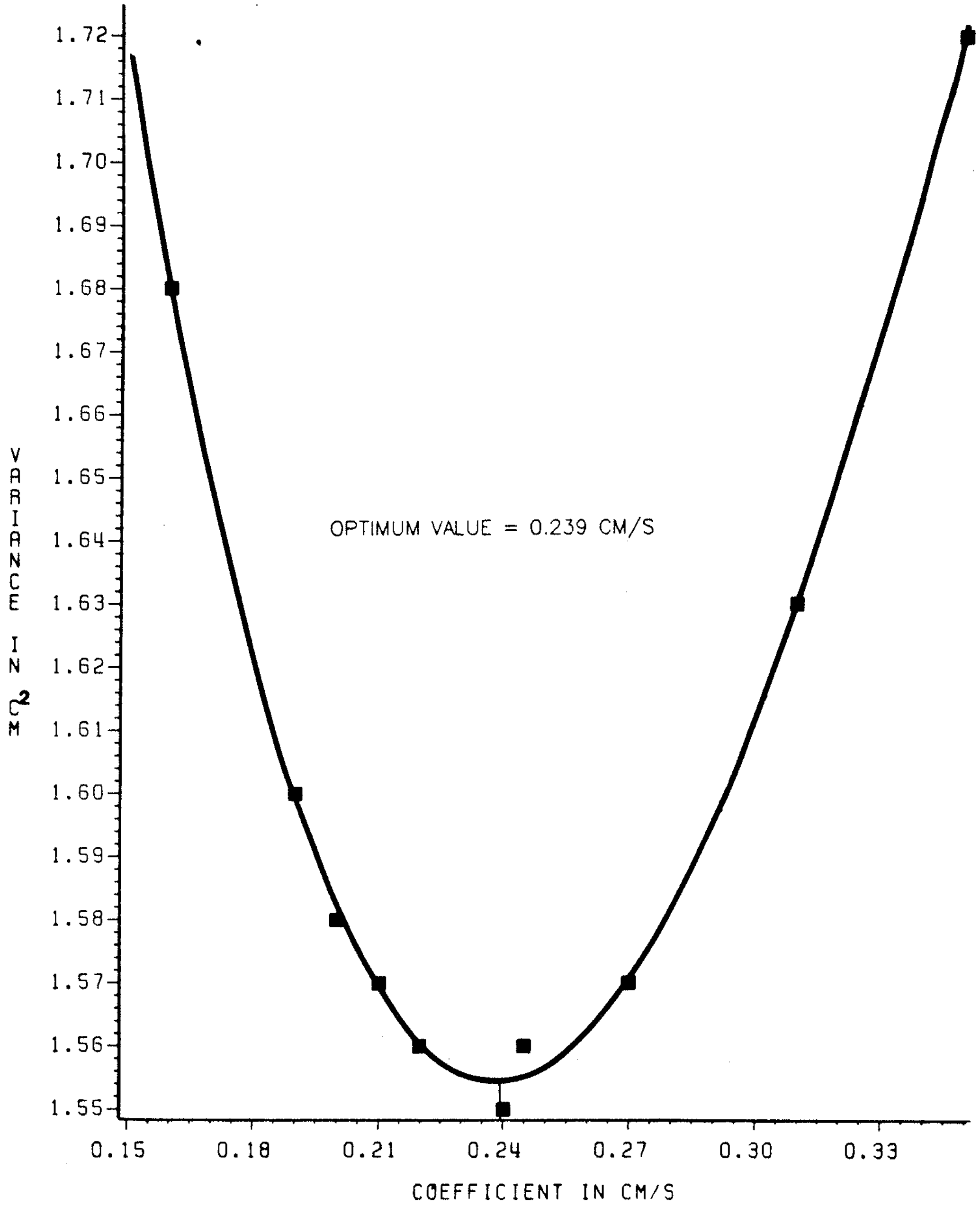

1.72
1.71
1.70
1.69
1.68
1.67
1.66
1.65
1.64
1.63
1.62
1.61
1.60
1.59
1.58
1.57
1.56
1.55
VARIANCE IN CM^2
OPTIMUM VALUE = 0.239 CM/S
0.15
0.18
0.21
0.24
0.27
0.30
0.33
COEFFICIENT IN CM/S

(c)

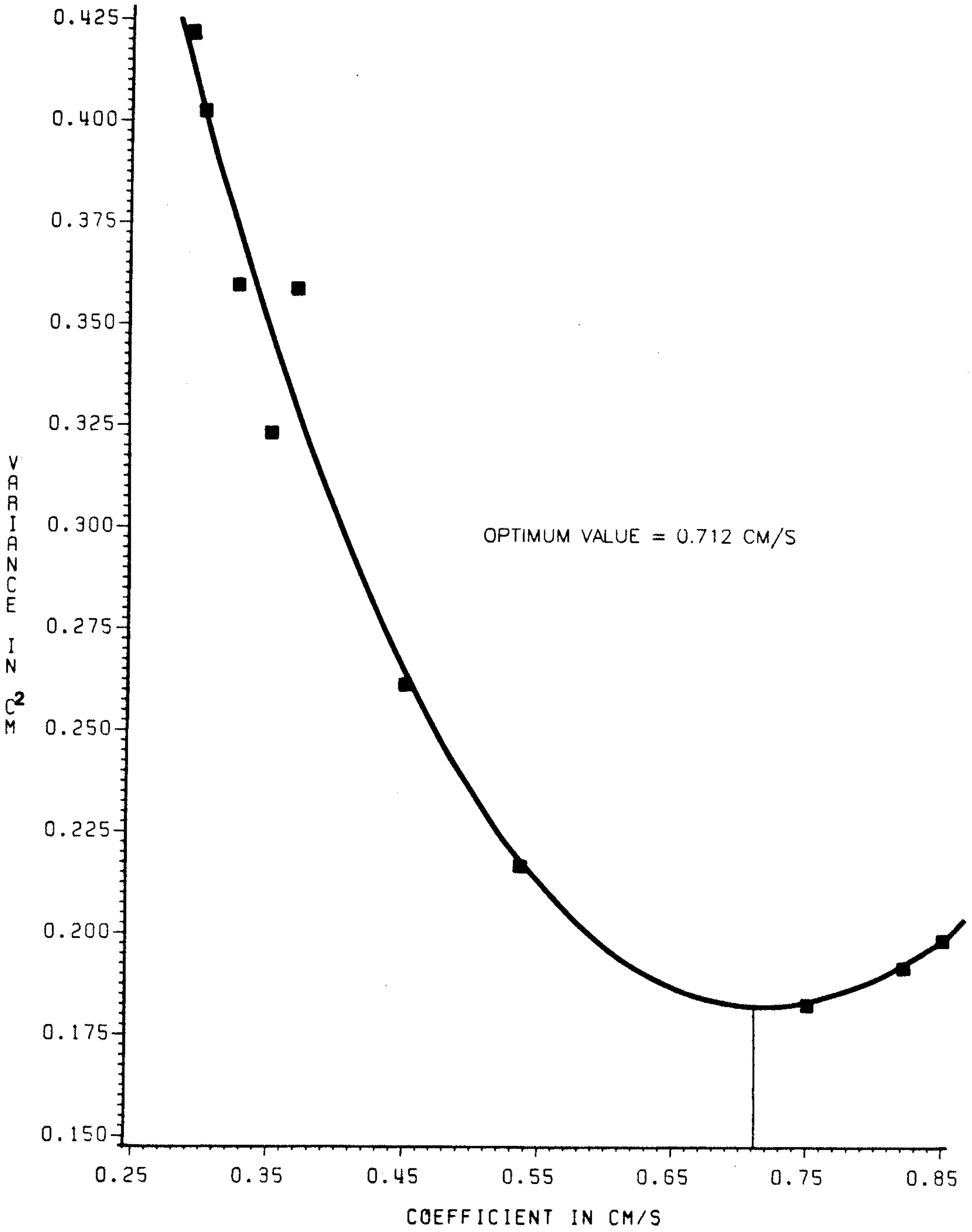

0.425
0.400
0.375
0.350
0.325
0.300
0.275
0.250
0.225
0.200
0.175
0.150
VARIANCE IN CM2
OPTIMUM VALUE = 0.712 CM/S
0.25
0.35
0.45
0.55
0.65
0.75
0.85
COEFFICIENT IN CM/S

(d)

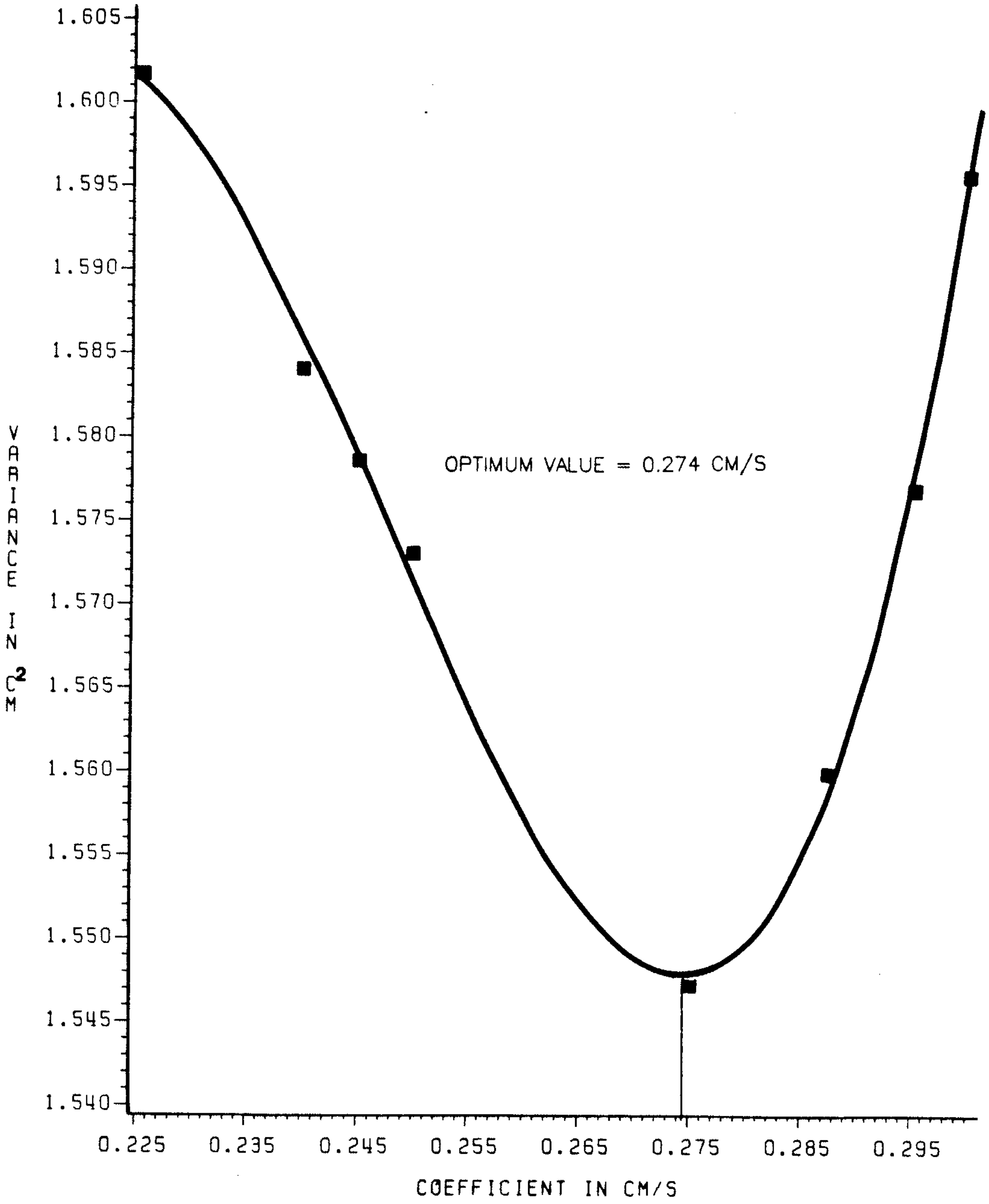
1.605
1.600
1.595
1.590
1.585
1.580
1.575
1.570
1.565
1.560
1.555
1.550
1.545
1.540
VARIANCE IN CM2
OPTIMUM VALUE = 0.274 CM/S
0.225
0.235
0.245
0.255
0.265
0.275
0.285
0.295
COEFFICIENT IN CM/S

(e)

the residual sea surface after the removal of the SS3 surface from the SEASAT-ALT measurements. The residual sea surface has almost a constant sea surface elevation and this results in large value of stress coefficient in order to generate such a surface numerically. The featurelessness of the residual sea surface ocassionally occurs because the SS3 surface also contains limited amount of informations about the transient sea surface variation, although it could possibly represent a long term equilibrium surface. In this case, a different approach or other suitable representation method of the equilibrium sea surface may be desired.

The procedure of estimating quadratic bottom friction coefficient and the water depth condition follows those used for the linear friction coefficient. The ocean bottom frictional dissipative terms in the equations of motion are subsituted by equation (6.6) and the model is run with different quadratic friction coefficient C. The variations of the measurement given by equation (6.8) as a function of C are depicted from Figure 6.6a to 6.6e for the selected satellite orbit tracks. Similar to the result from optimization of path 9 (revolution # 765) for linear bottom friction law, a high frictional dissipation in the modelling is required to obtain agreement between the satellite observations and theoretical values. Such a high and unrealistic dissipation is again due to the small magnitude from observations and from computations, so that random errors from both sources dominate the information. Regardless of this particular path, a mean value of quadratic friction coefficient determined through the optimization procedure is found to be 0.00234, a value which is slightly smaller in magnitude than the

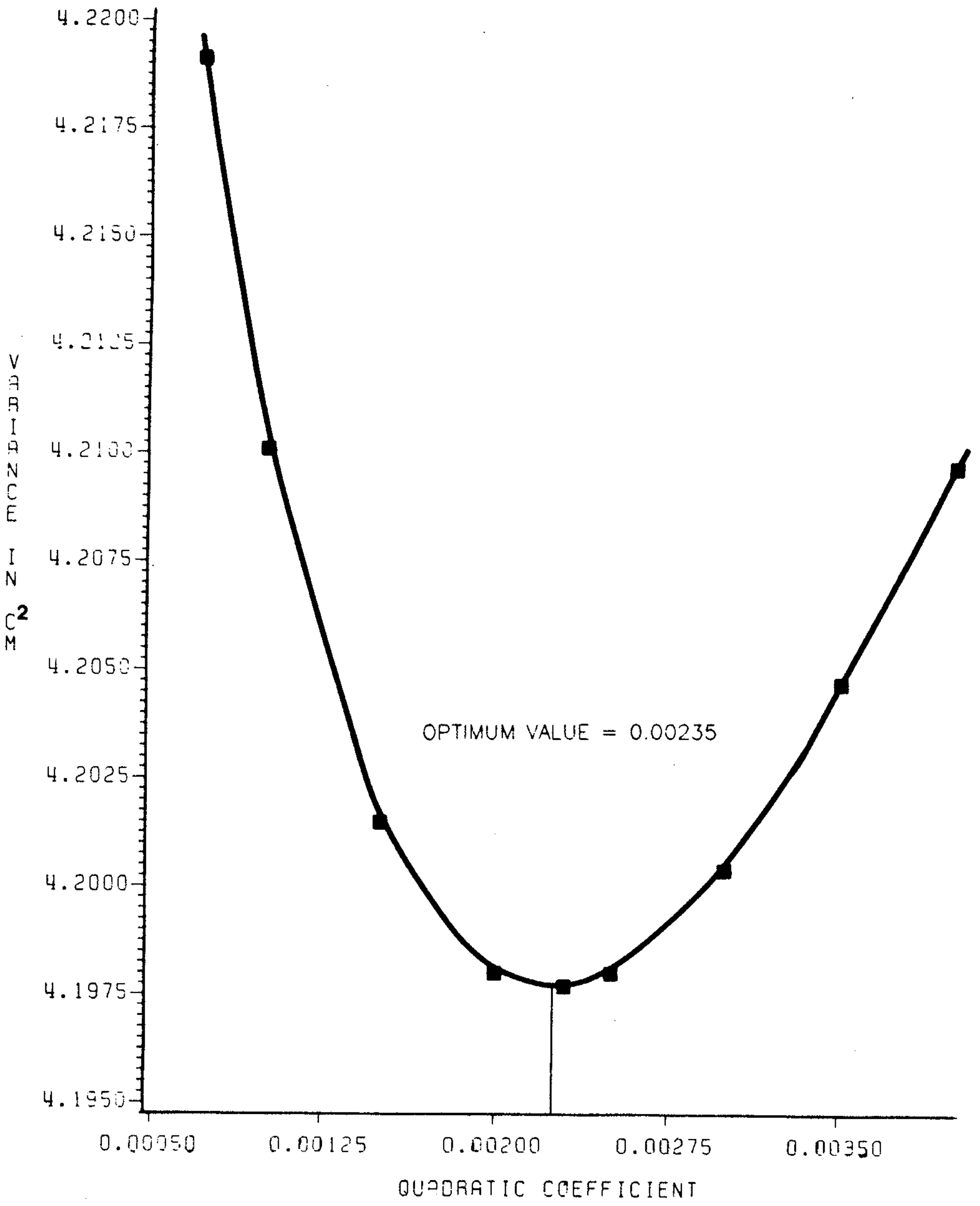

(a)

Figure 6.6: Hudson Bay Experiment Variance Curves Calculated From Observed and Simulated Sea Surface Profiles As a Function of Quadratic Frictional Coefficient: (a) Revolution 559, (b) Revolution 564, (c) Revolution 760, (d) Revolution 765 and (e) Revolution 789.

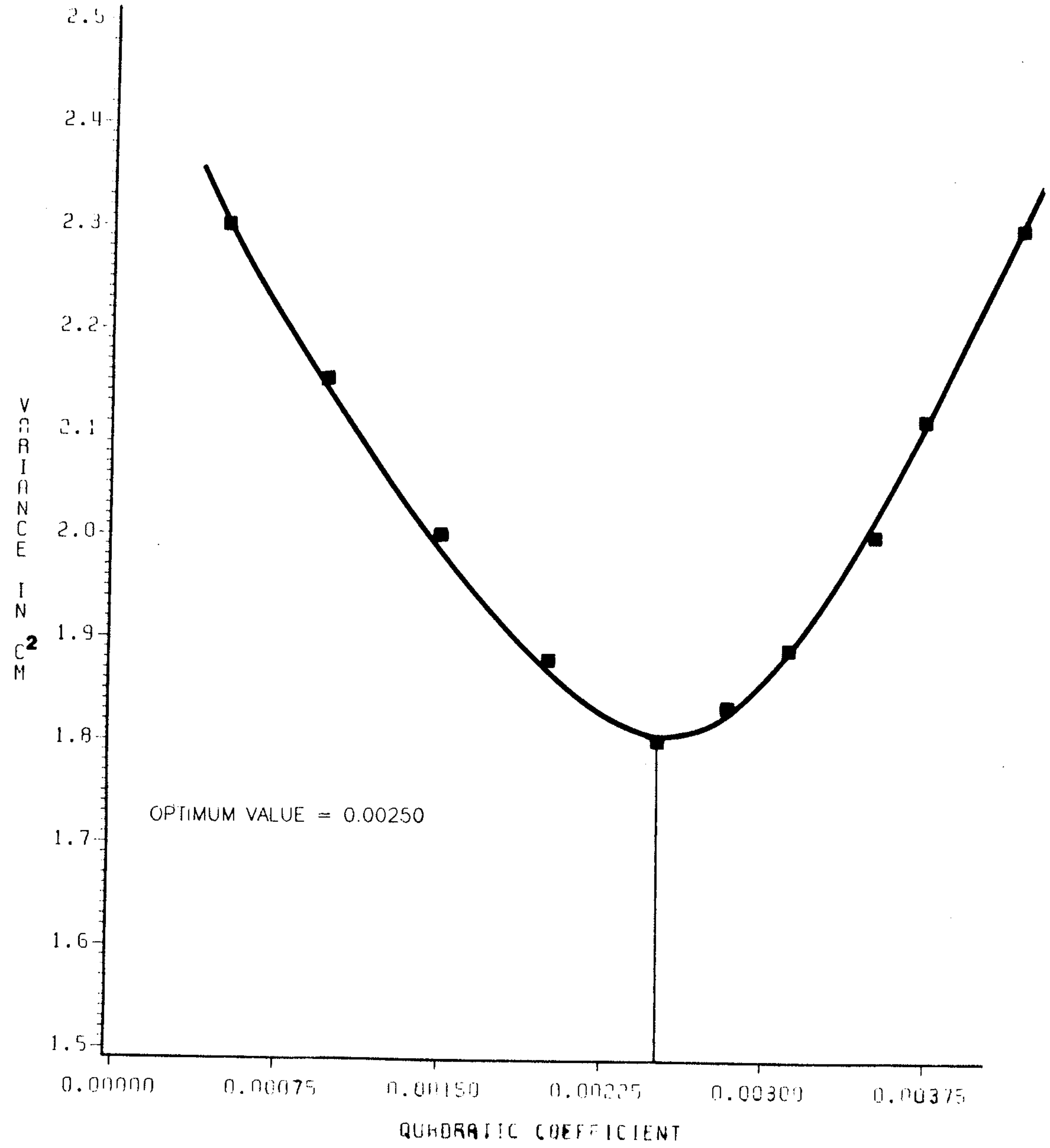
2.5
2.4
2.3
2.2
2.1
2.0
1.9
1.8
1.7
1.6
1.5
VARIANCE IN CM^2
OPTIMUM VALUE = 0.00250
0.00000
0.00075
0.00150
0.00225
0.00300
0.00375
QUADRATIC COEFFICIENT

(b)

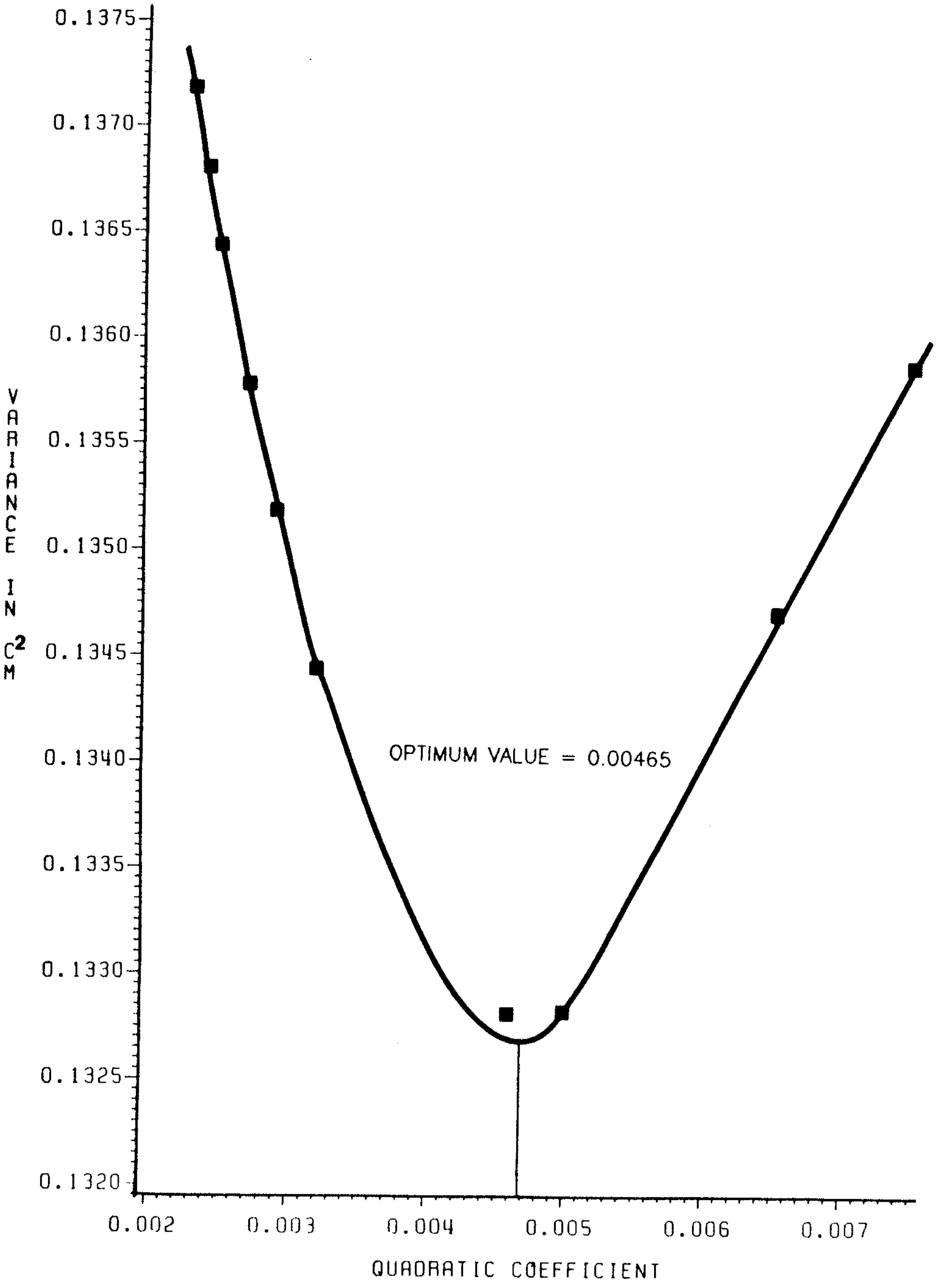

0.1375
0.1370
0.1365
0.1360
0.1355
0.1350
0.1345
0.1340
0.1335
0.1330
0.1325
0.1320
VARIANCE IN CM²
OPTIMUM VALUE = 0.00465
0.002
0.003
0.004
0.005
0.006
0.007
QUADRATIC COEFFICIENT

(c)

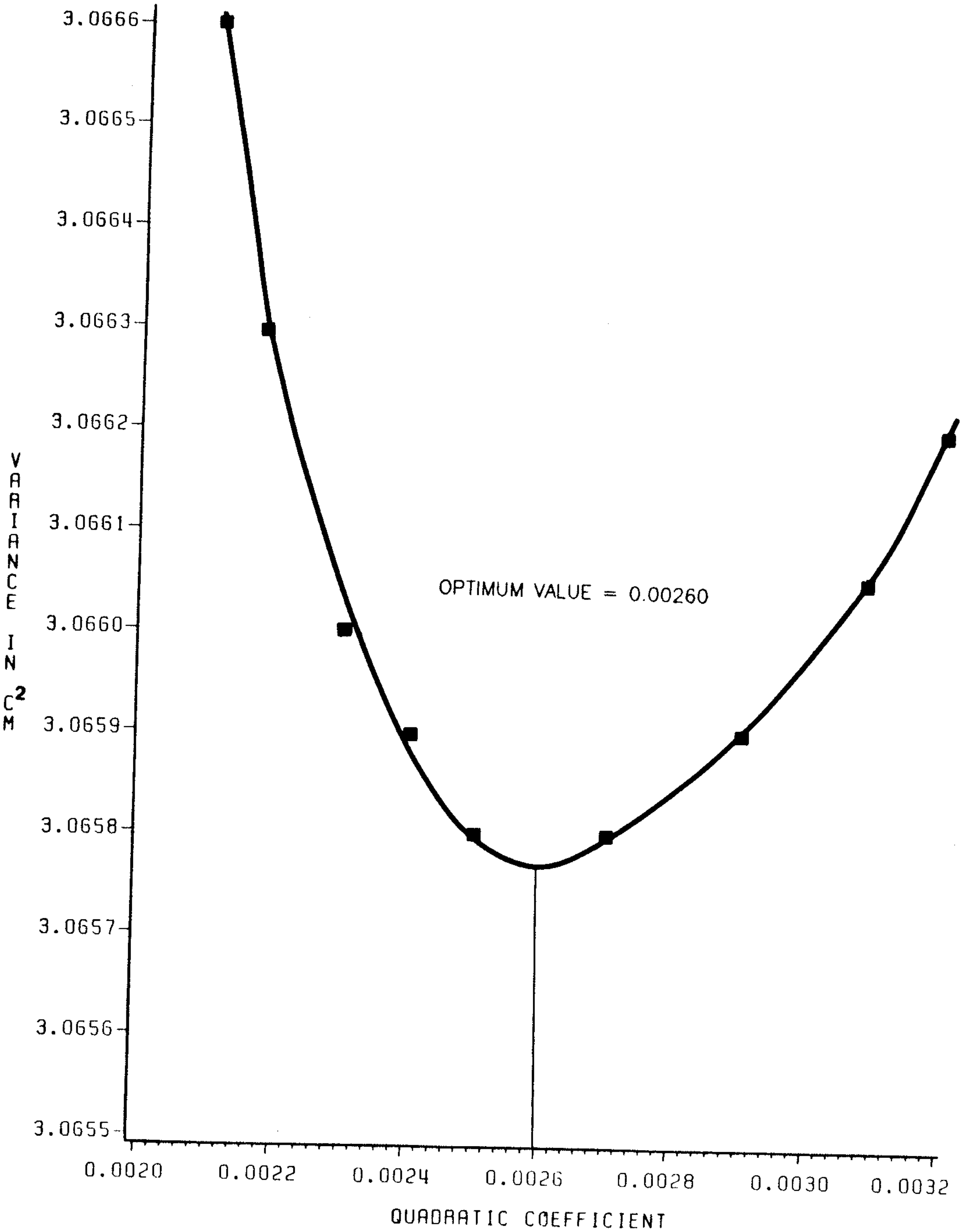
3.0666
3.0665
3.0664
3.0663
3.0662
3.0661
3.0660
3.0659
3.0658
3.0657
3.0656
3.0655
VARIANCE IN CM2
OPTIMUM VALUE = 0.00260
0.0020
0.0022
0.0024
0.0026
0.0028
0.0030
0.0032
QUADRATIC COEFFICIENT

(d)

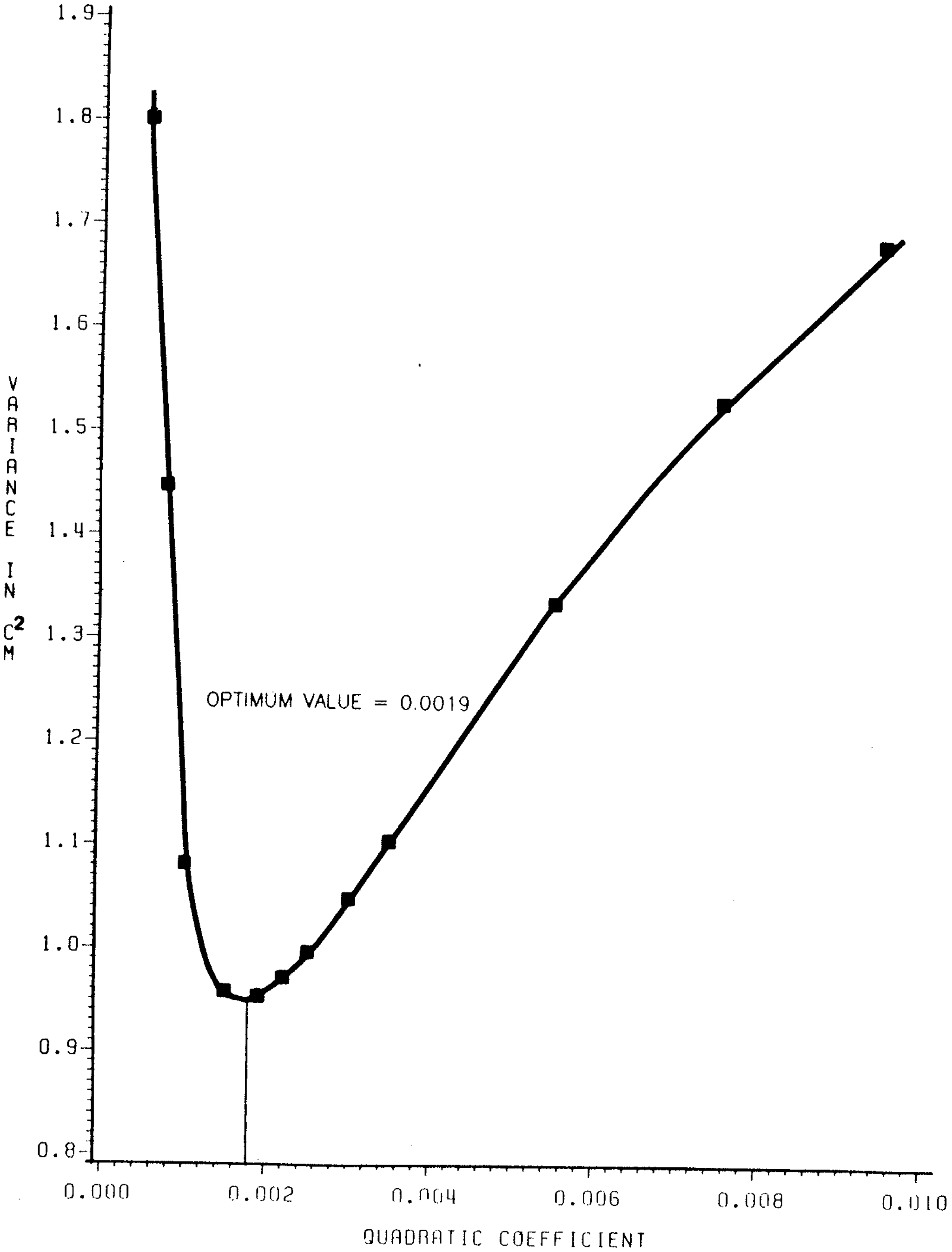
1.9
1.8
1.7
1.6
1.5
1.4
1.3
1.2
1.1
1.0
0.9
0.8
VARIANCE IN C_M^2
OPTIMUM VALUE = 0.0019
0.000
0.002
0.004
0.006
0.008
0.010
QUADRATIC COEFFICIENT

(e)

traditionally adopted value of 0.0025.

(b) East China Sea and Yellow Sea Results

The artifically offset geoid profiles for the two selected time periods are shown in Figure 6.7. These profiles indicate even less geoid undulation than those in Hudson Bay. They are mostly characterized by linear functions (extremely low frequency). The possible high frequency components in the geoid were also extracted along the satellite tracks similar to the Hudson Bay case. These high frequency compensated profiles are shown in Figure 6.8 and they indicate a low frequency content along the tracks. Thus the geoid, at least along these tracks, is basically long wavelength, and the reduction of the satellite data by the SS3 surface, a higher frequency reference surface, should further supress somewhat the small scale geoid anomalies if they exist.

Since tidal phenomena have been known to be important in this area, ocean tide was calculated separately and also inclusively together with surge analysis. Surges in this case have special importance because they were produced by tropical storms, typhoons. Figures 6.9a through 6.9j show the relative magnitude of surge alone, ocean tide alone, and body tide. Ocean tide was generated by 4 major tidal constituents (M_2, S_2, O_1 and K_1) and they have been shown to be sufficient for the reproduction of tide in this region (Choi (1980)). In general, the variations of ocean tide along the tracks is about 1.75 m with the largest value occurring in revolution 794 of 3 m. Surge amplitude was smaller according to computation, and a typical value being about 0.5 m. This value is 3

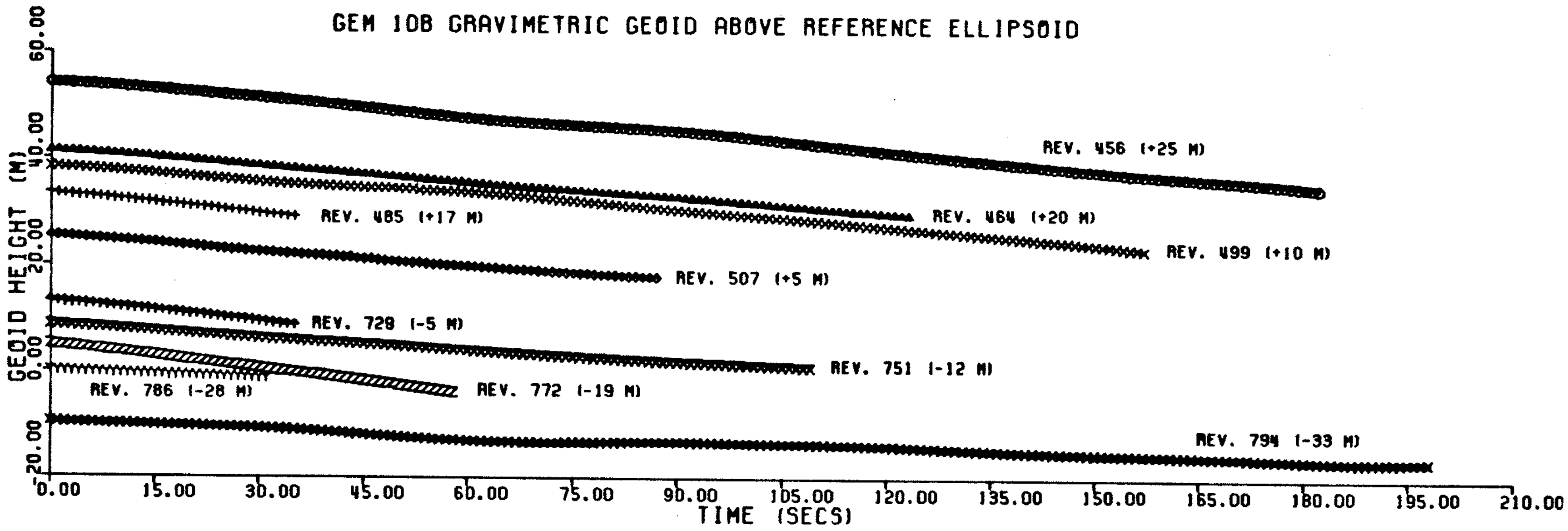

Figure 6.7: Geoid Profiles of the Satellite Orbit Tracks Used for the Modelling of Ocean Bottom Friction Coefficient in East China Sea and Yellow Sea Experiment.

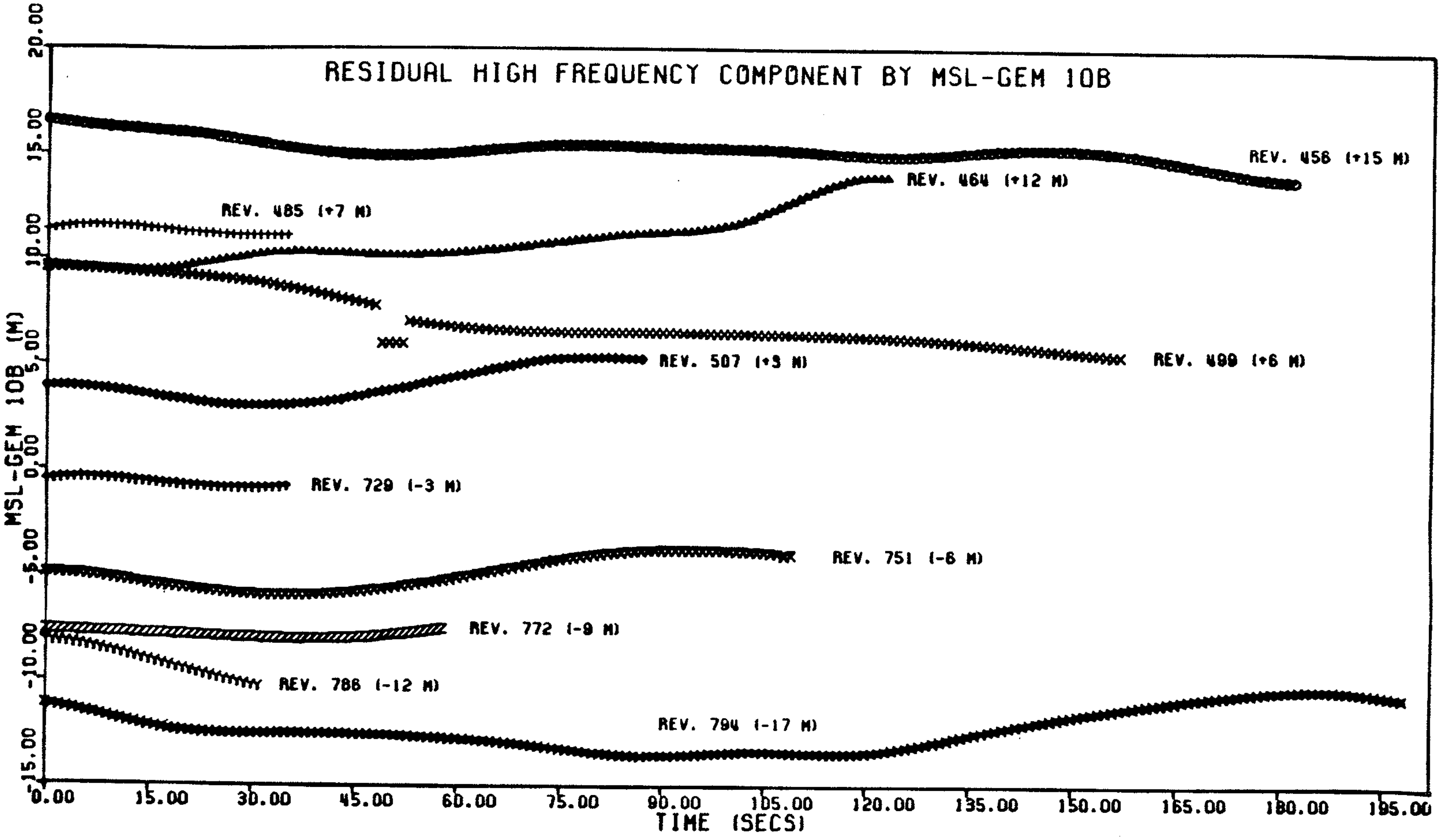

Figure 6.8: High Frequency Residual of the Altimetric Geoid (SS3) for the Tracks Shown in Figure 6.7.

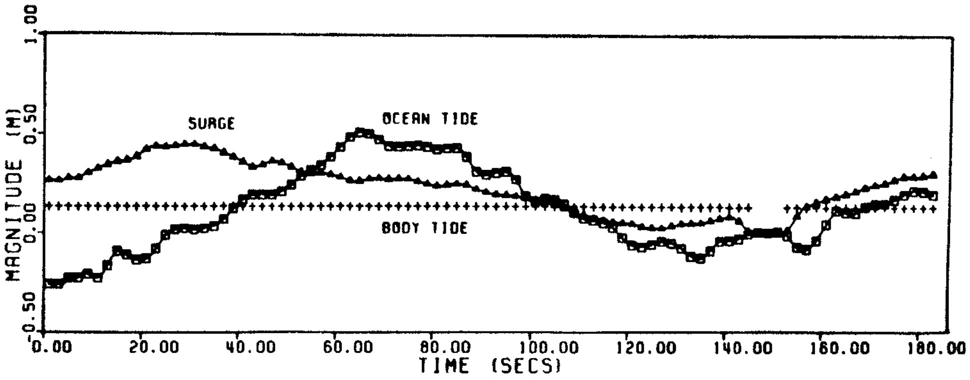

Figure 6.9a: Profiles of Body Tide, Surge and Ocean Tide Along Revolution 456.

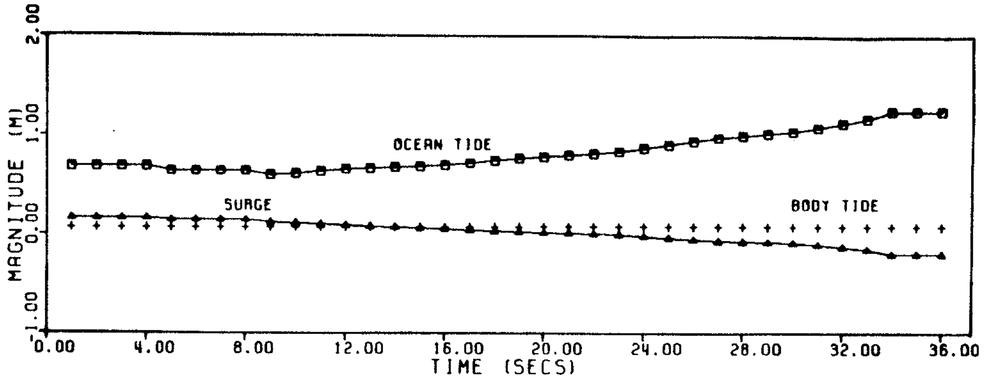

Figure 6.9b: Profiles of Body Tide, Surge and Ocean Tide Along Revolution 464.

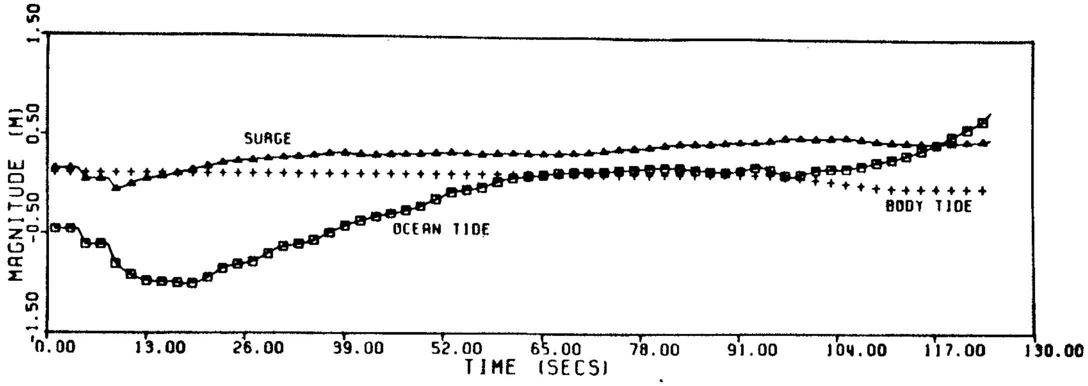

Figure 6.9c: Profiles of Body Tide, Surge and Ocean Tide Along Revolution 485.

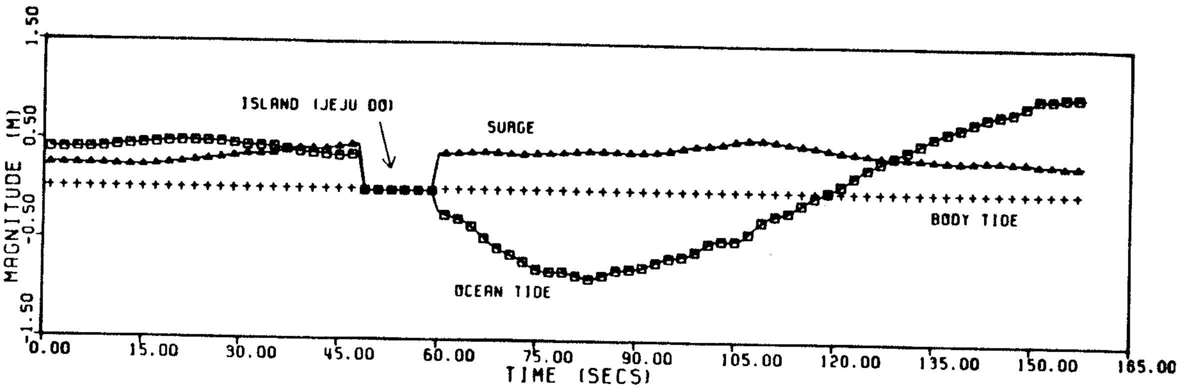

Figure 6.9d: Profiles of Body Tide, Surge and Ocean Tide Along Revolution 499.

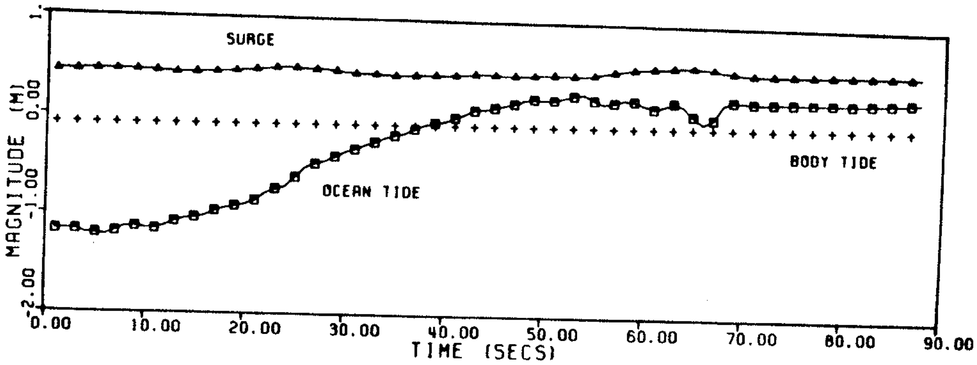

Figure 6.9e: Profiles of Body Tide, Surge and Ocean Tide Along Revolution 507.

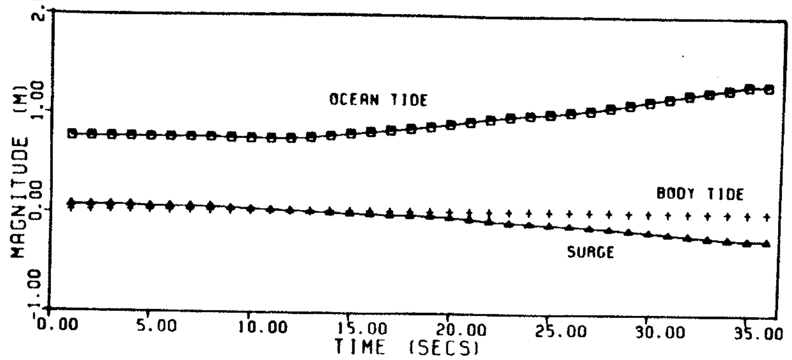

Figure 6.9f: Profiles of Body Tide, Surge and Ocean Tide Along Revolution 729.

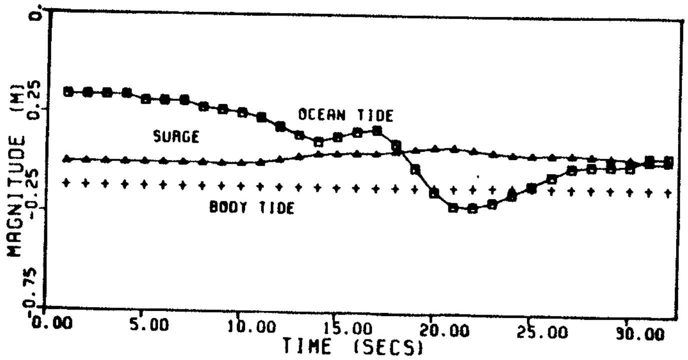

Figure 6.9g: Profiles of Body Tide, Surge and Ocean Tide Along Revolution 751.

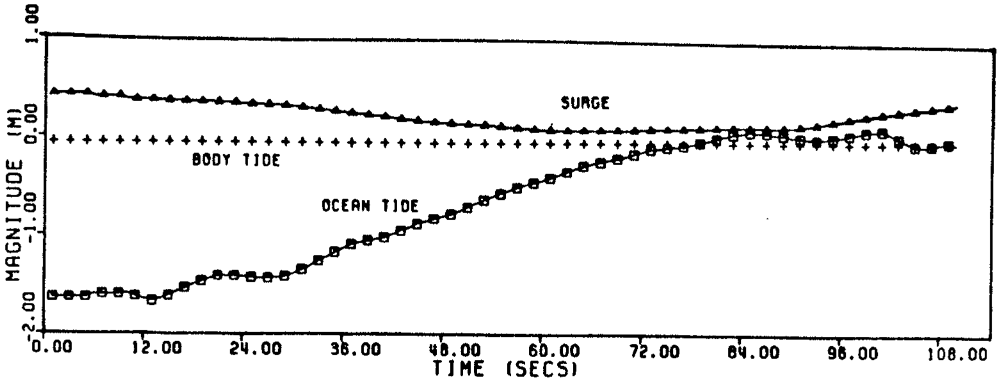

Figure 6.9h: Profiles of Body Tide, Surge and Ocean Tide Along Revolution 772.

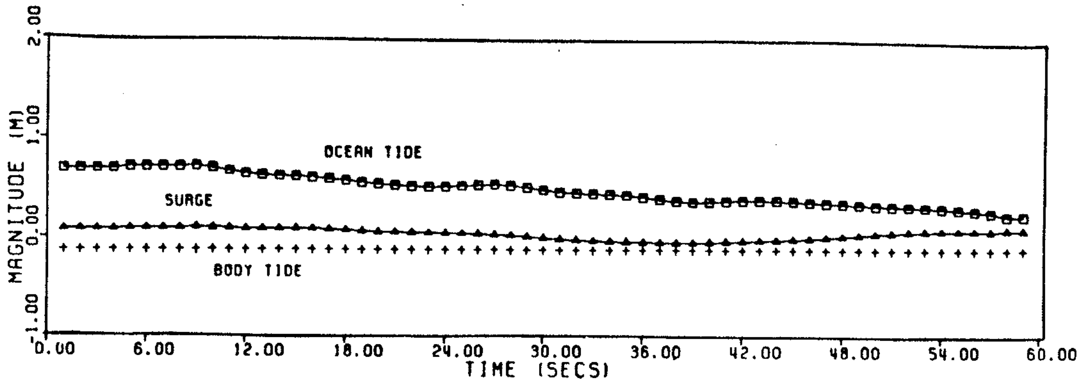

Figure 6.9i: Profiles of Body Tide, Surge and Ocean Tide Along Revolution 786.

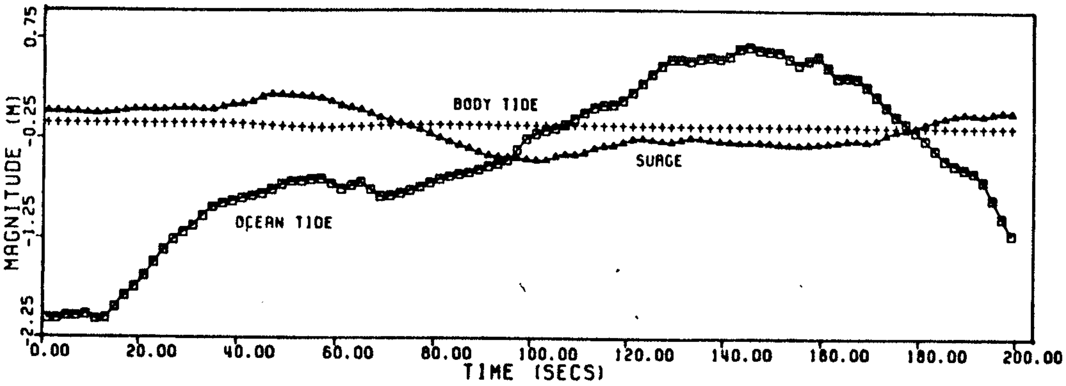

Figure 6.9j: Profiles of Body Tide, Surge and Ocean Tide Along Revolution 794.

to 4 times larger than the transient surge variation in Hudson Bay. The effect of computating surge and tide together may change the shape of these profiles as shown in Figure 6.9a to 6.9j, due to the surge and tide interaction. As illustrated in chapter V, the sea surface topography (surge + tide) along the tracks appears to be associated with the feature which has the largest relative magnitude, that is the ocean tide in this case. The surge profiles modify the profiles of ocean tide slightly by adding to them with a small residual probably caused by some interaction. It is also obvious from these diagrams that low frequency small magnitude body tides along the satellite tracks cause negligible vertical shift of the profiles when they are subtracted for correction, and thus they can be safely ignored.

Only the quadratic friction term is tested in this area simply because the nonlinearity of the term is consistent with the sea model formulation (advection) and other phenomena such as the influence of nonlinear interactions amoung the tidal constituents. The variance curves for the goodness of fit between the model and the altimeter derived observations for each revolution are displayed in Figure 6.10a through 6.10j. The results of the optimization are very consistent with each other with a range of values from 0.0023 to 0.0027. An averaged value is 0.002505 for the fiction coefficient of the quadratic law.

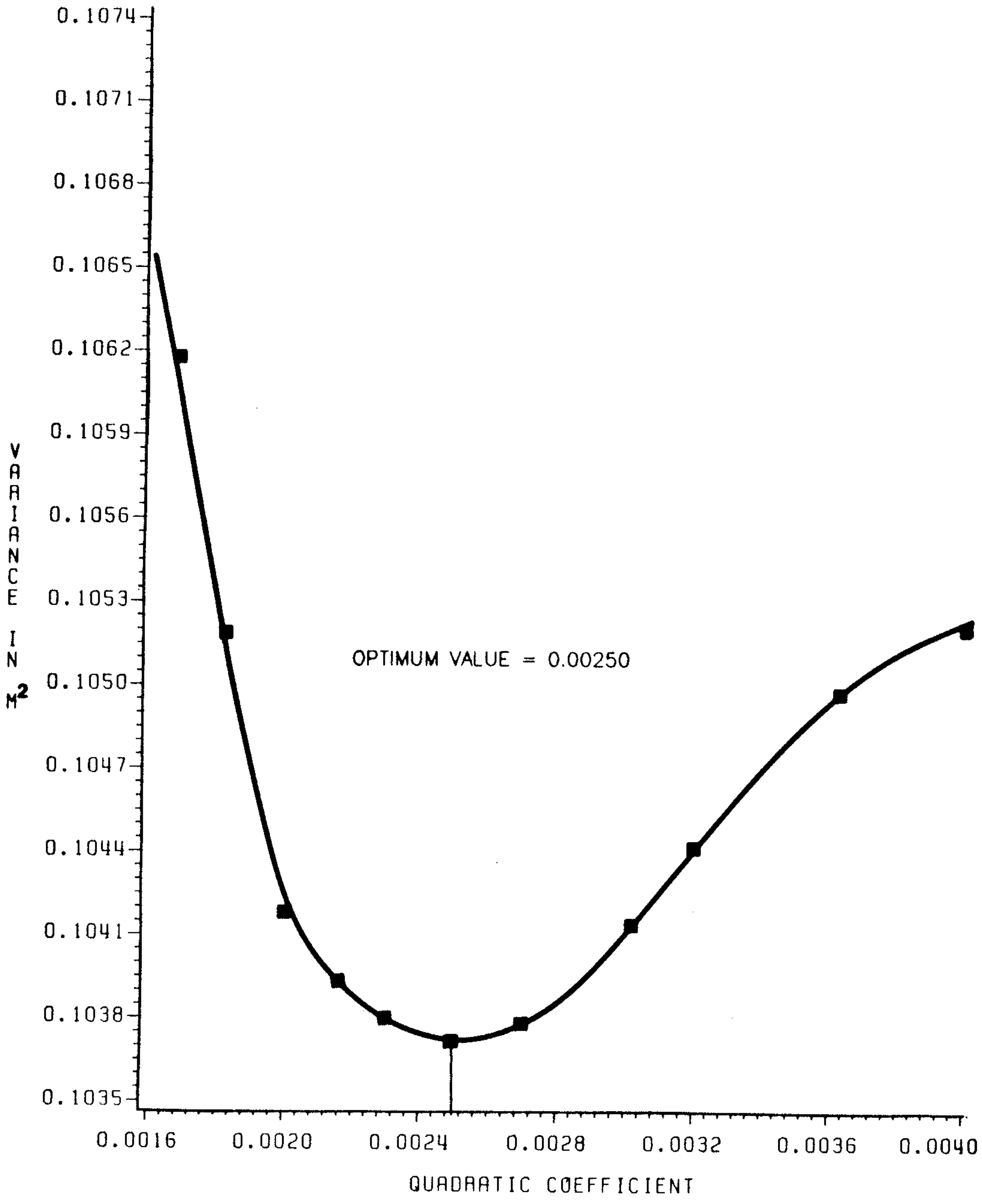

(a)

Figure 6.10: East China Sea and Yellow Sea Experiment Variance Curves Calculated From Observed and Simulated Sea Surface Profiles As a Function of Quadratic Frictional Coefficient: (a) Revolution 456, (b) Revolution 464, (c) Revolution 485, (d) Revolution 499, (e) Revolution 507, (f) Revolution 729, (g) Revolution 751, (h) Revolution 772, (i) Revolution 786 and (j) Revolution 794.

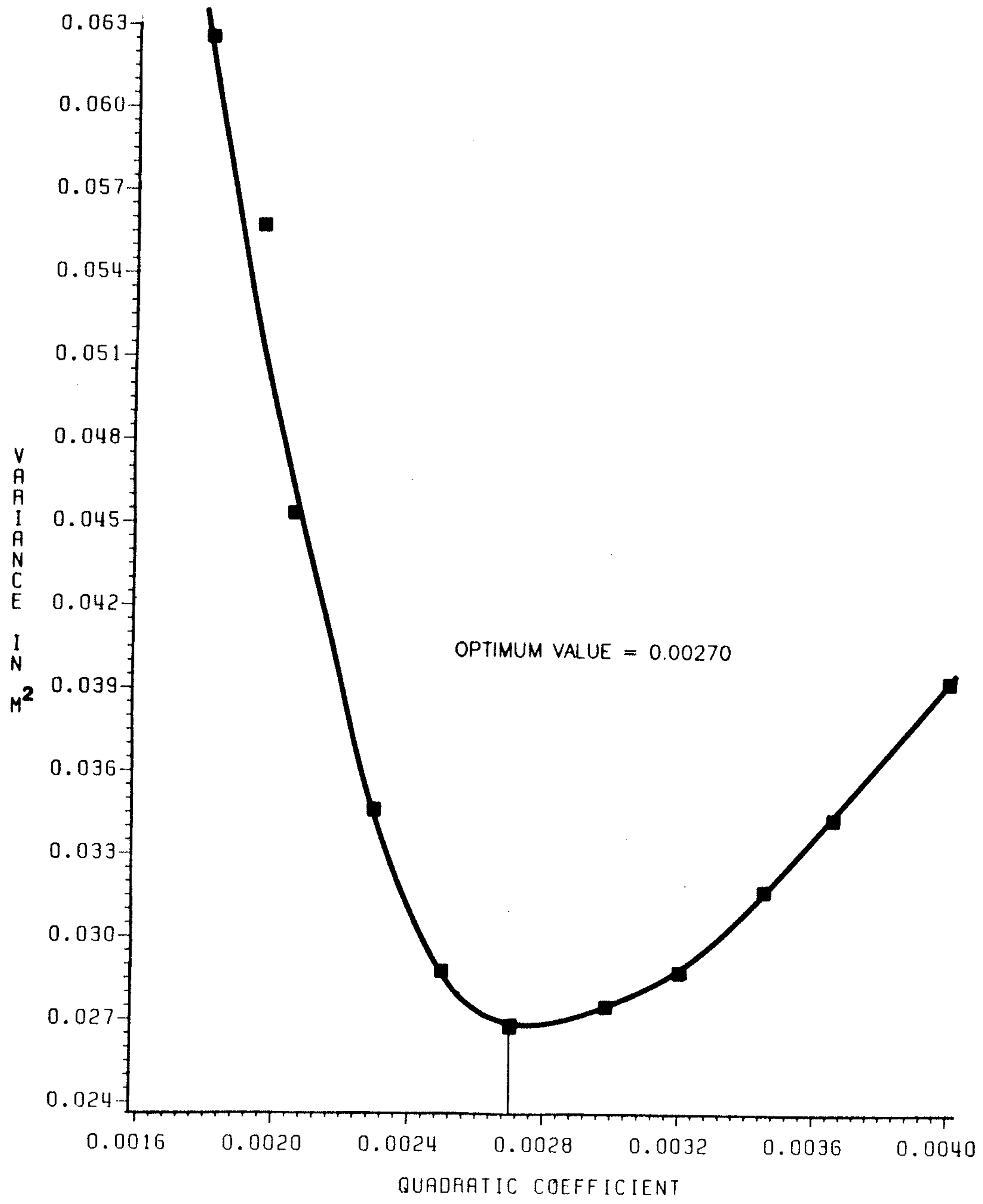

0.063
0.060
0.057
0.054
0.051
0.048
0.045
0.042
0.039
0.036
0.033
0.030
0.027
0.024
VARIANCE IN M^2
OPTIMUM VALUE = 0.00270
0.0016
0.0020
0.0024
0.0028
0.0032
0.0036
0.0040
QUADRATIC COEFFICIENT

(b)

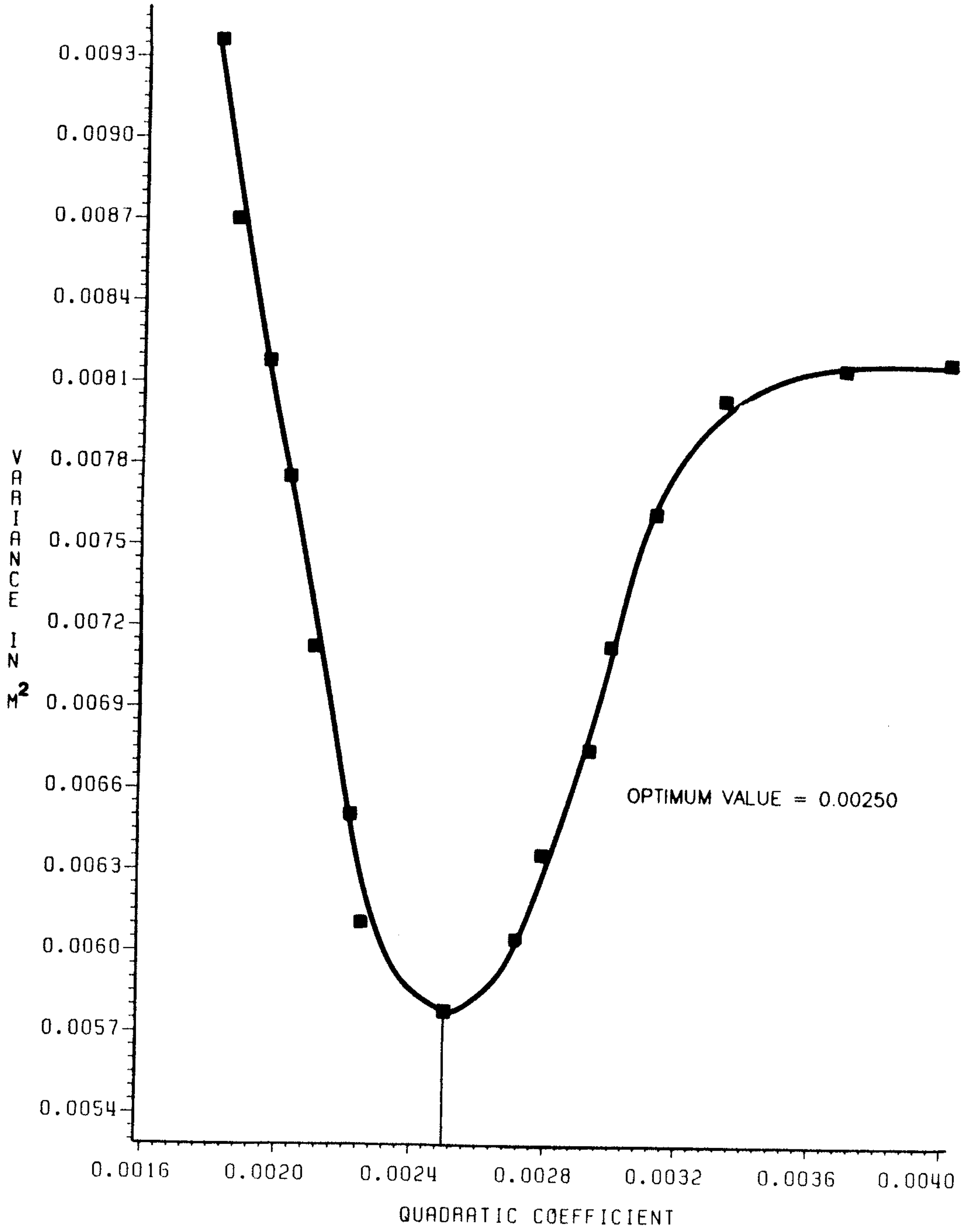
0.0093
0.0090
0.0087
0.0084
0.0081
0.0078
0.0075
0.0072
0.0069
0.0066
0.0063
0.0060
0.0057
0.0054
VARIANCE IN M²
0.0016
0.0020
0.0024
0.0028
0.0032
0.0036
0.0040
QUADRATIC COEFFICIENT
OPTIMUM VALUE = 0.00250

(c)

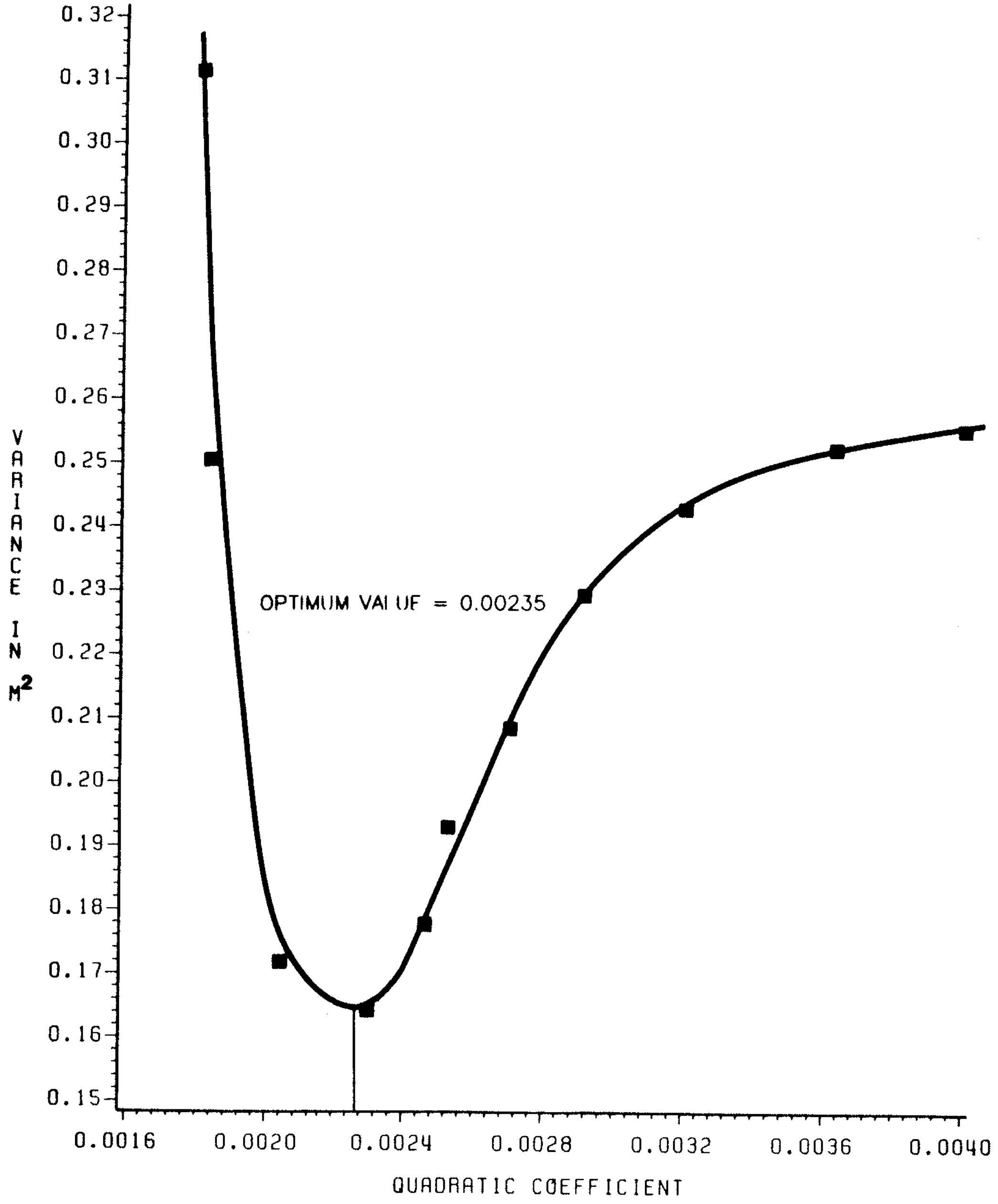
0.32
0.31
0.30
0.29
0.28
0.27
0.26
0.25
0.24
0.23
0.22
0.21
0.20
0.19
0.18
0.17
0.16
0.15
VARIANCE IN M2
OPTIMUM VALUE = 0.00235
0.0016
0.0020
0.0024
0.0028
0.0032
0.0036
0.0040
QUADRATIC COEFFICIENT

(d)

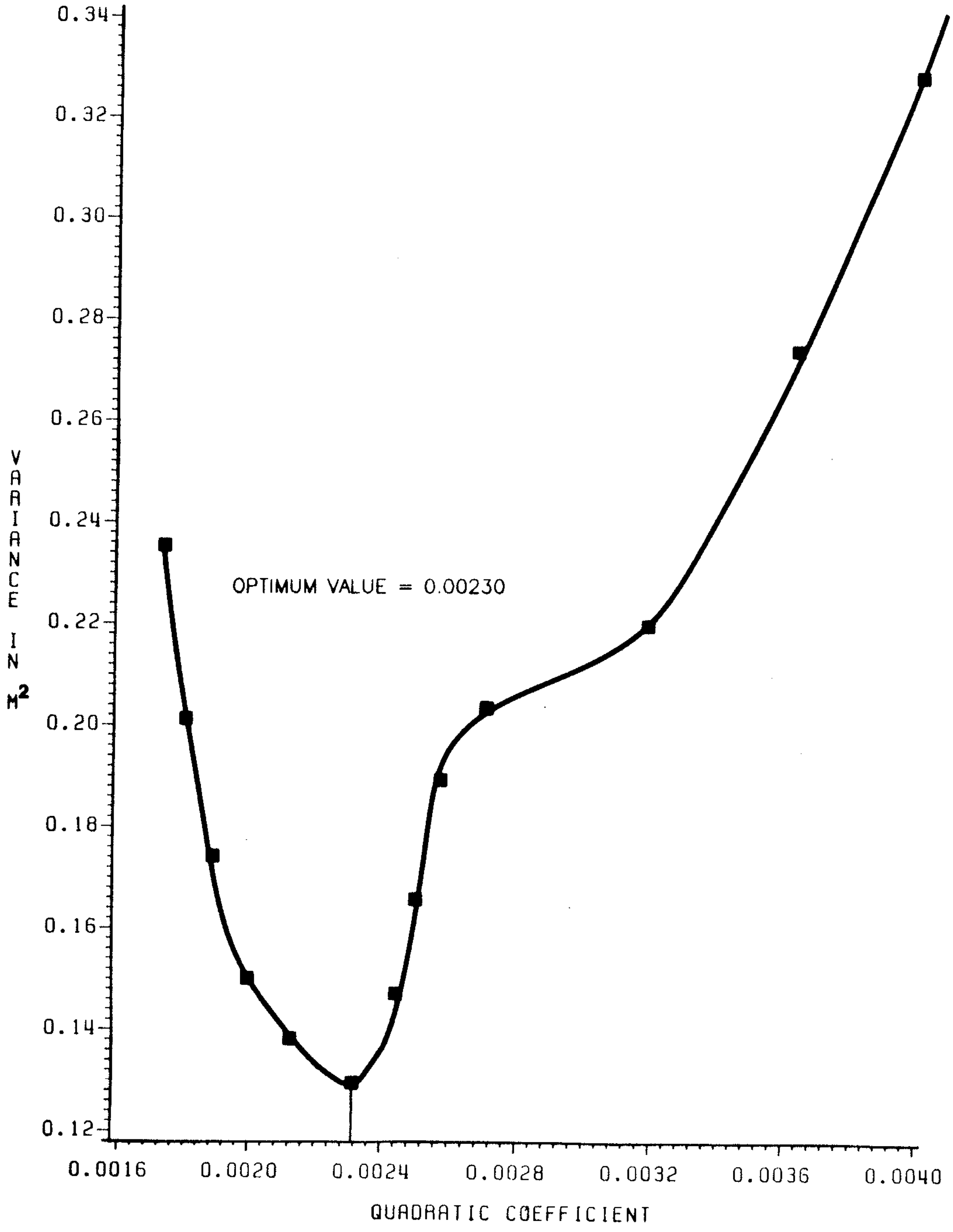
0.34
0.32
0.30
0.28
0.26
0.24
0.22
0.20
0.18
0.16
0.14
0.12
VARIANCE IN M²
OPTIMUM VALUE = 0.00230
0.0016
0.0020
0.0024
0.0028
0.0032
0.0036
0.0040
QUADRATIC COEFFICIENT

(e)

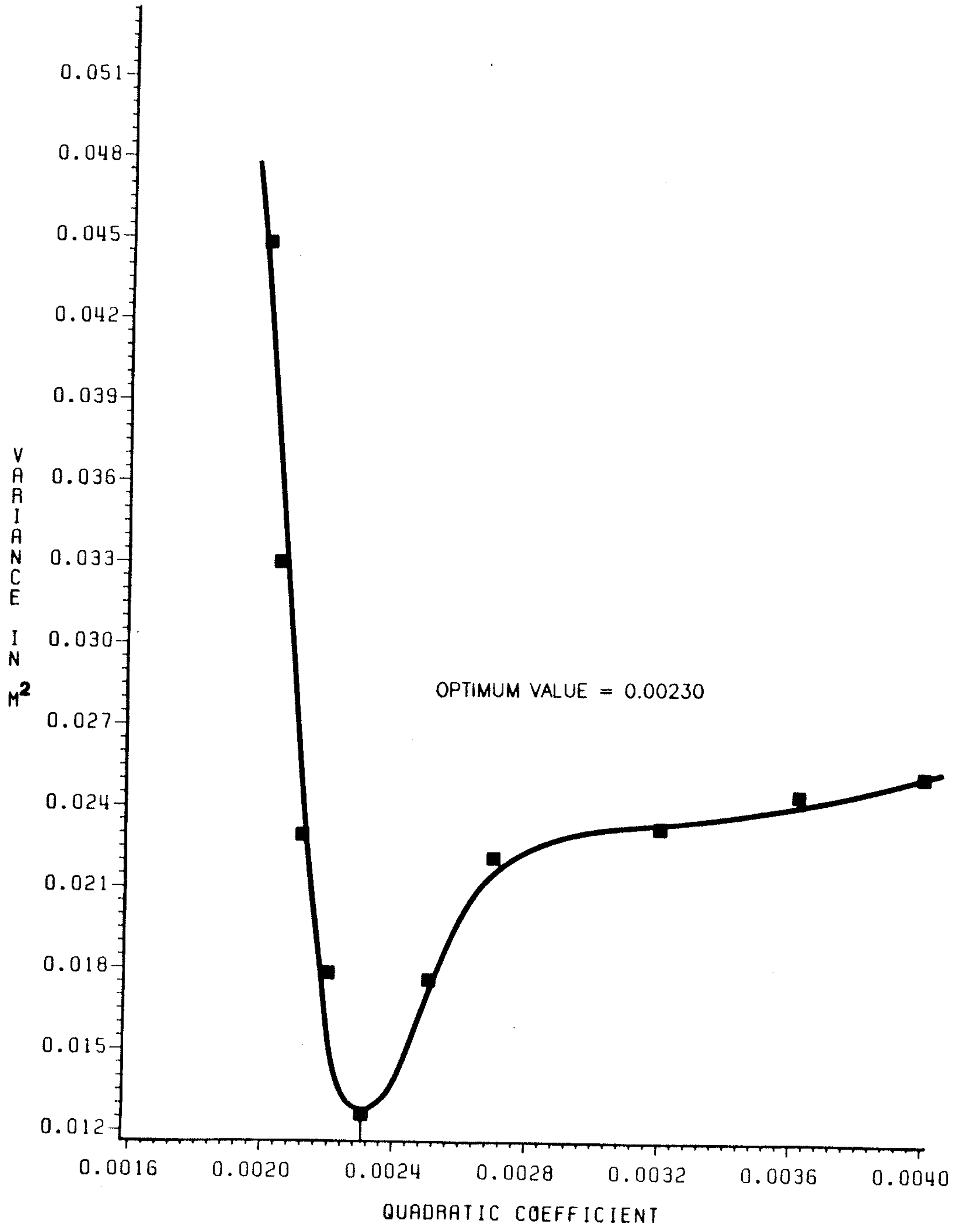

0.051
0.048
0.045
0.042
0.039
0.036
0.033
0.030
0.027
0.024
0.021
0.018
0.015
0.012
VARIANCE IN M2
OPTIMUM VALUE = 0.00230
0.0016
0.0020
0.0024
0.0028
0.0032
0.0036
0.0040
QUADRATIC COEFFICIENT

(f)

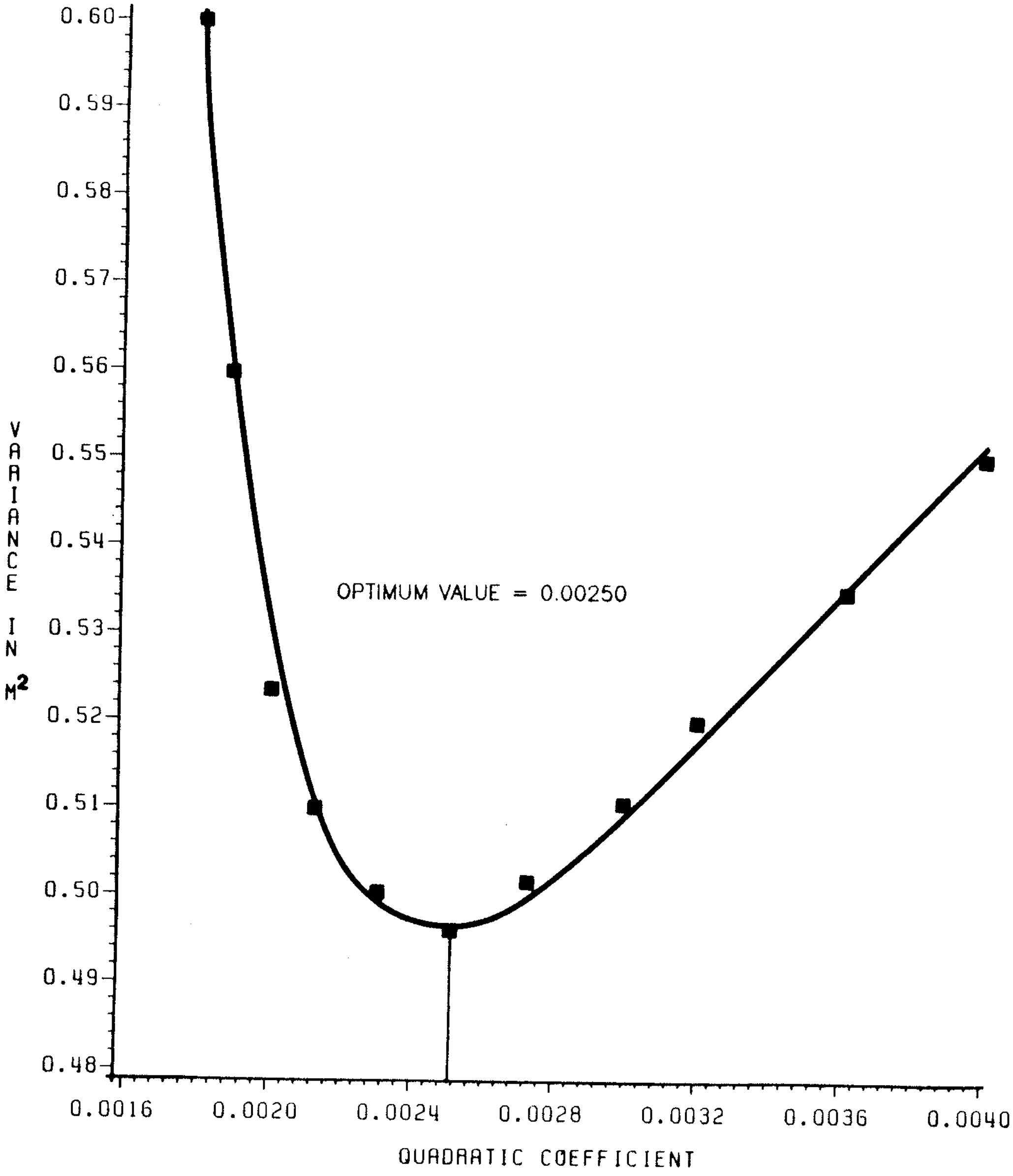
0.60
0.59
0.58
0.57
0.56
0.55
0.54
0.53
0.52
0.51
0.50
0.49
0.48
VARIANCE IN M²
OPTIMUM VALUE = 0.00250
0.0016
0.0020
0.0024
0.0028
0.0032
0.0036
0.0040
QUADRATIC COEFFICIENT

(g)

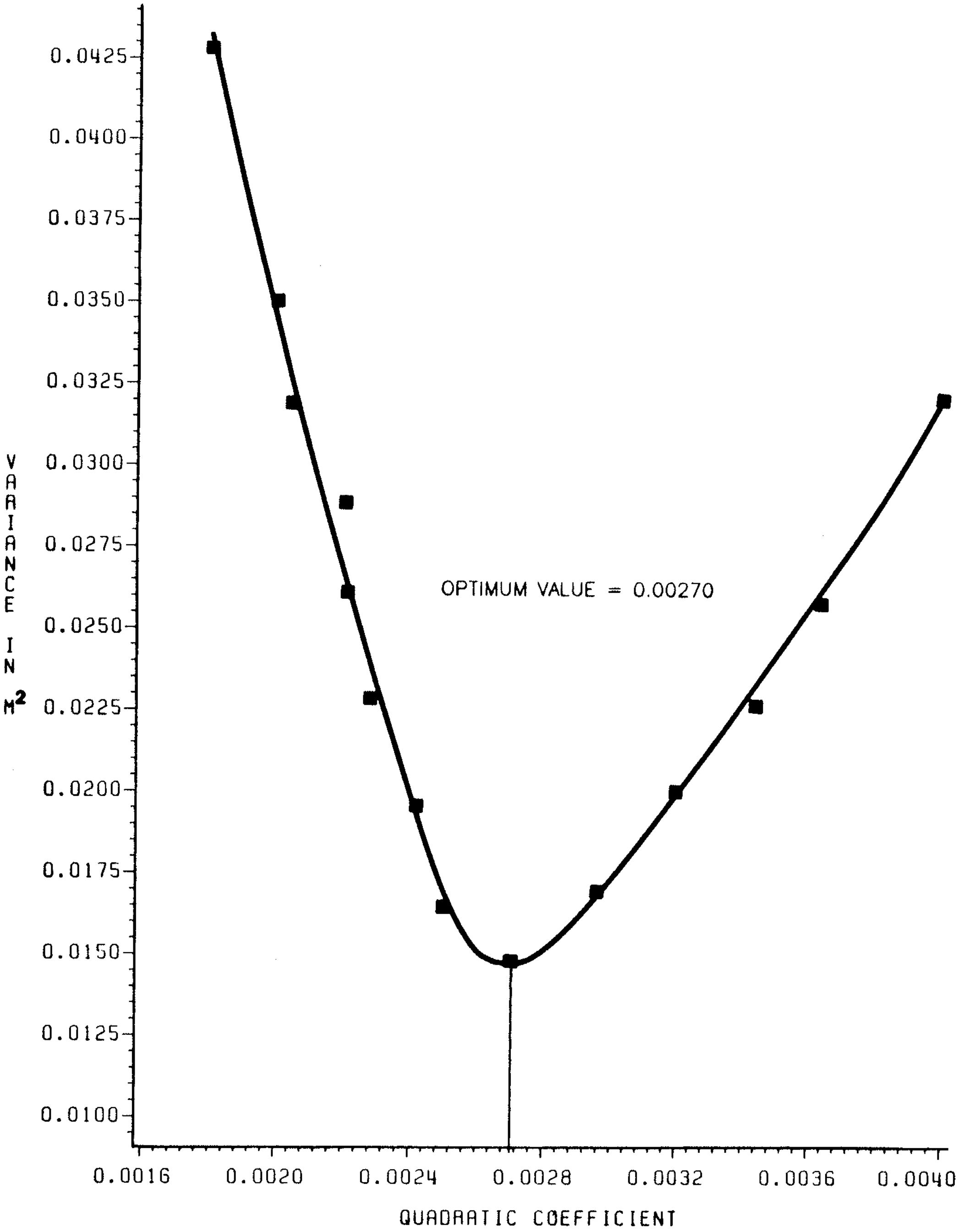
OPTIMUM VALUE = 0.00270
VARIANCE IN M²
0.0425
0.0400
0.0375
0.0350
0.0325
0.0300
0.0275
0.0250
0.0225
0.0200
0.0175
0.0150
0.0125
0.0100
0.0016
0.0020
0.0024
0.0028
0.0032
0.0036
0.0040
QUADRATIC COEFFICIENT

(h)

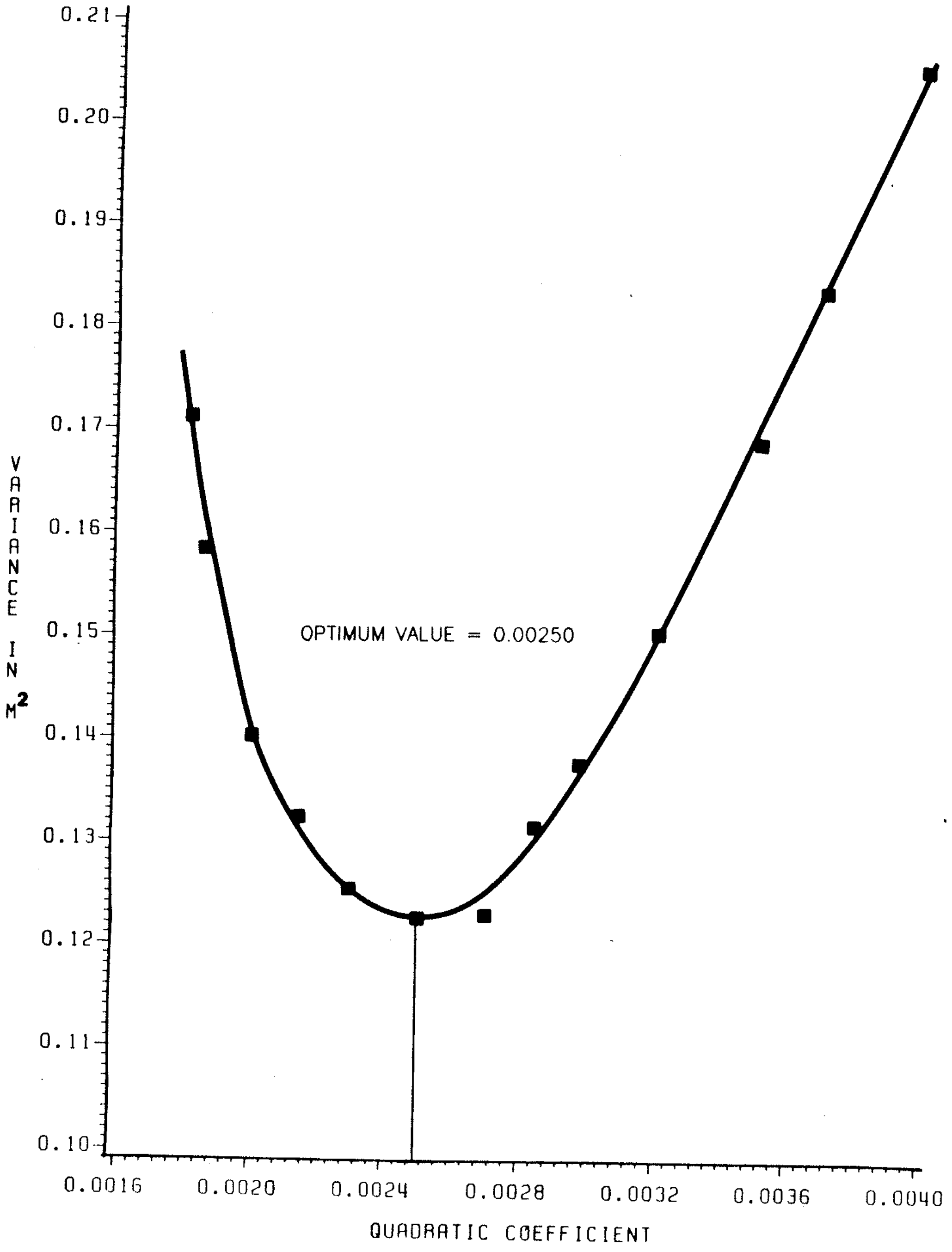
0.21
0.20
0.19
0.18
0.17
0.16
0.15
0.14
0.13
0.12
0.11
0.10
VARIANCE IN M^2
OPTIMUM VALUE = 0.00250
0.0016
0.0020
0.0024
0.0028
0.0032
0.0036
0.0040
QUADRATIC COEFFICIENT

(i)

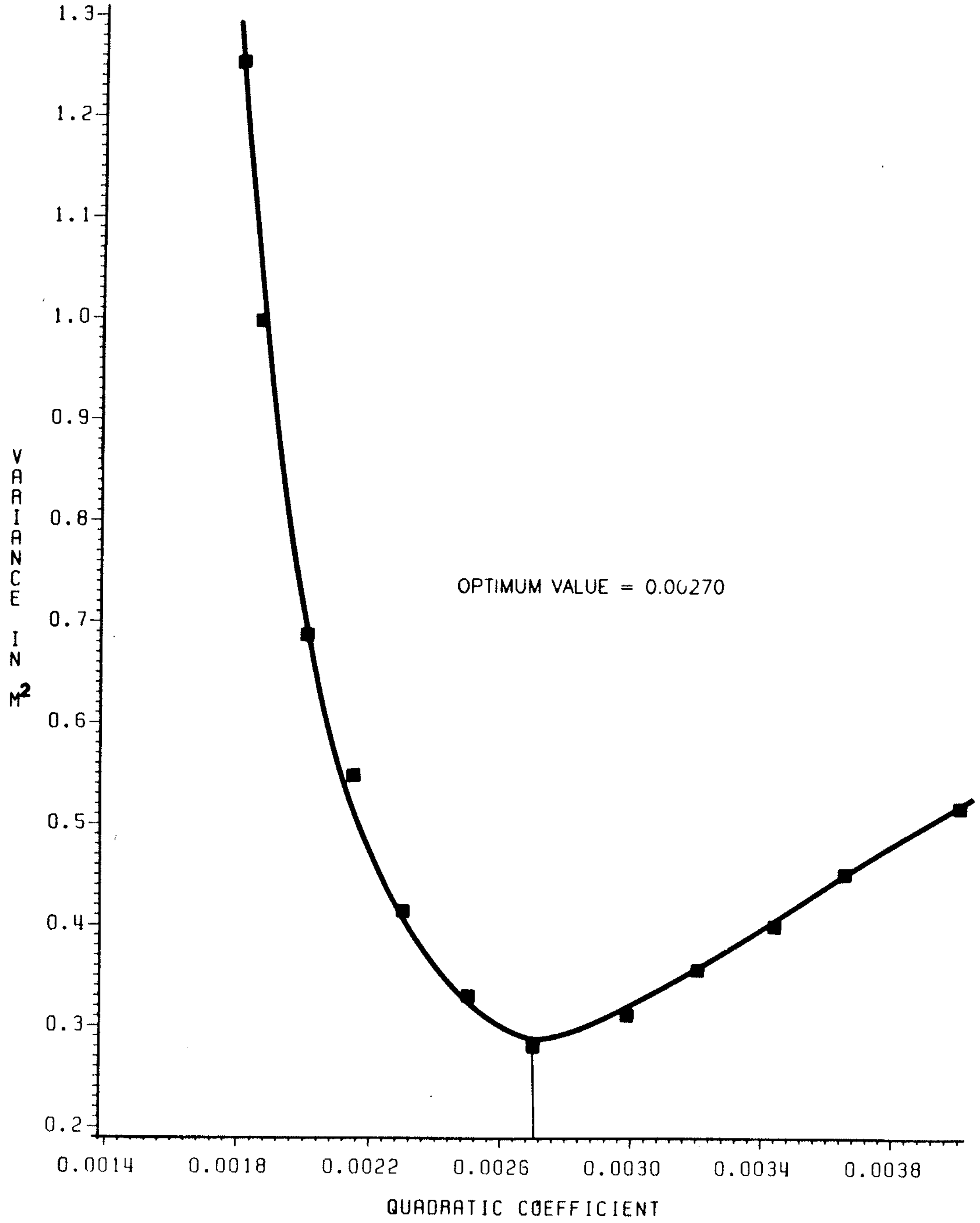
1.3
1.2
1.1
1.0
0.9
0.8
0.7
0.6
0.5
0.4
0.3
0.2
VARIANCE IN M^2
OPTIMUM VALUE = 0.00270
0.0014
0.0018
0.0022
0.0026
0.0030
0.0034
0.0038
QUADRATIC COEFFICIENT

(j)

CHAPTER VII

CONCLUSIONS

Two most common ocean bottom friction laws have been examined in this thesis. By implementing these laws and varying the bottom frictional coefficients in the numerical scheme, surprisingly good agreement between the SEASAT-ALT observation and theoretical value is obtained. The measurement of the variance between the observations and computations allows an optimum value for the ocean frictional coefficient to be derived. The results conclusively show a consistency with the conventional adopted values.

In the case of Hudson Bay, a range of linear frictional coefficient between 0.239 cm/s to 0.712 cm/s was found, although most values are in the neighbourhood of 0.255 cm/s. When quadratic bottom friction is implemented as a dissipation term, an optimum value for quadratic coefficient of 0.00234 is derived with an overall average of 0.0028. The deviation of the derived values is largely due to the inaccuracy of weather information and partly due to numerical approximations, ignorance of the low frequency effects and ocean tides and inaccuracy of the reference altimetric-derived geoid. Also the low magnitude wind speed associated with the selected time periods may further signify the dominance of the above quantities. The high values of linear coefficient of 0.712 cm/s and quadratic coefficient of 0.00465 in Hudson Bay can have uncertain but significant meaning. They might simply indicate an underestimation of current velocity in the bottom friction law, but with the available information in this area, this can not be explained.

With some improvement in the sea model, the procedure is extended to a different area, East China Sea and Yellow Sea, for more detailed testing. The well known ocean tidal phenomena in this area suggest the inclusion of ocean tide. Also the wind speed is chosen to be in the range of typhoon (up to 40 m/s) to study the influence of stormy environment on the ocean bottom friction study. The quadratic coefficient obtained through the objective optimization show a much smaller deviation ranging from 0.0023 to 0.0027 with a mean value of 0.0025.

Undoubtedly, the accuracy of the results in both areas have to be subjected to certain error bounds simply because the conclusions rest upon a series of steps, each of which has poorly defined sources of error that are difficult to quantify. Assuming all these small unresolvable problems are negligible, however, the numerical values of the linear and quadratic bottom friction coefficients obtained in these areas are acceptable for storm surge type or ocean tide modelling.

The simulation of the response of the sea due to the meteorological forcings has clearly demonstrated the importance of the transient sea state in SEASAT altimetry, an effect which is frequently ignored by most SEASAT users. By combining the wind prediction model with the iterative hydrodynamic modelling scheme, one could routinely make this type of transient sea state correction. This procedure can be incorporated with complex tidal modelling for more detailed oceanographic satellite data analysis, particularly in some areas where other global types of ocean tide models fail to give precise information on tide.

For about 780 comparisons made between the SEASAT-ALT inferred winds and the geostrophically sea surface winds, a mean difference of 1.4 m/s and a standard derivation of 1.8 m/s are obtained over a range of wind speed from 1 m/s to 10 m/s. The results of comparison show some degree of correlation of winds between two sources as described. However, it is still difficult at this stage to make any general statment on the accuracy since the reliability of both methods has yet to be fully determined. Whereas the accuracy of the wind speed derived from the mean sea level pressure depends on the quality of the charts, the three-branch logarithmic relationship, which is used to retrieve wind speeds from satellite altimetry, was obtained through the use of bouy measurements and ship reports. These data contain inherent uncertainty. The main advantage of using wind prediction model is its continuous estimation of wind speed pattern and its use of mean sea level atmospheric pressure data, so that the wind may be closer to the ground truth than that derived from remote areas along track satellite sensor.

References

Bowden, K. F., Physical problems of the benthic boundary layer, Geophysical Surveys, 3, 255-296, 1978.

Bowden, K.F. and L.A. Fairbairn, A determination of frictional forces in tidal current, Pro. Roy. Soc., A214, 371-392, 1952.

Bowden, K.F. and L.A. Fairbairn, Measurements of turbulent flucat-ions and Reynolds stresses in a tidal current, Proc. Roy. Soc. A237, 442-438, 1956.

Bowden, K.F. and S.R. Ferguson, Variation with height of the turbulent in the tidally-induced bottom boundary layer, in Marine Turbulent, ed. Nichoul, J.C.J., Elsevier Oceanography Series 28, 1980.

Bowden, K.F., L.A. Fairbairn and P. Hudges, The distribution of shearing stress in a tidal current, Geophys. J.R. Astro. Soc., 2, 288-305, 1959.

Brocks, K. and L. Krugermeyer, The hydrodynamics roughness of the Sea surface, In Gordon, K. (editor) Studies in Physical Oceanography, 1, 75-92, 1972.

Brown, G.S., H.R., Stanley, and N.A.,Roy, The wind speed measurement capability of spaceborne radar altimeter, IEEE J. Oceanic Eng., OE-6, 59-63, 1981.

Cartwright, D.E. and G.A. Alcock, On the precision of the sea surface elevations and slopes from SEASAT altimetry of the northeast Atlantic Ocean, Oceanography form Space, Gower, J.F.R. (editor), Plenum Publishing Corporation, 1981.

Charnock, H., Tidal friction from current near the North Sea bed, Geophys. J.R. Astro. Soc., 2, 215-221, 1959.

Charnock, H. and J. Crease, North Sea surges, Sci. Prog. London. 45 494-511, 1957.

Choi, B.H., A tidal model for East China Sea and Yellow Sea, Korea Ocean Research and Development Institute (KORDI), rep.

80-02, 1980.

Choi, B.H., Mathematical modelling of tides and surges in the East China Sea, Paper presented in the International Union of Geophysics and Geodesy, Hamburg, West Germany, 1983.

Choi, B.H., Personal Communication, 1984.

Chriss, T.M. and D.R. Caldwell, Evidence for influence of form drag on bottom boundary layer flow, J. Geophys. Res., 87, 4148-4154, 1982.

Davies, A.M.,Application of a fine mesh numerical model of the North Sea to the calculation of storm surge elevations and currents, Rep. Inst. Oceanogr. Sci., No. 28, 30 pp., 1976.

Davies, A.M. and R.A. Flather, Application of numerical models of the north-west European continental shelf and the North Sea to the computation of the storm surges of November to December, Dt. hydrogr. Z. Erganzungsheft, A., No.14, 1978.

Ferdor, L.S. and G.S. Brown, Waveheight and wind speed measurements from the SEASAT radar altimeter, J. Geophys. Res., 87, C5, 3254-3260, 1982.

Flather,R.A., Analytical and numerical studies in the theory of tides and storm surges, Ph.D. thesis, University of Liverpool, 1972.

Flather, R.A., A tidal model of the north-west European continental shelf, Mem. Soc. r. Sci. Liege, 6 ser., 10, 141-164, 1976.

Flather, R.A., Recent results from a storm surge prediction scheme for the North Sea, in Marine Forecasting, ed. Nihoul, J.C.J., Proc. 10th int. Liege Coll. Ocean Hydrodynamics, 1978, 385-409, 1979.

Flather,R.A. and A.M.Davies, On the specification of meteorological in numerical models for North Sea storm surge prediction, with application to the surge of 2 to 4 January 1976, Dt hydrogr. Z. Erganzungsheft, A, No.15, 51, 1978.

Flather, R.A. and N.S. Heaps, Tidal computation for Morecambe Bay, Geophys. J.R. Astr. Soc., 42, 489-517, 1975.

Fu, L.L., Recent progress in the application of satellite altimetry to observing the mesoscale variability and general circulation of the oceans, Rev. Geophys. Space Phys., 21, 1657-1666, 1983.

Garratt, J.R.,Review of drag coefficient over oceans and continents, Mon. Weather Rev., 105, 915-929, 1977.

Gerald, C.F., Applied numerical analysis, Addison-Wesley Publishing Company, 2 nd edition, 1980.

Grace, S.F., The influence of friction on the tidal motion of the Gulf of Suez, Mon. Notic. Roy. Astron. Soc., Geophys. Suppl., 2, 316, 1930.

Grace, S.F., The influence of friction on the tidal motion of the Gulf of Suez, Mon. Notic. Roy. Astron. Soc., Geophys. Suppl., 7, 309-318, 1931.

Groen, P. and Groves, G.W., Surges, in The Sea, 1, 611-646, e.d. Hill, M.N., Wiley, New York, 1962.

Hasse, L. and V. Wagner, On the relationship between geostrophic and surface wind on sea, Mon. Weather Rev., Wash., 99, 225-260, 1971.

Heaps, N.S., Storm surge on continental shelf, Phil. Trans. R. Soc., A, 257, 351-383, 1965.

Heaps, N.S., A two-dimensional numerical sea model, Phil. Trans. R. Soc., A, 265, 93-137, 1969.

Heaps, N.S., Storm surges, 1967-1982, Geophys. J.R. Astro. Soc., 74, 331-376, 1983.

Heaps, N.S. and J.E.Jones, Recent storm surge in Irish sea, Marine Forcasting, Elsevier Scientific Publishing Company, 1979.

Heathershaw, A.D., Measurement of turbulent in the Irish Sea benthic boundary layer, in The Benthic Boundary Layer, ed. McCave, I.N., Plenum Press, N.J.,11-31, 1976.

Hess, S.L.,Introduction to Theoretical Meteorology, Holt, Rinehart, and Winston, New York, 1959.

Hsueh, Y. and R.D., Romea, A comparison of observed and geostrophically calculated wintertime surface wind over the East China Sea, J. Geophys. Res., 88, C14, 9588-9594, 1983.

Jeffreys,H., On the turbulence in the ocean, Phil. Mag., 6, 578-586, 1920.

Jeffreys, H., Tidal frictional of shallow sea, Phil. Trans. R. Soc. (London), A221, 239-264, 1921.

Jones, W.L., D.H. Schroeder, D.H. Boggs, E.M. Bracalente, R.A.Brown, G.J. Dome, W.J. Pierson, and F.J. Wentz, The SEASAT - A Satellite Scatterometer: The geophysical evaluation of remotely sensed wind vectors over the ocean, J. Geophys. Res., 87, C5, 3297-3317, 1982.

Kagan, B.A., Sea bed friction in a one-dimensional tidal current, Izvestiya, Atmospheric and Oceanic Physics 8: 780-785, 1971.

Kolenkiewicz,R. and C.F.Martin, SEASAT altimeter height calibration J. Geophys. Res., 87, C5, 3187-3197, 1982.

Lambeck, K., Effects of tidal disspation in the oceans on the Moon's orbit and the Earth's rotation, J. Geophys. Res., 80, 2917-2925, 1975.

Lambeck, K., Tidal dissipation in the oceans: astronomical, geophysical and oceanographic consequences, Phil. Trans. R. Lond., A287, 554-594, 1977.

Lambeck, K., The Earth's Variable Rotation: Geophysical causes and consequences, Cambridge University Press, 1980.

Lame, D.B., G.H. Born, J.A. Dunne, A.J. Spear and C.A. Yamarone, SEASAT performance evaluation: The first two steps, IEEE J. Oceanic Eng., OE-5, 72-73, 1980.

Large, W.G., The turbulent fluxes of momentum and sensible heat over the open sea during moderate to strong wind, Ph.D. thesis, Univ. of British Columbia, Vancouver, Canada, 1979.

Larson ,L.H. and G.A. Cannon, Tides in the East China Sea, Paper presented to the Symposium on sedimentation on the continental shelf, Hangzhon, China, 1983.

Le Provost, C., An analysis of SEASAT altimeter measurements over a coastal area: The English Channel, J. Geophys. Res., 88, C3, 1647-1654, 1983.

Lerch, F.J., C.A. Wagner, S.M. Klosko, and B.H. Putney, Goddard earth models for oceanographic applications (GEM 10B and 10C), Marine Geodesy, 5(2), 2-43, 1981.

Lorell, J., M.E. Parke and J.F. Scott,SEASAT geophysical data record (GDR) user's handbook, JPL Intern. Rep. 622-97, revision A, Jet Propul. Lab., Pasadena, Calif., Sept 1980.

Lui, P.K., Personal Communication, 1982.

Marsh, J.G. and T.V. Martin, The SEASAT altimeter mean sea surface model, J. Geophys. Res., 87, C5, 3269-3280, 1982.

Marsh, J.G. and R.G. Williamson, Precision orbit analyses in support of the SEASAT altimeter experiment, J. Astronaut. Sci., XXVIII(4), 345-369, 1980.

Miller, G.R., Tsunamis and tides, Thesis, University of California, San Diego, 1964.

Miller, G.R., The flux of tidal energy out of the deep oceans, J. Geophys. Res., 71, 2485-2589, 1966.

Moon, W. and R. Tang, On the hydrodynamic correction of SEASAT altimeter data (Hudson Bay area of Canada), Marine Geodesy, (accepted for publication), 1984.

Munk, W.H. and G.J.F. MacDonald, The Rotation of the Earth, a geophysical discussion, Cambridge University Press, 1960.

Parke, M.E. and M.C. Hendershott, M2, S2, K1 models of the global ocean tide on an elastic earth, Marine Geodesy, vol 3, 379-408, 1980.

Pekeris, C.L. and Y. Accad, Solution of Laplace's equation for the M2 tide in the world oceans, Phil. Trans. Roy. Soc. London, A265, 413, 1969.

Phillips, O.M.,The dynamics of the upper ocean, Cambridge University Press, New York, 1977.

Prandle, D. and J. Wolf, The interaction of surge and tide in the North Sea and River Thames, Geophys. J. R. Astro. Soc., 55, 203-216, 1978a.

Prandle, D. and J. Wolf, Surge - tide interaction in the southern North Sea, in Hydrodynamics of Estuaries and Fjords, ed. Nihoul, J.C.J., Proc. 9th int. Liege Coll. Ocean Hydrodynamics, 1977, page 161 - 185, Elsevier, Amsterdam, 1978b.

Proudman, J., Dynamical Oceanography, Methuen, London. John-Wiley, New York. 1954.

Ramming, H.G., Numerical investigation of the influence of coastal stuuctures upon the dynamic off-shore process by application od a nested tidal model, in Hydrodynamics of Estuaries and Fjords, ed. Nihoul J.C.J., Elsevier Oceanography Series 23, 1978.

Ramming, H.G. and Z. Kowalik, Numerical Modelling of Marine Hydrodynamics, Elsevier Oceanography Series 26, 1980.

Roberts, K.V and N.O. Weiss, Convective difference schemes, Math. Comput., 20, 272-299, 1976.

Schultz, B.E., B.D. Tapley and C. Shum, Evaluation of the SEASAT altimeter time tag bias, J. Geophys. Res., 87, 3239-3245, 1982.

Schwiderski,E.W.,Global ocean tides, Part I: A detailed hydrodynamic interpolation model, NSWC/DL, Tr-3866, Naval Surface Weapons Center, Dahlgren, Va., 1978.

Schwiderski, E.W., On charting global ocean tides, Rev. of Geophs. and Space Phys., vol 18, 1, 1980.

Smith, S.D., Wind stress and heat flux over the ocean in gale force winds, J. Phys. Oceanogr., 10, 709-726, 1980.

Sternberg, R.W., Friction factors in tidal channels with differing bed roughness, Mar. Geol., 6, 243-260, 1968.

Stock, G.G., Modelling of tides and tidal dissipation in the Gulf of California, PhD dissertation, University of Califorina, San Diego, 1976.

Sverdrup, H.U., M.W., Johnson and R.H., Fleming, The oceans, their Physics, Chemistry and General Biology, Prentice-Hall Englewood, Cliffs, N.J., 1942.

Tang, R. and W. Moon, Finite difference transient sea surface modelling for the SEASAT altimeter data correction, Congressus Numerantium, vol 42, 299-312, 1984.

Tapley, B.D., B.E. Schultz, J.G. Marsh, W.F. Townsend and G.H. Born (Eds.) Accuracy assessment of the SEASAT orbit and altimeter height measurement, Tech. Rep. 79-5, Inst. for Advan. Stud. in Orbital Mech., Univ. of Tex. at Austin, 1979.

Tapley, B.D., G.H. Born, and M.E. Parke,The SEASAT altimeter data and its accuracy assessment. J. Geophys. Res., 87, C5, 3179-3188, 1982.

Townsend, W.F., An initial assessment of the performance acheived by the SEASAT-1 radar altimeter, IEEE J. Oceanic Eng., OE-5(2), 80-82, 1980.

Weatherly, G.L. and M. Wimbus, Near-bottom speed and temperature observations on the Blake-Bahama Outer Ridge, J. Geophys. Res., 85, 3971-3981, 1980.

Weenink, M.P.H., A theory and method of calculation of wind effects on sea levels in a partly-enclosed sea, with special application to the southern coast of the North Sea, Koninklijk Nederlands Meterologisch Instituut, Mededelingen en Verhandelingen, 73, 1958.

Wentz. F.J., V.J. Cardone, and L.S. Fedor,Intercomparisons of wind speeds inferred by the SASS, Altimeter, and SMMR. J. Geophys. Res., 87, C5, 3378-3384, 1982.

Wolf, J., Estimation of the shearing stress in a tidal current with application to the Irish Sea, in Marine Turbulence, ed. Nihoul, J.C.J., Elsevier Oceanography Series 28, 1980.

Wu, J., Wind stress and surface roughness at air-sea interface, J. Geophys. Res., 74, 444-455, 1969.

Wu, J., Wind-stress coefficients over sea surface near neutral conditions: A revisit, J. Phys. Oceanogr., 10 727-747, 1980.

Wu, J., Wind-stress coefficients over sea surface from breeze to hurricane, J. Geophys. Res., 87, C12, 9704-9706, 1982.

Zahel, W., The influence of solid earth deformations on semidiurnal and diurnal oceanic tides, in tidal friction and the earth's rotation, 98-124, Editor Brosche, P. and Sunderman, J., Springer-Verlag, New York, 1978.